

Nonlinear Evolution of Localized Internal Gravity Wave Packets:  
Theory and Simulations with Rotation, Background Flow, and Anelastic Effects

by

Alain Daniel Gervais

A thesis submitted in partial fulfillment of the requirements for the degree of

Doctor of Philosophy

in

APPLIED MATHEMATICS

Department of Mathematical and Statistical Sciences  
University of Alberta

© Alain Daniel Gervais, 2023

---

## Abstract

---

A series of three studies investigates theoretically and numerically the evolution, stability, and pseudomomentum transport of fully localized three-dimensional internal gravity wave packets, as they self-interact nonlinearly with their induced mean flow.

The first study considers a rotating, uniformly stratified Boussinesq fluid that is stationary in the absence of waves. We derive through perturbation theory an integral expression for the mean “Bretherton flow” induced by fully localized wave packets influenced by the Coriolis force. We perform numerical simulations of fully localized wave packets with the predicted Bretherton flow superimposed, for a range of initial amplitudes, wave packet aspect ratios, and relative vertical wavenumbers spanning the hydrostatic and nonhydrostatic regimes. Results are compared with predictions based on linear theory of wave breaking due to overturning, convection, self-acceleration, and shear instability. We find that nonhydrostatic wavepackets tend to destabilize due to self-acceleration, eventually overturning although the initial amplitude is well below the overturning amplitude predicted by linear theory. Strongly hydrostatic waves are found not to attain amplitudes sufficient to become shear unstable, overturning instead due to localized steepening of isopycnals. Results are discussed in the broader context of previous studies of one- and two-dimensional wave packet overturning, and recent observations of oceanic internal waves.

The second study considers the transmission and reflection of finite amplitude internal gravity wave packets across a reflection level in a nonrotating Boussinesq fluid with a nonuniform retrograde shear flow. We derive the critical amplitude for wave packets to transmit partially above the reflection level predicted by linear theory. We find that transmitted and reflected wave packets corresponding to strongly nonhydrostatic primary waves can interact resonantly to generate quadratically nonlinear secondary wave packets. We propose a novel

weakly nonlinear mechanism to explain the generation of secondary wave packets by non-breaking moderately nonhydrostatic primary waves, and predict the critical amplitude for its onset. Simulations are performed for a range of nonhydrostatic wave packets with small to moderately large initial amplitudes with their predicted Bretherton flow superimposed. Transmission is quantified using the pseudomomentum corresponding to upward-propagating waves above the reflection level. In most cases transmission transiently grows and decays as wave packets first cross and then reflect from the reflection level. For all but the most strongly nonhydrostatic wave packets, larger-amplitude waves exhibit smaller peak transmission, relative to the total pseudomomentum. Strongly nonhydrostatic wave packets exhibit continuous transmission well above the reflection level. When we consider the time interval for transmission to decrease to half its peak value, we find this becomes longer with larger initial amplitude. These behaviours result from the combined effects of modulational instability, and the generation and evolution of secondary wave packets. Results are discussed in the context of previous studies of one- and two-dimensional wave packet transmission and reflection.

The third study considers the transmission and reflection of three-dimensional internal gravity wave packets in an anelastic gas in which the background flow models the Quasi-Biennial Oscillation (QBO). We derive an integral expression for the anelastic Bretherton flow, and the conditions for wave packets to tunnel partially through the QBO winds. Simulations are performed for a range of moderately nonhydrostatic wave packets with their predicted Bretherton flow superimposed, incident upon two model QBO profiles. Transmission is quantified using the pseudomomentum of waves above the QBO. Transmission decreases as wave packets are initialized to be progressively more nonhydrostatic. Varying initial wave amplitude is found to have no quantitative effect on transmission (relative to the initial pseudomomentum) for physically relevant initial amplitudes because nonlinear interactions with the Bretherton flow occur on a significantly slower time scale than that of transmission. Transmitted wave packets tend to grow exponentially in amplitude due to the exponentially decreasing atmospheric background mass density, ultimately inducing a local mean flow that acts to drive the waves to overturn and break turbulently. Results are discussed in the context of previous studies of one- and two-dimensional wave packet transmission and reflection, and of the theorized role of internal gravity waves in driving QBO dynamics.

---

## Preface

---

A condensed version of Part I of this thesis has been published as [Gervais, A. D., Q. Ede, G. E. Swaters, T. S. van den Bremer, and B. R. Sutherland, 2021: Propagation and overturning of three-dimensional Boussinesq wave packets with rotation. \*Phys. Rev. Fluids\*, \*\*6\*\*, 044801, doi: 10.1103/PhysRevFluids.6.044801](#). I was responsible for project management, developing the theory, modifying and parallelizing the numerical code, running simulations, analyzing results, and composing and submitting the manuscript. Q. Ede performed some theory and exploratory simulations while working as a summer student. Professor Dr. G. E. Swaters contributed research support funding and final manuscript approval. Dr. T. S. van den Bremer contributed to the analysis and manuscript editing. Professor Dr. B. R. Sutherland proposed the research problem, contributed research support funding, secured supercomputing resources, parallelized some numerical routines, and edited the manuscript.

A condensed version of Part II of this thesis has been published as [Gervais, A. D., G. E. Swaters, and B. R. Sutherland, 2022: Transmission and reflection of three-dimensional Boussinesq internal gravity wave packets in nonuniform retrograde shear flow. \*Phys. Rev. Fluids\*, \*\*7\*\*, 114802, doi: 10.1103/PhysRevFluids.7.114802](#). I was responsible for proposing the research problem, project management, developing the theory, modifying the numerical code, running simulations, analyzing results, and composing and submitting the manuscript. Professor Dr. G. E. Swaters contributed research support funding and final manuscript approval. Professor Dr. B. R. Sutherland contributed research support funding, secured supercomputing resources, debugged some code, and edited the manuscript.

---

## Dedication

---

To my parents, Paul and Joanne, for their constant love and support.

---

## Acknowledgments

---

There are so many people to thank throughout the many years I've put into my education culminating in this PhD thesis. First and foremost, I want to thank my parents, Paul and Joanne, who have been behind me since the literal beginning, for raising me to want to never stop learning. To my siblings, Joël, Jules, and Chantelle, and extended family: thank you for lending an ear to listen to my rants about seemingly insurmountable challenges, and for celebrating with me when those challenges were ultimately vanquished.

To my supervisors, Drs. Gordon Swaters and Bruce Sutherland: thank you for your constant support over the years, in all the ways you expressed it—through your guidance, your endorsement through countless scholarship applications, by providing summer research funding, and through your generosity over casual chats at the University Club, or over smoked brisket, and kind hospitality in Kelowna. To the other members of my supervisory committee, Drs. Xinwei Yu and John Bowman: thank you for your interest in my work, for dedicating your time to reading my thesis, and for your service on my supervisory committee.

Although I can never thank each individual who played a part in getting me where I am today, I do want to thank a few particularly impactful people by name: my high school math teacher, Mme. Larose, who got me interested in math by teaching me the joys of calculus (merci!); my first university calculus instructor, Prof. Elizabeth Leonard, who solidified this enjoyment and inspired me to pursue a mathematics undergraduate degree; to my longtime friend Evan, whose friendship through our parallel academic journeys since the latter years of elementary school has been a source of constant motivation; and to my dear friend Gabrielle: for your encouraging words and listening ear over countless phone calls, video chats, and virtual beers, especially when I needed an audience to practice conference talks. By now you probably know about as much about internal gravity waves and induced mean flows as I do!

---

# Contents

---

<b>Contents</b>	<b>vii</b>
<b>List of tables</b>	<b>xiii</b>
<b>List of figures</b>	<b>xiv</b>
<b>1 Introduction</b>	<b>1</b>
1.1 Background and motivation . . . . .	1
1.1.1 Geophysical fluids and waves . . . . .	1
1.1.2 Internal gravity waves in general circulation models . . . . .	5
1.1.3 Wave packets and the wave-induced mean flow . . . . .	7
1.1.4 Goal of this thesis . . . . .	10
1.2 Essential concepts of internal gravity wave theory . . . . .	11
1.3 Outline of this thesis . . . . .	16
<hr/>	
<b>PART I Boussinesq wave packets with rotation</b>	<b>18</b>
<b>2 Theory</b>	<b>21</b>
2.1 Governing equations . . . . .	21
2.2 Wave-induced mean flow . . . . .	23
2.2.1 Perturbation theory . . . . .	25
2.2.2 Divergent-flux induced flow and response flow . . . . .	27
2.2.3 Bretherton flow . . . . .	29

2.2.4	Relative effect of rotation on the Bretherton flow . . . . .	34
2.3	Wave instability and critical amplitudes . . . . .	35
2.3.1	Static instability . . . . .	35
2.3.2	Convection instability . . . . .	36
2.3.3	Self-acceleration instability . . . . .	37
2.3.4	Stratified shear instability . . . . .	39
2.3.4.1	Comparison and analysis of gradient Richardson numbers . . . . .	41
<b>3</b>	<b>Numerical methods</b>	<b>43</b>
3.1	Governing equations . . . . .	44
3.2	Discretization, grid generation, and resolution . . . . .	45
3.3	Initialization . . . . .	49
3.3.1	Wave-induced mean flow . . . . .	50
3.4	Advection and temporal advancement . . . . .	51
<b>4</b>	<b>Results and discussion</b>	<b>55</b>
4.1	Evolution of a nonhydrostatic wave packet . . . . .	56
4.2	Evolution of a strongly hydrostatic wave packet . . . . .	59
4.3	Overturning of round wave packets . . . . .	60
4.4	Effect of changing wave packet aspect ratio . . . . .	63
4.5	Discussion and application to oceanographic observations . . . . .	64
<b>PART II Boussinesq wave packets in nonuniform background shear</b>		<b>67</b>
<b>5</b>	<b>Theory</b>	<b>71</b>
5.1	Linear theory . . . . .	71
5.2	Wave-induced mean flow and reflection level penetration . . . . .	74
5.3	Wave packet stability and critical amplitudes . . . . .	76
5.4	Secondary wave packet generation . . . . .	77
5.4.1	Triadic resonant instability . . . . .	78
5.4.2	Wave packet self-reflection . . . . .	80

5.5	Transmission coefficient . . . . .	82
<b>6</b>	<b>Numerical methods</b>	<b>86</b>
6.1	Governing equations . . . . .	86
6.2	Discretization, grid generation, and resolution . . . . .	87
6.3	Initialization . . . . .	88
6.3.1	Background flow . . . . .	89
6.3.2	Perturbation fields . . . . .	89
6.3.3	Wave-induced mean flow . . . . .	91
6.4	Advection and temporal advancement . . . . .	91
6.5	Dealiasing . . . . .	93
6.6	Transmission diagnostics . . . . .	94
6.6.1	Pseudomomentum conservation . . . . .	95
<b>7</b>	<b>Results and discussion</b>	<b>96</b>
7.1	Evolution of strongly nonhydrostatic wave packets . . . . .	97
7.1.1	Small amplitude wave packet: Linear evolution . . . . .	97
7.1.2	Moderately large amplitude wave packet: Transmission, reflection, and secondary wave generation . . . . .	99
7.1.3	Amplitude dependence of transmission . . . . .	102
7.2	Evolution of moderately nonhydrostatic wave packets . . . . .	103
7.3	Transmission analysis . . . . .	106
7.4	Discussion . . . . .	108
<b>PART III</b>	<b>Anelastic wave packets in nonuniform background flow</b>	<b>111</b>
<b>8</b>	<b>Theory</b>	<b>115</b>
8.1	From Boussinesq theory to an anelastic gas . . . . .	115
8.2	Governing equations . . . . .	117
8.3	Wave-induced mean flow . . . . .	119
8.3.1	Perturbation theory . . . . .	120

8.3.1.1	Expansion with respect to amplitude . . . . .	120
8.3.1.2	Expansion with respect to inverse wave packet extent . . . . .	121
8.3.2	Divergent-flux induced flow and response flow . . . . .	123
8.3.3	Bretherton flow . . . . .	126
8.4	Propagation of wave packets through a nonuniform background shear flow . . . . .	128
8.4.1	Linear theory . . . . .	129
8.4.2	Reflection level penetration . . . . .	130
8.4.3	Internal wave tunnelling . . . . .	132
8.5	Wave packet self-acceleration . . . . .	134
8.6	Idealized modelling of the Quasi-Biennial Oscillation . . . . .	136
8.6.1	Data selection . . . . .	137
8.6.2	Data postprocessing . . . . .	137
8.6.3	Model QBO profile . . . . .	138
8.7	Transmission coefficient . . . . .	142
<b>9</b>	<b>Numerical methods</b> . . . . .	<b>144</b>
9.1	Governing equations . . . . .	144
9.1.1	Anelastic scaling . . . . .	145
9.2	Discretization, grid generation, and resolution . . . . .	147
9.2.1	Approximation of vertical derivatives . . . . .	148
9.2.2	Boundary conditions . . . . .	150
9.2.2.1	Radiation boundary condition . . . . .	150
9.3	Initialization . . . . .	152
9.3.1	Wave-induced mean flow . . . . .	153
9.4	Pressure, advection, and temporal advancement . . . . .	154
9.4.1	Dynamic pressure diagnostic . . . . .	154
9.4.2	Advancing the prognostic fields . . . . .	155
9.4.3	Aliasing prevention . . . . .	156
9.5	Turbulence model . . . . .	157
9.6	Pseudomomentum diagnostics . . . . .	161

<b>10 Results and discussion</b>	<b>163</b>
10.1 Evolution of a small amplitude wave packet in a stationary atmosphere . . . .	165
10.1.1 Total pseudomomentum . . . . .	167
10.2 Evolution of wave packets incident upon the QBO-E . . . . .	169
10.2.1 Effect of amplitude on transmission . . . . .	171
10.2.2 Effect of vertical wavenumber on transmission . . . . .	172
10.3 Evolution of wave packets incident upon the QBO-W . . . . .	174
10.3.1 Reflection, transmission, and turbulent breaking of a nonhydrostatic wave packet . . . . .	174
10.3.2 Effect of vertical wavenumber and amplitude on transmission . . . . .	176
10.4 Discussion . . . . .	178
<hr/>	
<b>11 Summary and conclusions of thesis</b>	<b>180</b>
11.1 Summary and main results . . . . .	180
11.1.1 First project: Boussinesq wave packets with rotation . . . . .	181
11.1.2 Second project: Boussinesq wave packets in nonuniform background shear	183
11.1.3 Third project: Anelastic wave packets in nonuniform background flow .	185
11.2 Future work and final remarks . . . . .	187
<b>Bibliography</b>	<b>190</b>
<b>Appendices</b>	<b>207</b>
<b>A Polarization relations</b>	<b>207</b>
A.1 Waves in a Boussinesq fluid . . . . .	207
A.1.1 Dispersion relation and leading-order polarization relations . . . . .	208
A.1.2 Envelope-scale corrections to the leading-order polarization relations . .	209
A.2 Waves in an anelastic gas . . . . .	212
A.2.1 Dispersion relation and leading-order polarization relations . . . . .	212
A.2.2 Envelope-scale corrections to the leading-order polarization relations . .	214

<b>B Bretherton flow: Explicit form of the nonlinear forcing</b>	<b>216</b>
B.1 Boussinesq wave packets with rotation . . . . .	216
B.1.1 Divergent-flux induced flow . . . . .	217
B.1.2 Quadratically nonlinear forcing . . . . .	219
B.2 Anelastic wave packets . . . . .	226
B.2.1 Divergent-flux induced flow . . . . .	226
B.2.2 Quadratically nonlinear forcing . . . . .	228
<b>C Vertical profile of the maximum Bretherton flow</b>	<b>231</b>
<b>D Ray-theory prediction of wave packet path</b>	<b>233</b>
D.1 Ray theory . . . . .	233
D.2 Numerics . . . . .	234
D.3 Illustrative result . . . . .	235
<b>E Solution of the anelastic Poisson equation for dynamic pressure</b>	<b>237</b>
<b>F Subfilter-scale forcing terms for the anelastic evolution equations</b>	<b>241</b>

---

## List of tables

---

2.1	Leading-order and envelope-scale corrections to the polarization relations for Boussinesq wave packets with rotation. . . . .	26
4.1	Input conditions, domain size and resolution, and output diagnostics from a subset of fully nonlinear numerical simulations of Boussinesq wave packets with rotation. . . . .	56
7.1	Input conditions, domain size and resolution, and output diagnostics from a subset of fully nonlinear simulations of Boussinesq wave packets in a nonuniform background flow. . . . .	97
7.2	Data used to diagnose triadic resonant instability for a given simulation and time. . . . .	101
8.1	Leading-order and envelope-scale corrections to the polarization relations for anelastic wave packets. . . . .	123
8.2	Parameters for idealized models of mean easterly and westerly phases of the Quasi-Biennial Oscillation. . . . .	141
10.1	Input conditions, domain size and resolution, and predicted transmission coefficient from a subset of fully nonlinear simulations of anelastic wave packets in an idealized QBO wind. . . . .	164

---

## List of figures

---

1.1	Idealized profiles of mass density in the ocean and atmosphere, and of potential temperature in the atmosphere. . . . .	4
1.2	Example of a one-dimensional wave packet and its wave-induced mean flow. . .	8
1.3	Example of a two-dimensional wave packet and its wave-induced mean flow. . .	9
1.4	Example of a three-dimensional wave packet and cross sections of its wave-induced mean (Bretherton) flow. . . . .	10
1.5	Relationships between the dispersion relation and its first- and second-order partial derivatives with respect to its vertical and streamwise wavenumbers. . .	15
2.1	Horizontal cross sections of the initial nondimensionalized streamwise Bretherton flow for round, long, and wide wave packets and two Coriolis parameters. . .	33
2.2	Curves of marginal stability for wave packets in rotating Boussinesq fluid. . . .	36
4.1	Snapshots of a round, moderately large amplitude, nonhydrostatic wave packet.	57
4.2	Snapshots of a round, moderately large amplitude, strongly hydrostatic wave packet. . . . .	60
4.3	Time series of $\min\{\tilde{N}_T^2\}$ and $\min\{Ri_g\}$ for strongly nonhydrostatic and strongly hydrostatic wave packets. . . . .	61
4.4	Comparison of predicted stability regimes with the results of simulations of round wave packets. . . . .	62
4.5	Time series of $\min\{\tilde{N}_T^2\}$ and $\min\{Ri_g\}$ for nonhydrostatic and hydrostatic long and wide wave packets. . . . .	64

5.1	Critical amplitudes for reflection level penetration, self-acceleration instability, and secondary wave packet generation via self-reflection for wave packets in a Boussinesq fluid. . . . .	76
6.1	Sample profiles of background flow and corresponding shear. . . . .	90
7.1	Snapshots of a small amplitude nonhydrostatic wave packet in a vertically nonuniform background flow. . . . .	98
7.2	Time series of upward-propagating pseudomomentum above the reflection level for a set of nonhydrostatic simulations with $m_0 = -0.4k_0$ . . . . .	99
7.3	Snapshots of a moderately large amplitude nonhydrostatic wave packet and its constituent linear and quadratically nonlinear components. . . . .	100
7.4	Vertical time series of upward- and downward-propagating pseudomomentum associated with a moderately large amplitude nonhydrostatic wave packet. . . .	102
7.5	Vertical and horizontal cross sections at time $t = 200/N_0$ of the streamwise velocity field of a sequence of progressively more hydrostatic wave packets. . . .	104
7.6	Vertical time series of upward- and downward-propagating pseudomomentum associated with a sequence of progressively more hydrostatic wave packets. . . .	106
7.7	Pseudomomentum transmission diagnostics. . . . .	107
8.1	Vertical cross sections of the initial nondimensionalized streamwise Bretherton flow for a round wave packet without and with the anelastic growth factor. . .	128
8.2	Critical amplitudes for reflection level penetration and self-acceleration for wave packets in an anelastic gas. . . . .	131
8.3	Vertical time series of monthly-mean zonal QBO winds derived from radiosonde observations. . . . .	138
8.4	Profiles of selected QBO-E observations derived from radiosonde measurements, and profiles of their computed and modelled mean. . . . .	139
8.5	Profiles of selected QBO-W observations derived from radiosonde measurements, and profiles of their computed and modelled mean. . . . .	140

8.6	Transmission coefficient predicted from the numerical solution of the anelastic Taylor–Goldstein equation. . . . .	143
10.1	Snapshots of the vertical displacement field of a small amplitude wave packet in an anelastic atmosphere with no background flow. . . . .	166
10.2	Pseudomomentum density profiles and pseudomomentum time series for a small amplitude anelastic wave packet in a stationary atmosphere. . . . .	168
10.3	Snapshots of the vertical displacement field of a moderately nonhydrostatic wave packet tunnelling partially through the QBO-E. . . . .	170
10.4	Time series of pseudomomentum transmission above the QBO-E for moderately nonhydrostatic waves with a range of initial amplitudes. . . . .	172
10.5	Time series of pseudomomentum transmission above the QBO-E for small amplitude wave packets with a range of initial relative vertical wavenumbers. . . . .	173
10.6	Snapshots of the vertical displacement field of a moderately nonhydrostatic wave packet tunnelling partially through the QBO-W. . . . .	175
10.7	Time series of pseudomomentum transmission above the QBO-W for small amplitude wave packets with a range of initial relative vertical wavenumbers. . . . .	177
D.1	Predicted path traced by the centroid of a wave packet in a Boussinesq fluid with nonuniform background flow. . . . .	235

## Introduction

---

### 1.1 Background and motivation

A stratified fluid is one in which the effective density changes with height (e.g., [Sutherland, 2010](#)). Examples of stratified fluids are plentiful, existing in multiple physical contexts and across a broad range of spatial scales as small as a layered beverage and at least as large as stellar interiors ([Lecoanet, 2020](#)), representing horizontal scales spanning many orders of magnitude. In this thesis, we are interested in particular in stratified geophysical fluids on Earth, namely, the ocean and atmosphere.

#### 1.1.1 Geophysical fluids and waves

In the ocean, the mean profile of mass density of water increases with depth, due primarily to a decrease in temperature and an increase in salinity. The dominant between these factors is the temperature, whose profile is a result of the finite depth to which sunlight can penetrate (and hence warm) the water column (e.g., [Sutherland, 2010](#)). Because relatively warm, fresh water tends to overlie colder, more saline water, the fluid in this equilibrium state is said to be *stably stratified*. In this thesis, we consider *continuously stratified* fluids in which the effective density changes continuously as a function of height, as opposed to fluids in which the effective density changes abruptly, for example, at the interface where the ocean surface

meets the atmosphere.

In the atmosphere, the mass density of air likewise decreases with altitude, but the background temperature does not decrease monotonically through the depth of the atmosphere. The profile of background temperature effectively defines the layers of the atmosphere, in which temperature alternately decreases and increases within successive layers (e.g., [Ahrens et al., 2012](#)). The troposphere is the lowest layer of the atmosphere, extending from Earth’s surface to the tropopause, located at about 10–15 km altitude. Above this layer are the stratosphere, mesosphere, thermosphere, and exosphere, transitioning from one to the next at the stratopause, mesopause, and thermopause, respectively, where the background temperature trend reverses.\* Mean tropospheric temperature tends to decrease with altitude. Unlike in the ocean, relatively cold air aloft does not necessarily descend to displace the relatively warm air below. This is a consequence of compressibility: higher pressure compresses the air, and the mechanical energy of compression is converted to thermal energy (assuming the descending air has constant entropy). Such a process, in which thermodynamic properties are not exchanged between the descending air and the environment, is called *adiabatic*. If air is forced to rise adiabatically, the corresponding cooling is caused by expansion. An appropriate quantity to describe atmospheric stratification must account for these compressible dynamics. In particular, we adopt the *potential temperature*, that is, the temperature dry air would have if brought adiabatically to some reference height ([Holton and Hakim, 2013](#)). By this definition, the atmosphere is stably stratified where the potential temperature increases with altitude: potentially warmer air overlies potentially cooler (effectively denser) air.

One important difference between the ocean and the atmosphere is the rate at which mass density changes vertically. Due to the effective incompressibility of sea water, the magnitude of variations in mass density in the ocean represents a small fraction of the average mass density (e.g., [Vallis, 2006](#)). For this reason, when one considers such a fluid it is common to apply the so-called Boussinesq approximation, which treats the fluid as incompressible and mass density as constant except where it multiplies the buoyancy term in the vertical momentum equation

---

\*Bulk temperature, in the thermodynamic sense using the kinetic theory of gases, is poorly defined in the uppermost layers of the atmosphere due to the extremely sparse concentration of molecules there ([Ahrens et al., 2012](#)). Interactions between these molecules and ionized particles introduce additional complications (i.e., those described by plasma physics), and so wave dynamics in the upper atmosphere is outside the scope of this thesis.

(in which mass density is taken to depend on height alone). Conversely, in the atmosphere the mass density decreases with height approximately exponentially to effectively zero where the atmosphere transitions to the vacuum of outer space. It is therefore inappropriate to apply the Boussinesq approximation in the atmosphere, except where the vertical scale of motions is small compared to the  $e$ -folding depth of mass density, about 7–10 km (e.g., [Dutton and Fichtl, 1969](#)). The “anelastic” approximation<sup>†</sup> ([Ogura and Phillips, 1962](#)) and related models [e.g., the “pseudo-incompressible” model of [Durrán \(1989\)](#); see also [Klein \(2009\)](#)] were developed to overcome this severe restriction. Crucially, these models account for the idealized thermodynamics of expansion and compression in the atmosphere. The essential dynamical difference between the Boussinesq and anelastic approximations is that under the latter, perturbations to the background state of the fluid grow exponentially with height (this so-called “anelastic growth” will be quantified more specifically later). All of the approximations mentioned above have the effect of filtering sound waves from the equations of fluid motion. This feature is perhaps best appreciated when solving the governing equations numerically: without needing to resolve the fast dynamics of sound waves, models can take longer time steps while remaining numerically stable ([Durrán, 2010](#)). In this thesis, we invoke the Boussinesq and anelastic approximations when considering the ocean and atmosphere, respectively.

Idealized profiles of mass density in the ocean and atmosphere are shown in Figs. [1.1\(a\)](#) and [1.1\(b\)](#), respectively. The stratification in the ocean may be described using the mass density, whereas in the atmosphere the stratification may be described more appropriately by the potential temperature, an idealized profile of which is shown in Fig. [1.1\(c\)](#).

A conceptual approach that describes the fundamental behaviour of oscillations in stratified fluids generally is known as *parcel theory* [e.g., as discussed in the textbook by [Holton and Hakim \(2013\)](#)]. A parcel is a hypothetical deformable volume of fluid whose mass is fixed, and which does not exchange thermodynamic properties with its surroundings. If one considers a parcel of water displaced upward from its equilibrium position along the water surface, the vertically displaced fluid is surrounded by a less dense ambient (e.g., air), and so gravity forces

---

<sup>†</sup>The term *anelastic* was suggested by J. Charney to [Ogura and Phillips \(1962, footnote 3\)](#) because the approximate equations lack “elastic” energy (proportional to pressure perturbation squared) corresponding to the compressions/rarefactions of acoustic waves.

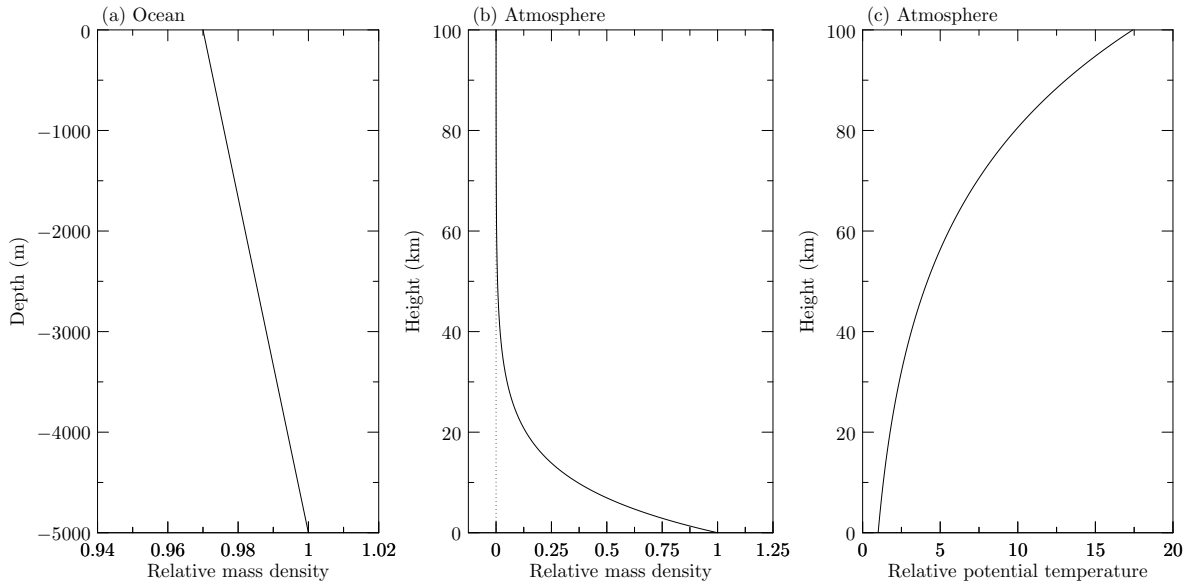


**Figure 1.1:** Idealized profiles of: mass density in the (a) ocean; and, (b) atmosphere; and, an idealized profile of potential temperature in the atmosphere (c). The quantities described on the horizontal axes are relative to a typical value of that quantity at the bottom of the domains shown on the vertical axes, corresponding to (a) the bottom of a relatively deep ocean; and, (b,c) the surface of the Earth.

the parcel to descend. The parcel, having mass, hence also having momentum corresponding to its downward velocity, overshoots its equilibrium position. The resulting depression in the fluid surface (occupied ostensibly by a parcel of air), is less dense than the surrounding water, and so buoyancy forces the water parcel to rise again. Gravity and buoyancy act upon the parcel to return it to its initial position at the water surface.

Motivated by parcel theory, gravity waves in general are defined as perturbations to the surfaces of constant effective density of a fluid otherwise in a stably stratified equilibrium state, in which gravity and buoyancy act to restore a disturbed fluid parcel to its initial unperturbed state. For example, an oscillatory disturbance propagating along the interface between water and air—such as a water wave propagating toward a beach—is called a surface gravity wave, and is restricted to propagate along the water surface. An *internal gravity wave* propagates not only horizontally but also vertically within a stably stratified fluid. This property allows internal gravity waves to transport energy and momentum horizontally and vertically within stably stratified fluids. Internal gravity waves, or simply internal waves, are the type of gravity wave considered in this thesis.

Many mechanisms exist across a broad range of spatial and temporal scales to excite

internal gravity waves in geophysical fluids. For example, in the ocean internal gravity waves are generated by surface wind stress (e.g., [Alford et al., 2016](#)), and in the lee of seamount chains by quasisteady flows such as the Antarctic Circumpolar Current through the Drake Passage ([Cusack et al., 2017](#)). Upward-propagating atmospheric internal gravity waves are generated by several mechanisms including flow over orography (e.g., [Smith, 2018](#), Sec. 6), and at the tropopause by convective processes such as overshooting convection from supercell thunderstorms ([Homeyer et al., 2017](#); [O’Neill et al., 2021](#)) and tropical cyclones ([Wright, 2019](#)). In both the atmosphere and ocean, environmental factors such as the structures of the background flow and stratification play a role in determining whether the variously generated waves dissipate locally, or continue propagating ultimately to transport their energy and momentum far from their source (e.g., [Alford et al., 2016](#); [Kaifler et al., 2015](#); [Bramberger et al., 2017](#)).

### 1.1.2 Internal gravity waves in general circulation models

So-called *general circulation models* are a type of highly sophisticated numerical model designed to simulate the large-scale flow of the atmosphere, ocean, or both. Essentially, these models integrate systems of partial differential equations representing the spatial and temporal evolution of, e.g., wind velocity, temperature, humidity, etc., while assimilating data from sources such as satellites and weather balloons (e.g., [Holton and Hakim, 2013](#), Chap. 13). General circulation models are used for a variety of purposes including weather forecasting and climate prediction. Because of their complexity, these models are run on high performance computing platforms (known colloquially as supercomputers).

Because of the special property of internal gravity waves to propagate both horizontally and vertically from a variety of sources, these waves represent an important mechanism for the redistribution of energy and momentum across a broad range of spatial scales within the ocean and atmosphere ([Hines, 1960](#); [Fritts and Alexander, 2003](#); [Sutherland et al., 2019](#)). Orographically-generated internal gravity waves (or at least their effects on the larger-scale flow) in general circulation models have long been recognized for their role in driving the dynamics of the lower and middle atmosphere ([Palmer et al., 1986](#); [McFarlane, 1987](#); [McLan-dress, 1998](#); [Scinocca and McFarlane, 2000](#)). One example of particular relevance to this thesis

is the *Quasi-Biennial Oscillation* (QBO; elaborated upon later), an equatorial stratospheric wind flowing alternately eastward and westward with an average period of about 28 months, driven by upward-propagating waves generated in the troposphere (Lindzen and Holton, 1968; Baldwin et al., 2001). On a more local scale, large amplitude waves lower in the atmosphere can pose a hazard to aircraft (e.g., Bramberger et al., 2018). The broad range of scales on which internal gravity waves exist presents one of several persistent challenges to resolving adequately these waves in numerical models of the ocean, atmosphere, and climate. A theoretical lower bound for the wavelengths resolvable by such models is proportional to the interval between points on the discrete grid on which the model equations are solved. For example, in version 8.0.0 of the [Global and Regional Deterministic Prediction Systems](#) [Canada’s operational numerical weather prediction models as of December 1st, 2021; see [Environment and Climate Change Canada \(2021a,b\)](#)], horizontal grid points are quasiuniformly spaced by about 15 km and 10 km, respectively. Hence, the shortest resolvable horizontal wavelength of a sinusoidal wave is approximately 120 km and 80 km, respectively (resolving rather coarsely a crest, trough, two zeros, and the curvature between these, requiring an additional four points). The effects of physical phenomena on smaller scales—in particular, energy and momentum transport by internal gravity waves—must be represented indirectly.

As internal gravity waves propagate vertically, their amplitude can grow so large that their evolution is dominated by nonlinear effects. Where wave amplitude is so large as to displace effectively denser fluid over less dense fluid, the waves are said to be *overturning*, and may eventually *break* (like water waves crashing against a beach), irreversibly depositing their momentum at the breaking location. Wave breaking acts locally to mix the ambient fluid, and crucially to exert a drag on the background flow (Lindzen, 1981). The turbulent wave breaking process is inherently three-dimensional and nonlinear (Andreassen et al., 1994; Fritts et al., 1994), and occurs on spatial and temporal scales too small to be resolved explicitly by general circulation models. These nonnegligible effects must therefore be *parameterized* in such models, that is, predicted using only the explicitly resolved variables (Holton and Hakim, 2013). An influential proposal early in the history of atmospheric wave drag parameterization schemes was the so-called “wave saturation” hypothesis of Lindzen (1981). Essentially, this hypothesis postulates that upward-propagating internal gravity waves grow in amplitude

eventually to break down turbulently, thus limiting further vertical wave propagation and amplitude growth. A drag scheme derived by [McFarlane \(1987\)](#) under the assumption of wave saturation was found to drive more realistic tropospheric and stratospheric winds in the Canadian Climate Centre global circulation model. Over 30 years after its implementation, this drag scheme remains in use to parameterize the effects of orographic gravity waves in Canada’s [Global](#) and [Regional Deterministic Prediction Systems](#).

Perhaps surprisingly, in light of their apparent success, operational gravity wave drag parameterization schemes involve numerous tunable parameters, and are typically derived under a rather restrictive set of assumptions. In particular, the scheme of [McFarlane \(1987\)](#) assumes that waves originate in the troposphere, are of small amplitude (hence propagate according to linear theory), are purely sinusoidal, and propagate instantaneously (i.e., do not evolve in time) through a vertical column without propagating laterally. Accounting for any of these effects is among the aforementioned challenges to improving wave drag parameterization schemes ([Plougonven et al., 2019](#)). For example, previous work ([Dosser and Sutherland, 2011](#); [Gervais et al., 2018](#)) modelling weakly nonlinear internal gravity waves has established that the small-amplitude assumption can lead to questionable estimates of wave breaking heights of geophysically relevant, moderately large amplitude waves.

### 1.1.3 Wave packets and the wave-induced mean flow

In real stratified fluids such as the ocean and atmosphere, internal gravity waves are not generated as perfectly sinusoidal (so-called “plane”) waves. Rather, internal gravity waves often exist as *wave packets*, defined generally as spatially localized groups of internal waves that travel together. We specify this localization in terms of a rectangular Cartesian coordinate system, in which we refer to the  $x$ ,  $y$ , and  $z$  coordinate directions as *streamwise* (left-right, or East-West geographically), *spanwise* (into and out of the page, or North-South), and *vertical* (up-down), respectively. In this convention, we reserve *horizontal* to refer to the streamwise and spanwise directions together. With this language, a wave packet can be categorized geometrically, as: (1) streamwise periodic, spanwise infinite, and vertically localized; (2) streamwise- and vertically localized, and spanwise infinite; or, (3) localized in all three spatial directions. These descriptions are of one-, two-, and fully three-dimensional (so-called “fully

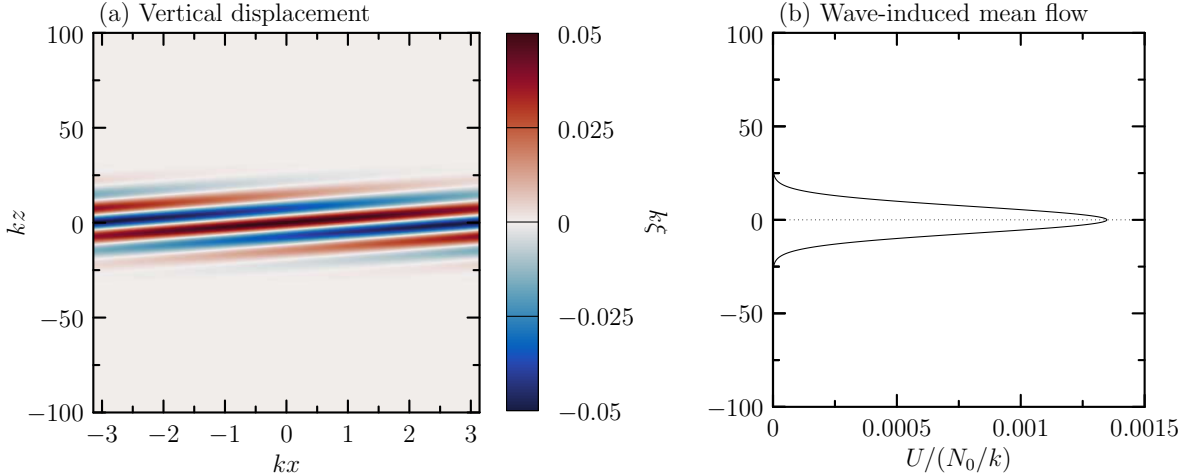


**Figure 1.2:** Example of (a) the vertical displacement field corresponding to a one-dimensional wave packet; and, (b) the unidirectional mean flow induced by the wave packet shown in (a).

localized”) wave packets, respectively. This categorization is somewhat arbitrary, as shown by [van den Bremer and Sutherland \(2018\)](#), who considered wave packets as they transitioned gradually from effectively two- to fully three-dimensional. In this thesis we only consider wave packets that fit the above categorization unambiguously. Examples of one-, two-, and three-dimensional wave packets are shown in Figs. [1.2\(a\)](#), [1.3\(a\)](#), and [1.4\(a,c\)](#), respectively. Whether a moderately large amplitude wave packet is one-, two-, or three-dimensional has a significant effect on its evolution qualitatively and quantitatively, in particular, through nonlinear self-interactions with its wave-induced mean flow.

Wave-induced mean flows in general are nonlinear corrections to the wave velocity field resulting in a relatively slow additional contribution to advection. A historically important example is the Stokes drift induced by surface waves on deep water ([Stokes, 1847](#); [Kundu et al., 2016](#)). This flow, existing at order amplitude-squared, acts to advect water parcels further forward during the passage of a crest than the passage of a trough, resulting in a net forward transport of water parcels in the direction of wave propagation. Plane internal gravity waves do not induce a mean flow because plane waves represent an exact solution to the fully nonlinear equations governing fluid motion<sup>‡</sup> (e.g., [Sutherland, 2010](#)).

Unlike plane waves, internal gravity wave packets induce qualitatively distinct mean flows

<sup>‡</sup>Mathematically, such solutions are valid in an inviscid fluid (i.e., one with zero viscosity) in an unbounded domain, where the effective density profile is of a certain class (to be elaborated upon later). Physically, these conditions are effectively satisfied in the ocean and atmosphere sufficiently far from boundaries.

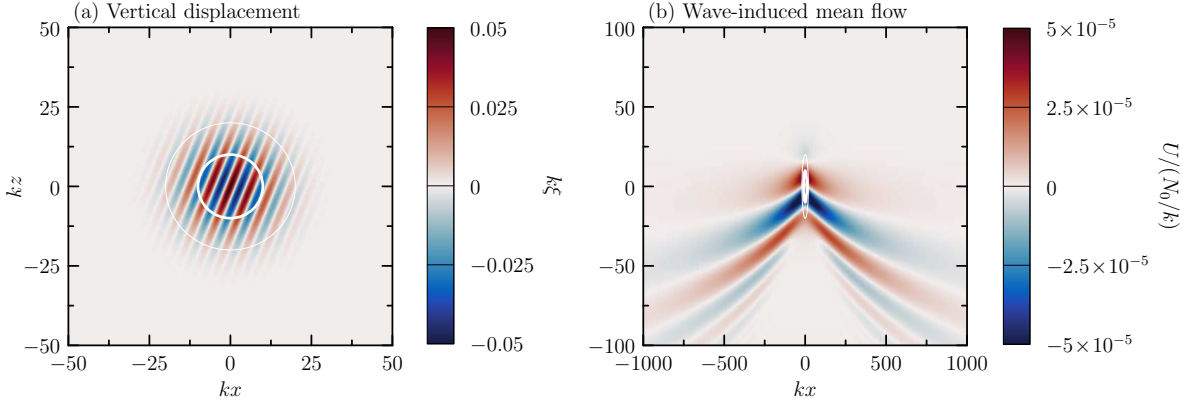


**Figure 1.3:** Example of (a) the vertical displacement field corresponding to a two-dimensional wave packet analogous to the one shown in Fig. 1.2(a); and, (b) the bow-wakelike mean flow induced by the wave packet shown in (a). Note that the horizontal scale in (b) is  $20\times$  longer than that in (a). The heavy and thin white ellipses in each panel indicate one and two standard deviations, respectively, about the centre of the wave packet.

depending on their geometry. One-dimensional wave packets induce a streamwise-uniform, unidirectional, mean flow that is concentrated in the vertical region occupied by the vertically propagating wave packet (Acheson, 1976), resulting from the vertical divergence of momentum flux (Sutherland, 2010). The mean flow induced by a one-dimensional wave packet is shown, for example, in Fig. 1.2(b). Two-dimensional wave packets in a nonrotating ambient similarly induce a mean flow resulting from a divergent momentum flux. Unlike in the one-dimensional case, the mean flow is itself divergent and so, for the fluid to remain incompressible, an order amplitude-squared pressure gradient is established. The induced mean flow manifests as hydrostatic long waves that extend far streamwise and vertically below the propagating wave packet (van den Bremer and Sutherland, 2014; Gervais et al., 2018). The mean flow induced by such a two-dimensional wave packet is shown, for example, in Fig. 1.3(b). Conversely, two-dimensional wave packets in a rotating ambient induce an evanescent (i.e., exponentially decaying) long wave response (Sutherland et al., 2020), provided the rotation rate is sufficiently fast (not shown). The horizontal component of the mean flow induced by three-dimensional wave packets resembles a dipole, the streamwise flow being positive through the centre of the wave packet, and negative on its spanwise flanks; a vertical cross section reveals a unidirectional structure analogous to the mean flow induced by one-dimensional wave packets. Since van den Bremer and Sutherland (2018), this flow has been referred to as the “Bretherton flow” after F. P. Bretherton, upon whose foundational work (Bretherton,

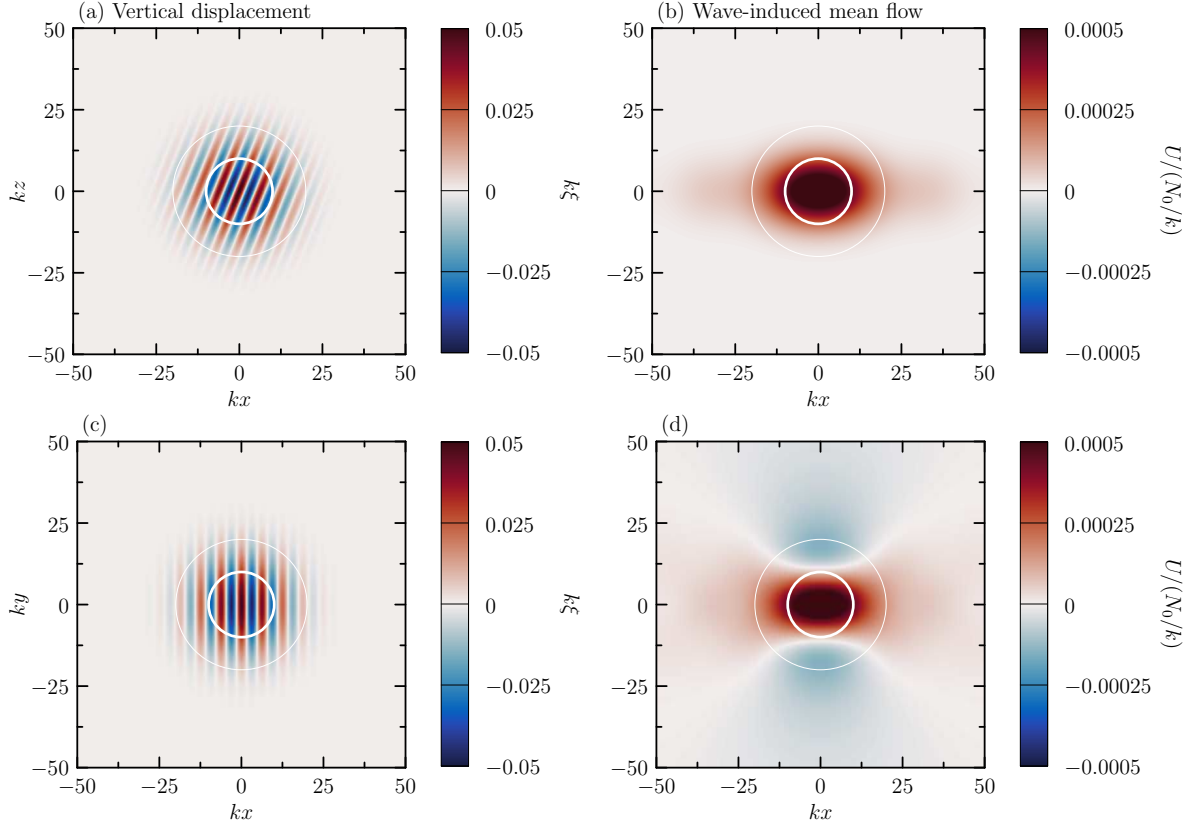


**Figure 1.4:** Cross sections through the vertical plane (top row) and horizontal plane (bottom row) of (a,c) the vertical displacement field corresponding to a fully three-dimensional wave packet analogous to those shown in Figs. 1.2(a) and 1.3(a); and, (b,d) the Bretherton flow induced by the wave packet shown in the corresponding panels in the left column. The heavy and thin white ellipses in each panel indicate one and two standard deviations, respectively, about the centre of wave packet.

1969) much understanding of wave-induced mean flows is based. Vertical and horizontal cross sections of the Bretherton flow through the centre of a three-dimensional wave packet are shown, for example, in Figs. 1.4(b) and 1.4(d), respectively.

#### 1.1.4 Goal of this thesis

Three-dimensional, fully localized wave packets, and the mean flow they induce, are the main objects of study in this thesis. In general, we are interested in studying the nonlinear evolution of these wave packets as they self-interact with their induced mean flow. In real stratified fluids, the nonlinear evolution of wave packets is complicated by multiple factors, including the linear influences of rotation, nonuniformities in the background state, and potentially rapid changes of mass density with height. In order eventually to improve the representation of internal gravity waves in general circulation models, there is a need to better understand

the combined linear and nonlinear dynamics governing wave evolution, whether toward wave breaking and the ensuing irreversible deposition of energy and momentum, or toward the redistribution of these quantities more generally by internal gravity waves.

The goal of the research presented in this thesis is to make progress toward understanding these combined dynamics by studying the nonlinear evolution of three-dimensional internal gravity wave packets in three idealized geophysical contexts: (1) an ocean interior influenced by Earth’s rotation; (2) a nonrotating ocean interior in which the background flow changes with height; and, (3) a nonrotating atmosphere in which the background flow models one observed in the equatorial stratosphere. This goal will be pursued using a combination of theory, modelling, analysis, and numerical simulations. With our goal in mind, in the next section we review some fundamental aspects of the theory of internal gravity waves and introduce some of the notation used throughout this thesis.

## 1.2 Essential concepts of internal gravity wave theory

Here we review some essential mathematical aspects of stratified fluids and internal gravity wave theory. The purpose is to set up a common starting point to ground the theoretical developments presented later in this thesis.

We denote by  $\bar{\rho} = \bar{\rho}(z)$  the profile of background mass density, and consider a fluid in which this quantity describes the stratification. That the background state of this fluid is continuously and stably stratified corresponds to the properties  $\bar{\rho} \in C^1$  and  $d\bar{\rho}/dz < 0$ , respectively. Within this context one can obtain the corresponding *buoyancy frequency* or *Brunt–Väisälä frequency*,

$$N(z) = \sqrt{-\frac{g}{\rho_0} \frac{d\bar{\rho}}{dz}},$$

where  $g$  is the gravitational acceleration and  $\rho_0$  is a constant reference density (e.g., [Sutherland, 2010](#)). The frequency  $N$  represents the natural frequency at which a vertically displaced fluid parcel will oscillate about its equilibrium level. Where  $N(z) = N_0$  is constant, the fluid is said to be *uniformly* stratified. This situation corresponds to a fluid in which background density increases (decreases) linearly with depth (height), as is effectively the case in the ocean interior (atmosphere over vertical distances less than the  $e$ -folding depth of mass density).

Alternatively, we now consider a fluid in which the stratification is described by the potential temperature, whose background profile is denoted by  $\bar{\theta} = \bar{\theta}(z)$ . Supposing again that the background state of this fluid is continuously and stably stratified, the corresponding properties  $\bar{\theta} \in C^1$  and  $d\bar{\theta}/dz > 0$  follow. One can similarly obtain the corresponding buoyancy frequency,

$$N(z) = \sqrt{\frac{g}{\bar{\theta}} \frac{d\bar{\theta}}{dz}}.$$

The fluid is uniformly stratified where  $N(z) = N_0$  is constant, equivalent to a fluid in which  $\bar{\theta}(z)$  increases exponentially with height. For convenience, in this thesis we only consider uniformly stratified fluids.

Plane (or monochromatic) internal gravity waves propagating in a uniformly stratified fluid are conveniently expressed in their most general form mathematically as a complex exponential

$$\eta(\mathbf{x}, t) = \frac{1}{2} A_\eta e^{i(\mathbf{k} \cdot \mathbf{x} - \omega t)} + \text{c.c.}, \quad (1.1)$$

where  $\eta$  is any wave field of interest, the constant  $A_\eta \in \mathbb{C}$  encodes the phase and amplitude of the wave, and c.c. denotes the complex conjugate, thus ensuring the wave field itself is real. It is sometimes convenient to omit the factor of 1/2 and the c.c. in Eq. (1.1) with the understanding that  $\eta$  is the real part of the resulting expression. The vector  $\mathbf{x} = (x, y, z)$  implies the three-dimensionality of the waves considered in this thesis. The corresponding wavenumber vector is  $\mathbf{k} = (k, \ell, m) = 2\pi(\lambda_x^{-1}, \lambda_y^{-1}, \lambda_z^{-1})$ , where the constants  $\lambda_x$ ,  $\lambda_y$ , and  $\lambda_z$  are the wavelengths in the respective directions. The *wavenumber* is so called because it represents literally the number of sinusoidal oscillations on an interval of length  $2\pi$  in a given direction. Wave frequency is  $\omega = \omega(\mathbf{k}) > 0$ , with the sign taken to ensure the waves propagate forward in time,  $t$ . The expression for  $\omega$  is set by the dispersion relation, which relates the frequency to the wavenumber. Mathematically, internal gravity waves are said to be *dispersive* because the dispersion relation has the property that at least one of  $\partial^2\omega/\partial k^2$ ,  $\partial^2\omega/\partial \ell^2$ , or  $\partial^2\omega/\partial m^2$  are not everywhere zero (e.g., Zauderer, 2006), the physical interpretation of which will be given shortly. Explicit expressions for  $\omega$  are specific to the wave propagation scenario under consideration, hence, in this thesis, the expression for  $\omega$  is given in each part as it arises.

Two quantities of fundamental importance in the theory of internal gravity waves are

derived from the dispersion relation, namely, the *phase velocity*,

$$\mathbf{c}_p = (c_{px}, c_{py}, c_{pz}) = \frac{\omega}{\|\mathbf{k}\|^2} \mathbf{k}, \quad (1.2)$$

and the *group velocity*,

$$\mathbf{c}_g = (c_{gx}, c_{gy}, c_{gz}) = \left( \frac{\partial \omega}{\partial k}, \frac{\partial \omega}{\partial \ell}, \frac{\partial \omega}{\partial m} \right). \quad (1.3)$$

The phase velocity describes the speed and direction of propagation of individual crests and troughs, whereas the group velocity describes the speed and direction at which internal gravity waves transport energy (Sutherland, 2010). A fundamental, and entirely unintuitive, property of internal gravity waves (in a Boussinesq fluid) corresponds to the identity  $\mathbf{c}_p \cdot \mathbf{c}_g = 0$ : energy is transported by internal gravity waves in a direction perpendicular to their phase propagation. Given the definition of  $\mathbf{c}_g$  in Eq. (1.3), nonzero second-order derivatives of  $\omega$  correspond to waves that transport energy at different rates as a function of wavenumber, hence acting analogously to diffusion to disperse the waves. Explicit expressions for the phase and group velocities are given, as needed, in the respective Parts of this thesis.

Quasimonochromatic internal gravity wave packets propagating in a uniformly stratified fluid are modelled by a plane wave modulated by a time-evolving amplitude envelope that bounds the waves spatially. In general,

$$\eta(\mathbf{x}, t) = \frac{1}{2} A_\eta(\mathbf{x}, t) e^{i(\mathbf{k} \cdot \mathbf{x} - \omega t)} + \text{c.c.},$$

where  $A_\eta : \mathbb{R}^3 \times \mathbb{R}^+ \rightarrow \mathbb{C}$  describes the amplitude envelope of the waves. Like plane waves, individual crests and troughs within the packet propagate with the phase velocity given by Eq. (1.2). The group velocity, given by Eq. (1.3), describes the speed and direction of the packet itself and of the energy it transports.

In Sec. 1.1.3 we described qualitatively internal gravity wave packets and the mean flows they induce. The aforementioned (weakly) nonlinear interactions between a wave packet and its wave-induced mean flow are described by a nonlinear Schrödinger equation (e.g., Sutherland, 2010). Explicitly,

$$\frac{\partial A}{\partial t} = -c_{gz} \frac{\partial A}{\partial z} + i \frac{1}{2} \frac{\partial^2 \omega}{\partial m^2} \frac{\partial^2 A}{\partial z^2} - ikUA, \quad (1.4)$$

where  $A = A(z, t)$  is set to be one-dimensional here for illustrative purposes, and  $U(z, t) \propto |A|^2$  is the corresponding wave-induced mean flow, where  $|\cdot|$  denotes the complex modulus. For the one-dimensional waves considered in this example,  $U \geq 0$  [cf. Fig. 1.2(b)]. The first two terms on the right-hand side of Eq. (1.4) model, respectively, the linear translation of the wave packet at the vertical group speed, and linear dispersion. Essentially, the wave-induced mean flow acts to Doppler-shift the wave frequency, resulting in a local change to the group velocity. Local increase (decrease) of the group velocity leads to wave spreading (accumulation), a characteristic manifestation of *modulational stability (instability)* (Whitham, 1965, 1974). As a result, the onset of overturning of one-dimensional waves is delayed (hastened), so that waves overturn above (below) the height predicted by linear theory (Akylas and Tabaei, 2005; Sutherland, 2006b; Dosser and Sutherland, 2011). For wave packets described by Eq. (1.4), the transition between the modulationally stable and unstable regimes occurs at a relative vertical wavenumber of  $|m/k| = 1/\sqrt{2} \approx 0.7$ , corresponding to wave packets propagating with the fastest vertical group speed. Modulational stability (instability) manifests where  $U\partial^2\omega/\partial m^2 > 0$  ( $< 0$ ). For wave packets described by Eq. (1.4),  $U \geq 0$ , and so the modulational stability properties are determined entirely by the sign of  $\partial^2\omega/\partial m^2$ . The relationships between the wave frequency, vertical group speed, and  $\partial^2\omega/\partial m^2$ , are shown in Fig. 1.5(a).

The weakly nonlinear evolution of two-dimensional wave packets is likewise described by a nonlinear Schrödinger equation (Tabaei and Akylas, 2007; Gervais et al., 2018), which is not reproduced here. The finite streamwise and vertical structure of two-dimensional wave packets means these packets are linearly dispersive in both directions independently, and “obliquely,” as described at leading-order by the term  $i\frac{\partial^2\omega}{\partial k\partial m}\frac{\partial^2 A}{\partial x\partial z} \neq 0$  in the nonlinear Schrödinger equation derived by Gervais et al. (2018), in which  $A = A(x, z, t)$ . Two-dimensional wave packets, unlike their one-dimensional counterparts, are always modulationally unstable, as the induced mean flow [long waves; cf. Fig. 1.3(b)] is positive above and negative below the centre of the wave packet. Although modulational instability of two-dimensional wave packets manifests to an extent in the streamwise direction (where  $U_{2D}\partial^2\omega/\partial k^2 < 0$ ), vertical modulations are dominant (Shrira, 1981; Gervais et al., 2018). The relationships between wave frequency, streamwise group speed, and  $\partial^2\omega/\partial k^2$  and  $\partial^2\omega/\partial k\partial m$ , are shown in Fig. 1.5(b).

A nonlinear Schrödinger equation describing the weakly nonlinear evolution of three-

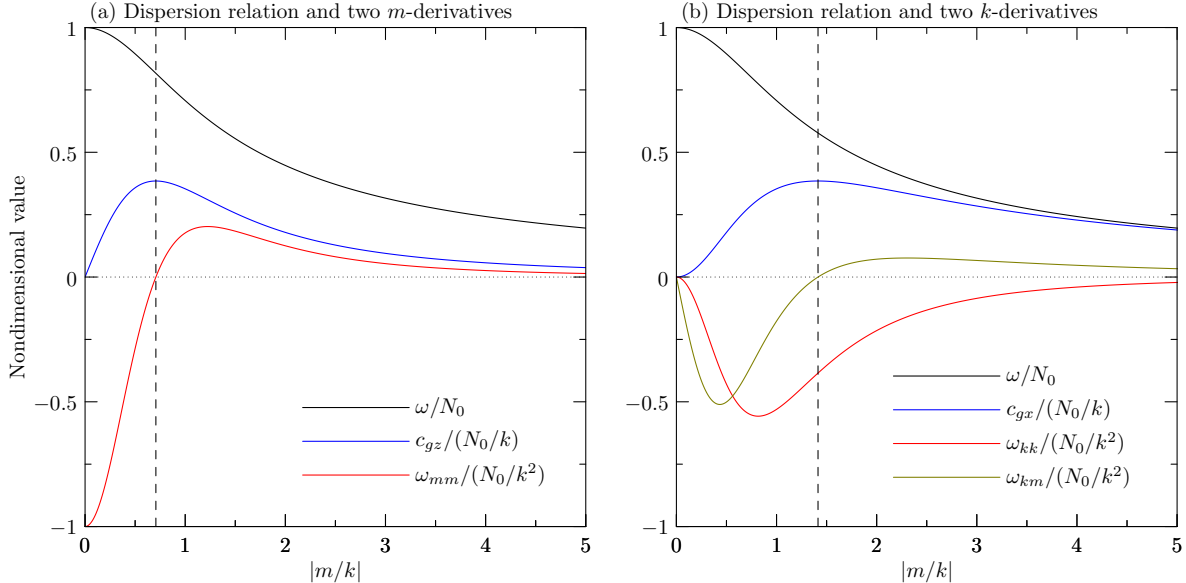


**Figure 1.5:** Nondimensionalized dispersion relation,  $\omega/N_0$ , for small amplitude Boussinesq waves in a nonrotating uniformly stratified fluid, and its relationships to: (a) vertical group speed  $c_{gz} = \partial\omega/\partial m$ , and  $\omega_{mm} := \partial^2\omega/\partial m^2$ ; and, (b) streamwise group speed  $c_{gx} = \partial\omega/\partial k$ , and  $\omega_{kk} := \partial^2\omega/\partial k^2$  and  $\omega_{km} := \partial^2\omega/\partial k\partial m$ . The specific analytic expressions for the plotted quantities are unimportant here. All curves correspond to upward-propagating waves, for which  $m/k < 0$ , but are plotted against  $|m/k|$  by convention. The dashed vertical lines in (a) and (b) indicate, respectively, the value of  $|m/k|$  corresponding to waves propagating with the fastest vertical and streamwise group speeds.

dimensional wave packets [i.e.,  $A = A(x, y, z, t)$ ] was derived by [Shrira \(1981\)](#). Although the wave packet envelope had spanwise structure, waves were assumed not to propagate in the spanwise direction (equivalent to setting  $\ell = 0$ ). As a result, the linear operator in [Shrira's](#) Schrödinger equation was identical to that in the two-dimensional one derived by [Gervais et al. \(2018\)](#), acting only on the streamwise and vertical structure of the wave packets. On these grounds we anticipate fully three-dimensional wave packets to likewise be prone to multidirectional dispersion. Because the mean flows induced by two- and three-dimensional wave packets are not of uniform sign, we also anticipate that the three-dimensional wave packets considered in this thesis are always modulationally unstable, this instability manifesting as nonlinear spreading and amplification of the wave packet envelopes nonuniformly in space.

Although the details of modulational stability and instability of three-dimensional wave packets are not the focus of this thesis, this mechanism is anticipated to be useful to understand the basic weakly nonlinear behaviour of the wave packets to be encountered in the upcoming chapters.

### 1.3 Outline of this thesis

The content of this thesis is organized in three major parts, corresponding to the three projects constituting my doctoral research program. As stated in the [Preface](#), [Parts I](#) and [II](#) correspond to published papers, although these parts generally are more substantial in content than the published versions. A manuscript based on the work presented in [Part III](#) is underway, to be submitted to the *Journal of the Atmospheric Sciences*. Each part begins with a topical introduction, and is then subdivided conveniently into chapters, generally separating theory, numerics, and results and discussion. The three parts, spanning related but distinct research projects, are largely self-contained, at the expense of some repetition.

[Part I](#) considers the evolution of three-dimensional internal gravity wave packets as they interact nonlinearly with their wave-induced mean flow in a rotating fluid. In [Chapter 2](#) we derive an integral expression for the Bretherton flow including the effect of rotation, and predict critical amplitudes corresponding to the onset of various internal wave instability mechanisms. In [Chapter 3](#) we provide details of the numerical code used to simulate the wave packet evolution. In [Chapter 4](#) we describe the results of the simulations for a range of wave packet parameters, and discuss the results in the context of observations of an internal gravity wave in the ocean.

[Part II](#) considers the combined linear and nonlinear influences of a height-dependent background flow and the wave-induced mean flow on the evolution of three-dimensional internal gravity wave packets without rotation. In [Chapter 5](#) we review the theory of linear (i.e., small amplitude) wave packet propagation in nonuniform background flow, derive the critical initial amplitude for wave packet penetration above the “reflection level,” describe two mechanisms for the generation of so-called secondary gravity waves, and define a transmission coefficient. In [Chapter 6](#) we provide details of the numerical code used to simulate the wave packet evolution. In [Chapter 7](#) we describe the results of the simulations for a range of wave packet and background flow parameters, compare the results with predictions, and discuss the results in the context of previous studies of one- and two-dimensional wave packet transmission and reflection.

[Part III](#) considers the nonlinear evolution of three-dimensional internal gravity wave packets

as they propagate through an anelastic atmosphere in which the background wind models a certain phase of the Quasi-Biennial Oscillation (QBO). In Chapter 8 we describe an anelastic gas, derive an integral expression for the anelastic Bretherton flow, adapt and extend the linear theory reviewed in Chapter 5 to wave tunnelling in an anelastic gas, define a transmission coefficient, and describe the procedure to model the QBO. In Chapter 9 we provide details of the numerical code used to simulate the wave packet evolution. In Chapter 10 we describe the results of the simulations for a range of wave packet and QBO parameters, and discuss the results in the context of the theorized role of internal gravity waves in QBO dynamics.

In Chapter 11 we summarize the research program and its main results, suggest possible directions for further research, and offer concluding remarks.

As a final note on style and formatting, I shall mention that all the figures I produced for this thesis were created using the vector graphics language Asymptote (Bowman and Hammerlindl, 2008), and that a subset of figures that represent values using colour gradients used the “cmocean” colourmap designed by Thyng et al. (2016). Lastly, readers of a digital version of this thesis may navigate the document via hyperlinks, indicated by blue text; alternatively, I hope readers of a print copy of this thesis will enjoy turning its pages the old-fashioned way.

# PART I

---

## Boussinesq wave packets with rotation

---

Geophysical fluids, in general, are characterized not only by stratification, but also by the fact they exist on a rotating planet (e.g., [Sutherland et al., 2019](#)). Earth rotates counterclockwise when viewed from above the North Pole. Rotation acts on fluid parcels through the *Coriolis force*, an apparent force that tends to deflect fluid parcels to the right (left) in the Northern (Southern) Hemisphere. This so-called *Coriolis effect* is straightforwardly visualized if one considers an air parcel advecting directly southward from the North Pole: the parcel appears to deflect rightward relative to a fixed point on Earth's surface that rotates eastward, away from the parcel. Leftward deflection is visualized similarly if one considers the analogous scenario of an air parcel advecting northward from the South Pole. The magnitude of the Coriolis effect increases with latitude (to be shown quantitatively in Chapter 2).

A complete mathematical model of fluid dynamics as it is influenced by Earth's rotation is perhaps most conveniently described in spherical coordinates. Except for singularities at the North and South Poles in the governing equations, the resulting model would theoretically be valid globally. However, the wave packets we are interested in studying will be assumed to exist on such small spatial scales that the sphericity of the Earth may be neglected, and so globally valid equations are unnecessary. In practice, it is common to model the effects of rotation using the so-called *f*-plane approximation, which assumes the motions of interest are restricted latitudinally so that the Coriolis effect can be treated as having effectively constant

magnitude locally (e.g., Vallis, 2006). The  $f$ -plane is tangent to Earth’s surface and so the locally valid approximate equations of fluid motion may be written conveniently in Cartesian coordinates. We invoke the  $f$ -plane approximation in this study, and state the corresponding governing equations explicitly in Chapter 2.

A study of three-dimensional wave packets subject to the Coriolis effect was conducted by Tabaei and Akylas (2007), who examined wave packets that were either: (1) ‘round’ (for which the wave packet extents were comparable in all three dimensions) and strongly nonhydrostatic;\* (2) two-dimensional (having infinite spanwise extent, but comparable streamwise and vertical extents); or, (3) ‘flat’ (for which the horizontal wave packet extents were both much larger than the vertical extent). Rotation was anticipated to play a negligibly weak role in the evolution of fully three-dimensional wave packets in the nonhydrostatic regime they considered. For this reason, their analysis focused primarily on effectively two-dimensional, as opposed to fully three-dimensional, wave packets. A similar study was conducted by van den Bremer and Sutherland (2018), though neglecting the Coriolis effect. Their study focused, in part, on understanding the transition between qualitatively different induced mean flows as a wave packet’s spanwise extent broadened, transitioning from three- to effectively two-dimensional. The wave packets we will study will be assumed to be fully three-dimensional, and so the long waves induced by effectively two-dimensional wave packets [cf. Fig. 1.3(b)] will not be considered.

The purpose of this study is to build on the work of Sutherland (2001) and of van den Bremer and Sutherland (2018) to compare with linear theory the overturning times of fully three-dimensional wave packets. Our study differs in scope from both Tabaei and Akylas (2007) and van den Bremer and Sutherland (2018) in that we derive an explicit integral formula for the Bretherton flow subject to rotation, and examine through fully nonlinear numerical simulations a broader range of nonhydrostatic and more strongly hydrostatic waves. One aspect of our investigation is to characterize the overturning time in terms of various

---

\*In this thesis the terms *nonhydrostatic* and *hydrostatic* describe waves that propagate, respectively, with a significant vertical component, and primarily in the horizontal. Somewhat arbitrarily, these waves are distinguished quantitatively as those with relative vertical wavenumbers  $|m/k| \lesssim 0.7$  and  $\gtrsim 0.7$ , respectively. This cutoff corresponds to wave packets propagating upward with the fastest vertical group speed. Equivalently, one can quantify strongly nonhydrostatic (hydrostatic) waves as those propagating with frequency of comparable magnitude to the buoyancy (Coriolis) frequency.

hydrodynamic instability mechanisms affecting internal gravity wave evolution.

In Chapter 2 we first extend the work of [van den Bremer and Sutherland \(2018\)](#) to derive through perturbation theory an integral expression for the Bretherton flow subject to the Coriolis force. We then extend to the three-dimensional rotating context the work of [Sutherland \(2001\)](#) to predict the critical initial amplitude above which a wave is anticipated to become unstable to overturning, convection, self-acceleration, and shear. Using the code described in Chapter 3, we perform numerical simulations of fully localized wave packets with the predicted Bretherton flow superimposed, for a range of initial amplitudes, wave packet aspect ratios, and relative vertical wavenumbers spanning the hydrostatic and nonhydrostatic regimes. Results are described in Chapter 4 and compared with the instability amplitudes predicted using linear theory. Results are discussed in the broader context of previous studies of one- and two-dimensional wave packet overturning, and recent observations of oceanic internal waves.

---

## Theory

---

In this chapter we derive an explicit integral expression for the mean flow induced by three-dimensional wave packets in a uniformly stratified Boussinesq fluid, subject to the Coriolis force but otherwise at rest, and ignoring diffusive and viscous effects. We follow the approach of [van den Bremer and Sutherland \(2018, vdBS18\)](#), who derived an explicit integral expression for the Bretherton flow without rotation. This practice has the benefit of serving as a check on our algebra, as the results of [vdBS18](#) at any step in the derivation ought to be recovered in the limit as the rotation term vanishes. This step-by-step comparison, however, revealed an error in the derivation by [vdBS18](#) in which a small number of terms were omitted. Our derivation reconciles this error, which will be shown ultimately to be inconsequential for the nonrotating results. We then derive, using linear theory, predictions of critical amplitudes for the onset of instabilities due to overturning, self-acceleration, and shear.

### 2.1 Governing equations

The fully nonlinear Euler momentum equations under the Boussinesq approximation, including buoyancy and rotation terms, are given in vector form by

$$\frac{D\mathbf{u}}{Dt} - f_0 v \hat{\mathbf{e}}_x + f_0 u \hat{\mathbf{e}}_y = -\frac{1}{\rho_0} \nabla p - \frac{g}{\rho_0} \rho \hat{\mathbf{e}}_z, \quad (2.1)$$

where  $D/Dt = \partial/\partial t + \mathbf{u} \cdot \nabla$  is the material derivative, in which  $\mathbf{u} = (u, v, w)$  is the velocity vector in Cartesian coordinates  $\mathbf{x} = (x, y, z)$  with corresponding standard unit basis vectors  $\hat{\mathbf{e}}_x$ ,  $\hat{\mathbf{e}}_y$ , and  $\hat{\mathbf{e}}_z$ ,  $f_0$  is the Coriolis parameter, described below,  $\rho_0$  is a constant reference mass density,  $p$  is dynamic pressure,  $g$  is the acceleration of gravity, and  $\rho$  is perturbation mass density.

Also included in the full set of governing equations is that for internal energy, expressed as an evolution equation for perturbation mass density,

$$\frac{D\rho}{Dt} = -w \frac{d\bar{\rho}}{dz}, \quad (2.2)$$

where  $\bar{\rho} = \bar{\rho}(z)$  is the background mass density profile.

The set of governing equations is closed by the inclusion of a statement of mass conservation for an incompressible Boussinesq fluid,

$$\nabla \cdot \mathbf{u} = 0. \quad (2.3)$$

This condition effectively filters acoustic waves from the governing equations. In addition to being dynamically insignificant on the length and time scales of internal waves, acoustic waves in numerically-integrated solutions (detailed in Chapter 3) present unnecessary numerical challenges associated with their relatively fast propagation speed (e.g., [Durrán, 2010](#)).

The effect of rotation is modelled by the inclusion of the aforementioned Coriolis parameter,  $f_0 = 2\Omega_e \sin(\phi)$ , where  $\Omega_e = 2\pi \text{ rad day}^{-1}$  is Earth's rotation rate, and  $\phi$  is latitude, with  $\phi > 0$  ( $\phi < 0$ ) in the Northern (Southern) hemisphere. For the midlatitudes of interest, a typical value of the nondimensionalized Coriolis parameter is  $f_0/N_0 = 0.01$ , although a small number of simulations will use  $|f_0/N_0| = 0.05$ . The value of the Coriolis parameter for a given simulation, reported on in Chapter 4, will always be specified, although without loss of generality the value is arbitrary in the derivation of the wave-induced mean flow below.

## 2.2 Wave-induced mean flow

It is convenient to express the governing equations in terms of vertical displacement as opposed to perturbation mass density. These quantities are related by

$$\rho = -\xi \frac{d\bar{\rho}}{dz}, \quad (2.4)$$

which is obtained from a Taylor series expansion of  $\bar{\rho}$  about a vertical displacement  $\xi$ . Substituting Eq. (2.4) into Eqs. (2.1) and (2.2), we obtain the governing equations in a directly useful form,

$$\frac{Du}{Dt} - f_0 v = -\frac{1}{\rho_0} \frac{\partial p}{\partial x}, \quad (2.5)$$

$$\frac{Dv}{Dt} + f_0 u = -\frac{1}{\rho_0} \frac{\partial p}{\partial y}, \quad (2.6)$$

$$\frac{Dw}{Dt} = -\frac{1}{\rho_0} \frac{\partial p}{\partial z} - N_0^2 \xi, \quad (2.7)$$

$$\frac{D\xi}{Dt} = w, \quad (2.8)$$

and closed by Eq. (2.3), which does not change as a result of Eq. (2.4). The buoyancy term in Eq. (2.7) is now expressed in terms of the squared buoyancy frequency,

$$N_0^2 = -\frac{g}{\rho_0} \frac{d\bar{\rho}}{dz} \quad (2.9)$$

which is constant in our assumed uniformly stratified fluid.

The pressure terms may be eliminated from Eqs. (2.5)–(2.7) by taking the curl of these equations, resulting in a single vector equation for the evolution of vorticity,

$$\frac{D\boldsymbol{\zeta}}{Dt} = (\boldsymbol{\zeta} \cdot \nabla) \mathbf{u} + f_0 \frac{\partial \mathbf{u}}{\partial z} - N_0^2 \left( \frac{\partial \xi}{\partial y} \hat{\mathbf{e}}_x - \frac{\partial \xi}{\partial x} \hat{\mathbf{e}}_y \right), \quad (2.10)$$

where  $\boldsymbol{\zeta} = \nabla \times \mathbf{u}$  is the vorticity vector. The linear dependence of Eq. (2.10) on vertical displacement is eliminated by first taking the derivative of Eq. (2.10) with respect to  $t$ , so that mixed space- and time-derivatives of  $\xi$  remain on the right-hand side of the resulting equation. These are eliminated, in turn, by substituting the expressions one obtains by taking derivatives with respect to  $x$  and  $y$  of Eq. (2.8). It is convenient to express the resulting equation with the linear terms—consisting only of velocity components—on the left-hand side and quadratically

nonlinear terms on the right-hand side. Explicitly,

$$\begin{aligned}
& \underbrace{\begin{bmatrix} -f_0\partial_{tz} & -\partial_{ttz} & (\partial_{tt} + N_0^2)\partial_y \\ \partial_{ttz} & -f_0\partial_{tz} & -(\partial_{tt} + N_0^2)\partial_x \\ -\partial_{tty} & \partial_{ttx} & -f_0\partial_{tz} \end{bmatrix}}_{:=\mathbf{L}} \mathbf{u}^{(2)} \\
& = \underbrace{\overline{\nabla \cdot \{ -\partial_t(\boldsymbol{\zeta} \otimes \mathbf{u}) - N_0^2 [(\hat{\mathbf{e}}_y \otimes \partial_x(\xi \mathbf{u})) - (\hat{\mathbf{e}}_x \otimes \partial_y(\xi \mathbf{u}))] \}} + \partial_t[(\boldsymbol{\zeta} \cdot \nabla)\mathbf{u}]}_{:=\mathbf{F}}. \quad (2.11)
\end{aligned}$$

This equation models the linear response,  $\mathbf{L}\mathbf{u}^{(2)}$ , induced by the *mean* self-interaction  $\mathbf{F}$  of waves within the wave packet on the scale of the wave packet. The superscript on  $\mathbf{u}^{(2)}$  denotes that this quantity arises from quadratic wave-wave interactions, and the overbar in Eq. (2.11) denotes averaging over the fast wave scales.

Solutions of Eq. (2.11) correspond to a range of qualitatively and quantitatively distinct wave-induced mean flows, depending on the aspect ratios of the wave packets (vdBS18) and magnitude of the Coriolis parameter (Sutherland et al., 2020). If a wave packet is significantly broader in its streamwise and spanwise extents than in its vertical extent, it is effectively one-dimensional and induces primarily unidirectional mean flows (Sutherland, 2001, 2006b; Dosser and Sutherland, 2011); if a wave packet is significantly wider in spanwise extent than in its streamwise and vertical extents, the wave packet is effectively two-dimensional and induces primarily long waves (van den Bremer and Sutherland, 2014; Gervais et al., 2018), provided rotation is negligibly weak (Sutherland et al., 2020). Of particular interest is the Bretherton flow, induced by fully localized wave packets, i.e., those with aspect ratios of order unity in each direction.

To that end, following vdBS18, the induced mean flow is decomposed conceptually into a long-wave and Bretherton-flow response:  $\mathbf{u}^{(2)} = \mathbf{u}_{\text{LW}} + \mathbf{u}_{\text{BF}}$ . This distinction is made more explicit by writing  $\mathbf{F} = (F_x, F_y, F_z)^\top$ . The Bretherton flow, existing as a primarily horizontal flow (Bretherton, 1969), is forced by the vertical component of Eq. (2.11),

$$\mathbf{L}\mathbf{u}_{\text{BF}} = \begin{bmatrix} 0 \\ 0 \\ F_z \end{bmatrix}, \quad (2.12)$$

to be solved subject to  $\nabla \cdot \mathbf{u}_{\text{BF}} = 0$ , using perturbation theory as described below.

### 2.2.1 Perturbation theory

We seek solutions of Eq. (2.12) in terms of quasimonochromatic wave packets. Without loss of generality, we orient our coordinate system such that waves propagate in the  $xz$ -plane, with wavenumber vector  $\mathbf{k} = (k, 0, m)$ . For convenience we assume wave packets propagate forward in  $x$  and  $t$ , and upward in  $z$ , so that  $k > 0$  and  $m < 0$ . The corresponding frequency,  $\omega > 0$ , is given by the dispersion relation,

$$\omega = \frac{(N_0^2 k^2 + f_0^2 m^2)^{1/2}}{\|\mathbf{k}\|}, \quad (2.13)$$

where  $\|\mathbf{k}\| = (k^2 + m^2)^{1/2}$ , derived in Appendix A.1.1.

We define a slow time scale  $T$  and slow spatial variables,  $\mathbf{X} = (X, Y, Z)$ , in a frame translating at group velocity of the wave packet,  $\mathbf{c}_g = (c_{gx}, 0, c_{gz})$ , where

$$c_{gx} = \frac{km^2(N_0^2 - f_0^2)}{\omega\|\mathbf{k}\|^4}, \quad (2.14a)$$

$$c_{gz} = -\frac{k^2m(N_0^2 - f_0^2)}{\omega\|\mathbf{k}\|^4}. \quad (2.14b)$$

Explicitly,  $X = \epsilon_x(x - c_{gx}t)$ ,  $Y = \epsilon_y y$ , and  $Z = \epsilon_z(x - c_{gz}t)$ , where  $\epsilon_x = 1/(k\sigma_x)$ ,  $\epsilon_y = 1/(k\sigma_y)$ , and  $\epsilon_z = 1/(k\sigma_z)$  are small parameters that are inversely proportional to the wave packet extent,  $\sigma_x$ ,  $\sigma_y$ , and  $\sigma_z$ , in their respective directions. The slow variable  $T = \epsilon^2 t$  describes the time scale for dispersion of the wave packet, where it is assumed that  $\epsilon = \max\{\epsilon_x, \epsilon_y, \epsilon_z\} \ll 1$  for quasimonochromatic wave packets, i.e., the wave packet is most strongly dispersive in the direction with the smallest wave packet extent. As  $\epsilon \ll 1$ , the wave packets are of sufficiently broad extent that dispersive effects are effectively ignored on the time scales relevant to the present derivation.

With this notation, the representation of a given wave field  $\eta$  is given at leading order by

$$\eta_0^{(1)} := \frac{1}{2} A_\eta(\mathbf{X}, T) e^{i\varphi} + \text{c.c.}, \quad (2.15)$$

where the subscript and superscript on  $\eta_0^{(1)}$  denote, respectively, the field's order in  $\epsilon$  and amplitude,  $\varphi = \mathbf{k} \cdot \mathbf{x} - \omega t$  is the phase, and c.c. denotes the complex conjugate. As a result

Field	$O(\alpha^1 \epsilon^0)$	$O(\alpha^1 \epsilon^1)$
Vertical displacement	$\xi_0^{(1)} = A$	$\xi_1^{(1)} = i\beta_x \left\{ A_X - \frac{k}{m} A_Z \right\}$
Streamwise velocity	$u_0^{(1)} = i\omega \frac{m}{k} A$	$u_1^{(1)} = \frac{m}{k} \left\{ (c_{gx} - \frac{\omega}{k} - \omega\beta_x) A_X + i\frac{f_0}{k} A_Y \right. \\ \left. + (c_{gz} + \frac{\omega}{m} - \omega\frac{k}{m}\beta_x) A_Z \right\}$
Spanwise velocity	$v_0^{(1)} = f_0 \frac{m}{k} A$	$v_1^{(1)} = i\frac{m}{k^2} \left\{ f_0 B A_X - i\omega A_Y - f_0 \frac{k}{m} B A_Z \right\}$
Vertical velocity	$w_0^{(1)} = -i\omega A$	$w_1^{(1)} = - \left\{ (c_{gx} - \omega\beta_x) A_X + (c_{gz} + \frac{k}{m}\omega\beta_x) A_Z \right\}$
Streamwise vorticity	$\zeta_{x0}^{(1)} = -if_0 \frac{m^2}{k} A$	$\zeta_{x1}^{(1)} = \frac{m^2}{k^2} \left\{ f_0 B A_X - i\omega K A_Y - f_0 \frac{k}{m} (1+B) A_Z \right\}$
Spanwise vorticity	$\zeta_{y0}^{(1)} = -\omega \frac{\ \mathbf{k}\ ^2}{k} A$	$\zeta_{y1}^{(1)} = i\frac{m^2}{k} \left\{ [K(c_{gx} - \omega\beta_x) - \frac{\omega}{k}] A_X + i\frac{f_0}{k} A_Y \right. \\ \left. + [K(c_{gz} + \frac{k}{m}\omega\beta_x) + \frac{\omega}{m}(2 + \frac{k}{m})] A_Z \right\}$
Vertical vorticity	$\zeta_{z0}^{(1)} = if_0 m A$	$\zeta_{z1}^{(1)} = -f_0 \left\{ m\beta_x A_X - B A_Z \right\}$

**Table 2.1:** Expressions for the amplitude envelopes of various fields as they relate to the amplitude envelope,  $A$ , of the vertical displacement field. The centre column contains the leading-order (wave-scale) relationships and the right column contains their respective first-order (envelope-scale) corrections (with respect to  $\epsilon$ ). Subscripts on  $A$  denote partial derivatives,  $\beta_x$  is a constant given by Eq. (2.25a), and we have defined  $B := 1 + k\beta_x$  and  $K := 1 + k^2/m^2$  for convenience. By convention, the actual fields are taken to be the real parts of  $e^{i(\mathbf{k}\cdot\mathbf{x} - \omega t)}$  times the tabulated expressions.

of the adoption of slow variables, derivatives of wave fields defined as in Eq. (2.15) become

$$\partial_x \rightarrow \epsilon_x \partial_X + ik, \quad (2.16a)$$

$$\partial_y \rightarrow \epsilon_y \partial_Y, \quad (2.16b)$$

$$\partial_z \rightarrow \epsilon_z \partial_Z + im, \quad (2.16c)$$

$$\partial_t \rightarrow \epsilon^2 \partial_T - \epsilon_x c_{gx} \partial_X - \epsilon_z c_{gz} \partial_Z - i\omega. \quad (2.16d)$$

At leading-order, the various wave fields are related by the *polarization relations* for plane (sinusoidal) waves—algebraic relationships derived by substituting a plane wave solution into the linearized governing equations and using Eqs. (2.16a)–(2.16d). The leading-order polarization relations are summarized in the centre column of Table 2.1, and the details of their derivation are included in Appendix A.1.1.

Throughout this section, the nondimensional amplitude is defined by  $\alpha := kA_0$ , where  $A_0 = \max_{\mathbf{X}} |A|$  is the maximum vertical displacement of waves in the packet, and we have defined  $A := A_\xi$  for convenience. An alternative choice of amplitude parameter is  $\alpha_0 = |mA_0|$ ,

which is a more direct measure of amplitude relative to that of overturning waves, for which  $|mA_0| = 1$ . (This diagnostic is elaborated on in Sec. 2.3.) The particular choice of definition is unimportant for the derivation presented here, and so we choose  $\alpha$  for consistency with our convention of using the streamwise wavenumber  $k$  for spatial nondimensionalization.

The polarization relations at the next order in  $\epsilon$  account for the finite spatial extent of the wave packet. To obtain these, it is necessary to impose the initial structure of one field. Without loss of generality, we impose the structure of the vertical displacement field at both leading- and first-order in  $\epsilon$ , i.e.,  $\xi = \xi_0^{(1)} + \xi_1^{(1)}$ , as this is a physically intuitive quantity. Explicitly,

$$\begin{aligned}\xi_0^{(1)} &= \frac{1}{2}Ae^{i\varphi} + \text{c.c.}, \\ \xi_1^{(1)} &= i\frac{1}{2}(\epsilon_x\beta_x\partial_X + \epsilon_y\beta_y\partial_Y + \epsilon_z\beta_z\partial_Z)Ae^{i\varphi} + \text{c.c.},\end{aligned}$$

where  $\beta_x$ ,  $\beta_y$ , and  $\beta_z$  are constants to be determined. The resulting polarization relations at  $O(\alpha^1\epsilon^1)$  are summarized in the right column of Table 2.1, and the details of their derivation are included in Appendix A.1.2. In derivations of wave-induced mean flows in one (Sutherland, 2001, 2006b; Dosser and Sutherland, 2011) and two dimensions (van den Bremer and Sutherland, 2014; Gervais et al., 2018), higher-order corrections to the vertical displacement field were not considered, because the set of polarization relations would then be under-determined. Conversely, it is necessary to introduce  $\xi_1^{(1)}$  in three dimensions to obtain an analytically tractable integral expression for  $\mathbf{u}_{\text{BF}}$  in terms of  $|A|^2$  only. This will be shown when we identify and reconcile the terms mistakenly omitted by vdBS18.

### 2.2.2 Divergent-flux induced flow and response flow

Using Eqs. (2.16a)–(2.16d), the first two rows of Eq. (2.12) at leading order are  $\partial_Y w_{\text{BF}} = 0$  and  $\partial_X w_{\text{BF}} = 0$ , respectively. Hence, at leading order  $w_{\text{BF}}$  is independent of the horizontal structure of the wave packet envelope, and so the only physically meaningful solution is  $w_{\text{BF}} = 0$ . As a result, the Bretherton flow is governed by the third row of Eq. (2.12),

$$\partial_{tt}(\partial_x v_{\text{BF}} - \partial_y u_{\text{BF}}) = \overline{\partial_t \{ \boldsymbol{\zeta} \cdot \nabla w - \nabla \cdot (\boldsymbol{\zeta}_z \mathbf{u}) \}}, \quad (2.17)$$

subject to  $\partial_x u_{\text{BF}} + \partial_y v_{\text{BF}} = 0$ . We omitted the term  $-f_0 \partial_{tz} w_{\text{BF}}$  on the left-hand side of Eq. (2.17) because  $|w_{\text{BF}}| \ll |u_{\text{BF}}|, |v_{\text{BF}}|$  for three-dimensional wave packets (Bretherton, 1969; Bühler and McIntyre, 1998, 2003; Tabaei and Akylas, 2007; Wagner and Young, 2015; Xie and Vanneste, 2015; van den Bremer and Sutherland, 2018).

Now, the Bretherton flow is decomposed into physically distinct contributions,

$$\mathbf{u}_{\text{BF}} = \mathbf{u}_{\text{DF}} + \mathbf{u}_{\text{RF}}, \quad (2.18)$$

where  $\mathbf{u}_{\text{DF}}$  is the *divergent-flux induced flow* and  $\mathbf{u}_{\text{RF}}$  is the *response flow*. The divergent-flux induced flow arises as the mean effect of nonlinear advection in Eqs. (2.5)–(2.7), and is given by the solution of

$$\frac{\partial \mathbf{u}_{\text{DF}}}{\partial t} = \overline{-\nabla \cdot (\mathbf{u}^{(1)} \otimes \mathbf{u}^{(1)})}. \quad (2.19)$$

An explicit expression for Eq. (2.19) is found by substituting into the right-hand side the leading-order polarization relations, and computing the mean of each term. Writing Eq. (2.15) to include explicitly its complex conjugate,  $\eta_0^{(1)} = \frac{1}{2} A_\eta e^{i\varphi} + \frac{1}{2} A_\eta^* e^{-i\varphi}$ , the averaging operation gives

$$\overline{\eta_0^{(1)} \eta_0^{(1)}} = \frac{1}{4} \overline{A_\eta^2 e^{i2\varphi} + 2|A_\eta|^2 + A_\eta^{*2} e^{-i2\varphi}} = \frac{1}{2} |A_\eta|^2, \quad (2.20)$$

where  $|\cdot|$  denotes the modulus. Hence, we find that

$$\frac{\partial \mathbf{u}_{\text{DF}}}{\partial t} = -\frac{1}{2} \frac{m^2}{k^2} \left( \omega^2 (\epsilon_x \partial_X - \frac{k}{m} \epsilon_z \partial_Z) |A|^2, f_0^2 \epsilon_y \partial_Y |A|^2, -\omega^2 \frac{k}{m} (\epsilon_x \partial_X - \frac{k}{m} \epsilon_z \partial_Z) |A|^2 \right), \quad (2.21)$$

the details of which are provided in Appendix B.1.1. In the equivalent expression without rotation [vdBS18, Eq. (3.8)], it is possible to equate the spatial derivatives on the right-hand side to the  $O(\epsilon^1)$  part of Eq. (2.16d). The resulting expression can be integrated in time, thereby obtaining an explicit solution  $\mathbf{u}_{\text{DF}}$ . This is not possible here because  $f_0 \neq 0$ , and so it is convenient to defer the solution of Eq. (2.21) until we solve for the components of  $\mathbf{u}_{\text{BF}}$  itself.

### 2.2.3 Bretherton flow

Ignoring dispersion, which acts at  $O(\epsilon^2)$ , and expanding the nonlinear forcing  $F_z$ , given by the right-hand side of Eq. (2.17), up to fourth-order in  $\epsilon$ , we have

$$\begin{aligned}
F_z = & \overline{\partial_t \left\{ (\zeta_{x0}^{(1)} + \zeta_{x1}^{(1)})(ik + \epsilon_x \partial_X)(w_0^{(1)} + w_1^{(1)}) + (\zeta_{y0}^{(1)} + \zeta_{y1}^{(1)})\epsilon_y \partial_Y (w_0^{(1)} + w_1^{(1)}) \right.} \\
& + \overline{(\zeta_{z0}^{(1)} + \zeta_{z1}^{(1)})(im + \epsilon_z \partial_Z)(w_0^{(1)} + w_1^{(1)}) - \epsilon_x \partial_X [(\zeta_{z0}^{(1)} + \zeta_{z1}^{(1)})(u_0^{(1)} + u_1^{(1)})]} \\
& \left. - \epsilon_y \partial_Y [(\zeta_{z0}^{(1)} + \zeta_{z1}^{(1)})(v_0^{(1)} + v_1^{(1)})] + \epsilon_z \partial_Z [(\zeta_{z0}^{(1)} + \zeta_{z1}^{(1)})(w_0^{(1)} + w_1^{(1)})] \right\}. \quad (2.22)
\end{aligned}$$

Substituting the polarization relations into the right-hand side of  $F_z$  and computing the mean we find, in sequence, that  $(F_z)_1^{(2)} \equiv 0$  and  $(F_z)_2^{(2)} \equiv 0$ . The leading nonzero expression is found at  $O(\alpha^2 \epsilon^3)$ , and is given explicitly by

$$\begin{aligned}
(F_z)_3^{(2)} = & \frac{1}{2} \frac{\partial}{\partial t} \left\{ \omega^2 \frac{m^2}{k^2} \left[ \epsilon_x \epsilon_y \partial_{XY} - \frac{k}{m} \epsilon_y \epsilon_z \partial_{YZ} \right] |A|^2 - f_0^2 \frac{m^2}{k^2} \epsilon_x \epsilon_y \partial_{XY} |A|^2 \right\} \\
& - \frac{1}{2} \frac{\partial}{\partial t} \left\{ \left[ \frac{m^2}{k^2} (\omega^2 + f_0^2) + \omega^2 \frac{\|\mathbf{k}\|^2}{k} \beta_x \right] \epsilon_x \epsilon_y A \partial_{XY} A + \omega^2 \frac{\|\mathbf{k}\|^2}{k} \beta_y \epsilon_y^2 A \partial_{YY} A \right. \\
& \left. - \left[ \frac{m}{k} (\omega^2 + f_0^2) - \omega^2 \frac{\|\mathbf{k}\|^2}{k} \beta_z \right] \epsilon_y \epsilon_z A \partial_{YZ} A \right\}. \quad (2.23)
\end{aligned}$$

The detailed derivations of the expressions for  $F_z$  at the various orders are provided in Appendix B.1.2, in which the amplitude envelope is assumed to be complex. The expressions simplify significantly [i.e., Eq. (2.23)] if one insists the amplitude envelope is real initially.

Using Eq. (2.21), it is straightforward to show that the first braced expression on the right-hand side of Eq. (2.23) is equal to  $\partial_t (\nabla \times \partial_t \mathbf{u}_{\text{DF}}) \cdot \hat{\mathbf{e}}_z$ . The remaining terms in Eq. (2.23) were erroneously omitted in the corresponding expression without rotation [vdBS18, Eq. (A 3)]. It will be shown that certain values of  $\beta_x$ ,  $\beta_y$ , and  $\beta_z$  lead this omission to be of no consequence for their results.

Substituting Eq. (2.23) into the right-hand side of Eq. (2.17) and using Eq. (2.18), then cancelling  $\partial_t (\nabla \times \partial_t \mathbf{u}_{\text{DF}}) \cdot \hat{\mathbf{e}}_z$  on both sides of the resulting expression, we find that

$$\begin{aligned}
\partial_{tt} (\nabla \times \mathbf{u}_{\text{RF}}) \cdot \hat{\mathbf{e}}_z = & - \frac{1}{2} \frac{\partial}{\partial t} \left\{ \left[ \frac{m^2}{k^2} (\omega^2 + f_0^2) + \omega^2 \frac{\|\mathbf{k}\|^2}{k} \beta_x \right] \epsilon_x \epsilon_y A \partial_{XY} A \right. \\
& \left. + \omega^2 \frac{\|\mathbf{k}\|^2}{k} \beta_y \epsilon_y^2 A \partial_{YY} A - \left[ \frac{m}{k} (\omega^2 + f_0^2) - \omega^2 \frac{\|\mathbf{k}\|^2}{k} \beta_z \right] \epsilon_y \epsilon_z A \partial_{YZ} A \right\}. \quad (2.24)
\end{aligned}$$

We now invoke the horizontal irrotationality of  $\mathbf{u}_{\text{RF}}$  (Bretherton, 1969), which imposes the values of  $\beta_x$ ,  $\beta_y$ , and  $\beta_z$  so that the right-hand side of Eq. (2.24) is identically zero. Explicitly, we find

$$\beta_x = -\frac{m^2}{k\|\mathbf{k}\|^2} \left(1 + \frac{f_0^2}{\omega^2}\right), \quad (2.25a)$$

$$\beta_y = 0, \quad (2.25b)$$

$$\beta_z = -\frac{k}{m}\beta_x. \quad (2.25c)$$

In the nonrotating limit (as  $f_0 \rightarrow 0$ ),  $\beta_x \rightarrow -c_{gx}/\omega$  and  $\beta_z \rightarrow -c_{gz}/\omega$ . The horizontal irrotationality of  $u_{\text{RF}}$  implies that the aforementioned omitted terms in the derivation of vdBS18 vanish identically so there is no change to their results.

Using Eqs. (2.25a)–(2.25c) in Eq. (2.17) and integrating once with respect to time yields

$$\begin{aligned} -\mathbf{c}_g \cdot \nabla (\epsilon_x \partial_X v_{\text{BF}} - \epsilon_y \partial_Y u_{\text{BF}}) &= \epsilon_x \partial_X (\partial_t v_{\text{DF}}) - \epsilon_y \partial_Y (\partial_t u_{\text{DF}}) \\ &= -\frac{1}{2} \frac{m^2}{k^2} \left\{ f_0^2 \epsilon_x \epsilon_y \partial_{XY} - \frac{\omega^2}{c_{gx}} \epsilon_y \mathbf{c}_g \cdot \nabla \partial_Y \right\} |A|^2, \end{aligned} \quad (2.26)$$

where we have used  $\partial_t \approx -\mathbf{c}_g \cdot \nabla = -\epsilon_x c_{gx} \partial_X - \epsilon_z c_{gz} \partial_Z$  [cf. Eq. (2.16d)] on the left-hand side, and we have used Eq. (2.19) and the identity  $-k/m = c_{gz}/c_{gx}$  on the right-hand side. Note that the ‘constant’ (with respect to time) of integration that would usually be included on the right-hand side of Eq. (2.26) is identically zero, because the time integration effectively inverted the time derivative applied previously to the vorticity equation [cf. Eq. (2.10), which contains no steady terms], in the course of obtaining Eq. (2.11) governing the evolution of general wave-induced mean flows.

A partial differential equation for  $u_{\text{BF}}$  alone is found by taking the  $Y$ -derivative of Eq. (2.26) and eliminating the resulting mixed  $\partial_{XY} v_{\text{BF}}$  term on the left-hand side using the  $X$ -derivative of the Bretherton incompressibility condition,

$$\epsilon_x \partial_X u_{\text{BF}} + \epsilon_y \partial_Y v_{\text{BF}} = 0. \quad (2.27)$$

Similarly, a partial differential equation for  $v_{\text{BF}}$  alone is obtained using the  $X$ -derivative of

Eq. (2.19) and the  $Y$ -derivative of Eq. (2.27) to eliminate the mixed  $\partial_{XY}u_{\text{BF}}$  term. Explicitly,

$$(\mathbf{c}_g \cdot \nabla) \nabla_{\perp}^2 u_{\text{BF}} = -\frac{1}{2} \frac{m^2}{k^2} \left\{ f_0^2 \epsilon_x \epsilon_y^2 \partial_{XY} - \frac{\omega^2}{c_{gx}} \epsilon_y^2 \mathbf{c}_g \cdot \nabla \partial_{YY} \right\} |A|^2, \quad (2.28)$$

$$-(\mathbf{c}_g \cdot \nabla) \nabla_{\perp}^2 v_{\text{BF}} = -\frac{1}{2} \frac{m^2}{k^2} \left\{ f_0^2 \epsilon_x^2 \epsilon_y \partial_{XX} - \frac{\omega^2}{c_{gx}} \epsilon_x \epsilon_y \mathbf{c}_g \cdot \nabla \partial_{XY} \right\} |A|^2, \quad (2.29)$$

where  $\nabla_{\perp}^2 = \epsilon_x^2 \partial_{XX} + \epsilon_y^2 \partial_{YY}$  is the slow horizontal Laplacian operator.

Equations (2.28)–(2.29) are solved using Fourier transforms with respect to *unscaled* translating coordinates  $\tilde{\mathbf{x}} = (\tilde{x}, \tilde{y}, \tilde{z}) = (X/\epsilon_x, Y/\epsilon_y, Z/\epsilon_z)$ , which we adopt for convenience following vdBS18. To that end, we denote by  $\hat{\eta}$  the Fourier transform of a field  $\eta$ , and define the Fourier transform pair

$$\hat{\eta}(\boldsymbol{\kappa}) := \frac{1}{(2\pi)^3} \int_{\mathbb{R}^3} \eta(\tilde{\mathbf{x}}) e^{-i\boldsymbol{\kappa} \cdot \tilde{\mathbf{x}}} d\tilde{x} d\tilde{y} d\tilde{z}, \quad (2.30a)$$

$$\eta(\tilde{\mathbf{x}}) := \int_{\mathbb{R}^3} \hat{\eta}(\boldsymbol{\kappa}) e^{i\boldsymbol{\kappa} \cdot \tilde{\mathbf{x}}} d\boldsymbol{\kappa} d\lambda d\mu, \quad (2.30b)$$

where  $\boldsymbol{\kappa} = (\kappa, \lambda, \mu)$  is the vector of transform variables. Under the change to unscaled variables,  $\epsilon_x \partial_X \rightarrow \partial_{\tilde{x}}$ ,  $\epsilon_y \partial_Y \rightarrow \partial_{\tilde{y}}$ , and  $\epsilon_z \partial_Z \rightarrow \partial_{\tilde{z}}$ . Then, under the Fourier transform,  $\partial_{\tilde{x}} \rightarrow i\kappa$ ,  $\partial_{\tilde{y}} \rightarrow i\lambda$ , and  $\partial_{\tilde{z}} \rightarrow i\mu$ . Using these with the Fourier transform of Eqs. (2.28)–(2.29) converts these partial differential equations into algebraic equations that are readily solved for  $\widehat{u_{\text{BF}}}$  and  $\widehat{v_{\text{BF}}}$ . Inverse transforming, we find

$$\begin{bmatrix} u_{\text{BF}} \\ v_{\text{BF}} \end{bmatrix} = \frac{1}{2} \frac{m^2}{k^2} \int_{\mathbb{R}^3} \frac{\lambda}{\kappa^2 + \lambda^2} \left( \frac{\omega^2}{c_{gx}} - f_0^2 \frac{\kappa}{\mathbf{c}_g \cdot \boldsymbol{\kappa}} \right) \begin{bmatrix} \lambda \\ -\kappa \end{bmatrix} |\widehat{A}|^2 e^{i\boldsymbol{\kappa} \cdot \tilde{\mathbf{x}}} d\boldsymbol{\kappa} d\lambda d\mu, \quad (2.31)$$

This represents the solution to the special case of a Poisson equation [Bühler and McIntyre (1998), Eq. (9.29)] for the streamfunction associated with the Bretherton flow, in the limit of no background flow and no variation of the Coriolis parameter with latitude. Unlike Eq. (2.31), derived using classical perturbation methods, Eq. (9.29) of Bühler and McIntyre (1998) was derived in a potential vorticity framework and applying *generalized Lagrangian-mean* theory [a versatile formalism developed in the seminal papers by Andrews and McIntyre (1978a,b) for analyzing wave-mean flow interactions, but which is overly sophisticated for our purposes]. Equation (2.31) likewise represents a solution to Eq. (22) in Tabaei and Akylas (2007). In the nonrotating limit, Eq. (2.31) indeed recovers Eq. (3.15) of vdBS18, as anticipated. Rotation is responsible for certain additional dynamics not captured by the nonrotating analogue of

Eq. (2.31), namely, that the rotating Bretherton flow is not restricted to the isopycnals that intersect the wave packet. This relatively high-order response is represented by the term  $-f_0 \partial_{tz} w_{\text{BF}}$  which was omitted from the left-hand side of Eq. (2.17). More explicitly, in Eq. (9.29) of Bühler and McIntyre (1998) the response to the nonlinear forcing contains a term proportional to  $f_0^2$  times the vertical gradient of buoyancy acceleration.

In principle, Eq. (2.31) predicts the evolution at early times of the Bretherton flow induced by wave packets with any sufficiently localized amplitude envelope  $A$ . However, in practice we prescribe the initial amplitude using the Gaussian envelope

$$A(x, y, z, t = 0) = A_0 \exp \left[ -\frac{1}{2} \left( \frac{x^2}{\sigma_x^2} + \frac{y^2}{\sigma_y^2} + \frac{z^2}{\sigma_z^2} \right) \right]. \quad (2.32)$$

This envelope is convenient qualitatively because it is easily visualized, and mathematically because it possesses desirable analytical properties. In particular, the Fourier transform of  $A$ , (and more importantly, that of  $|A|^2$ ) can be computed explicitly. Using Eq. (2.30a),

$$\widehat{|A|^2} = \frac{1}{8\pi^{3/2}} \sigma_x \sigma_y \sigma_z A_0^2 \exp \left[ -\frac{1}{4} (\sigma_x^2 k^2 + \sigma_y^2 \lambda^2 + \sigma_z^2 \mu^2) \right]. \quad (2.33)$$

The horizontal components of the initial Bretherton flow are found by substituting Eq. (2.33) into Eq. (2.31) and integrating numerically (the details of which are discussed in Sec. 3.3.1).

Horizontal cross sections of nondimensionalized  $\tilde{u}_{\text{BF}}(x, y, 0, t = 0) = u_{\text{BF}}(x, y, 0, 0)/(N_0/k)$  are shown in Fig. 2.1 for round, long, and wide wave packets and two Coriolis parameters. In each case, the wave packet amplitude was set by the Gaussian envelope given in Eq. (2.32). Waves were initialized with a peak vertical displacement of  $A_0 = 0.08k^{-1}$  and a relative vertical wavenumber of  $m/k = -11.4$ , corresponding to hydrostatic internal waves propagating at a nearly horizontal angle of  $\Theta = \tan^{-1} |m/k| = 85^\circ$  to the vertical. The Coriolis parameter was set to be  $f_0 = 0.01N_0$  and  $0.05N_0$  in the top and bottom rows, respectively, with corresponding wave frequencies  $\omega/f_0 = 8.80$  and  $2.01$ . These choices represent relatively weak and strong rotation, respectively. In each panel, the heavy and light white ellipses [defined by the curve  $(x/\sigma_x)^2 + (y/\sigma_y)^2 = a^2$ ] indicate  $a = 1$  and  $a = 2$  standard deviations about the wave packet centre, respectively. Black contours are 20 evenly-spaced streamlines,

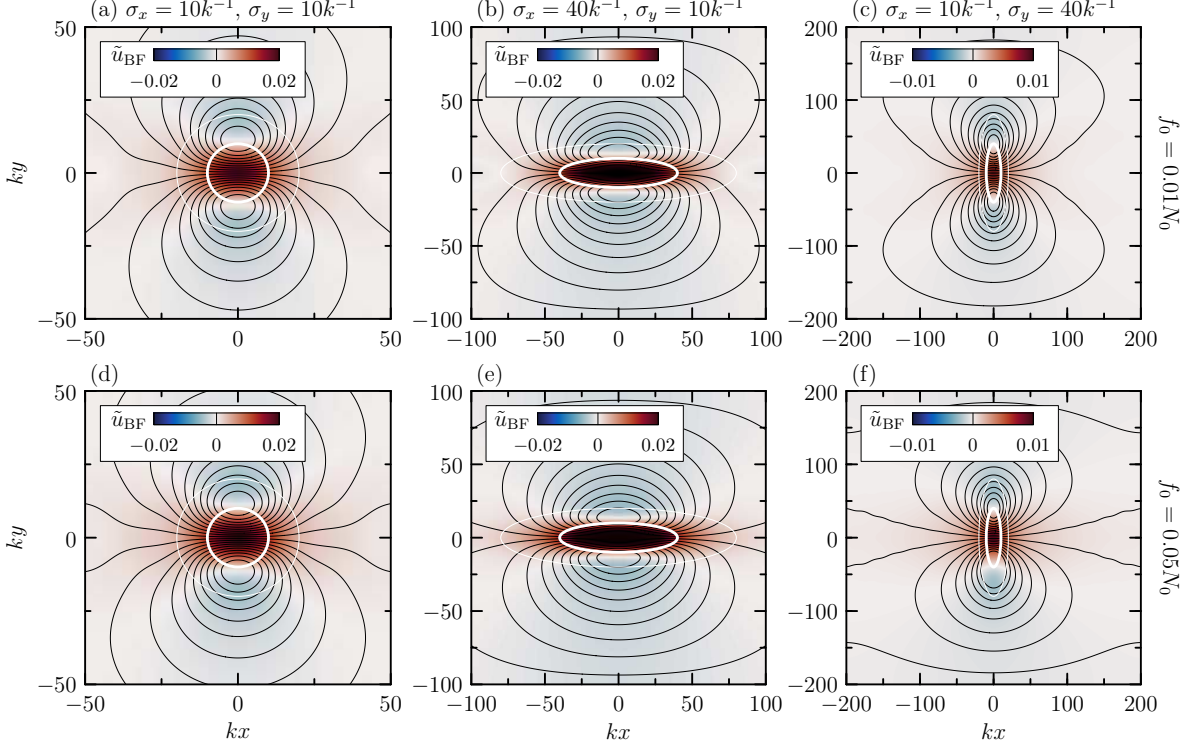


**Figure 2.1:** Horizontal slices of the initial nondimensionalized Bretherton flow,  $\tilde{u}_{\text{BF}} = u_{\text{BF}}(x, y, z = 0, t = 0)/(N_0/k)$ , given by Eq. (2.31), for (a,d) round; (b,e) long; and, (c,f) wide Gaussian wave packets with rotation set by  $f_0 = 0.01N_0$  (a–c) and by  $f_0 = 0.05N_0$  (d–f). The wave packets shown were initialized with a peak vertical displacement amplitude of  $A_0 = 0.08k^{-1}$ , a relative vertical wavenumber of  $m/k = -11.4$ , and a vertical extent of  $\sigma_z = 10k^{-1}$ . Black contours are isolines of nondimensionalized streamfunction,  $\tilde{\psi}_{\text{BF}} = \psi_{\text{BF}}/(N_0/k^2)$ , defined implicitly by Eqs. (2.34a)–(2.34b). Heavy and light white ellipses show one and two standard deviations, respectively, about the centre of the Gaussian wave packet.

$\tilde{\psi}_{\text{BF}} = \psi_{\text{BF}}/(N_0/k^2)$ , defined implicitly by

$$u_{\text{BF}} := -\partial_y \psi_{\text{BF}}, \quad (2.34a)$$

$$v_{\text{BF}} := \partial_x \psi_{\text{BF}}. \quad (2.34b)$$

The dipolelike recirculating structure of the Bretherton flow manifests clearly in the colouration and streamlines about each wave packet, as was found with no rotation (Bretherton, 1969; van den Bremer and Sutherland, 2018): the dominant factor responsible for the structure of the Bretherton flow is the wave packet geometry as described by  $A$ . For both values of  $f_0$ , the weakest Bretherton flow is associated with wide wave packets [Fig. 2.1(c,f)]. This is consistent with the nonrotating results of vdBS18, who showed that the magnitude of the Bretherton flow decreases as  $1/R_y$ , in which  $R_y = \sigma_y/\sigma_x$  is the spanwise aspect ratio (see also Bühler, 2009). The effect of rotation is to broaden the area over which the Bretherton flow

is nonnegligible, represented by the broadened extent of the streamlines in Fig. 2.1(d–f) compared to those in Fig. 2.1(a–c). Rotation also acts to break streamline symmetry across the  $x$ -axis, although this is only subtly distinguished in Fig. 2.1(f) by the increased concentration of closed streamlines near  $ky = 50$  compared to  $ky = -50$ . Quantitatively, increasing the Coriolis parameter from  $f_0 = 0.01N_0$  to  $0.05N_0$  increases the magnitude of the Bretherton flow. The largest contribution of rotation was to increase  $u_{\text{BF}}(\mathbf{0})$  by 16% for round wave packets and by 19% for long and wide wave packets.

#### 2.2.4 Relative effect of rotation on the Bretherton flow

Because rotation acts to influence the Bretherton flow at a relatively high order as described above, the dominant contribution to the Bretherton flow is modelled by the first term in parentheses in the integrand of Eq. (2.31). It follows that, for a fixed streamwise wavenumber, Coriolis parameter, and amplitude,

$$\frac{|u_{\text{BF}}(\mathbf{0})|}{A_0^2} \approx \frac{m^2 \omega^2}{k^2 c_{gx}} = \frac{k}{N_0^2 - f_0^2} \sqrt{1 + \frac{m^2}{k^2}} \left[ N_0^2 + f_0^2 \frac{m^2}{k^2} \right]^{3/2}$$

increases with  $|m/k|$ , i.e., as waves become more hydrostatic. Therefore, the peak magnitude of the Bretherton flow (relative to  $A_0^2$ ) induced by a hydrostatic wave packet is *greater* than that induced by a nonhydrostatic wave packet of the same amplitude. This analysis suggests that interactions between waves and their induced Bretherton flow contribute to the overturning of moderately large amplitude nonhydrostatic wave packets and relatively small amplitude hydrostatic wave packets alike. This result is somewhat unintuitive because the nonlinear influence of the order amplitude-squared Bretherton flow is anticipated to decrease quadratically as amplitude decreases.

Without the preceding analysis, one might erroneously ignore the effects of the rotating Bretherton flow on the evolution of hydrostatic wave packets (which typically exist at small amplitude), as it is common practice to ignore nonlinearity in the study of small amplitude waves more generally.

## 2.3 Wave instability and critical amplitudes

In this section we consider several instability mechanisms that can lead to internal wave breaking. We follow Sutherland (2001) to predict the critical amplitudes for static, convection, and self-acceleration instabilities influenced by rotation. We then consider the effect of rotation on instability due to the shear between adjacent wave velocity crests and troughs, which was not examined by Sutherland (2001). It is convenient to normalize all critical amplitudes [except those in Fig. 2.2(b)] using the streamwise wavelength,  $\lambda_x = 2\pi/k$ , so that  $\tilde{A} = A/\lambda_x$  is an intuitive nondimensional measure of vertical displacement amplitude.

### 2.3.1 Static instability

An internal gravity wave is overturning if it is of sufficiently large amplitude that relatively dense fluid is lifted above relatively less dense fluid. As a result the vertical gradient of the total mass density field is positive somewhere in the flow field:  $d\bar{\rho}(z)/dz + \partial\rho(\mathbf{x}, t)/\partial z > 0$ . This inequality can be recast in terms of vertical displacement using Eq. (2.4), then multiplied by  $-g/\rho_0$  and using Eq. (2.9) to obtain the equivalent overturning condition

$$N_T^2(\mathbf{x}, t) := N_0^2 + \Delta N^2 = N_0^2 \left( 1 - \frac{\partial\xi}{\partial z} \right) < 0, \quad (2.35)$$

where we have defined  $N_T^2$ , the so-called *total squared buoyancy frequency*, and  $\Delta N^2 = -N_0^2 \partial\xi/\partial z$  is the local change in the squared buoyancy frequency due to waves. The exponent on  $N_T^2$  makes explicit the physical units of this quantity (*frequency squared*), even though Eq. (2.35) effectively models the leading-order change in squared buoyancy due to vertical variations of the *linear* vertical displacement field. The corresponding critical amplitude at which a wave is predicted to overturn is found by substituting a plane wave into  $1 - \partial\xi/\partial z < 0$  [having used the fact that  $N_0^2$  is constant and so can be divided out of the right-hand side of Eq. (2.35)] and rearranging the resulting expression to find

$$\tilde{A}_{\text{OT}} = \frac{1}{2\pi} \left| \frac{k}{m} \right| = \frac{1}{2\pi} \cot \Theta, \quad (2.36)$$

where  $\Theta = \tan^{-1} |m/k|$  is the angle between lines of constant phase and the vertical.

Rotation has no direct effect on  $\tilde{A}_{\text{OT}}$  because Eq. (2.36) was derived using the leading-

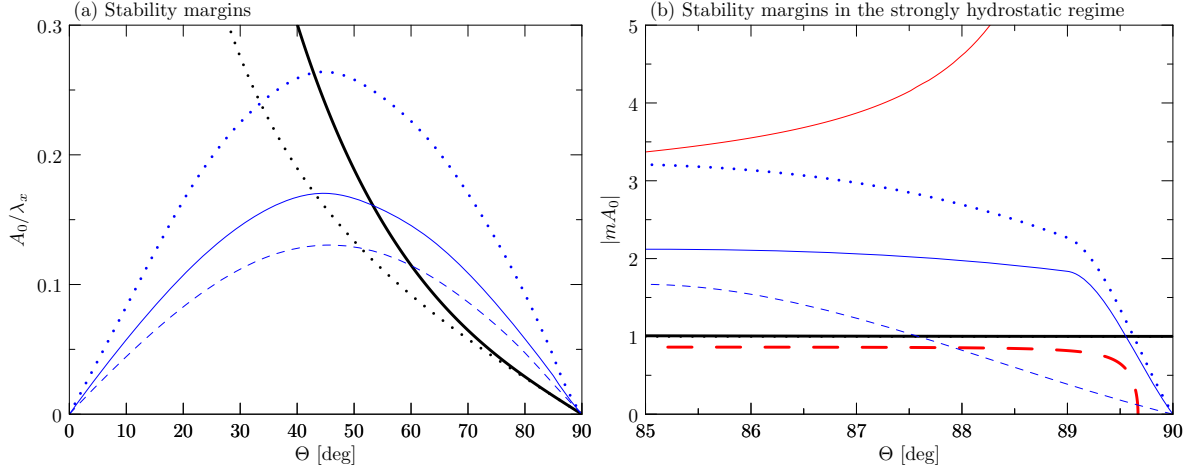


**Figure 2.2:** Curves of marginal stability emphasizing waves in the (a) nonhydrostatic, and (b) strongly hydrostatic wavenumber regimes. The  $\Theta$ -axis corresponds to waves spanning the frequency range (a)  $N_0 \geq \omega \geq f_0$ ; and, (b)  $8.77 \gtrsim \omega/f_0 \geq 1$ , with  $f_0 = 0.01N_0$ . The black dotted and solid curves indicate the amplitude above which a plane wave is predicted to be statically and convectively unstable, respectively, according to Eqs. (2.36) and (2.37). The blue solid, dotted, and dashed curves indicate the amplitude above which a three-dimensional wave packet with spanwise aspect ratio  $R_y = 1, 1/4,$  and  $4$ , respectively, is predicted to be unstable to self-acceleration according to Eq. (2.41). The solid and dashed red curves in (b) indicate the amplitude above which a wave packet is predicted to be shear unstable using respectively our definition of the gradient Richardson number, Eq. (2.43), and that of Fritts and Rastogi (1985) and Achatz (2007) given by Eq. (2.48).

order vertical displacement field which itself depends only indirectly on rotation through the wave frequency,  $\omega = \omega(\mathbf{k}; f_0)$ , according to Eq. (2.13). The overturning condition given by Eq. (2.36) may be stated equivalently in terms of the steepness of a monochromatic internal wave in one dimension,  $s := u/c_p$  (with overturning corresponding to  $s = 1$ ), where  $c_p = \omega/k$  is the phase speed of a one-dimensional plane wave. The curve of marginal stability corresponding to Eq. (2.36) is shown as the black dotted curve in Fig. 2.2.

### 2.3.2 Convection instability

A statically unstable wave is prone to develop convective instabilities. Whether such instabilities materialize, ultimately to drive the wave to breaking, depends on the relative time scale for the growth of convective instability compared to the period of the waves. Sutherland (2001) found that the relatively rapid oscillation of high frequency nonhydrostatic waves was able to restore static stability to locally unstable fluid parcels, thus delaying the onset of convective instability.

The condition for convective instability to outpace the restorative oscillatory motion of

plane waves was found by [Sutherland \(2001\)](#) to be  $N_0\sqrt{|m|A-1} > \omega$ , where the left-hand side expression represents the maximum instability growth rate. Using the definition of  $\omega$  [cf. Eq. (2.13)] in this inequality and rearranging the resulting expression yields the critical amplitude at which a plane was predicted to become convectively unstable:

$$\tilde{A}_{\text{CV}} = \frac{1}{2\pi} \cot \Theta \left( 1 + \cos^2 \Theta + \frac{f_0^2}{N_0^2} \sin^2 \Theta \right). \quad (2.37)$$

In the nonrotating limit, this expression recovers that derived by [Sutherland \(2001\)](#). The curve of marginal stability corresponding to Eq. (2.37) with  $f_0 = 0.01N_0$  is shown as the solid black curve in Fig. 2.2. Note that  $\tilde{A}_{\text{CV}} > \tilde{A}_{\text{OT}}$  even as  $\Theta \rightarrow 90^\circ$  (achieved as  $\omega \rightarrow f_0$ , corresponding to purely inertial oscillations confined to the horizontal plane).

### 2.3.3 Self-acceleration instability

The earliest reference to “self-acceleration” appears to be in the work of [Fritts and Dunkerton \(1984, p. 3273\)](#), in the context of internal gravity wave packets that alter significantly their phase structure when propagating in the vicinity of a critical level (the height where the streamwise phase speed is equal to that of the background flow).

Internal gravity waves are prone to self-acceleration even in the absence of a preexisting background flow. Somewhat heuristically, [Sutherland \(2001\)](#) proposed that a one-dimensional wave packet in an otherwise stationary fluid was prone to instability due to self-acceleration if the wave-induced mean flow exceeded the streamwise group speed of the wave packet. This heuristic condition was found to be in good agreement with results of simulations of one-, but not two-dimensional wave packets ([Sutherland, 2001](#)). [The poor agreement for two-dimensional wave packets may have been due to the assumed model of the mean flow induced by two-dimensional wave packets, which did not account for the long waves generated by these wave packets as found by [Bretherton \(1969\)](#) and [van den Bremer and Sutherland \(2014\)](#).] For a one-dimensional wave packet without rotation, the wave-induced mean flow is given by

$$U_{\text{1D}} = \frac{1}{2} N_0 \|\mathbf{k}\| |A|^2. \quad (2.38)$$

This expression has been alternatively derived using the principle of wave action ([Acheson, 1976](#)), Hamiltonian fluid mechanics ([Scinocca and Shepherd, 1992](#)), and momentum conser-

vation (e.g., [Sutherland, 2010](#)). Comparing Eq. (2.38) to the streamwise group speed of wave packets in a nonrotating fluid [cf. Eq. (2.14a), in the limit as  $f_0 \rightarrow 0$ ], the critical amplitude for self-acceleration is  $\tilde{A}_{\text{SA}} = \sin(2\Theta)/(\pi\sqrt{8})$  ([Sutherland, 2001](#)).

In three dimensions, the mean flow induced by fully localized wave packets is the Bretherton flow with maximum initially at  $\mathbf{x} = \mathbf{0}$ , so it is necessary to compare  $c_{gx}$  to  $u_{\text{BF}}(\mathbf{0})$ . Hence we find generally

$$\tilde{A}_{\text{SA}} = \frac{A_0 k}{2\pi} \sqrt{\frac{c_{gx}}{u_{\text{BF}}(\mathbf{0})}}. \quad (2.39)$$

For Gaussian wave packets in particular, using the envelope given by Eq. (2.33) in the first row of Eq. (2.31) we find

$$\begin{aligned} u_{\text{BF}}(\mathbf{0}) &= \frac{1}{16\pi^{3/2}} \frac{m^2}{k^2} \frac{\omega^2}{c_{gx}} \sigma_x \sigma_y \sigma_z A_0^2 \int_{\mathbb{R}^3} \frac{\lambda^2}{\kappa^2 + \lambda^2} e^{-(\sigma_x^2 \kappa^2 + \sigma_y^2 \lambda^2 + \sigma_z^2 \mu^2)/4} d\boldsymbol{\kappa} \\ &\quad - f_0^2 \frac{1}{16\pi^{3/2}} \frac{m^2}{k^2} \sigma_x \sigma_y \sigma_z A_0^2 \int_{\mathbb{R}^3} \frac{\lambda^2}{\kappa^2 + \lambda^2} \frac{\boldsymbol{\kappa}}{\mathbf{c}_g \cdot \boldsymbol{\kappa}} e^{-(\sigma_x^2 \kappa^2 + \sigma_y^2 \lambda^2 + \sigma_z^2 \mu^2)/4} d\boldsymbol{\kappa}. \end{aligned} \quad (2.40)$$

The first line of Eq. (2.40) can be integrated explicitly [the details of which are provided in Appendix C; see also [Bühler \(2009\)](#)], and is equal to

$$\frac{1}{2} \frac{m^2}{k^2} \frac{\omega^2}{c_{gx}} \frac{A_0^2}{R_y + 1},$$

equivalent to setting  $z = 0$  in Eq. (C.3).

The integral in second line of Eq. (2.40) cannot be integrated explicitly on account of the singularities along  $\mathbf{c}_g \cdot \boldsymbol{\kappa} = 0$ . Hence, this integral must be evaluated numerically using the procedure described in Sec. 3.3.1. To proceed analytically, for convenience we recast the singular integrand in terms of nondimensional variables  $\tilde{\kappa} = \sigma_x \kappa$ ,  $\tilde{\lambda} = \sigma_y \lambda$ , and  $\tilde{\mu} = \sigma_z \mu$ , so that the corresponding integral is written  $\frac{1}{c_{gx}} \int_{\mathbb{R}^3} I d\tilde{\boldsymbol{\kappa}}$ , where

$$I = I(\tilde{\boldsymbol{\kappa}}; R_y, R_z, k/m) = \frac{\tilde{\lambda}^2 e^{-(\tilde{\kappa}^2 + \tilde{\lambda}^2 + \tilde{\mu}^2)/4}}{(R_y^2 \tilde{\kappa}^2 + \tilde{\lambda}^2)[1 - R_z^{-1}(k/m)(\tilde{\mu}/\tilde{\kappa})]},$$

in which  $R_z = \sigma_z/\sigma_x$  is the wave packet vertical aspect ratio. Together with Eq. (2.40), the critical amplitude for self-acceleration instability is

$$\tilde{A}_{\text{SA}} = \frac{k^2}{\sqrt{2\pi}|m|} c_{gx} \left[ \frac{\omega^2}{R_y + 1} - \frac{f_0^2}{8\pi^{3/2}} \int_{\mathbb{R}^3} I d\tilde{\boldsymbol{\kappa}} \right]^{-1/2}. \quad (2.41)$$

Curves of marginal stability corresponding to Eq. (2.41) for spanwise aspect ratios  $R_y = 1$ ,

1/4, and 4 (with  $\sigma_x = \sigma_z = 10k^{-1}$  fixed) are shown in Fig. 2.2 as the solid, dashed, and dotted blue curves, respectively. In practice, these curves were plotted by first computing  $\tilde{A}_{\text{SA}}$  using Eq. (2.39) with  $u_{\text{BF}}(\mathbf{0})$  taken from a selection of simulation outputs at  $t = 0$ , and interpolating between them using cubic splines. The interpolation is more obvious in the kinks in the solid and dotted blue curves in Fig. 2.2(b) at  $\Theta = 89^\circ$ . Note that it was not feasible computationally to obtain  $\tilde{A}_{\text{SA}}$  at  $\Theta = 89^\circ$  for  $R_y = 1/4$ , and so the dashed blue curve in Fig. 2.2(b) is likely an underestimate.

### 2.3.4 Stratified shear instability

Strongly hydrostatic internal gravity waves have phase lines that are oriented nearly horizontally. Consequently, the motion of adjacent velocity crests and troughs resembles locally an (approximately) parallel shear flow. It is natural to ask whether shear (Kelvin–Helmholtz) instability can develop at the inflection point where velocity crests and troughs meet. The shear stability of a truly parallel shear flow  $U = U(z)$ , with stratification described by the buoyancy frequency  $N$  (not necessarily constant), restricted to the  $xz$ -plane is characterized by the gradient Richardson number (e.g., [Drazin and Reid, 1981](#)),

$$\text{Ri}_g := \frac{N^2}{(dU/dz)^2}. \quad (2.42)$$

Internal gravity waves that are influenced by rotation are not restricted to propagate in the  $xz$ -plane, and so it is necessary to incorporate into the definition of the gradient Richardson number the shear associated with  $u$  and  $v$ . However, a definition of such a gradient Richardson number remains elusive: the definition in Eq. (2.42) emerges from an analysis of the Taylor–Goldstein equation ([Taylor, 1931](#); [Goldstein, 1931](#)), which describes the linear dynamics of Kelvin–Helmholtz instability for stratified shear flows in *two dimensions*. Crucially, a search of existing literature suggests that an analogous equation describing the dynamics in three dimensions under the same assumptions has not been derived, from which an analogous gradient Richardson number might emerge naturally. As this nontrivial task appears not to have been attempted, there is to date no unambiguous definition of the corresponding gradient Richardson number.

In the absence of a rigorously derived definition of  $\text{Ri}_g$  for three-dimensional rotating

flows, various authors have somewhat heuristically adopted physically reasonable definitions. For example, [Fritts and Rastogi \(1985\)](#) and [Achatz \(2007\)](#) defined  $\text{Ri}_g$  using the squared magnitude of the vertical shear vector,  $\|(\partial_z u, \partial_z v)\|^2 = (\partial u/\partial z)^2 + (\partial v/\partial z)^2$ . Their results suggested strongly hydrostatic waves favour the development of shear instability as opposed to convective instability.

We model the local velocity shear by the vertical gradient of the magnitude of the horizontal velocity vector,  $\|(u, v)\| = \sqrt{u^2 + v^2}$ , rather than the magnitude of the shear vector, so that the gradient Richardson number is defined by

$$\text{Ri}_g := \frac{N_0^2 + \Delta N^2}{\left(\frac{\partial}{\partial z} \|(u, v)\|\right)^2} = \left[ \frac{N_0 k}{m(\omega^2 - f_0^2)} \right]^2 \frac{1}{\alpha_0^2} \underbrace{\frac{(1 - \alpha_0 \sin \varphi)[(\omega^2 - f_0^2) \sin^2 \varphi + f_0^2]}{\sin^2 \varphi \cos^2 \varphi}}_{:=\Phi(\varphi)}, \quad (2.43)$$

where we have modelled the effect of stratification by considering the total squared buoyancy, given by Eq. (2.35), we used the leading-order polarization relations (cf. Table 2.1) on the right-hand side, and we defined  $\alpha_0 := |mA|$ .

Because we wish to investigate shear instability between adjacent crests and troughs, we proceed to determine  $\min_{\varphi} \text{Ri}_g$ , corresponding to critical values  $\varphi_c$  satisfying

$$\frac{d\text{Ri}_g}{d\varphi} = \left[ \frac{N_0 k}{m(\omega^2 - f_0^2)} \right]^2 \frac{d\Phi}{d\varphi} = 0, \quad (2.44)$$

where

$$\begin{aligned} \frac{d\Phi(\varphi)}{d\varphi} &= \frac{-2\alpha_0 \omega^2 \sin^5 \varphi + 2\omega^2 \sin^4 \varphi - \alpha_0 \omega^2 \sin^3 \varphi \cos^2 \varphi + \alpha_0 f_0^2 \sin \varphi \cos^4 \varphi - 2f_0^2 \cos^4 \varphi}{\sin^3 \varphi \cos^3 \varphi} \\ &= -\sec^3 \varphi \csc^3 \varphi \left\{ \alpha_0 (\omega^2 - f_0^2) \sin^5 \varphi - 2(\omega^2 - f_0^2) \sin^4 \varphi + \alpha_0 (\omega^2 + 2f_0^2) \sin^3 \varphi \right. \\ &\quad \left. - 4f_0^2 \sin^2 \varphi - \alpha_0 f_0^2 \sin \varphi + 2f_0^2 \right\}. \end{aligned}$$

This equation relates  $\varphi_c$  and  $\alpha_0$  for a fixed  $k/m$  and  $f_0$ . A second relation is found by setting  $\text{Ri}_g = 1/4$  in Eq. (2.43) as a threshold for instability ([Miles, 1961](#); [Howard, 1961](#)), which together with Eq. (2.44) forms a closed system of equations that has no analytically tractable solution. Therefore, solutions were found numerically for a broad range of  $m/k$  and with  $f_0 = 0.01N_0$  fixed, and from these the critical amplitude  $\tilde{A}_{\text{SHR}}$  was found. The results are plotted as the solid red curve in Fig. 2.2(b).

### 2.3.4.1 Comparison and analysis of gradient Richardson numbers

For comparison, the minimization procedure described above may be performed analytically if one considers the definition of  $\text{Ri}_g$  used by [Fritts and Rastogi \(1985\)](#) and ([Achatz, 2007](#)), for which

$$\text{Ri}_g = \left(\frac{N_0 k}{m}\right)^2 \frac{1 - \alpha_0 \sin \varphi}{\alpha_0^2 \omega^2 \cos^2 \varphi + f_0^2 \sin^2 \varphi}, \quad (2.45)$$

$$\frac{d\text{Ri}_g}{d\varphi} = -\left(\frac{N_0 k}{m}\right)^2 \frac{1}{\alpha_0^2} \frac{\cos \varphi [\alpha_0(\omega^2 - f_0^2) \sin^2 \varphi - 2(\omega^2 - f_0^2) \sin \varphi + \omega^2 \alpha_0]}{(\omega^2 \cos^2 \varphi + f_0^2 \sin^2 \varphi)^2}. \quad (2.46)$$

Setting  $d\text{Ri}_g/d\varphi = 0$  in Eq. (2.46) yields four distinct candidates for  $\varphi_c$ , which can be recast in terms of  $\sin \varphi_c$ . From  $\cos \varphi_c = 0$  we have  $\sin \varphi_c = \pm 1$ , and from the term in square brackets in Eq. (2.46) we have

$$\sin \varphi_c = \frac{1 \pm \sqrt{1 - \alpha_0^2 \omega^2 / (\omega^2 - f_0^2)}}{\alpha_0}. \quad (2.47)$$

Setting  $\text{Ri}_g = 1/4$  in Eq. (2.45), using  $\cos \varphi_c = 0$  and  $\sin \varphi_c = \pm 1$  on the right-hand side, and rearranging the resulting expression for  $\alpha_0$  as a function of  $m/k$  gives

$$\alpha_0 = 2 \left\{ \mp \left(\frac{N_0/f_0}{m/k}\right)^2 + \left[ \left(\frac{N_0/f_0}{m/k}\right)^4 + \left(\frac{N_0/f_0}{m/k}\right)^2 \right]^{1/2} \right\}, \quad (2.48)$$

where we have added (as opposed to subtracted) the radical term arising from the use of the quadratic formula, thus ensuring  $\alpha_0 \not\prec 0$ . The choice of  $\mp$  corresponds to  $\sin \varphi_c = \pm 1$ . In particular, taking  $\sin \varphi_c = 1$  restricts the wave amplitudes to  $0 \leq \alpha_0 \leq 1$  for all  $|m/k|$ , corresponding to waves that are of smaller amplitude than that predicted for overturning by Eq. (2.36). The corresponding curve of marginal stability is shown in Fig. 2.2(b) as the dashed red curve.

The alternative choice of  $\varphi_c$ , given implicitly by Eq. (2.47), leads to unphysical results. This is shown by first setting  $\text{Ri}_g = 1/4$  in Eq. (2.45) and using Eq. (2.47) to find  $\frac{1}{4} = \frac{1}{2}(N_0 k/m)^2 / [(\omega^2 - f_0^2)(1 \pm \sqrt{d})]$ , where  $d$  is the discriminant in Eq. (2.47). Solving for  $\alpha_0$  gives

$$\alpha_0 = 2 \frac{N_0 k}{\omega m} \sqrt{1 - \left(\frac{N_0 k}{m}\right)^2 \frac{1}{\omega^2 - f_0^2}}.$$

Because  $\alpha_0 \in \mathbb{R}$ , shear instability cannot develop if  $1 - (N_0 k/m)^2 / (\omega^2 - f_0^2) < 0$ , or equivalently, if  $N_0^2 k^2 + f_0^2 m^2 > 0$ , which is always true.

Because the solid red curve lies above the curves corresponding to static and convective instability, our definition of  $\text{Ri}_g$  given by Eq. (2.43) predicts that strongly hydrostatic waves are always overturning before attaining sufficiently large amplitudes to become shear-unstable. This counterintuitive prediction may be established analytically by evaluating Eq. (2.43) for a wave on the cusp of overturning, for which  $\alpha_0 = 1$  according to Eq. (2.36). Defining for convenience the nonnegative constants  $\tilde{f}^2 := f_0^2/(\omega^2 - f_0^2)$  and  $\tilde{k}^2 := k^2/m^2$ , Eq. (2.43) is

$$\text{Ri}_g = \frac{N_0^2(1 + \tilde{k}^2)}{N_0^2 - f_0^2} \frac{1}{\alpha_0^2} \frac{(1 - \alpha_0 \sin \varphi)(\sin^2 \varphi + \tilde{f}^2)}{\sin^2 \varphi \cos^2 \varphi},$$

having used  $\omega^2 - f_0^2 = \tilde{k}^2(N_0^2 - f_0^2)/(1 + \tilde{k}^2)$  in the leading coefficient. It follows that

$$\text{Ri}_g \Big|_{\alpha_0=1} = \frac{N_0^2}{N_0^2 - f_0^2} \frac{(1 + \tilde{k}^2)(1 - \sin \varphi)(\sin^2 \varphi + \tilde{f}^2)}{\sin^2 \varphi(1 - \sin^2 \varphi)} > \frac{1 + \tilde{k}^2}{1 + \sin \varphi} \geq \frac{1}{2}(1 + \tilde{k}^2) \geq \frac{1}{2}, \quad (2.49)$$

where we used  $\sin^2 \varphi / \sin^2 \varphi \equiv 1$ , which remains finite even as the denominator  $\sin \varphi \rightarrow 0$ , corresponding to the fact that shear tends locally to zero at the point in the phase where the wave approaches overturning.

The analytical bound obtained in Eq. (2.49) has been established previously by [Gossard et al. \(1971\)](#), who used an alternative definition of  $\text{Ri}_g$ . These independent analyses suggest a strongly hydrostatic internal gravity wave will remain shear stable until attaining its critical amplitude for overturning. Further amplitude growth to  $\alpha_0 > 1$  drives  $\text{Ri}_g$  to jump below zero discontinuously. This disparity between our predictions and those of [Fritts and Rastogi \(1985\)](#) and [Achatz \(2007\)](#) suggests that the shear between adjacent crests and troughs of a strongly hydrostatic internal gravity wave cannot alone induce a shear instability of sufficient strength to drive a wave to overturn ([Gossard et al., 1971](#); [Klostermeyer, 1991](#)). This prediction is investigated in Chapter 4 using the results of fully nonlinear numerical simulations, described in Chapter 3.

---

## Numerical methods

---

A rudimentary fully nonlinear code (i.e., one solving the fully nonlinear governing equations) for three-dimensional Boussinesq internal gravity wave packets without rotation was provided by Dr. Bruce Sutherland. The core of the code used the numerical algorithms of [Press et al. \(2007\)](#). I enabled the functionality within this code to simulate wave packets in a rotating fluid; wrote a faster and more memory-efficient subroutine to superimpose the initial Bretherton flow onto the wave packet; and, performed a loop-level parallelization using [OpenMP](#). A further increase in speed was achieved by preallocating *en masse* the memory for data arrays needed by the most heavily used subroutines (as suggested by postdoctoral researcher Dr. David Deepwell), as opposed to allocating and deallocating memory dynamically once each per function call as was done in the rudimentary code. I upgraded the time-stepping routine from a second-order leapfrog to a third-order Runge–Kutta scheme, and I wrote the code to diagnose whether waves are shear unstable.

This rotation-enabled and parallelized code became the first of, and basis for, a suite of three successively generalized codes used for the projects reported on in this thesis. All three fully nonlinear codes were written in C.

All simulations were run in parallel on either the Béluga, Cedar, Graham, or Narval high-performance computing (HPC) clusters operated by the [Digital Research Alliance of Canada](#) (formerly Compute Canada). A typical simulation used between 8 and 64 cores, the latter

being the effective maximum number of cores available on a single shared memory node on the aforementioned clusters.

A typical simulation required a total execution time of  $O(100 - 1000)$  core-hours; to reduce the amount of time a simulation might wait in the submission queue, Dr. Deepwell suggested to submit recursively each simulation, with each submission requesting a relatively short execution time (usually 3, 6, 12, or 24 hours). To that end, to accelerate the periodic checkpointing step, I implemented parallel reading and writing of the input and output data [often of  $O(10 - 100)$  gigabytes] needed to restart a simulation. This was accomplished by subdividing the single file (used previously in the rudimentary code) containing the checkpoint data into multiple files each representing part of a field in a subset of the total physical domain. A key danger in this approach was the risk that the requested execution time might expire during the crucial step of writing the checkpoint data, which would result catastrophically in the inability to restart a simulation. To guard against this, I introduced in the code a runtime self-diagnostic that timed each iteration of the main loop (which advanced the fields by one nondimensional time unit per iteration). The program exited if the remaining execution time was less than the duration of the longest loop plus a heuristically chosen factor of 10%.

### 3.1 Governing equations

The fully nonlinear code solved the incompressible Navier–Stokes equations with rotation under the Boussinesq approximation. Without explicitly separating the wave fields into their perturbation and induced-mean flow components, the prognostic equations for the horizontal components of velocity and internal energy conservation (in which vertical displacement is used as a proxy for perturbation mass density) in flux form are given dimensionally by

$$\frac{\partial u}{\partial t} = -\frac{1}{\rho_0} \frac{\partial p}{\partial x} + f_0 v - \nabla \cdot (\mathbf{u}\mathbf{u}) + \nu \mathcal{D}u, \quad (3.1)$$

$$\frac{\partial v}{\partial t} = -\frac{1}{\rho_0} \frac{\partial p}{\partial y} - f_0 u - \nabla \cdot (\mathbf{v}\mathbf{u}) + \nu \mathcal{D}v, \quad (3.2)$$

$$\frac{\partial \xi}{\partial t} = w - \nabla \cdot (\xi \mathbf{u}) + \kappa \mathcal{D}\xi, \quad (3.3)$$

where  $\mathbf{u} = (u, v, w)$  is the velocity vector,  $\xi$  is vertical displacement, related to perturbation mass density by  $\xi = -\rho/\bar{\rho}'$ , and  $f_0$  is the Coriolis parameter. The constants  $\nu$  and  $\kappa$  are the kinematic viscosity and thermal diffusivity, respectively, and  $\mathcal{D}$  is a scale-specific Laplacianlike diffusion operator that acted on all spanwise and vertical wavenumbers, but only on horizontal wavenumbers greater than a specified ‘viscous diffusion cutoff wavenumber,’  $\kappa_d$ . Although these terms were excluded when we considered inviscid wave theory in Chapter 2, they are included here to assist with numerical stability by damping small-scale (high-wavenumber) numerical noise while not acting to attenuate the waves.

The system of equations Eqs. (3.1)–(3.3) is closed by the inclusion of the following diagnostic equations\* for dynamic pressure and vertical velocity:

$$\begin{aligned} \frac{1}{\rho_0} \nabla^2 p = & - \left[ \frac{\partial^2(u^2)}{\partial x^2} + \frac{\partial^2(v^2)}{\partial y^2} + \frac{\partial^2(w^2)}{\partial z^2} \right] - 2 \left[ \frac{\partial^2(uv)}{\partial x \partial y} + \frac{\partial^2(uw)}{\partial x \partial z} + \frac{\partial^2(vw)}{\partial y \partial z} \right] \\ & - f_0 \left( \frac{\partial u}{\partial y} - \frac{\partial v}{\partial x} \right) - N_0^2 \frac{\partial \xi}{\partial z}, \end{aligned} \quad (3.4)$$

$$\frac{\partial w}{\partial z} = - \frac{\partial u}{\partial x} - \frac{\partial v}{\partial y}. \quad (3.5)$$

The Poisson equation for dynamic pressure  $p$  is found by taking the divergence of the momentum equations and invoking the incompressibility condition  $\nabla \cdot \mathbf{u} = 0$  to eliminate the time derivative terms. The diagnostic equation for vertical velocity is equivalent to the incompressibility condition. Therefore, incompressibility is enforced numerically both implicitly by Eq. (3.4) and explicitly by Eq. (3.5).

## 3.2 Discretization, grid generation, and resolution

The relative scales for space and time variables were set by fixing  $N_0 = 1$  and  $k = 1$  (with arbitrary units of inverse time and inverse length, respectively). The physical domain was of size  $L_x \times L_y \times L_z$ , and was triply periodic. The domain was set to be large enough that self-interaction of the waves across the periodic boundaries would be negligible over the duration of a simulation (either the default maximum simulation duration,  $t_{\max} = 100/N_0$ , or the first instance of diagnosed wave overturning,  $t_{\text{OT}}$ , after which the code became numerically

---

\*In this context, *diagnostic* refers to the lack of explicit time derivative term, unlike the *prognostic* equations, Eqs. (3.1)–(3.3), which must be advanced in time.

unstable and results were of no interest). In particular, the streamwise and vertical dimensions were set by specifying the number of wavelengths  $n_{w,x}$  and  $n_{w,z}$  that span  $L_x$  and  $L_z$ , respectively. Hence

$$L_x = \frac{2\pi}{k} n_{w,x},$$

$$L_z = \frac{2\pi}{|m|} n_{w,z}.$$

A typical streamwise domain size was set by specifying  $n_{w,x} = 64$ . The vertical domain size varied from one simulation to another, but the bounds on this range were set by specifying  $n_{w,x} = 8$  for nonhydrostatic wave packets, up to  $n_{w,z} = 128$  for the most strongly hydrostatic simulated wave packets.

The minimum number of (evenly spaced) grid points needed to resolve one wavelength of a sinusoidal oscillation—containing one crest, one trough, two roots, and the curvature between them—is eight. Higher resolution is desirable, with multiples of eight grid points per wavelength ideally. Typically, the streamwise and vertical dimensions were discretized so that 16 and 32 grid points spanned one wavelength in the respective directions. The spanwise domain size and resolution were specified directly, because our coordinate system was oriented such that there was no wave propagation in the spanwise direction. Typically,

$$L_y = \frac{200}{k},$$

and this was discretized by  $n_y = 256$  evenly spaced grid points. Therefore, the physical computational mesh consisted of the set of colocated nodes  $\{x_i\}_{i=0}^{n_x} \times \{y_j\}_{j=0}^{n_y} \times \{z_k\}_{k=0}^{n_z}$ , where

$$x_i = -\frac{L_x}{2} + i\Delta x,$$

$$y_j = -\frac{L_y}{2} + j\Delta y,$$

$$z_k = -\frac{L_z}{2} + k\Delta z,$$

separated by the constant increments of length  $\Delta x = L_x/n_x$ ,  $\Delta y = L_y/n_y$ , and  $\Delta z = L_z/n_z$ . The number of points in the streamwise and vertical directions,  $n_x$  and  $n_z$ , varied from one simulation to another (the values for specific simulations are provided in Chapter 4). In all

cases, however,  $n_x$  and  $n_z$  were defined as the product of the number of wavelengths times the number of grid points per wavelength in the respective directions, and were always equal to a (positive) integer power of two. This last requirement was crucial in order to represent efficiently the wave fields by their Fourier spectra, as described below.

Because wave packets exist generally as a superposition of a spectrum of waves, and because the physical domain was periodic in each direction, the Fourier spectral method is a natural choice to represent the simulated wave packets. Given a periodic function defined on a (one-dimensional) mesh, say  $\eta : \{x_i\} \rightarrow \mathbb{R}^{n+1}$ ,  $i = 0, \dots, n$ ,  $\eta(x_0) = \eta(x_n)$  (with  $n$  assumed even and not necessarily equal to  $n_x$ ), the discrete Fourier transform (e.g. Press et al., 2007) returns the complex amplitude spectrum  $\hat{\eta}_n$  for a corresponding set of Fourier modes  $\{\kappa_n\}$ . Because  $\eta_i = \eta(x_i)$  was real, the spectrum has Hermitian symmetry property  $\hat{\eta}_{-n} = \hat{\eta}_n^*$ , where the asterisk denotes the complex conjugate. Hence, the spectrum  $\hat{\eta}$  needs only to contain  $1 + n/2$  nonnegative wavenumber components. Hermitian symmetry is not exploited in this code when performing the discrete Fourier transform in multiple dimensions: the three-dimensional Fourier transform consists essentially of three iterated Fourier transforms, with those in the  $y$ - and  $z$ -directions acting on the full set of complex data resulting from the previous transform.

Setting  $n_x$ ,  $n_y$ , and  $n_z$  to be powers of two enables the use of the *fast Fourier transform* (Cooley and Tukey, 1965; Press et al., 2007), which efficiently performs the one-dimensional discrete Fourier transform in  $O(n \log_2 n)$  operations—a substantial improvement compared to  $O(n^2)$  operations for arbitrary  $n \in \mathbb{N}$  when  $n$  is relatively large. With the fast Fourier transform method in mind, the Fourier spectral domain was discretized in the streamwise direction by  $1 + n_x/2$  Fourier modes,  $\kappa_n = n\Delta\kappa$ , separated by an increment of  $\Delta\kappa = 2\pi/L_x$ . In the spanwise and vertical directions, the Fourier spectral domain was discretized by  $1 + n_y$  and  $1 + n_z$  Fourier modes,  $\lambda_\ell = (\ell - n_y/2)\Delta\lambda$  and  $\mu_m = (m - n_z/2)\Delta\mu$ , separated by the increments  $\Delta\lambda = 2\pi/L_y$  and  $\Delta\mu = 2\pi/L_z$ , respectively.

Under the discrete Fourier transform, partial differentiation with respect to a spatial variable is equivalent to multiplication by Fourier modes according to

$$\frac{\partial}{\partial x} \rightarrow i\kappa_n, \tag{3.6}$$

$$\frac{\partial}{\partial y} \rightarrow i\lambda_\ell, \quad (3.7)$$

$$\frac{\partial}{\partial z} \rightarrow i\mu_m, \quad (3.8)$$

so that differentiation is a relatively computationally inexpensive operation. (Note that  $i$  is the imaginary unit here, and not an integer index.) Integration in spectral space, being equivalent to division by Fourier modes, is equally straightforward.

One disadvantage of the fast Fourier transform method is that the smallest increase in resolution in a given direction necessarily doubles the memory requirement for a large number of three-dimensional arrays used by the code. A typical simulation running on an HPC cluster used a moderate proportion of the memory available on a single general-purpose compute node; doubling resolution was found in most cases to exceed the available memory. The compute clusters operated by the [Digital Research Alliance of Canada](#) (formerly Compute Canada, at the time these simulations were performed) had a small number of large-memory nodes but these were found to be in such high demand that queuing for their use was not a productive use of time. Another alternative was to fundamentally rewrite the code to abandon the use of the shared-memory paradigm (i.e., [OpenMP](#), which restricts the code to run on a single compute node) in favour of a distributed-memory paradigm (i.e., [MPI](#)). However, this gargantuan undertaking was deemed not to be feasible.

For these reasons, only a very restrictive set of domain size and resolution tests could be performed with relatively small simulations of nonhydrostatic wave packets. A series of such tests was performed using a domain of size  $2L_x \times 2L_y \times 2L_z$  but with no change in resolution, and with a domain of size  $L_x \times L_y \times L_z$  but with the resolution doubled in each direction. Domain size was found to have no significant qualitative or quantitative effects on the results; resolution doubling resulted in wave overturning diagnosed at most one buoyancy period,  $T_B = 2\pi/N_0$ , earlier than in the reference simulation. It was assumed that similar results would emerge if the same tests could be performed with simulations of hydrostatic waves. All this is to say that the values of  $n_x$ ,  $n_y$ , and  $n_z$  for specific simulations reported on in [Chapter 4](#) represent highest practical resolution available.

### 3.3 Initialization

All simulations were initialized in physical space with a trivariate Gaussian wave packet whose vertical displacement field was prescribed at leading- and first-order to be

$$\xi(x, y, z, 0) = A(x, y, z, 0) \left[ \cos(kx + mz) + \beta_x \left( \frac{x}{\sigma_x^2} - \frac{k}{m} \frac{z}{\sigma_z^2} \right) \sin(kx + mz) \right].$$

The constant  $\beta_x$  is given by Eq. (2.25a), and the initial amplitude envelope was given by Eq. (2.32), reproduced here for convenience:

$$A(x, y, z, 0) = A_0 \exp \left[ -\frac{1}{2} \left( \frac{x^2}{\sigma_x^2} + \frac{y^2}{\sigma_y^2} + \frac{z^2}{\sigma_z^2} \right) \right], \quad (3.9)$$

in which  $A_0$  is the peak vertical displacement, and  $\sigma_x$ ,  $\sigma_y$ , and  $\sigma_z$  are the wave packet extents in the streamwise, spanwise, and vertical directions, respectively. Vertical displacement was chosen as this is a physically intuitive quantity, and its Gaussian amplitude envelope was chosen for convenience.

Using the envelope given by Eq. (3.9), the horizontal components of velocity  $u(x, y, z, 0)$  and  $v(x, y, z, 0)$  were initialized using the polarization relations for  $u_0^{(1)}$  and  $v_0^{(1)}$  from linear theory, given in the centre column of Table 2.1. The respective  $O(\alpha^1 \epsilon^1)$  corrections,  $u_1^{(1)}$  and  $v_1^{(1)}$ , given in the right column of Table 2.1, were superimposed onto the leading-order fields. Explicitly,

$$\begin{aligned} u(x, y, z, 0) &= -A(x, y, z, 0) \frac{m}{k} \left\{ \left( \omega + \frac{f_0}{k} \frac{y}{\sigma_y^2} \right) \sin(kx + mz) \right. \\ &\quad \left. - \left[ \frac{x}{\sigma_x^2} \left( c_{gx} - \frac{\omega}{k} - \omega \beta_x \right) + \frac{z}{\sigma_z^2} \left( c_{gz} + \frac{\omega}{m} - \omega \frac{k}{m} \beta_x \right) \right] \cos(kx + mz) \right\}, \\ v(x, y, z, 0) &= A(x, y, z, 0) \frac{m}{k} \left\{ \left( f_0 - \frac{\omega}{k} \frac{y}{\sigma_y^2} \right) \cos(kx + mz) \right. \\ &\quad \left. + \frac{f_0}{k} (1 + k \beta_x) \left( \frac{x}{\sigma_x^2} - \frac{k}{m} \frac{z}{\sigma_z^2} \right) \sin(kx + mz) \right\}. \end{aligned}$$

It was necessary to include the respective first-order corrections when initializing the perturbation fields, as the  $O(\alpha^1 \epsilon^1)$  fields account for the finite extent of the wave packet on scales that are intermediate between the linear wave fields and the quadratically nonlinear wave-induced mean flow field.

### 3.3.1 Wave-induced mean flow

The predicted initial Bretherton flow was initialized in spectral space and inverse fast Fourier transformed before being superimposed onto the initial horizontal velocity field. The initial Bretherton flow in physical space was predicted by Eq. (2.31), reproduced here:

$$\begin{bmatrix} u_{\text{BF}} \\ v_{\text{BF}} \end{bmatrix} = \frac{1}{2} \frac{m^2}{k^2} \int_{\mathbb{R}^3} \frac{\lambda}{\kappa^2 + \lambda^2} \left( \frac{\omega^2}{c_{gx}} - f_0^2 \frac{\kappa}{\mathbf{c}_g \cdot \boldsymbol{\kappa}} \right) \begin{bmatrix} \lambda \\ -\kappa \end{bmatrix} \widehat{|A|^2} e^{i\boldsymbol{\kappa} \cdot \mathbf{x}} d\boldsymbol{\kappa} d\lambda d\mu, \quad (3.10)$$

where

$$\widehat{|A|^2} = \frac{1}{8\pi^{3/2}} \sigma_x \sigma_y \sigma_z A_0^2 e^{-(\sigma_x^2 \kappa^2 + \sigma_y^2 \lambda^2 + \sigma_z^2 \mu^2)/4}$$

is the three-dimensional Fourier transform of the square of the initial Gaussian envelope given by Eq. (3.9).

It was physically necessary to include the Bretherton flow when initializing the horizontal velocity fields of wave packets whose initial amplitude was large enough that the waves were subject to weakly nonlinear interactions with their wave-induced mean flow initially. Previous studies of wave packet evolution have examined the role of the initial wave-induced mean flow: neglecting to superimpose the predicted initial induced mean flow was found to result in an unphysical ‘‘error flow’’ (van den Bremer and Sutherland, 2018), ‘‘deficit’’ (Dosser and Sutherland, 2011), or generally a residual steady flow that remained at the initial wave packet location, and was of equal magnitude but opposite sign of the predicted induced mean flow (van den Bremer and Sutherland, 2014; Sutherland et al., 2020). Although it is not necessary to superimpose the Bretherton flow on initially small-amplitude wave packets (in which case the Bretherton flow, being quadratic in amplitude, is of negligible magnitude), in order to ensure consistency across the simulations reported on in Chapter 4, all wave packets were initialized to include their Bretherton flow.

One nontrivial aspect of the numerical implementation of the initial Bretherton flow is the presence of singularities in spectral space in the integrand of Eq. (3.10). The singularity  $\kappa^2 + \lambda^2 = 0 \Leftrightarrow \kappa = \lambda = 0$  arises from the Fourier transform of the horizontal Laplacian operator. In order to integrate over this singularity, we appeal to physical insight: the Fourier mode  $\kappa = 0$  ( $\lambda = 0$ ) corresponds to a ‘wave’ in the limit of an infinitely long streamwise (spanwise) wavelength, i.e., a constant value for all  $x$  ( $y$ ). Because the Bretherton flow is

a localized response to a forcing by the waves within the wave packet, and hence is of zero magnitude far from the wave packet, this constant value must also be zero. Therefore, when initializing the Bretherton flow numerically, the array entries corresponding to the discrete Fourier mode  $\kappa_n = \lambda_\ell = 0$  (for all  $\mu_m$ ) were set to zero.

The singularity  $\mathbf{c}_g \cdot \boldsymbol{\kappa} = c_{gx}\kappa + c_{gz}\mu = 0 \Leftrightarrow \kappa = \frac{k}{m}\mu$  arises from the Fourier transform of the operator  $\mathbf{c}_g \cdot \nabla$ . To integrate over this singularity, we appeal to Hermitian symmetry in the streamwise spectrum, i.e.,  $\kappa \geq 0$  (as this was the first direction in which the fast Fourier transform was applied in practice). Because we assumed the wave packet propagates upward and rightward initially,  $k > 0$  and  $m < 0$ , and so  $\frac{k}{m}\mu \geq 0 \Rightarrow \mu \leq 0$ . Hence, for a fixed  $\lambda$ , it follows that  $\kappa = \frac{k}{m}\mu$  is a curve of singularities in the  $\kappa\mu$ -quarter-plane with  $\mu \leq 0$ . Using symmetry about the  $\kappa$ -axis at time  $t = 0$  (for a fixed  $\lambda_\ell$ ), the array entries containing the spectral amplitudes of the Bretherton flow along the (discretized) curve of singularities were overwritten with their respective complex conjugates. In practice, the array entries corresponding to singularities were identified by  $(c_{gx}\kappa_n + c_{gz}\mu_m)/N_0 < \epsilon$ , for fixed  $\lambda_\ell$ . We somewhat arbitrarily set  $\epsilon = 10^{-10}$ .

Before the above procedure was discovered (when the suite of simulations for this project was well underway), array entries were instead set to zero along the discretized curve of singularities corresponding to  $\mathbf{c}_g \cdot \boldsymbol{\kappa} = 0$ . This missing spectral information manifested as an unphysical small amplitude beam of negative induced mean flow oriented diagonally across the  $xz$ -plane and passing through the wave packet. Comparisons of simulations initializing the Bretherton flow with and without the above procedure revealed that the beam had no quantitative effect on the solutions.

### 3.4 Advection and temporal advancement

At a given time step, the code first diagnosed the vertical velocity by integrating Eq. (3.5) in spectral space. Explicitly,

$$\hat{w}_{\mathbf{n}} = \begin{cases} -\frac{1}{\mu_m}(\kappa_n \hat{u}_{\mathbf{n}} + \lambda_\ell \hat{v}_{\mathbf{n}}), & \mu_m \neq 0 \\ 0, & \mu_m = 0, \end{cases}$$

in which we used Eqs. (3.6)–(3.8) and the caret denotes that the underlying quantity has been fast Fourier transformed. The vector index  $\mathbf{n} = (n, \ell, m)$  denotes the field’s functional dependence on the Fourier modes  $\kappa_n$ ,  $\lambda_\ell$ , and  $\mu_m$ . The  $\mu_m = 0$  component of  $\hat{w}_{\mathbf{n}}$ , corresponding to the mean perturbation vertical velocity, was set to zero on physical grounds.

The code then proceeded to build the forcing,  $\hat{F}_p$ , on the right-hand side of the Poisson equation for dynamic pressure. Explicitly, Fourier transforming the right-hand side of Eq. (3.4) yields

$$\begin{aligned} \hat{F}_p = & \kappa_n^2 (\widehat{u^2})_{\mathbf{n}} + \lambda_\ell^2 (\widehat{v^2})_{\mathbf{n}} + \mu_m^2 (\widehat{w^2})_{\mathbf{n}} + 2 \left[ \kappa_n \lambda_\ell (\widehat{uv})_{\mathbf{n}} + \kappa_n \mu_m (\widehat{uw})_{\mathbf{n}} + \lambda_\ell \mu_m (\widehat{vw})_{\mathbf{n}} \right] \\ & - i f_0 (\lambda_\ell \hat{u}_{\mathbf{n}} - \kappa_n \hat{v}_{\mathbf{n}}) - i N_0^2 \mu_m \hat{\xi}_{\mathbf{n}}. \end{aligned}$$

The linear contribution to this forcing was computed directly in spectral space. The nonlinear contribution was computed by convolving the linear velocity fields and differentiating the results. The convolution was performed by inverse fast Fourier transforming the input fields, multiplying entry-wise the arrays containing the physical fields, and fast Fourier transforming the result. The dynamic pressure field (divided by  $\rho_0$ ) was then given by

$$\frac{1}{\rho_0} \hat{p}_{\mathbf{n}} = \begin{cases} -\frac{1}{\kappa_n^2 + \lambda_\ell^2 + \mu_m^2} \hat{F}_p, & (\kappa_n, \lambda_\ell, \mu_m) \neq (0, 0, 0), \\ 0, & (\kappa_n, \lambda_\ell, \mu_m) = (0, 0, 0), \end{cases} \quad (3.11)$$

where the  $(\kappa_n, \lambda_\ell, \mu_m) = (0, 0, 0)$  component of  $\hat{p}_{\mathbf{n}}$ , corresponding to the mean pressure perturbation averaged over the entire domain, was set to zero on physical grounds.

With the diagnostic fields in place, the code proceeded to compute the time derivatives of the prognostic fields, denoted by  $\dot{\hat{u}}_{\mathbf{n}}$ ,  $\dot{\hat{v}}_{\mathbf{n}}$ , and  $\dot{\hat{\xi}}_{\mathbf{n}}$ , according to the Fourier-transformed right-hand sides of Eqs. (3.1)–(3.3). Explicitly,

$$\dot{\hat{u}}_{\mathbf{n}} = -i \kappa_n \frac{\hat{p}_{\mathbf{n}}}{\rho_0} + f_0 \hat{v}_{\mathbf{n}} - i \left[ \kappa_n (\widehat{u^2})_{\mathbf{n}} + \lambda_\ell (\widehat{uv})_{\mathbf{n}} + \mu_m (\widehat{uw})_{\mathbf{n}} \right] + \frac{1}{\text{Re}} \mathcal{D} \hat{u}_{\mathbf{n}}, \quad (3.12)$$

$$\dot{\hat{v}}_{\mathbf{n}} = -i \lambda_\ell \frac{\hat{p}_{\mathbf{n}}}{\rho_0} - f_0 \hat{u}_{\mathbf{n}} - i \left[ \kappa_n (\widehat{uv})_{\mathbf{n}} + \lambda_\ell (\widehat{v^2})_{\mathbf{n}} + \mu_m (\widehat{vw})_{\mathbf{n}} \right] + \frac{1}{\text{Re}} \mathcal{D} \hat{v}_{\mathbf{n}}, \quad (3.13)$$

$$\dot{\hat{\xi}}_{\mathbf{n}} = \hat{w}_{\mathbf{n}} - i \left[ \kappa_n (\widehat{u\xi})_{\mathbf{n}} + \lambda_\ell (\widehat{v\xi})_{\mathbf{n}} + \mu_m (\widehat{w\xi})_{\mathbf{n}} \right] + \frac{1}{\text{RePr}} \mathcal{D} \hat{\xi}_{\mathbf{n}}, \quad (3.14)$$

where the quadratic products of perturbation fields were retained from the pressure calculation step, and the coefficients on the diffusion terms are given explicitly in terms of the Reynolds

and Prandtl numbers,  $\text{Re} := N_0/(k^2\nu) = 1000$  and  $\text{Pr} := \nu/\kappa = 1$ , respectively, following the scaling of Eqs. (3.1)–(3.3) by the relative time and space scales  $N_0$  and  $k$ . The scale-specific diffusion operator  $\mathcal{D}$  acted on the perturbation fields, denoted generically here by  $\hat{\eta}_{\mathbf{n}}$ , according to

$$\mathcal{D}\hat{\eta}_{\mathbf{n}} = -(\kappa_n^2 + \lambda_\ell^2 + \mu_m^2)\hat{\eta}_{\mathbf{n}}, \quad \kappa_n \geq \kappa_d,$$

where the viscous diffusion cutoff wavenumber was set to  $\kappa_d = \kappa_{257}$ .

The perturbation fields were advanced in time using the third-order accurate, low-storage Williamson–Runge–Kutta (WRK3) scheme (Williamson, 1980; Durran, 2010). Denote by  $\hat{\mathbf{u}}^j = (\hat{u}_{\mathbf{n}}^j, \hat{v}_{\mathbf{n}}^j, \hat{\xi}_{\mathbf{n}}^j)$  the state of the perturbation fields at time step  $t_j = t_0 + j\Delta t$ . Denote by  $\hat{\mathbf{u}}_{1,2} = \hat{F}(\hat{\mathbf{u}}^{j_{1,2}}, t_{j_{1,2}}) = (\hat{u}_{\mathbf{n}}^{j_{1,2}}, \hat{v}_{\mathbf{n}}^{j_{1,2}}, \hat{\xi}_{\mathbf{n}}^{j_{1,2}})$  two vectors of dummy fields defined by the right-hand sides of Eqs. (3.12)–(3.14) at times corresponding to successive Runge–Kutta substeps  $j_1$  and  $j_2$ . To advance the perturbation fields by one  $\Delta t$ , the WRK3 scheme proceeds by executing the following six-step procedure:

$$\hat{\mathbf{u}}_1 \leftarrow \hat{F}(\hat{\mathbf{u}}^j, t_j) \qquad \hat{\phi}_{(1)} \leftarrow \hat{\mathbf{u}}^j + \frac{\Delta t}{3}\hat{\mathbf{u}}_1 \qquad (3.15\text{a,b})$$

$$\hat{\mathbf{u}}_2 \leftarrow \hat{F}(\hat{\phi}_{(1)}, t_{j+1/3}) - \frac{5}{9}\hat{\mathbf{u}}_1 \qquad \hat{\phi}_{(2)} \leftarrow \hat{\phi}_{(1)} + \frac{15\Delta t}{16}\hat{\mathbf{u}}_2 \qquad (3.15\text{c,d})$$

$$\hat{\mathbf{u}}_1 \leftarrow \hat{F}(\hat{\phi}_{(2)}, t_{j+5/12}) - \frac{153}{128}\hat{\mathbf{u}}_2 \qquad \hat{\mathbf{u}}_{j+1} \leftarrow \hat{\phi}_{(2)} + \frac{8\Delta t}{15}\hat{\mathbf{u}}_1, \qquad (3.15\text{e,f})$$

where  $\hat{\phi}_{(1)}$  and  $\hat{\phi}_{(2)}$  are vectors of intermediate temporary fields. In practice, these fields were written to the 1st and 2nd three-dimensional subarrays of the four-dimensional arrays allocated for each of  $\hat{u}$ ,  $\hat{v}$ , and  $\hat{\xi}$ , thus realizing an additional memory savings. For all simulations, the time step was taken to be the small increment  $\Delta t = 0.05N_0^{-1}$ . Results of test simulations (not shown) using a time step of  $\Delta t = 0.025N_0^{-1}$  revealed no significant qualitative or quantitative differences.

The WRK3 scheme offers an  $O(\Delta t^2)$  improvement over the rudimentary code’s second-order leapfrog scheme: this latter scheme suffers from a spurious numerical mode, leading to so-called ‘splitting’ errors, for which there are two commonly used remedies (Williams, 2009).

(1) The effects of splitting errors may be reduced by performing periodically an Euler backstep, which consists of integrating the equations backward in time by one  $\Delta t$  and averaging the forward- and backward-integrated results. Although computationally straightforward, this

approach reduces the accuracy of the leapfrog scheme effectively to that of the Euler scheme, namely,  $O(\Delta t)$ . (2) An alternative approach is to apply the so-called Robert–Asselin time filter (Robert, 1966; Asselin, 1972), which displaces the second of three consecutive (in time) function values, so as to reduce the curvature between the three values. This filter was found by Williams (2009) to damp the nonphysical mode while reducing the accuracy of the leapfrog scheme. A modified filter proposed by Williams (2009) and applied to the time integration of Eqs. (3.12)–(3.14) was found to act on scales comparable to the Bretherton flow, resulting in significant qualitative differences to the induced flow. For these reasons, backstepping and filtering approaches were abandoned in favour of the WRK3 scheme.

---

## Results and discussion

---

In this chapter we examine for which initial vertical displacement amplitudes fully localized wave packets eventually overturn, and characterize the physical mechanisms responsible. A series of numerical simulations were performed to diagnose the time of wave overturning for a range of initial amplitudes, relative vertical wavenumbers, and wave packet aspect ratios. In particular, simulations evolved wave packets with initial vertical displacement amplitudes between  $A_0 = 0.03k^{-1} \approx 0.005\lambda_x$  and  $A_0 = 1.2k^{-1} \approx 0.19\lambda_x$ , and relative vertical wavenumbers between  $m = -0.2k$  and  $m = -11.4k$  (with the spanwise wavenumber  $\ell = 0$  fixed for all simulations). Thus our simulations spanned a range of small and moderately large amplitude, strongly nonhydrostatic and hydrostatic upward-propagating wave packets. The range of relative vertical wavenumbers corresponds to waves whose lines of constant phase made angles  $\Theta = \tan^{-1} |m/k| = 11^\circ$  and  $\Theta = 85^\circ$  to the vertical, respectively. The Coriolis parameter was set to  $f_0 = 0.01N_0$  for all simulations (unless otherwise noted), as this is a typical value in the midlatitudes of interest. The vertical extent of the wave packet was set to  $\sigma_z = 10k^{-1}$  for all simulations. With this value of  $\sigma_z$ , we configure the geometry of *round* wave packets (which are of primary interest in this chapter), by setting  $\sigma_x = \sigma_y = \sigma_z$ . For comparison, selected combinations of initial amplitude and relative vertical wavenumber were simulated for *long* wave packets, for which we set  $\sigma_x = 4\sigma_y = 4\sigma_z$ , and *wide* wave packets, for which we set  $\sigma_x = \frac{1}{4}\sigma_y = \sigma_z$ . A subset of the full suite of simulations is discussed in detail in this

ID	$A_0k$	$\frac{\tilde{A}_0}{\tilde{A}_{\text{OT}}}$	$\frac{\tilde{A}_0}{\tilde{A}_{\text{OT}}}$	$ \frac{m}{k} $	$\Theta$	$R_y$	$L_yk \times L_zk$	$n_y \times n_z$	RT	$N_0t_{\text{OT}}$
NH1	0.5	0.10	1.24	0.2	$11^\circ$	1	$200.0 \times 251.3$	$256 \times 256$	196	49
NH2	0.35	0.07	0.86	0.2	$11^\circ$	1	$200.0 \times 251.3$	$256 \times 256$	332	111
NH3	0.2	0.04	0.49	0.2	$11^\circ$	1	$200.0 \times 251.3$	$256 \times 256$	631	—
NH4	0.4	0.28	0.52	0.7	$35^\circ$	1/4	$400.0 \times 143.6$	$512 \times 512$	778	32
NH5	0.5	0.35	0.65	0.7	$35^\circ$	1/4	$400.0 \times 143.6$	$512 \times 512$	586	25
NH6	0.4	0.28	0.26	0.7	$35^\circ$	4	$400.0 \times 143.6$	$512 \times 512$	734	29
NH7	0.4	0.28	0.40	0.7	$35^\circ$	1	$200.0 \times 143.6$	$256 \times 512$	264	32
NH8	0.6	0.42	0.60	0.7	$35^\circ$	1	$200.0 \times 143.6$	$256 \times 512$	224	21
NH9 <sup>-</sup>	0.2	0.40	0.24	2.0	$63^\circ$	1	$200.0 \times 100.5$	$256 \times 1024$	909	39
H1	0.08	0.91	0.43	11.4	$85^\circ$	1	$200.0 \times 70.5$	$256 \times 4096$	4896	45
H1 <sup>+</sup>	0.08	0.91	0.43	11.4	$85^\circ$	1	$200.0 \times 70.5$	$256 \times 4096$	4108	40
H2	0.15	0.81	0.39	5.4	$80^\circ$	1	$200.0 \times 74.5$	$256 \times 2048$	1562	32
H3	0.15	0.81	0.48	5.4	$80^\circ$	1/4	$400.0 \times 74.5$	$512 \times 2048$	3200	32
H4	0.15	0.81	0.25	5.4	$80^\circ$	4	$400.0 \times 74.5$	$512 \times 2048$	3144	32

**Table 4.1:** Initial conditions, domain size and resolution, and output diagnostics from the subset of the fully nonlinear numerical simulations discussed or explicitly mentioned in-text. Columns are: simulation ID, vertical displacement amplitude nondimensionalized by  $k$  and as a fraction of the predicted amplitudes for static and self-acceleration instability [given by Eqs. (2.36) and (2.41), respectively, where  $\tilde{A}_0 = A_0/\lambda_x$ ], absolute relative vertical wavenumber  $|m/k|$  and corresponding  $\Theta = \tan^{-1}|m/k|$  [deg], spanwise aspect ratio  $R_y = \sigma_y/\sigma_x$ , spanwise  $\times$  vertical domain size  $L_yk \times L_zk$  and resolution  $n_y \times n_z$ , approximate simulation runtime (RT) in core-hours, and diagnosed overturning time  $N_0t_{\text{OT}}$ . IDs with a superscript  $-$  or  $+$  sign respectively denote simulations performed with  $f_0 = -0.05N_0$  and  $+0.05N_0$ . All simulations used a streamwise domain of length  $L_xk = 402.1$  resolved by  $n_x = 1024$  grid points.

chapter. The initial conditions, domain size and resolution, and select output diagnostics of each simulation explicitly discussed or mentioned in-text are summarized in Table 4.1.

## 4.1 Evolution of a nonhydrostatic wave packet

Snapshots of the evolution of a round moderately large amplitude nonhydrostatic wave packet initialized with  $A_0 = 0.5k^{-1}$  and  $m = -0.2k$  (NH1 in Table 4.1) are shown in Fig. 4.1. The top row shows cross sections of the streamwise velocity field  $\tilde{u} = u/(N_0/k)$  through the horizontal plane  $z = c_{gz}t$ , and the bottom row shows cross sections of the vertical displacement field  $\tilde{\xi} = k\xi$  through the vertical plane  $y = 0$ . The white cross in each panel indicates the centre

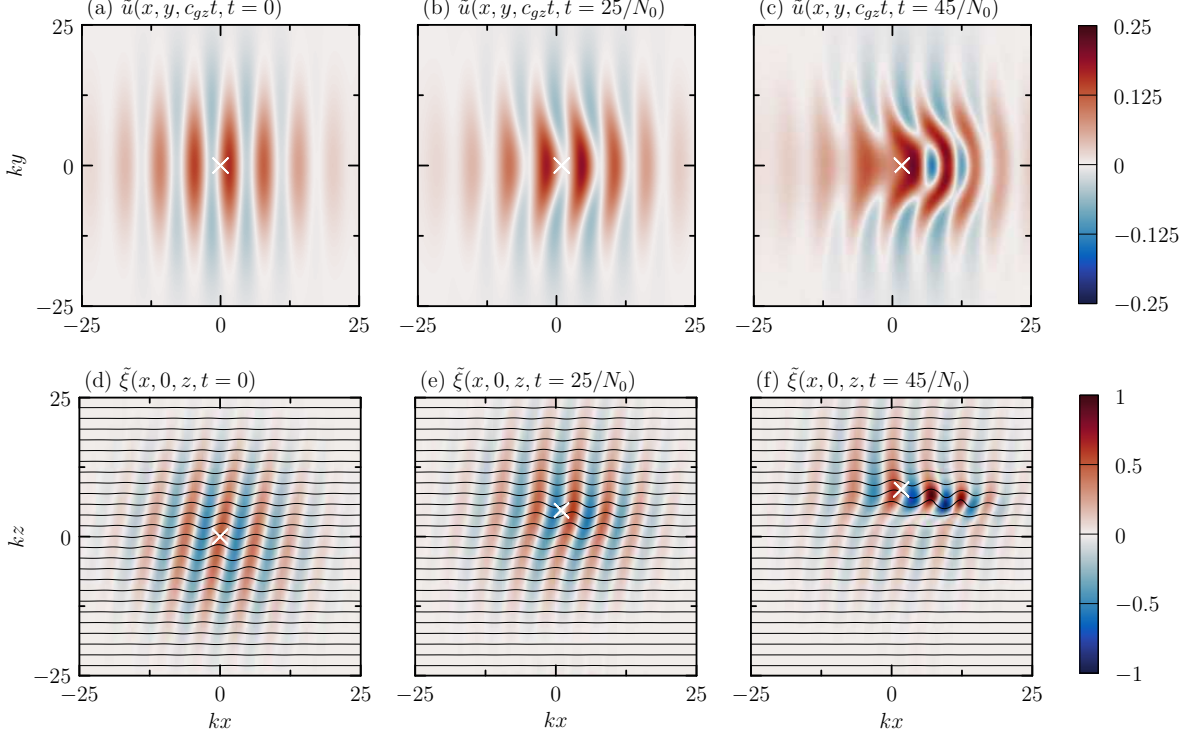


**Figure 4.1:** Snapshots of the streamwise velocity field  $\tilde{u} = u/(N_0/k)$  through the horizontal plane  $z = c_{gz} t$  (a–c) and of the vertical displacement field  $\tilde{\xi} = k\xi$  through the vertical plane  $y = 0$  (d–f) of a round, moderately large amplitude, nonhydrostatic wave packet initialized with  $A_0 = 0.5k^{-1}$  and  $m = -0.2k$  (NH1). Images have been cropped to focus on the region of the domain containing the wave packet, and resolution was enhanced in postprocessing. The white crosses indicate the centre of the wave packet predicted by linear theory, and the black curves in the bottom row represent isopycnal surfaces.

of the wave packet predicted using linear theory, and the black curves in the bottom row represent isopycnal surfaces. The times shown in each column are representative of the wave packet at early, midlife, and near-overturning stages of its evolution.

The wave packet was initially of such large amplitude as to be unstable to self-acceleration, predicted using Eq. (2.41). This instability is evident in Fig. 4.1(b,c), as crests near the centre of the wave packet begin to merge with—and eventually overtake—troughs, owing to the magnitude of the induced mean flow there:  $\max\{u_{\text{BF}}|_{t=25/N_0}\} \approx 0.09N_0/k > c_{gx} \approx 0.04N_0/k$ . The dipolelike horizontal structure of the Bretherton flow causes the symmetric deformation of the wave crests about the  $kx$ -axis [e.g., Fig. 4.1(b)]. The assumed Gaussian vertical structure of the Bretherton flow is similarly responsible for the asymmetric phase shift seen in the corresponding vertical cross section of  $\tilde{\xi}$  [Fig. 4.1(e)]: as an individual crest propagates downward toward the vertical centre of the wave packet, hence toward the region

of strongest positive induced mean flow, the part of the phase nearest  $\max\{u_{\text{BF}}\}$  is advected differentially, resulting in an apparent steepening of phase lines just above the centre of the wave packet, and a flattening of the phase lines below. Qualitatively similar behaviour was observed by [Sutherland \(2001\)](#) in his study of one- and two-dimensional wave packets, who identified this behaviour as resulting from self-acceleration.

Shortly before overturning [Fig. 4.1(f)], the wave evolution is dominated by nonlinear effects: the peak vertical displacement has nearly doubled to  $\max\{\tilde{\xi}|_{t=45/N_0}\} = 0.99$  from its initial value of 0.5, while streamwise and vertical asymmetry of isopycnal surfaces develops owing to interactions between the waves and the induced mean flow. Isopycnals near the centre of the wave packet show the steepening of wave fronts as a result of nonlinear amplitude growth. The wave packet continued to evolve nonlinearly until overturning at  $t = 49/N_0$  and ultimately breaking at  $t = 56/N_0$ . Turbulent wave breaking evolves on a range of spatial scales, a significant subrange of which lies below the smallest spatial scale resolved by the numerical code. The convective instabilities associated with breaking wave lead to the rapid growth of gridscale features that drove the code to numerical instability, at which time the simulation ended automatically.

The phase steepening and flattening behaviour characterized above as resulting from self-acceleration was likewise observed for nonhydrostatic wave packets (not shown) with initial amplitudes well below those predicted for the onset of self-acceleration. The phase deformations result from a local Doppler shift in wave frequency, increasing (decreasing) above (below) the centre of the wave packet. Hence nonhydrostatic waves generally evolved under the effects of modulational instability (stability), and so we find that the critical amplitude for self-acceleration poorly predicted the initial amplitude for which most nonhydrostatic waves eventually overturned. [Sutherland \(2001\)](#) similarly found that horizontal modulations of two-dimensional wave packets resulted generally in poorer agreement between the predicted amplitude for self-acceleration and simulation results (compared to the relatively good agreement found for one-dimensional wave packets).

## 4.2 Evolution of a strongly hydrostatic wave packet

Snapshots of the evolution of a round strongly hydrostatic wave packet initialized with  $m = -11.4k$  and  $A_0 = 0.08k^{-1}$  (H1) are shown in Fig. 4.2. The top and bottom rows are as in Fig. 4.1. The times shown in each column are representative of the wave packet at early, pre-, and postoverturning times. From initialization through the majority of their evolution, the waves exhibit behaviour qualitatively similar to the evolution at early times of nonhydrostatic waves. In particular, the induced mean flow advects differentially the waves near the centre of the wave packet [Fig. 4.2(b)]. The associated phase changes observed in the nonhydrostatic case are less pronounced in the vertical cross section for the hydrostatic wave packet [Fig. 4.2(e)]. Isopycnal surfaces (represented by black curves) are found to steepen sharply at the inflection point of the streamwise velocity where the vertical shear of the waves is largest. However, the streamwise-localized nature of the steepening is more characteristic of nonlinear steepening than shear instability. Unlike nonhydrostatic wave packets (e.g., NH1), the vertical displacement amplitude decreased in time due to linear dispersion. The waves overturned nonetheless at  $t = 45/N_0$ . The waves continued to evolve nonlinearly until  $t = 62/N_0$ , at which time the growth of subgrid scale convective instabilities was too strong to be reliably resolved by our code.

For comparison, a simulation identical to H1 but with  $f_0 = 0.05N_0$  was performed (H1<sup>+</sup>). The initial Bretherton flow induced by this wave packet was shown in Fig. 2.1(d). The evolution of this wave packet was similar qualitatively to that of H1 from initialization through wave overturning. Despite the peak vertical displacement amplitude decreasing in time due to linear dispersion, the waves overturned at  $t = 40/N_0$  (nearly one buoyancy period,  $T_B = 2\pi/N_0$ , earlier than those in H1) due to the increased magnitude of the Bretherton flow with  $f_0 = 0.05N_0$  compared to that with  $0.01N_0$ . Isopycnal surfaces (not shown) exhibited nonlinear steepening similar to that found with H1, suggesting shear instability likewise did not drive the waves with  $f_0 = 0.05N_0$  to overturning.

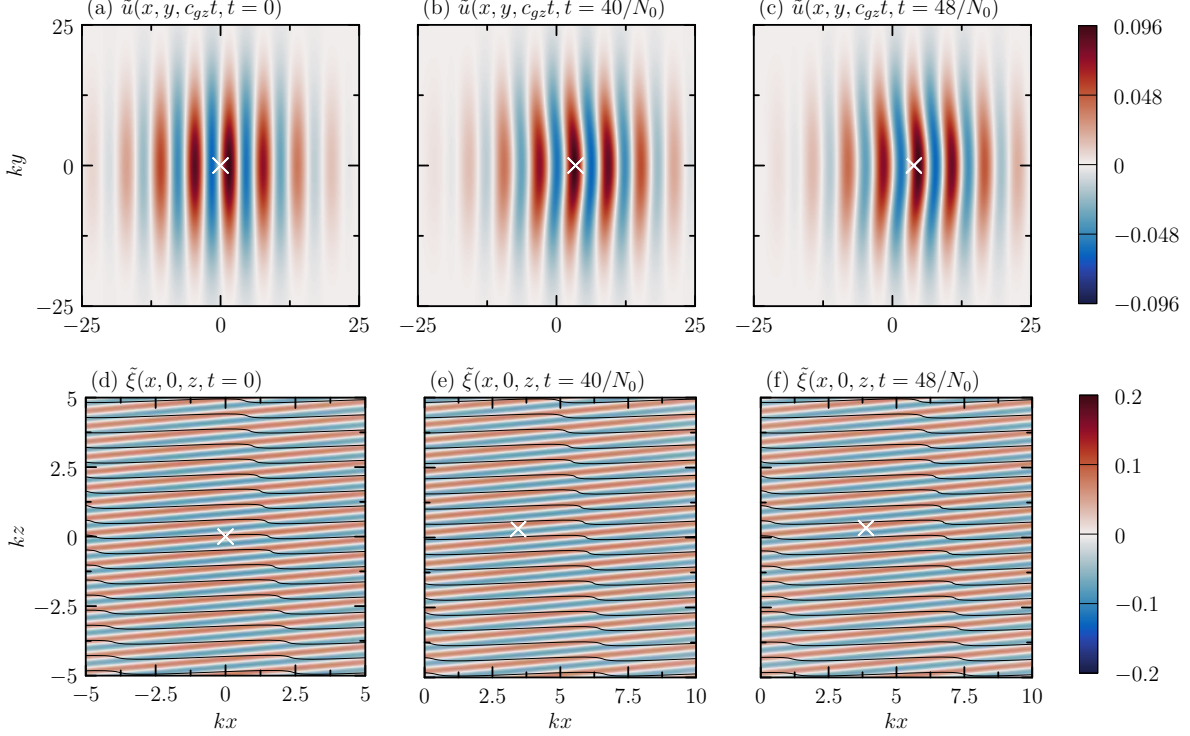


**Figure 4.2:** As in Fig. 4.1 but for a strongly hydrostatic wave packet initialized with  $A_0 = 0.08k^{-1}$  and  $m = -11.4k$  (H1).

### 4.3 Overturning of round wave packets

The overturning of wave packets is diagnosed by the criterion  $N_T^2 < 0$  (cf. the discussion in Sec. 2.3.1). For convenience we define the nondimensional squared total buoyancy frequency by

$$\tilde{N}_T^2 := \frac{N_T^2}{N_0^2}, \quad (4.1)$$

where  $N_T^2$  was defined in Eq. (2.35). Time series of  $\min\{\tilde{N}_T^2\}$  (with the minimum taken over the entire spatial domain) are shown in Fig. 4.3(a) for simulations with  $m = -0.2k$  and initial amplitudes  $A_0 = 0.5k^{-1}$  (NH1; solid curve),  $A_0 = 0.35k^{-1}$  (NH2; dashed curve), and  $A_0 = 0.2k^{-1}$  (NH3; heavy dotted curve). The approach to overturning is diagnosed by decreasing values of  $\min\{\tilde{N}_T^2\}$  in time. The decrease occurs more rapidly if the initial amplitude is larger but still well below the overturning amplitude predicted by linear theory.

Figure 4.3(b) shows time series of  $\min\{\tilde{N}_T^2\}$  (solid black curve) and  $\min\{\text{Ri}_g\} - 1/4$  (solid and dashed red curves) for a strongly hydrostatic round wave packet with  $m = -11.4k$  and  $A_0 = 0.08k^{-1}$  (H1). The evolution of  $\min\{\tilde{N}_T^2\}$  shows little change until  $N_0 t \approx 30$  when

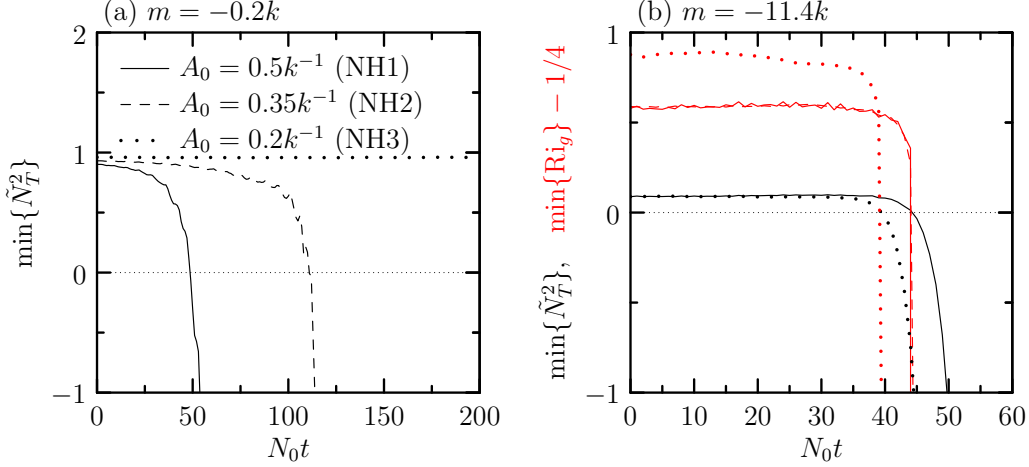


**Figure 4.3:** Time series of  $\min\{\tilde{N}_T^2\}$  (black curves), and  $\min\{Ri_g\} - 1/4$  (red curves), in which  $\tilde{N}_T^2$  and  $Ri_g$  are given respectively by Eqs. (4.1) and (2.43), for (a) strongly nonhydrostatic wave packets with  $m = -0.2k$  ( $\Theta = 11^\circ$ ) with initial amplitudes  $A_0 = 0.5k^{-1}$  (NH1),  $A_0 = 0.35k^{-1}$  (NH2), and  $A_0 = 0.2k^{-1}$  (NH3); and, (b) strongly hydrostatic wave packets with  $A_0 = 0.08k^{-1}$  and  $m = -11.4k$  ( $\Theta = 85^\circ$ ) with  $f_0 = 0.01N_0$  (H1; solid curves) and  $f_0 = 0.05N_0$  (H1+; heavy dotted curves). The dashed red curve is a time series of  $\min\{Ri_g\} - 1/4$  from H1 but using  $Ri_g = N_T^2 / \|(\partial_z u, \partial_z v)\|^2$  as in Fritts and Rastogi (1985) and Achatz (2007).

nonlinear effects rapidly drive the wave packet to overturning. In comparison, the evolution of  $\min\{Ri_g\} - 1/4$  (solid red curve) shows little change until just before overturning. The dashed red curve, showing a time series of  $\min\{Ri_g\} - 1/4$  using the definition of  $Ri_g$  in Fritts and Rastogi (1985) and Achatz (2007), evolves in a nearly identical manner. By either measure, the shear instability condition  $Ri_g < 1/4$  was attained for the first time simultaneously as  $\min\{\tilde{N}_T^2\} < 0$ . Likewise, these instability conditions were satisfied simultaneously in time series of  $\min\{\tilde{N}_T^2\}$  and  $\min\{Ri_g\} - 1/4$  from H1+ (heavy dotted black and red curves, respectively). This suggests that shear instability alone cannot grow sufficiently quickly to overturn strongly hydrostatic waves, in agreement with previous predictions (Gossard et al., 1971; Klostermeyer, 1991) and those in Sec. 2.3.4.

From a total of 79 simulations of round wave packets, the time to overturn was diagnosed and compared with stability criteria as shown by crosses in Fig. 4.4. Each cross corresponds to the initial amplitude and relative vertical wavenumber of a single simulation, with greyscale values interpolating overturning times between the discrete data points.\* In all but the

\*Greyscale values were obtained by first interpolating overturning times between amplitudes for fixed  $\Theta$ , and using the results to interpolate between  $\Theta$  values for each amplitude. The interpolant was the monotonic cubic spline of Steffen (1990). The monotonic property of this interpolant was designed to avoid spurious oscillations between interpolation points, to which classical (nonmonotonic) cubic splines are prone.

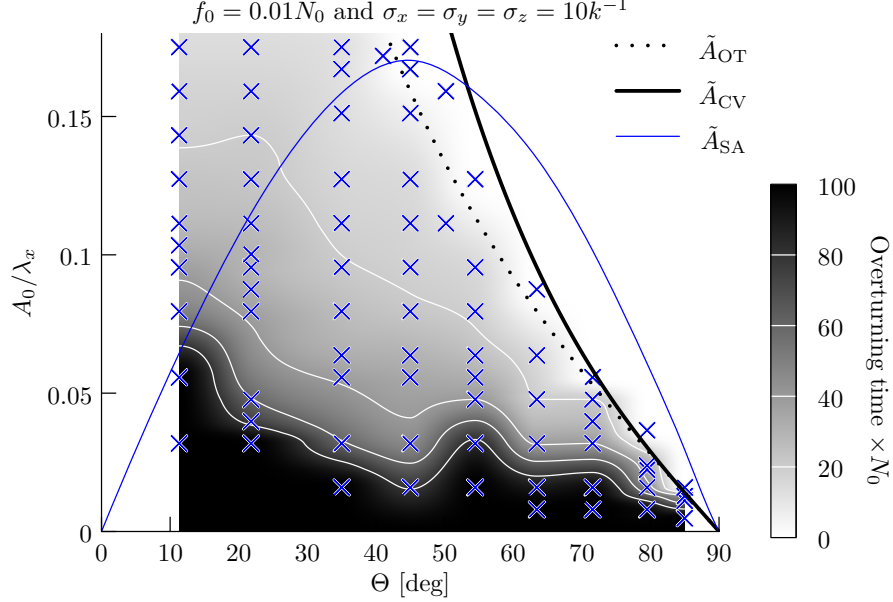


**Figure 4.4:** Comparison of stability regimes with the results of simulations of round wave packets using initial vertical displacement amplitudes  $A_0/\lambda_x$  and  $\Theta = \tan^{-1} |m/k|$  with rotation set by  $f_0 = 0.01N_0$ . The critical amplitudes predicted by linear theory for overturning ( $\tilde{A}_{OT}$ ), convective instability ( $\tilde{A}_{CV}$ ), and self-acceleration ( $\tilde{A}_{SA}$ ) are given by Eqs. (2.36), (2.37), and (2.41). Each cross corresponds to the initial amplitude and wavenumber of a single simulation. Greyscale values represent overturning times,  $t_{OT}$ , interpolated using cubic polynomials (Steffen, 1990). White curves are isolines of constant overturning time corresponding to  $N_0 t_{OT} = 20, 40, 60,$  and  $80$ .

smallest amplitude cases, overturning occurred even though the initial wave amplitude was well below that predicted for overturning according to linear theory.

Waves with relative vertical wavenumber  $m = -0.2k$  propagate at a shallow angle of  $\Theta = 11^\circ$  to the vertical. For this reason the waves spanning the range of small to moderately large initial amplitudes ( $A_0/\lambda_x = 0.096 = 1.48\tilde{A}_{SA}$ ) were able to evolve without overturning until beyond  $32/N_0$  [a somewhat heuristically chosen stability threshold used by Sutherland (2001)]. In simulations with larger  $\Theta$ , the maximum initial amplitude of waves that do not overturn until after  $32/N_0$  becomes smaller (relative to  $\lambda_x$ ), but increases relative to  $\tilde{A}_{OT}$ . For example, a hydrostatic wave packet (H2) with  $m = -5.4k$  ( $\Theta \approx 80^\circ$ ) and  $A_0/\lambda_x = 0.024 = 0.81\tilde{A}_{OT}$  overturned at  $t = 32/N_0$ , whereas one with  $m = -11.4k$  ( $\Theta = 85^\circ$ ) and  $A_0/\lambda_x = 0.013 = 0.91\tilde{A}_{OT}$  (H1) overturned at  $t = 45/N_0$ .

## 4.4 Effect of changing wave packet aspect ratio

Simulations of long and wide wave packets required significantly larger computational resources. For this reason only a limited series of simulations were performed with  $m = -0.7k$ , initialized with  $A_0 = 0.4k^{-1}$  and  $A_0 = 0.5k^{-1}$ , and with  $m = -5.4k$  and initial amplitude  $A_0 = 0.15k^{-1}$ . These combinations were chosen as representative cases of nonhydrostatic waves in the transitional regime between overturning before and after  $32/N_0$  (the cases with  $m = -0.7k$ ), and of hydrostatic waves near the marginal stability value of  $\tilde{A}_{\text{OT}}$ .

Time series of  $\min\{\tilde{N}_T^2\}$  (black curves) and  $\min\{\text{Ri}_g\} - 1/4$  (red curves) for long and wide wave packets are shown in Fig. 4.5. The nonhydrostatic simulations of long wave packets [NH4–5; Fig. 4.5(a)], for which we set  $\sigma_x = 40k^{-1}$  and  $\sigma_y = 10k^{-1}$  ( $R_y = 1/4$ ), overturned within one  $N_0t$  unit of the corresponding simulations of round wave packets. Wide wave packets in general are anticipated to interact with the Bretherton flow and induced long waves (van den Bremer and Sutherland, 2018). However, the wide wave packets reported on here were of such small spanwise extent that induced long waves were predicted to be of negligible magnitude relative to the Bretherton flow. Wide wave packets, for which we set  $\sigma_x = 10k^{-1}$  and  $\sigma_y = 40k^{-1}$  ( $R_y = 4$ ), were generally less stable than corresponding round and long wave packets. For example, the case with  $A_0 = 0.4k^{-1}$  [NH6; Fig. 4.5(b)] overturned at  $t = 29/N_0$ , compared with the round (NH7) and long (NH4) wave packets,<sup>†</sup> which both overturned at  $t = 32/N_0$ . This result contradicts the predicted increased stability of wide, compared to round, wave packets, shown in Fig. 4.4.

The wave packet aspect ratio appears to have had no effect on the results of the hydrostatic long and wide simulations. Wave packets initialized with  $A_0 = 0.15k^{-1}$  ( $A_0/\lambda_x = 0.024 = 0.81\tilde{A}_{\text{OT}}$ ) were no more or less stable than their round counterparts. In particular,  $\min\{\tilde{N}_T^2\}$  increased slightly due to linear dispersion until  $t \approx 13/N_0$  [round (H2) and long wave packets (H3); Fig. 4.5(a)] and  $t \approx 17/N_0$  [wide wave packets (H4); Fig. 4.5(b)], before decreasing approximately monotonically until overturning at  $t = 32/N_0$ . These results, although spanning only a small region within the stability regimes shown in Fig. 2.2, are somewhat inconsistent

<sup>†</sup>In Gervais et al. (2021), the simulation IDs NH4 and NH7 were erroneously switched in-text. These IDs, as they appear in Table 4.1 and the corresponding table in Gervais et al. (2021), are correct.

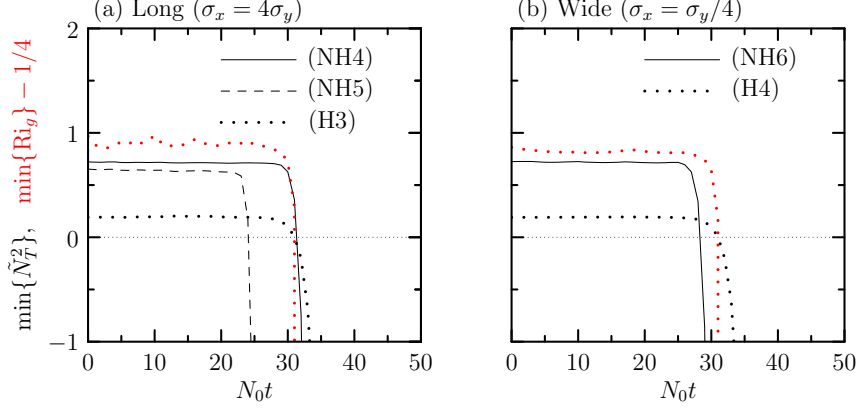


**Figure 4.5:** As in Fig. 4.3 but for (a) long wave packets with  $m = -0.7k$  and  $A_0 = 0.4k^{-1}$  (NH4) and  $A_0 = 0.5k^{-1}$  (NH5), and  $A_0 = 0.15k^{-1}$  and  $m = -5.4k$  (H3); and, (b) wide wave packets with  $A_0 = 0.4k^{-1}$  and  $m = -0.7k$  (NH6), and  $A_0 = 0.15k^{-1}$  and  $m = -5.4k$  (H4).

with the prediction that long and wide wave packets are respectively less and more stable than their round counterparts. The open question regarding the stability and overturning of long and wide wave packets merits further study.

## 4.5 Discussion and application to oceanographic observations

Our results for round wave packets revealed that fully localized wave packets were unstable at lower amplitudes than their one- and two-dimensional analogues without rotation (Sutherland, 2001). For example, a nonhydrostatic wave packet (NH8) with  $m = -0.7k$  and  $A_0 = 0.6k^{-1}$  overturned between  $32/N_0$  and  $100/N_0$  in the one-dimensional case, after  $100/N_0$  in the two-dimensional case, but at  $t = 21/N_0$  in the three-dimensional case. The most strongly hydrostatic waves examined by Sutherland (2001) (for which  $\Theta = 80^\circ$ ) overturned after  $100/N_0$  even with initial amplitudes as large as  $\tilde{A}_{OT}$  in both the one- and two-dimensional cases. Conversely, the equivalent three-dimensional wave packet with  $A_0 = 0.15k^{-1}$  ( $A_0/\lambda_x = 0.024 = 0.81\tilde{A}_{OT}$ ) overturned at  $t = 32/N_0$ . We have shown that standard linear theory predictions for wave packet stability significantly overpredict the initial amplitude for which overturning eventually occurs. This demonstrates that it is necessary to include the weakly nonlinear influence of the induced mean flow acting upon waves themselves. That said, at this time a theoretical prediction for the empirical results of fully nonlinear numerical simulations of fully three-dimensional wave packets remains elusive. Our

results suggest the need for further theoretical and numerical investigations of wave packet evolution.

As an application of our results, we contextualize our findings in terms of recent observations of internal gravity wave packets in the ocean. Therein, the internal wave frequency spectrum is dominated by strongly hydrostatic waves near the inertial frequency,  $f_0$ , forced by tidal flow over bathymetry and surface wind stress (e.g., Alford et al., 2016). However, turbulent breaking of nonhydrostatic waves has recently become of increasing interest for its potential role in larger scale oceanic processes, such as the global overturning circulation (Talley, 2013; Melet et al., 2014; Waterhouse et al., 2014; Cusack et al., 2017). For our purposes, we focus on a region about the thermocline where  $N^2$  is nearly constant.

The Drake Passage has been identified as a source of lee waves, generated as the Antarctic Circumpolar Current flows over seamount chains. Using two EM-APEX floats, Cusack et al. (2017) measured a lee wave in the northernmost region of the Shackleton Fracture Zone (near  $60^\circ$  S, with corresponding  $f_0 \approx -1.26 \times 10^{-4} \text{ s}^{-1}$ ) with  $A_0 = 100\text{--}140$  m and  $|m/k| \approx 0.6\text{--}2.5$  ( $\Theta \approx 32^\circ\text{--}68^\circ$ , hence  $15.0 \gtrsim \omega/|f_0| \gtrsim 6.5$ ). Assuming the wave to be monochromatic and evolving linearly, Cusack et al. (2017) estimated  $\lambda_x = 4000$  m. No measurements were taken of the wave’s spanwise structure. However, the strongest velocity perturbations were measured within 20 km of a prominent ridge feature of finite spanwise extent, suggesting the observed wave existed as a localized wave packet. On this basis, the observed wave corresponded to a wave packet with  $A_0/\lambda_x \approx 0.10\text{--}0.14\tilde{A}_{\text{OT}}$  (for  $|m/k| \approx 0.6$ ) and  $A_0/\lambda_x \approx 0.39\text{--}0.55\tilde{A}_{\text{OT}}$  (for  $|m/k| \approx 2.5$ ) propagating in a fluid with  $f_0/N_0 \approx -0.06$  (using the reported local-mean buoyancy frequency,  $N_0 \approx 2.2 \times 10^{-3} \text{ rad s}^{-1}$ ). For comparison, we consider a corresponding simulation (NH9<sup>-</sup>) with  $|m/k| = 2$  and  $A_0 = 0.2k^{-1}$  ( $\Theta \approx 63^\circ$  and  $A_0/\lambda_x = 0.03 = 0.4\tilde{A}_{\text{OT}}$ ) and  $f_0/N_0 = -0.05$  (with corresponding  $\omega/|f_0| \approx 9.0$ ). Setting  $z_0 = 0$  and  $t_0 = 0$  as the ridge top and time of observation, respectively, overturning was diagnosed at  $(x, z) = (13.0, 2.1)k^{-1}$  and  $t = 39/N_0 \approx 4.9$  h. Simulations with  $f_0/N_0 = 0.01$  and  $0.05$  that were otherwise identical to NH9<sup>-</sup> resolved the same overturning time and location. The observed wave propagated against the Antarctic Circumpolar Current (with mean zonal velocity  $33 \text{ cm s}^{-1}$ ), hence the corresponding overturning site would be  $x \approx 2.4$  km upstream of and  $z \approx 1.3$  km above the ridge (or approximately 200 m below the ocean surface). Although the observed wave was not

measured through its evolution, static and shear instability were proposed as playing a role in driving the wave eventually to overturning (Cusack et al., 2017), despite remarking (as we have) that the initial amplitude was below both instability thresholds. Our results suggest the waves overturned due to nonlinear interactions with their induced mean flow. Time series of  $\min\{\tilde{N}_T^2\}$  and  $\min\{\text{Ri}_g\} - 1/4$  (not shown) indicate the simulated wave packet did not become shear unstable before overturning. This result was consistent across our simulated wave packets for all initial amplitudes and relative vertical wavenumbers. Similarly, although beyond the scope of our numerical simulations, near-inertial wave packets with  $\omega \gtrsim f_0$  induced by tidal flow over ridges (Alford, 2010) and by hurricanes alike (Sanford et al., 2011) have been found to remain shear-stable through their observed evolution, in agreement with predictions.

Although our simulations diagnosed *overturning* for a range of wave packet parameters, the turbulent dynamics leading to wave *breaking* were not resolved as this process evolves on small spatial and temporal scales that were prohibitively fine to be resolved by our numerical code. Furthermore, our results are highly idealized, having assumed an infinite, rotating but otherwise stationary medium under the Boussinesq approximation. In Part II of this thesis, we take one step toward a more realistic description of gravity wave evolution by accounting for a nonzero background flow that is nonuniform with height.

## PART II

---

### Boussinesq wave packets in nonuniform background shear

---

In Part I we assumed, for convenience, that wave packets were influenced by Earth’s rotation through the Coriolis force, but that the fluid was otherwise stationary in the absence of waves. This assumption was useful to understand wave packet evolution and stability in a simplified setting. However, geophysical fluids are not stationary in general, but flow with velocities varying greatly in space and time. To complicate matters, the background flow at different locations can simultaneously generate internal gravity waves [e.g., where it encounters topography; see [Long \(1953\)](#) and [Aguilar et al. \(2006\)](#)] and itself be driven *by* internal gravity waves (e.g., as in the middle and upper atmosphere; cf. Sec. 1.1.2).

To make slightly more tractable the problem of wave–mean-flow interactions, we will assume the background flow, denoted  $\bar{u} = \bar{u}(z)$ , is a function of height alone. The independence of the background flow on the horizontal coordinates corresponds to the assumption that the waves are oriented to propagate in the streamwise direction, parallel to the background flow [as the streamwise wavenumber is typically aligned with the flow; e.g., [Sutherland \(2010, Secs. 5.4 and 6.5.1\)](#)]. The steady (time-invariant) property of the background flow corresponds to the assumption that the background flow evolves on a much slower time scale than that of the waves. This latter assumption effectively decouples the evolution of the background flow from the waves, which in turn simplifies the theory (to be considered in Chapter 5). Under these assumptions, in this study we are interested in the combined linear influence of

nonuniform background flow and the nonlinear interaction between moderately large amplitude quasimonochromatic wave packets and their wave-induced mean flow. We are interested in particular in nonhydrostatic waves, which are essentially unaffected by the Coriolis force, and so we do not consider the effect of rotation in this study.

A steady nonuniform background shear flow\* that depends on height alone acts to Doppler-shift the wave frequency (to be quantified in Chapter 5). If the wave phase propagates in the same direction as the background flow, i.e.,  $c_{px}\bar{u} > 0$ , linear theory (e.g., Sutherland, 2010) predicts that the wave frequency will be Doppler-shifted toward zero, corresponding to waves with progressively more ‘flattened’ phase lines. The Doppler-shifted frequency equals zero where  $c_{px} = \bar{u}$ , and the corresponding height is called a *critical level*. Provided the Richardson number is larger than unity, linear theory predicts that waves are “absorbed” at the critical level, transferring their momentum to the background flow at that height (Booker and Bretherton, 1967). Conversely, consider now the alternative scenario in which the wave phase propagates opposite the direction of the background flow, i.e.,  $c_{px}\bar{u} < 0$ : the background flow Doppler-shifts the upward-propagating waves ( $c_{gz} > 0$ ) toward higher frequencies, corresponding to waves with progressively vertically oriented phase lines. The waves ultimately reach a *reflection level* at the height where their Doppler-shifted frequency is equal to the local background buoyancy frequency. Consequently, at the reflection level the local vertical group velocity is zero. Further Doppler-shifting of the waves causes  $c_{gz} < 0$ , and as a result waves reflect and begin propagating downward. This latter scenario is the one which will be considered in this study. Using the quantitative language of group velocity, we define a *retrograde* shear flow as one in which a wave packet propagates against the background flow initially, i.e.,  $c_{gx}\bar{u} < 0$ . Without loss of generality, we consider only wave packets for which  $c_{gx} > 0$  initially and  $\bar{u}(z) \leq 0$ .

Although we have assumed throughout this thesis that the fluids have a uniformly stratified background state, linear theory predicts that internal gravity waves can reflect in a fluid in which the stratification weakens with height. We will invoke the concept of wave reflection in nonuniform stratification to motivate what I have called “self-reflection.” Through this weakly

---

\*Given a general background flow  $\bar{u} = \bar{u}(z)$ , *nonuniform shear* refers to the property that  $d\bar{u}/dz \neq s_0$ , where  $s_0$  is a constant.

nonlinear mechanism, moderately large amplitude nonbreaking wave packets supposedly self-induce partial reflection by decreasing locally the total stratification, and as a result generate so-called *secondary wave packets* (observed unexpectedly in some of our numerical results).

Studies investigating the relationship between internal gravity waves and mean flows have typically considered the isolated case of either the interactions between waves and an existing background flow (e.g., [Bretherton, 1966](#); [Bretherton and Garrett, 1969](#); [Dunkerton and Fritts, 1984](#); [Fritts and Dunkerton, 1984](#); [Blumen, 1985](#); [Eckermann, 1997](#); [Huang et al., 2008, 2010](#); [Heale and Snively, 2015](#)), or between waves and their induced mean flow in an otherwise stationary fluid (e.g., [Grimshaw, 1977](#); [Sutherland, 2001](#); [Akylas and Tabaei, 2005](#); [Tabaei and Akylas, 2007](#); [Dosser and Sutherland, 2011](#); [Gervais et al., 2018, 2021](#)). Relatively few studies (e.g., [Robinson, 1997](#); [Sutherland, 2000](#); [Eberly and Sutherland, 2014](#)) have examined the nonlinear evolution of a moderately large amplitude wave packet as it interacts with both its induced mean flow and an existing nonuniform background flow. Using ray theory, [Robinson \(1997\)](#) predicted the trajectory of a one-dimensional wave packet with its induced mean flow superimposed, propagating in an existing linear shear flow. In particular, the Doppler-shifted frequency predicted by linear theory was modified to itself be Doppler-shifted by the induced mean flow. The idealized analysis suggested that the competing effects of the oppositely-signed background and induced mean flows allowed the waves to propagate higher before reflecting than without the influence of the induced mean flow. The reflection time was delayed correspondingly. These results were more pronounced as amplitude increased, owing to the magnitude of the induced mean flow increasing quadratically with amplitude. [Sutherland \(2000\)](#) performed fully nonlinear simulations of small and moderately large amplitude one- and two-dimensional nonhydrostatic wave packets in uniform retrograde shear flow. Wave packets with sufficiently large initial amplitude were able to propagate well above the reflection level predicted by linear theory provided the magnitude of the vertical shear associated with the wave-induced mean flow was somewhere greater than that of the background shear. The superimposed background and wave-induced *shears*, being locally equal and opposite, allowed a wave packet to propagate as if the background flow was effectively uniform in the vicinity of the advancing wave packet.

The purpose of this study is to extend to three dimensions the reflection level penetration

predictions of [Sutherland \(2000\)](#), and to quantify the transmission of waves above the reflection level as it depends on initial wave amplitude and relative vertical wavenumber. Our study differs from those of [Robinson \(1997\)](#) and [Sutherland \(2000\)](#) in that we combine ray theory and numerical simulations to examine the evolution of fully localized three-dimensional wave packets with amplitude envelopes that are Gaussian in all three spatial dimensions, in a nonuniform background flow that transitions smoothly with height from stationary to linearly decreasing.

In [Chapter 5](#) we first review the theory of linear (i.e., small amplitude) wave packet propagation in nonuniform background flow, and extend the work of [Sutherland \(2000\)](#) to derive the critical amplitude for three-dimensional wave packet penetration above the reflection level. We describe secondary wave packet generation by triadic resonant instability and self-reflection, and we define a transmission coefficient. Using the code described in [Chapter 6](#), we perform numerical simulations of round wave packets with the predicted Bretherton flow superimposed, spanning a range of initial amplitudes, relative vertical wavenumbers, and background shear magnitudes. Results are described in [Chapter 7](#) and compared with theoretical predictions. Results are discussed in the context of previous studies of one- and two-dimensional wave packet transmission and reflection.

---

## Theory

---

In this chapter we first review the ray theory equations which predict the path traced by the centroid of a small amplitude wave packet as it propagates in an inviscid Boussinesq fluid without rotation but with a nonuniform background shear flow. The solutions of the ray theory equations thus provide predictions for the height and time at which a small amplitude wave packet is anticipated to reflect. We then describe how the Bretherton flow is anticipated to modify the linear dynamics of moderately large amplitude wave packets. This will motivate our derivation of the critical amplitude at which a wave packet is anticipated to penetrate significantly above the reflection level. We then present two nonlinear theories for the generation of secondary wave packets. The chapter concludes with the definition of an appropriate transmission diagnostic.

### 5.1 Linear theory

We begin by considering a nonrotating, uniformly stratified, inviscid Boussinesq fluid that is stationary in the absence of waves. Without loss of generality the coordinate system is assumed to be oriented such that there is no wave propagation in the spanwise direction. With these considerations, monochromatic internal gravity waves propagate in the  $xz$ -plane with intrinsic frequency

$$\omega_0 = \frac{N_0 k_0}{\sqrt{k_0^2 + m_0^2}}, \quad (5.1)$$

where  $k_0 > 0$  and  $m_0$  are the streamwise and vertical wavenumbers, respectively, and  $N_0$  is the background buoyancy frequency, given by Eq. (2.9), a constant in our assumed uniformly stratified fluid. Equation (5.1) is equivalent to Eq. (2.13) in the nonrotating limit (i.e., as the Coriolis parameter  $f_0 \rightarrow 0$ ).

We emphasize a subtle change of notation compared to that used in Part I, namely, the adornment of quantities  $k_0$ ,  $m_0$ ,  $\omega_0$ , and others henceforth, as needed, with a subscript 0. This is to distinguish these quantities as having fixed values, inherent to the waves, that remain fixed even as waves propagate through the nonuniform background flow. With this notation, a given wave field  $\eta$  is represented as a wave packet by

$$\eta(\mathbf{x}, t) = \frac{1}{2} A_\eta(\mathbf{x}, t) e^{i\varphi_0} + \text{c.c.},$$

where  $\varphi_0 = \mathbf{k}_0 \cdot (\mathbf{x} - \mathbf{x}_0) - \omega_0 t$  is the phase, in which  $\mathbf{k}_0 = (k_0, 0, m_0)$  is the wavenumber vector (with the second component,  $\ell_0 = 0$ , corresponding to no wave propagation in the  $y$ -direction). Note that the wave packet envelope  $A_\eta$  can vary in  $y$ . Taking a somewhat more general approach than in Chapter 2, the wave packet may be offset from the origin initially by  $\mathbf{x}_0 = (x_0, y_0, z_0)$ .

A nonuniform background flow,  $\bar{u}(z)$ , acts to Doppler-shift the intrinsic frequency, with the resulting Doppler-shifted (extrinsic) frequency given by

$$\Omega = \omega_0 - k_0 \bar{u}. \quad (5.2)$$

The path traced by the centroid of a small amplitude wave packet from an initial position  $(x_0, 0, z_0)$  through a nonuniform background flow is predicted using ray theory (e.g., [Sutherland, 2010](#), Sec. 6.5), provided  $\bar{u}$  does not change significantly over a vertical wavelength. This latter condition is imposed to ensure conformity with the Wentzel–Kramers–Brillouin–Jeffreys (WKBJ) approximation that is central to ray theory. Under this condition the path traced by the centroid of the wave packet is given by the solution to the differential equations

$$\frac{dx}{dt} = c_{gx}(m(z)) + \bar{u}(z), \quad (5.3a)$$

$$\frac{dz}{dt} = c_{gz}(m(z)). \quad (5.3b)$$

These differential equations state that a small amplitude wave packet is advected in the streamwise direction by the background flow as it translates at its group velocity  $\mathbf{c}_g = (c_{gx}, 0, c_{gz})$ , with components given explicitly by

$$c_{gx} = \frac{N_0 m^2}{\|\mathbf{k}\|^3}, \quad (5.4a)$$

$$c_{gz} = -\frac{N_0 k_0 m}{\|\mathbf{k}\|^3}, \quad (5.4b)$$

where  $\|\mathbf{k}\| = (k_0^2 + m^2)^{1/2}$  is the Euclidean norm of the *local* wavenumber vector  $\mathbf{k} = (k_0, 0, m)$ , in which  $k_0$  is constant but  $m$  varies with height in response to Doppler-shifting by the background flow. A diagnostic equation for the local vertical wavenumber  $m = m(z)$  is found by equating the Doppler-shifted and local intrinsic frequency, Eqs. (5.2) and (5.1), respectively (e.g., [Huang et al., 2008](#)), to obtain the auxiliary equation

$$m = m(z(t)) = \text{sign}(m) k_0 \sqrt{\frac{N_0^2}{\Omega^2(z(t))} - 1}, \quad (5.5)$$

in which  $\text{sign}(m) = -1$  if the wave packet is propagating upward ( $c_{gz} > 0$ ) and  $\text{sign}(m) = 1$  if the wave packet is propagating downward ( $c_{gz} < 0$ ).

An initially upward-propagating wave packet [i.e., one with  $k_0 > 0$  constant and  $m(z(t_0)) = m(z_0) = m_0 < 0$ ] is anticipated to propagate until it reaches the *reflection level*, denoted  $z_r$ . This is the height at which  $\Omega = N_0$ , corresponding to the height at which  $m(z_r) = 0$ . The reflection time  $t_r$  is the time at which  $z(t) = z_r$ . In practice, for a steady but otherwise general background flow profile that varies only with height, Eqs. (5.3a)–(5.5) cannot be solved analytically. Therefore, the reflection level and time must be determined numerically from the solution of Eq. (5.3b). Details of the nontrivial numerical solution procedure are provided in [Appendix D](#).

If a wave packet is initially of moderately large amplitude, the reflection behaviour described above may be altered significantly by nonlinear interactions with the wave-induced mean flow, described below.

## 5.2 Wave-induced mean flow and reflection level penetration

It has been known since [Bretherton \(1969\)](#) that as a moderately large amplitude fully localized internal gravity wave packet propagates, an order amplitude-squared Eulerian induced mean flow—the Bretherton flow—is generated which acts to locally accelerate the fluid in the vicinity of the wave packet ([Bühler and McIntyre, 1998](#); [Tabaei and Akylas, 2007](#); [van den Bremer and Sutherland, 2018](#)). In the absence of an existing background flow, the horizontal components of the Bretherton flow induced by a wave packet with vertical displacement envelope  $A := A_\xi$  are given initially by the Fourier integral

$$\begin{bmatrix} u_{\text{BF}} \\ v_{\text{BF}} \end{bmatrix} = \frac{1}{2} N_0 \|\mathbf{k}_0\| \int_{\mathbb{R}^3} \frac{\lambda}{\kappa^2 + \lambda^2} \begin{bmatrix} \lambda \\ -\kappa \end{bmatrix} \widehat{|A|^2} e^{i\boldsymbol{\kappa} \cdot (\mathbf{x} - \mathbf{x}_0)} d\boldsymbol{\kappa} d\lambda d\mu, \quad (5.6)$$

first derived explicitly by [van den Bremer and Sutherland \(2018\)](#). Equation (5.6) is equivalent to Eq. (2.31) in the limit as  $f_0 \rightarrow 0$ , and in which we set  $\mathbf{x} \rightarrow \mathbf{x} - \mathbf{x}_0$  in the complex exponential to account for wave packets offset from the origin initially.

In an idealized study of one-dimensional wave packet transmission and reflection, [Robinson \(1997\)](#) used ray theory to trace the path of wave packets with their predicted wave-induced mean flow superimposed as they propagated in a uniform retrograde shear flow. It was found that the oppositely-signed background and wave-induced mean flows locally cancelled transiently at the heights where they were equal and opposite, thus allowing the wave packet to propagate higher than the reflection level predicted by linear theory. However, this study did not account for the nonlinear evolution of the wave packets as they propagated. Conversely, in a fully nonlinear numerical study of one- and two-dimensional wave packet transmission and reflection in uniformly stratified and sheared flow, [Sutherland \(2000\)](#) found that rather than displacing the reflection level as predicted by [Robinson \(1997\)](#), a wave packet could transmit partially above the predicted reflection level. This was achieved for wave packets of sufficiently large amplitude that the magnitude of the vertical shear associated with the wave-induced mean flow was locally greater than that of the background shear,  $|s|$ . In three dimensions, the wave-induced mean flow is the Bretherton flow, and the corresponding penetration condition is given explicitly by

$$\left| \frac{\partial u_{\text{BF}}}{\partial z} \right| > |s|. \quad (5.7)$$

For example, we consider solutions of this inequality for a triply Gaussian wave packet with vertical displacement amplitude envelope  $A(\mathbf{x}, t)$  given initially by Eq. (2.32), in which we set  $z \rightarrow z - z_0$ . Explicitly,

$$A(\mathbf{x}, 0) = A_0 \mathcal{A}(\mathbf{x}, 0) = A_0 \exp \left[ -\frac{1}{2} \left( \frac{x^2}{\sigma_x^2} + \frac{y^2}{\sigma_y^2} + \frac{(z - z_0)^2}{\sigma_z^2} \right) \right], \quad (5.8)$$

in which we have defined for later reference the nondimensional amplitude  $\mathcal{A}$ , of order unity initially, to be the Gaussian factor. The initial peak amplitude is  $A_0$ , and  $\sigma_x$ ,  $\sigma_y$ , and  $\sigma_z$  are the wave packet extents in the streamwise, spanwise, and vertical directions. Squaring and Fourier transforming Eq. (5.8) using Eq. (2.30a), in which we set  $\tilde{\mathbf{x}} \rightarrow \mathbf{x} - \mathbf{x}_0$ , gives  $|\widehat{A}|^2$ , the expression for which is identical to that in Eq. (2.33). Using this expression in Eq. (5.6), it follows that the largest value of  $|u_{\text{BF}}|$ , hence also that of  $|\partial u_{\text{BF}}/\partial z|$  in Eq. (5.7), at any given height is aligned with the horizontal centre of the wave packet. Accordingly, we obtain an analytically tractable integral expression for the vertical profile of largest  $|u_{\text{BF}}|$  by setting  $\mathbf{x} = (0, 0, z_0)$  in the streamwise component of Eq. (5.6). The resulting integral may be evaluated using the method described in Appendix C to find

$$\max_{x,y} |u_{\text{BF}}| = u_{\text{BF}}(0, 0, z, t = 0) = \frac{1}{2} N_0 \|\mathbf{k}_0\| \frac{A_0^2}{R_y + 1} e^{-(z-z_0)^2/\sigma_z^2}, \quad (5.9)$$

where  $R_y = \sigma_y/\sigma_x$  is the spanwise aspect ratio of the wave packet. The expression on the right-hand side of Eq. (5.9) is equivalent to that in Eq. (C.3) but with  $z \rightarrow z - z_0$ .

Differentiating Eq. (5.9) with respect to  $z$ , one obtains the initial profile of largest wave-induced mean shear,

$$s_{\text{BF}} := \frac{d}{dz} \max_{x,y} |u_{\text{BF}}| = -N_0 \|\mathbf{k}_0\| \frac{A_0^2}{R_y + 1} \frac{z - z_0}{\sigma_z^2} e^{-(z-z_0)^2/\sigma_z^2}.$$

Differentiating  $s_{\text{BF}}$  with respect to  $z$  and setting the result equal to zero, it is straightforward to show that the maximum wave-induced mean shear occurs below the centre of the wave packet at  $z - z_0 = -\sigma_z/\sqrt{2}$ , with corresponding maximum

$$\frac{1}{R_y + 1} \frac{N_0 \|\mathbf{k}_0\|}{\sqrt{2e}\sigma_z} A_0^2.$$

Substituting this expression into the penetration condition, Eq. (5.7), yields the critical amplitude,  $A_{\text{RP}}$ , above which a triply Gaussian wave packet is predicted to penetrate partially

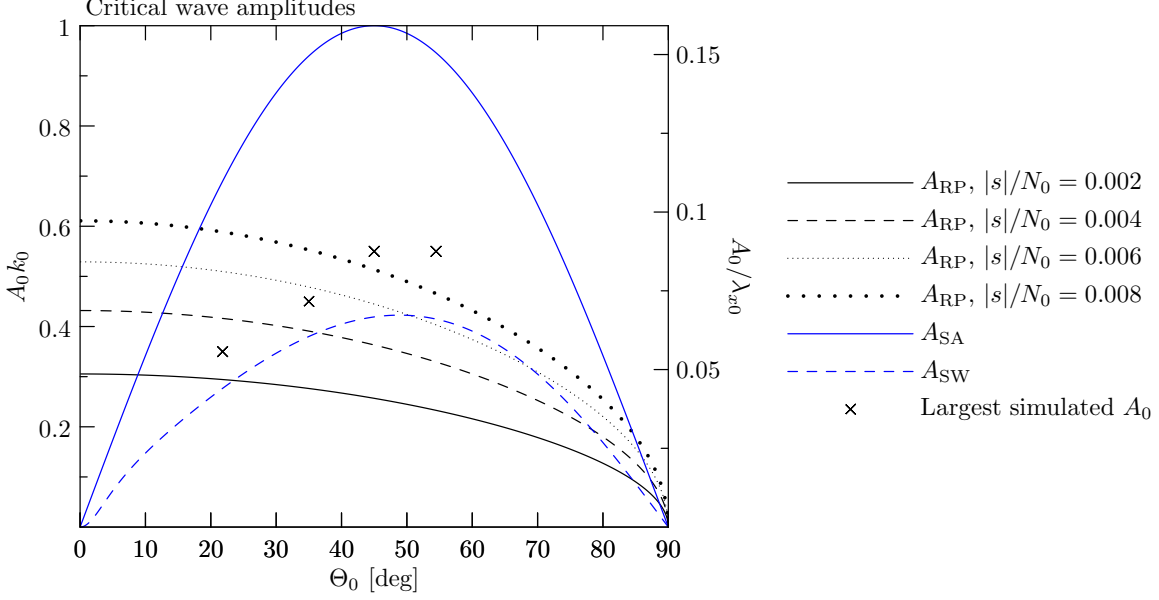


**Figure 5.1:** Critical amplitudes for a wave packet with  $R_y = 1$  and  $\sigma_z = 10k_0^{-1}$  to penetrate above a reflection level predicted by linear theory for a range of shear strength parameters (black curves), given by Eq. (5.10); for self-acceleration instability (solid blue curve), given by Eq. (5.11); and, for secondary wave packet generation via self-reflection (dashed blue curve), given by Eq. (5.15). Crosses indicate the largest initial amplitude of waves propagating initially with corresponding  $\Theta_0 = \tan^{-1} |m_0/k_0|$ .

above a reflection level:

$$A_{\text{RP}} = \sqrt{\frac{\sigma_z (R_y + 1) \sqrt{2e} |s|}{\|\mathbf{k}_0\| N_0}}. \quad (5.10)$$

This critical amplitude is plotted as the black curves in Fig. 5.1, corresponding to wave packets with  $R_y = 1$  and  $\sigma_z = 10k_0^{-1}$  for a range of relative shear strength parameters,  $|s|/N_0$ .

### 5.3 Wave packet stability and critical amplitudes

In Sec. 2.3.1, overturning was described as the lifting of more dense fluid over less dense fluid by a wave of sufficiently large amplitude. This dynamical situation characterizes static instability. The approach to overturning is diagnosed by decreasing values of  $\min\{N_T^2\}$  in time (Sutherland, 2001; Gervais et al., 2021). Here,  $N_T^2 = N_0^2 + \Delta N^2$  is the total squared buoyancy frequency, given by Eq. (2.35), in which  $\Delta N^2 = -N_0^2 \partial \xi / \partial z$  is the local change in (squared) buoyancy due to waves. Overturning is diagnosed by the condition  $\min\{N_T^2\} \leq 0$ , which corresponds to the (dimensional) critical amplitude  $A_{\text{OT}} = 1/|m_0|$ , given nondimensionally by Eq. (2.36) and plotted as heavy black curve in Fig. 2.2.

Another important parameter to consider is the critical amplitude at which waves are

prone to become unstable to self-acceleration. In Sec. 2.3.3 we proposed, following Sutherland (2001), that a wave packet was prone to self-acceleration instability if the streamwise component of its Bretherton flow was locally greater than its streamwise group speed. A similar analysis comparing Eqs. (5.6) and (5.4a) yields the dimensional critical amplitude

$$A_{\text{SA}} = \frac{1}{\sqrt{2}k_0} \sin(2\Theta_0) \sqrt{R_y + 1}, \quad (5.11)$$

which is equivalent to Eq. (2.41) in the limit as  $f_0 \rightarrow 0$ , but without the normalization factor  $\lambda_x = 2\pi/k_0$ . The curve of marginal stability corresponding to Eq. (5.11) is plotted in Fig. 5.1 as the solid blue curve for a wave packet with  $R_y = 1$  and  $\sigma_z = 10k_0^{-1}$ .

For nonhydrostatic fully localized wave packets with  $R_y = 1$ ,  $A_{\text{OT}} > A_{\text{SA}}$ . We are interested in simulating such nonhydrostatic wave packets with a range of small to moderately large initial amplitudes, but not so large that the waves overturn during the simulation. Consequently,  $A_{\text{SA}}$  suggests an upper bound for the initial amplitudes considered for numerical simulation in Chapter 7.

## 5.4 Secondary wave packet generation

In general, *secondary gravity waves* refer to internal gravity waves that may be generated as a response to a variety of gravity wave forcings, and the language around secondary waves arises accordingly in several contexts (e.g., Fritts and Alexander, 2003). Observational studies of secondary gravity wave generation have focused on their excitation as a response to primary gravity wave breaking in the middle and upper atmosphere (Fritts et al., 2002; Smith et al., 2013; Bossert et al., 2017). Numerical simulations have similarly examined their excitation as a response to breaking of convectively and orographically generated three-dimensional primary waves (Holton and Alexander, 1999; Lane and Sharman, 2006; Becker and Vadas, 2018; Fritts et al., 2020; Lund et al., 2020; Fritts et al., 2021). Theoretical studies have modelled secondary gravity waves as a linear response to momentum deposition by breaking primary waves (Vadas and Fritts, 2001, 2002; Vadas et al., 2003; Vadas and Fritts, 2006). Primary wave breaking is the common factor among these three broad investigative approaches. I am unaware of any investigations of secondary wave packet generation by *nonbreaking* primary waves. The

motivation to examine their generation in this thesis is grounded in a subset of numerical results, discussed in Chapter 7, in which secondary wave packets were generated unexpectedly, apparently by nonbreaking primary waves.

Secondary wave packets are identified in the simulation results as wave packets existing at  $O(\alpha^2)$ , where  $\alpha = k_0 A$  is the nondimensional measure of vertical displacement amplitude introduced in Chapter 2. Wave packets at this order are distinguished from those at  $O(\alpha)$  using two simulations with initial amplitude  $A_0$ , but with the phase of the waves in the second simulation shifted by  $180^\circ$  (Baldock et al., 1996; McAllister et al., 2018), an approach we borrow from analyses of surface gravity waves in laboratory experiments. In practice, the phase shift was achieved by equivalently setting  $A_0 \rightarrow -A_0$  in the second simulation. Pairs of results are combined in postprocessing using

$$u^{(1)} = \frac{1}{2}(u_+ - u_-), \quad (5.12a)$$

$$u^{(2)} = \frac{1}{2}(u_+ + u_-), \quad (5.12b)$$

in which the superscript denotes the order of the postprocessed field with respect to  $\alpha$ , and the subscript  $+$  or  $-$  signs denote whether the associated wave field corresponds to the result from a positive or negative amplitude (phase-shifted) simulation.

Upward- and downward-propagating secondary wave packets are identified in our simulation results, and appear to be generated by distinct mechanisms, described below.

#### 5.4.1 Triadic resonant instability

Triadic resonant instability (TRI) occurs when waves with wavenumber vectors  $\mathbf{k}_1$  and  $\mathbf{k}_2$  and corresponding frequencies  $\omega_1 = \omega(\mathbf{k}_1)$  and  $\omega_2 = \omega(\mathbf{k}_2)$  interact through the nonlinear advection terms in the governing equations to produce a third wave with wavenumber vector  $\mathbf{k}_3$  and frequency  $\omega_3 = \omega(\mathbf{k}_3)$  (Phillips, 1960; Müller et al., 1986; Sutherland, 2010). Plane wave solutions to the fully nonlinear inviscid governing equations are prone to this instability even with infinitesimally small amplitudes (Davis and Acrivos, 1967; Mied, 1976).

Typically, TRI is studied in the context of plane waves or internal gravity wave beams (e.g., as discussed in the review paper by Dauxois et al., 2018). However, it will be shown in Chap-

ter 7 that upward-propagating secondary wave packets, generated in simulations of the most strongly nonhydrostatic primary waves (with initial absolute relative vertical wavenumber  $|m_0/k_0| \lesssim 0.7$ ), result from TRI between transmitted and reflected wave packets. Similarly, it will be shown that downward-propagating secondary wave packets, generated in simulations of moderately nonhydrostatic primary waves ( $|m_0/k_0| \gtrsim 0.7$ ) do not result from TRI between transmitted and reflected waves.

In the simulation results, the wavenumber vectors corresponding to transmitted (or incident) waves and reflected waves will be identified respectively as  $\mathbf{k}_{\{t,i\}} = \mathbf{k}_1$  and  $\mathbf{k}_r = \mathbf{k}_2$ , with corresponding frequencies  $\omega_{\{t,i\}}$  and  $\omega_r$ . Candidates for the wavenumber vector and frequency of secondary wave packets,  $\mathbf{k}_s$  and  $\omega_s$ , are predicted using the triad interaction equations,

$$\begin{aligned}\pm \mathbf{k}_{\{t,i\}} \pm \mathbf{k}_r &= \mathbf{k}_s, \\ \pm \omega_{\{t,i\}} \pm \omega_r &= \omega_s,\end{aligned}$$

where the  $\pm$  signs span all possible combinations of coefficients  $+1$  and  $-1$ . Predicted values of  $\mathbf{k}_s$  and  $\omega_s$  will be compared to the actual wavenumber vector and frequency of the secondary wave packets,  $\mathbf{k}_s^{(2)}$  and  $\omega_s^{(2)}$ , diagnosed from the results of the numerical simulations.

To diagnose whether TRI is active, the wavenumber vectors corresponding to the transmitted (or incident) and reflected wave packets will be identified as the Fourier modes corresponding to peaks in the power spectrum of the linear wave field,  $|\hat{u}^{(1)}|$ , obtained using the Fourier transform of Eq. (5.12a), such that

$$\begin{aligned}\mathbf{k}_{\{t,i\}} &= \operatorname{argmax} \{ |\hat{u}^{(1)}| : m_{\{t,i\}} < 0 \}, \\ \mathbf{k}_r &= \operatorname{argmax} \{ |\hat{u}^{(1)}| : m_r > 0 \},\end{aligned}$$

in which the Fourier mode  $m_t$ ,  $m_i$  or  $m_r$  is associated with the corresponding literal vertical wavenumber. Similarly, the wavenumber vector corresponding to the secondary wave packet will be identified as the Fourier modes corresponding to peaks in the power spectrum of the quadratically nonlinear wave field:

$$\mathbf{k}_s^{(2)} = \operatorname{argmax} \{ |\hat{u}^{(2)}| \},$$

in which  $|\hat{u}^{(2)}|$  is obtained from the Fourier transform of Eq. (5.12b). Although the wave number vectors have three components corresponding to the streamwise, spanwise, and vertical Fourier modes, in practice the argmax operation was performed considering streamwise and vertical values only. This restriction to  $\ell = 0$  in the spanwise spectrum was not anticipated to impact negatively the results of the analysis because there is no wave propagation in the  $y$ -direction and so peaks in the spanwise spectrum tend accordingly to be centred about  $\ell = 0$ . This restriction was necessary on pragmatic grounds as the fully three-dimensional output files are typically of such a large size as to be unwieldy in postprocessing.

The incident, transmitted, reflected, and secondary waves exist as packets with broad spectra, as opposed to a plane wave whose spectrum consists of power at a single Fourier mode. Hence, one does not anticipate that  $\mathbf{k}_s = \mathbf{k}_s^{(2)}$  and  $\omega_s = \omega_s^{(2)}$  exactly, if indeed TRI is active. For this reason, TRI will only be declared as the generation mechanism of secondary wave packets provided the predicted  $\mathbf{k}_s$  lies within a (somewhat heuristically chosen) 50% contour of the secondary spectral peak value  $|\hat{u}^{(2)}(\mathbf{k}_s^{(2)})|$ , and if the value of  $\omega_s$  is within 50% of that of  $\omega_s^{(2)}$ .

#### 5.4.2 Wave packet self-reflection

Unlike upward-propagating secondary wave packets resulting from nonlinear interactions between transmitted and reflected strongly nonhydrostatic waves, downward-propagating secondary wave packets appear to be generated prior to reflection by moderately nonhydrostatic waves. As a preliminary attempt to explain the unexpected emergence of these secondary wave packets, we appeal somewhat heuristically to weakly nonlinear theory to propose a generation mechanism based on a process I called wave “self-reflection.” I am unaware of any literature prior to [Gervais et al. \(2022, Sec. II.C.2\)](#), on which this section is based, describing self-induced reflection of internal gravity waves.

The motivation to explore the concept of self-induced wave reflection is grounded in the apparent cusping trajectory traced by the centroid of a typical downward-propagating secondary wave packet and the phase orientation of its constituent waves. Both of these features resemble qualitatively those anticipated from the linear theory of wave reflection in nonuniform stratification [see, e.g., [Sutherland \(2010\)](#), Fig. 6.8(a)]. In particular, linear theory predicts

that small amplitude internal gravity waves propagating in a stationary fluid with weakening stratification with height will reflect at the height  $z_r$  at which their frequency equals the local buoyancy frequency,  $\omega_0 = N(z_r)$ . Moderately large amplitude wave packets propagating in an otherwise uniformly stratified ambient change locally the stratification within the volume occupied by the wave packet (cf. Sec. 2.3.1). The resulting squared total buoyancy frequency,  $N_T^2(\mathbf{x}, t)$ , is given by Eq. (2.35). Here we derive the critical amplitude for a wave to reflect partially due to an assumed self-induced local buoyancy decrease. For convenience, the derivation assumes the background flow is zero, as this situation occurs in practice in the part of the domain where downward-propagating secondary wave packets appear.

To account for finite-amplitude effects, we suppose a moderately large amplitude wave packet will induce self-reflection at the height at which the wave frequency is equal to  $N_T$ . To that end, we assume the wave frequency is set by the weakly nonlinear dispersion relation,

$$\omega = \omega_0 + \omega_2|A|^2, \quad (5.13)$$

where  $\omega_0$  is given by Eq. (5.1), and  $\omega_2$  is a constant to be determined. The term  $\omega_2|A|^2$  accounts for local Doppler-shifting of the wave frequency by the wave-induced mean flow. Setting  $N_T^2 = \omega^2$  and retaining terms of up to  $O(\alpha^2)$  yields the leading-order weakly nonlinear condition for self-reflection,

$$N_0^2 - N_0^2 \frac{\partial \xi}{\partial z} = \omega_0^2 + 2\omega_0\omega_2|A|^2. \quad (5.14)$$

Waves are anticipated to reflect at the height where the left-hand side of Eq. (5.14) is smallest, hence where  $\partial \xi / \partial z$  is largest. Although the amplitude envelope  $A$  also depends spatially on  $\mathbf{x}$ ,  $A$  varies relatively slowly compared with  $\xi$ , and so is treated as effectively constant for the time being.

To obtain  $\omega_2$  in general, one typically analyzes a particular nonlinear Schrödinger equation modelling the weakly nonlinear evolution of a wave packet envelope as it interacts with its wave-induced mean flow (Shrira, 1981; Akylas and Tabaei, 2005; Sutherland, 2006b; Tabaei and Akylas, 2007; Dosser and Sutherland, 2011; Gervais et al., 2018). In this approach,  $\omega_2$  is associated with the coefficient on the leading-order (cubically) nonlinear term (Sutherland, 2000, 2001; Tabaei and Akylas, 2007; Gervais et al., 2018). By analogy with one-, two-, and

three-dimensional wave packets, we use Eq. (5.9) and set  $\omega_2|A|^2 = k_0 u_{\text{BF}}(0, 0, z, t = 0)$  in the weakly nonlinear dispersion relation, Eq. (5.13), to find that

$$\omega_2 = \frac{1}{2} \frac{N_0 k_0 \|\mathbf{k}_0\|}{R_y + 1}.$$

We remark that this expression for  $\omega_2$  differs from that for one-dimensional wave packets only by the multiplicative factor  $1/(R_y + 1)$  due to the analogous vertical structure of the mean flows induced by these two types of wave packets.

Now, the vertical displacement field is set by  $\xi = A_0 \mathcal{A} \cos[k_0 x + m_0(z - z_0)]$ , in which  $\mathcal{A}$  is the nondimensional amplitude envelope [for example, given for a triply Gaussian wave packet by Eq. (5.8)], and its vertical gradient  $\partial\xi/\partial z$  is maximized numerically. For convenience, we define the maximum  $M_*$  obtained using this procedure by

$$M_* := M_*(x_*, z_*) = \max_{x, z} \left\{ \frac{\partial}{\partial z} \mathcal{A} \cos[k_0 x + m_0(z - z_0)] \right\},$$

where  $(x_*, z_*)$  is the maximizer. With this notation we define a corresponding envelope value,  $\mathcal{A}_* := \mathcal{A}(x_*, 0, z_*, t = 0)$ . Finally, using  $M_*$  and  $\omega_2$  in Eq. (5.14) yields the dimensional critical amplitude for secondary wave packet generation by self-reflection:

$$A_{\text{SW}} = \frac{1}{2} \frac{R_y + 1}{k_0^2 |\mathcal{A}_*|^2} \left[ -M_* + \left( M_*^2 + 4 \frac{|\mathcal{A}_*|^2}{R_y + 1} \frac{k_0^2 m_0^2}{\|\mathbf{k}_0\|^2} \right)^{1/2} \right]. \quad (5.15)$$

The critical amplitude  $A_{\text{SW}}$  with  $R_y = 1$  is plotted as the dashed blue curve in Fig. 5.1. Although in theory Eq. (5.15) is valid for the full range of values of  $\Theta_0 = \tan^{-1} |m_0/k_0|$ , downward-propagating secondary wave packets are found only in simulations of primary waves with  $\Theta \gtrsim 35^\circ$ .

## 5.5 Transmission coefficient

In order ultimately to quantify the transmission and reflection of internal gravity waves, we must first identify a quantity that is conserved in some sense even as it is redistributed within the domain by waves and the background shear flow. In general, a conserved quantity  $\mathcal{B}$  is one whose density  $B(\mathbf{x}, t)$  satisfies the conservation law

$$\frac{\partial B}{\partial t} = -\nabla \cdot \mathbf{F}_B, \quad (5.16)$$

where  $\mathbf{F}_B$  is the flux of  $B$ . In this context, the *density* of a quantity refers to its spatial and temporal distribution per unit volume, and *conserved* describes the property that the volume-integrated density, subject to appropriate boundary conditions, is constant.

As a motivating example, consider a uniformly stratified, inviscid, incompressible Boussinesq fluid that is stationary in the absence of waves. In such a fluid the energy  $\mathcal{E}$ , with density  $E = E_K + E_P$ , is conserved, where  $E_K = \frac{1}{2}\rho_0\|\mathbf{u}\|^2$  and  $E_P = \frac{1}{2}\rho_0N_0^2\xi^2$  are the densities of kinetic and available potential energy, respectively. The expression for  $E_K$  may be obtained by taking the dot product of  $\mathbf{u}$  and the momentum equations and using the incompressibility condition  $\nabla \cdot \mathbf{u} = 0$  (e.g., Sutherland, 2010, Sec. 3.4). The expression for  $E_P$  may be obtained by multiplying the internal energy equation (written in terms of  $\xi$ ) by  $\rho_0N_0^2\xi$  and using  $\nabla \cdot \mathbf{u} = 0$ . The resulting equation for  $E$  can be written in the form of Eq. (5.16) with  $\mathbf{F}_E = (E + p)\mathbf{u}$ . Integrating over the volume of the domain  $V$  gives the total energy,  $\mathcal{E} = \int_V E(\mathbf{x}, t)dV$ , which may be shown to be conserved by applying the Divergence theorem with appropriate boundary conditions:

$$\frac{d\mathcal{E}}{dt} = \int_V \frac{\partial}{\partial t} E(\mathbf{x}, t)dV = - \int_V \nabla \cdot \mathbf{F}_E dV = - \int_{\partial V} \mathbf{F}_E \cdot \hat{\mathbf{n}} dS = 0,$$

where  $\hat{\mathbf{n}}$  denotes the outward unit vector normal to the boundary  $\partial V$  of the domain. Periodic and no-flux are examples of boundary conditions that satisfy  $d\mathcal{E}/dt = 0$ .

If one attempts to follow the above procedure but for a fluid with a background flow  $\bar{u} = \bar{u}(z)$  that is nonuniform with height, one obtains the energy density equation

$$\frac{\partial E}{\partial t} = -\nabla \cdot \mathbf{F}_E - \rho_0 u w \frac{d\bar{u}}{dz}, \quad (5.17)$$

where  $\mathbf{F}_E = (E + p)\mathbf{u} + \bar{u}E\hat{\mathbf{e}}_x$ . The rightmost term in Eq. (5.17) is the so-called *energy production term*, which describes how waves can extract energy from and deposit energy to the background shear flow. The existence of this term means Eq. (5.17) cannot be written in the form of Eq. (5.16). Consequently, energy is not conserved when internal gravity waves propagate in a fluid with a nonuniform background flow, and so it is not appropriate to quantify wave transmission and reflection by examining the redistribution of wave energy in the domain by waves and the background flow.

Unlike energy, *pseudomomentum* is one among a family of so-called “wave activity” quan-

ties that is conserved in a vertically nonuniform background flow (Eliassen and Palm, 1961; Bretherton and Garrett, 1969; Acheson, 1976; Andrews and McIntyre, 1976, 1978b). The expression for the pseudomomentum density  $\mathcal{P}(\mathbf{x}, t)$  corresponding to moderately large amplitude waves restricted to propagate in the  $xz$ -plane was derived by Scinocca and Shepherd (1992) using Hamiltonian fluid mechanics. Extending the Hamiltonian approach to small amplitude three-dimensional disturbances in a Boussinesq fluid, the corresponding expression for the pseudomomentum density [Shaw and Shepherd (2008), integrand of Eq. (3.24)] was found to be

$$\mathcal{P}(\mathbf{x}, t) = -\rho_0 \left[ \frac{1}{2} \frac{d^2 \bar{u}}{dz^2} \xi^2 + \zeta_y \xi \right], \quad (5.18)$$

where  $\zeta_y = (\nabla \times \mathbf{u}) \cdot \hat{\mathbf{e}}_y = \partial u / \partial z - \partial w / \partial x$  is the spanwise component of vorticity. In the limit as  $\bar{u} \rightarrow 0$ , and equivalently in a uniform background shear flow, for which  $d\bar{u}/dz = s_0$  is constant, Eq. (5.18) reduces to the expression for the pseudomomentum density of small amplitude plane internal waves confined to propagate in the  $xz$ -plane [derived using conservation of momentum by Sutherland (2010)], from which the corresponding pseudomomentum is found by averaging over a horizontal wavelength.

Transmission is characterized by the horizontally integrated pseudomomentum density associated with upward-propagating waves, vertically integrated above the reflection level predicted by linear theory, as a fraction of the total pseudomomentum. To distinguish the upward-propagating components of a given wave field, we apply the Hilbert filter (Garnier et al., 2003; Mercier et al., 2008; Gregory and Sutherland, 2010). We denote by  $H^\uparrow$  and  $H^\downarrow$  the Hilbert-filtering operator that extracts the upward- and downward-propagating part of a wave field, respectively, with the property that  $H^\uparrow + H^\downarrow = I$ , where  $I$  is the identity operator. In practice,  $H^\uparrow \eta$  is obtained by Fourier transforming  $\eta$ , and setting the Fourier coefficients to zero in the open half-space  $\mu > 0$ , which contains the spectrum of downward-propagating waves (provided  $k_0 > 0$ , which we always set). The Fourier coefficients with  $\mu = 0$ , corresponding to the vertical mean of  $\eta$ , are multiplied by 1/2. In this way the downward-propagating part of a wave field is equivalent to  $\eta - H^\uparrow \eta$ . With this notation and Eq. (5.18) we define the pseudomomentum density field associated with upward-propagating waves by

$$\mathcal{P}^\uparrow(\mathbf{x}, t) := -\rho_0 \left[ \frac{1}{2} \frac{d^2 \bar{u}}{dz^2} (H^\uparrow \xi)^2 + (H^\uparrow \zeta_y)(H^\uparrow \xi) \right]. \quad (5.19)$$

The transmission coefficient is then defined explicitly by

$$T_{\mathcal{P}}(t) := \frac{1}{\mathcal{P}_0} \int_{z_r}^{z_{\max}} \langle \mathcal{P}^\dagger(\mathbf{x}, t) \rangle dz, \quad (5.20)$$

where  $\mathcal{P}_0$  is the (constant) total pseudomomentum, defined as the integral of Eq. (5.18) over the entire spatial domain, and the angle brackets denote integration over the horizontal domain. The normalization factor  $\mathcal{P}_0$  can in principle be defined at any time  $t$  because pseudomomentum is a conserved quantity. For numerical convenience, the reasons for which are discussed in Sec. 6.6, we set the value of  $\mathcal{P}_0$  at  $t = 0$  as the total pseudomomentum.

---

## Numerical methods

---

The fully nonlinear code described in this chapter was adapted from the one described in Chapter 3. The key modifications were (1) to include the effects of Doppler-shifting of the waves by the background flow; (2) to introduce additional diagnostics to quantify wave transmission; and, (3) to implement an improved method of damping small-scale numerical noise. The focus of this chapter is to provide details on the differences that distinguish this code from the rotation-enabled code described in Chapter 3.

### 6.1 Governing equations

The fully nonlinear code solved the incompressible Euler equations under the Boussinesq approximation, without rotation but with an explicit, height-dependent background flow  $\bar{u}(z)$ . The prognostic equations for the horizontal components of velocity and internal energy conservation (in which vertical displacement is used as a proxy for perturbation mass density) in flux form are given dimensionally by

$$\frac{\partial u}{\partial t} = -\frac{1}{\rho_0} \frac{\partial p}{\partial x} - \nabla \cdot (u\mathbf{u}) - \bar{u} \frac{\partial u}{\partial x} - w \frac{d\bar{u}}{dz}, \quad (6.1)$$

$$\frac{\partial v}{\partial t} = -\frac{1}{\rho_0} \frac{\partial p}{\partial y} - \nabla \cdot (v\mathbf{u}) - \bar{u} \frac{\partial v}{\partial x}, \quad (6.2)$$

$$\frac{\partial \xi}{\partial t} = w - \nabla \cdot (\xi\mathbf{u}) - \bar{u} \frac{\partial \xi}{\partial x}, \quad (6.3)$$

where  $\mathbf{u} = (u, v, w)$  is the velocity vector, and  $\xi$  is vertical displacement, related to perturbation mass density by  $\xi = -\rho/\rho'$ .

The system of equations (6.1)–(6.3) is closed by inclusion of the diagnostic equations for dynamic pressure and vertical velocity:

$$\frac{1}{\rho_0} \nabla^2 p = - \left[ \frac{\partial^2(u^2)}{\partial x^2} + \frac{\partial^2(v^2)}{\partial y^2} + \frac{\partial^2(w^2)}{\partial z^2} \right] - 2 \left[ \frac{\partial^2(uv)}{\partial x \partial y} + \frac{\partial^2(uw)}{\partial x \partial z} + \frac{\partial^2(vw)}{\partial y \partial z} \right] - 2 \frac{d\bar{u}}{dz} \frac{\partial w}{\partial x} - N_0^2 \frac{\partial \xi}{\partial z}, \quad (6.4)$$

$$\frac{\partial w}{\partial z} = - \frac{\partial u}{\partial x} - \frac{\partial v}{\partial y}. \quad (6.5)$$

The only difference between the dynamic pressure equation here and the one with rotation [Eq. (3.4)] is the presence of a linear forcing by the product of background shear and the streamwise gradient of vertical velocity. The diagnostic equation for vertical velocity is equivalent to the incompressibility condition,  $\nabla \cdot \mathbf{u} = 0$ , so that Eqs. (6.4) and (6.5) serve to numerically enforce incompressibility.

## 6.2 Discretization, grid generation, and resolution

The relative scales for space and time variables were set by fixing  $N_0 = 1$  and  $k_0 = 1$  (with arbitrary units of inverse time and inverse length, respectively). The physical domain was triply periodic and of size

$$L_x \times L_y \times L_z = \frac{2\pi}{k_0} n_{w,x} \times \frac{200}{k_0} \times \frac{2\pi}{|m_0|} n_{w,z}, \quad (6.6)$$

where  $n_{w,x}$  and  $n_{w,z}$  are the number of wavelengths initially spanning the streamwise and vertical domains, respectively. These values varied from one simulation to another; typically,  $n_{w,x} = 32$  and  $64$  for small- and moderately large-amplitude simulations, and  $n_{w,z} = 16, 32,$  and  $64$  as the initial relative vertical wavenumber  $m_0/k_0$  increased from strongly to moderately nonhydrostatic. The spanwise domain was specified directly because our coordinate system was oriented such that there was no wave propagation in the spanwise direction. The domain was set to be large enough that self-interaction of the waves across the periodic boundaries would be negligible over the time scales for wave packet reflection and partial transmission; typically,  $t_{\max} = 450/N_0$ .

The physical domain was discretized by specifying 16 and 32 evenly spaced grid points per streamwise and vertical wavelength, respectively, and by  $n_y = 256$  evenly spaced grid points in the spanwise direction. Hence, the physical computational mesh consisted of the set of collocated nodes  $\{x_i\}_{i=0}^{n_x} \times \{y_j\}_{j=0}^{n_y} \times \{z_k\}_{k=0}^{n_z}$ . Values of  $n_x$ ,  $n_y$ , and  $n_z$  for specific simulations are provided in Chapter 7.

Setting  $n_x$ ,  $n_y$ , and  $n_z$  to be powers of two enabled the use of the fast Fourier transform algorithm of Press et al. (2007) (cf. Sec. 3.2). Hence, the Fourier spectral domain was  $\{\kappa_n\}_{n=0}^{1+n_x/2} \times \{\lambda_\ell\}_{\ell=0}^{n_y} \times \{\mu_m\}_{m=0}^{n_z}$ . Under the discrete Fourier transform, the spatial partial differentiation operators are  $\frac{\partial}{\partial x} \rightarrow i\kappa_n$ ,  $\frac{\partial}{\partial y} \rightarrow i\lambda_\ell$ , and  $\frac{\partial}{\partial z} \rightarrow i\mu_m$  [cf. Eqs. (3.6)–(3.8)].

Our use of the fast Fourier transform assumes spatial periodicity of the physical fields. It is natural to question the applicability of the fast Fourier transform to this code given that the background flow is vertically aperiodic. However, because the amplitude of the perturbation fields and their  $x$ -derivatives remain small near the vertical boundaries, products involving these terms and  $\bar{u}$  and  $d\bar{u}/dz$  also remain small near the vertical boundaries. There is therefore no immediate consequence for the applicability of the fast Fourier transform method, although some modifications to the code were needed to account for effects of the background flow, which are described in Sec. 6.4

Rigorous resolution testing was not performed, following the results of the resolution tests performed with the rotation-enabled code (cf. Sec. 6.4). However, enlarged streamwise and vertical domains were needed for larger-amplitude wave packets, which were prone to generate secondary wave packets, and those prone to stronger horizontal dispersion. For all simulations, we attempted to use the highest practical resolution available for an appropriately sized domain.

### 6.3 Initialization

In a stationary, uniformly stratified fluid, it is convenient to initialize small amplitude internal gravity wave fields using the polarization relations, which relate these fields algebraically to a single known wave field (e.g., vertical displacement). The procedure to determine the polarization relations analytically (cf. Appendix A) relies on the fact that the linearized governing

equations have constant coefficients, and so admit wavelike solutions. This is not the case in a fluid with a general height-dependent background flow, in which case approximate or numerical approaches are required in order to determine the vertical structure of a given wave field. Moreover, that approach is valid only for small amplitude waves, and so is particularly poorly suited to initialize the range of small and moderately large amplitude waves we would like to simulate.

A straightforward solution that offers a compromise between the generality of the background flow and ease of derivation and implementation, is to restrict ourselves to a class of idealized background flow profiles, described below, that are effectively zero over some finite depth of the domain. The polarization relations, valid in the region of stationary flow, are then used to initialize the wave fields.

### 6.3.1 Background flow

The background flow profile  $\bar{u}(z)$  was chosen to be zero from  $z_{\min}$  up to just below a specified “shear onset” height,  $z_s$ . Centred at  $z_s$  was a region over which the flow velocity transitioned smoothly over a distance  $L_s$  to a retrograde shear flow increasing linearly in magnitude. Such a profile is described by an integral of a scaled hyperbolic tangent function offset from the  $z$ -axis, with the constant of integration chosen so that the integrated profile tends asymptotically to zero below  $z_s$ . Explicitly, after some manipulation

$$\bar{u}(z) := \frac{sL_s}{2} \left[ \ln \left( 1 + e^{-2(z-z_s)/L_s} \right) + 2 \frac{z - z_s}{L_s} \right]. \quad (6.7)$$

In all simulations, we somewhat arbitrarily fixed  $L_s = 10k_0^{-1}$  and  $z_s = -20k_0^{-1}$ . Shear strength and direction were set by  $s < 0$ . Values of  $|s|$  for specific simulations are provided in Chapter 7. Sample profiles of background flow and corresponding shear for a range of  $|s|$  values are plotted in Fig. 6.1.

### 6.3.2 Perturbation fields

Given the background flow profile Eq. (6.7), all simulations were initialized well below  $z_s$  in physical space with a trivariate Gaussian wave packet whose vertical displacement field was

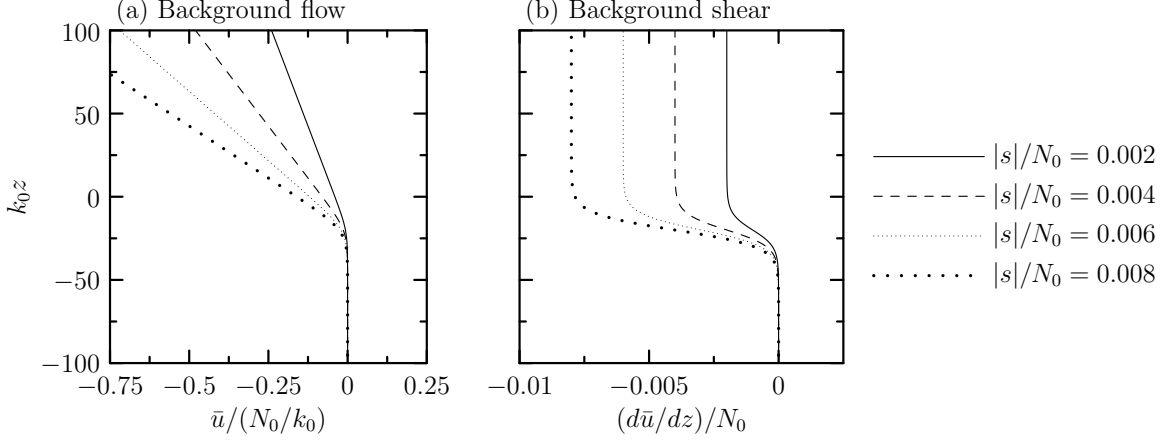


**Figure 6.1:** Sample profiles of background flow and corresponding shear for a range of shear strength parameters  $|s|$  using the default values of  $L_s = 10k_0^{-1}$  and  $z_s = -20k_0^{-1}$ .

prescribed at leading- and first-order to be

$$\xi(\mathbf{x}, 0) = A(\mathbf{x}, 0) \left\{ \cos[k_0 x + m_0(z - z_0)] - \frac{c_{gx0}}{\omega_0} \left( \frac{x}{\sigma_x^2} - \frac{k_0}{m_0} \frac{z - z_0}{\sigma_z^2} \right) \sin[k_0 x + m_0(z - z_0)] \right\},$$

where

$$A(\mathbf{x}, 0) = A_0 \exp \left[ -\frac{1}{2} \left( \frac{x^2}{\sigma_x^2} + \frac{y^2}{\sigma_y^2} + \frac{(z - z_0)^2}{\sigma_z^2} \right) \right] \quad (6.8)$$

was the initial amplitude envelope, in which  $A_0$  is the peak vertical displacement,  $\sigma_x$ ,  $\sigma_y$ , and  $\sigma_z$  are the wave packet extents in the streamwise, spanwise, and vertical directions, respectively, and we somewhat arbitrarily set  $z_0 = -35k_0^{-1}$ . This value was found to be sufficiently far below  $z_s$  that the wave packet was unaffected by the background flow initially.

Using the envelope given by Eq. (6.8), the horizontal components of velocity  $u(\mathbf{x}, 0)$  and  $v(\mathbf{x}, 0)$  were initialized using the polarization relations for  $u_0^{(1)}$  and  $v_0^{(1)}$  from linear Boussinesq theory. The respective expressions are equivalent to those given in the centre column of Table 2.1 with  $f_0 \rightarrow 0$ . The respective  $O(\alpha^1 \epsilon^1)$  corrections,  $u_1^{(1)}$  and  $v_1^{(1)}$ , given in the right column of Table 2.1 with  $f_0 \rightarrow 0$ , were superimposed onto the leading-order fields (cf. Sec. 3.3).

Explicitly,

$$u(\mathbf{x}, 0) = -A(\mathbf{x}, 0) \frac{m_0}{k_0} \left\{ \omega_0 \sin(\varphi_0) + \left[ \frac{x}{\sigma_x^2} \left( 2c_{gx0} - \frac{\omega_0}{k_0} \right) + \frac{z - z_0}{\sigma_z^2} \frac{\omega_0}{k_0} \right] \cos(\varphi_0) \right\},$$

$$v(\mathbf{x}, 0) = -A(\mathbf{x}, 0) \frac{m_0}{k_0} \omega_0 \frac{y}{\sigma_y^2} \cos(\varphi_0).$$

### 6.3.3 Wave-induced mean flow

The predicted initial Bretherton flow was initialized in spectral space, corresponding to Eq. (2.31) with  $f_0 \rightarrow 0$  [cf. Eq. (3.15) of van den Bremer and Sutherland (2018)], and inverse fast Fourier transformed before being superimposed onto the initial horizontal velocity field (Dosser and Sutherland, 2011; van den Bremer and Sutherland, 2014, 2018; Sutherland et al., 2020). The initial Bretherton flow in physical space was predicted to be

$$\begin{bmatrix} u_{\text{BF}} \\ v_{\text{BF}} \end{bmatrix} = \frac{1}{2} N_0 \|\mathbf{k}_0\| \int_{\mathbb{R}^3} \frac{\lambda}{\kappa^2 + \lambda^2} \begin{bmatrix} \lambda \\ -\kappa \end{bmatrix} |\widehat{A}|^2 e^{i\mathbf{k} \cdot (\mathbf{x} - \mathbf{x}_0)} d\kappa d\lambda d\mu, \quad (6.9)$$

where

$$|\widehat{A}|^2 = \frac{1}{8\pi^{3/2}} \sigma_x \sigma_y \sigma_z A_0^2 e^{-(\sigma_x^2 \kappa^2 + \sigma_y^2 \lambda^2 + \sigma_z^2 \mu^2)/4}$$

is the three-dimensional Fourier transform of the square of the initial Gaussian envelope given by Eq. (6.8). The array entries corresponding to the singularity  $\kappa^2 + \lambda^2 = 0$  were overwritten with zeros according to the procedure described in Sec. 3.3.

## 6.4 Advection and temporal advancement

The code advanced the perturbation fields following essentially the same procedure as that described in Sec. 3.4 with modifications, described below, to account for forcings by the nonuniform background flow and its vertical shear.

At a given time step, the code first integrated Eq. (6.5) in spectral space to obtain an intermediate field,  $\widehat{w}_{\mathbf{n}}$ , equivalent to the vertical velocity plus a height-independent term. Explicitly,

$$\widehat{w}_{\mathbf{n}} = \hat{C}_{(n,\ell,0)} + \begin{cases} -\frac{1}{\mu_m} (\kappa_n \hat{u}_{\mathbf{n}} + \lambda_\ell \hat{v}_{\mathbf{n}}), & \mu_m \neq 0 \\ 0, & \mu_m = 0, \end{cases}$$

where  $\hat{C}_{(n,\ell,0)}$  arose in the intermediate solution due to the nonzero background flow. In physical space,  $C(x, y)$  manifested as unphysical small amplitude ‘columns’ of constant vertical velocity spanning the height of the domain. These were efficiently removed by inverse fast Fourier transforming the intermediate field  $\widehat{w}_{\mathbf{n}}$ , subtracting the bottom boundary value column-wise from the physical solution, and fast Fourier transforming the result:  $\hat{w}_{\mathbf{n}} = \widehat{w}_{\mathbf{n}} - \hat{C}_{(n,\ell,0)}$ . This

procedure incurred little additional computational cost compared to the calculation of  $\hat{w}_{\mathbf{n}}$  described in Sec. 3.4, as the physical field [after subtraction of  $C(x, y)$ ] was retained for the calculation of the nonlinear terms in the dynamic pressure calculation.

The Fourier-transformed right-hand side of the Poisson equation for dynamic pressure, Eq. (6.4), is given by

$$\begin{aligned} \hat{F}_p = & \kappa_n^2 (\widehat{u^2})_{\mathbf{n}} + \lambda_\ell^2 (\widehat{v^2})_{\mathbf{n}} + \mu_m^2 (\widehat{w^2})_{\mathbf{n}} + 2 \left[ \kappa_n \lambda_\ell (\widehat{uv})_{\mathbf{n}} + \kappa_n \mu_m (\widehat{uw})_{\mathbf{n}} + \lambda_\ell \mu_m (\widehat{vw})_{\mathbf{n}} \right] \\ & + 2i\kappa_n (\widehat{\bar{u}'w})_{\mathbf{n}} + iN_0^2 \mu_m \hat{\xi}_{\mathbf{n}}. \end{aligned}$$

The quadratically nonlinear terms were computed by convolution using the procedure described in Sec. 3.4. Similarly, the shear term  $(\widehat{\bar{u}'w})_{\mathbf{n}}$  was computed by inverse fast Fourier transforming  $\hat{w}_{\mathbf{n}}$  in the vertical only, multiplying  $\bar{u}'(z_k) \hat{w}_{(n,\ell)}(z_k)$  entry-wise, and fast Fourier transforming the result with respect to  $z$ . The expression for the dynamic pressure field (divided by  $\rho_0$ ) was identical to Eq. (3.11), and so is not reproduced here.

Using the diagnostic fields, the code computed the time derivatives of the prognostic fields,  $\dot{\hat{u}}_{\mathbf{n}}$ ,  $\dot{\hat{v}}_{\mathbf{n}}$ , and  $\dot{\hat{\xi}}_{\mathbf{n}}$ , according to the Fourier-transformed right-hand sides of Eqs. (6.1)–(6.3). Explicitly,

$$\dot{\hat{u}}_{\mathbf{n}} = -i\kappa_n \frac{\hat{p}_{\mathbf{n}}}{\rho_0} - i \left[ \kappa_n (\widehat{u^2})_{\mathbf{n}} + \lambda_\ell (\widehat{uv})_{\mathbf{n}} + \mu_m (\widehat{uw})_{\mathbf{n}} \right] - i\kappa_n (\widehat{\bar{u}u})_{\mathbf{n}} - (\widehat{\bar{u}'w})_{\mathbf{n}}, \quad (6.10)$$

$$\dot{\hat{v}}_{\mathbf{n}} = -i\lambda_\ell \frac{\hat{p}_{\mathbf{n}}}{\rho_0} - i \left[ \kappa_n (\widehat{uv})_{\mathbf{n}} + \lambda_\ell (\widehat{v^2})_{\mathbf{n}} + \mu_m (\widehat{vw})_{\mathbf{n}} \right] - i\kappa_n (\widehat{\bar{u}v})_{\mathbf{n}}, \quad (6.11)$$

$$\dot{\hat{\xi}}_{\mathbf{n}} = \hat{w}_{\mathbf{n}} - i \left[ \kappa_n (\widehat{u\xi})_{\mathbf{n}} + \lambda_\ell (\widehat{v\xi})_{\mathbf{n}} + \mu_m (\widehat{w\xi})_{\mathbf{n}} \right] - i\kappa_n (\widehat{\bar{u}\xi})_{\mathbf{n}}, \quad (6.12)$$

where the products of perturbation fields and  $\bar{u}$  and  $\bar{u}'$  were computed using the convolution procedure described above, and quadratically nonlinear products of perturbation fields were retained from the pressure calculation step.

The perturbation fields were advanced in time using the third-order Williamson–Runge–Kutta scheme described in Sec. 3.4. For all simulations, the time step was set to  $\Delta t = 0.05N_0^{-1}$ . A small number of test simulations performed with a time step of  $0.025N_0^{-1}$  resulted in no significant qualitative or quantitative changes to the reference solutions.

## 6.5 Dealiasing

When computing the quadratic products of perturbation fields on a discrete mesh, features below a certain resolvable lengthscale (i.e., above a certain wavenumber) are *aliased* onto longer-wavelength parts (i.e., lower-wavenumber modes) of the resulting field. This manifests as an unphysical accumulation of power at high wavenumbers in the Fourier spectra of the transformed products. In order to maintain numerical stability, the spectral amplitudes of such high-wavenumber components must be damped. The code described in Chapter 3 attempted to achieve this through viscous damping and thermal diffusivity, following the success of that approach in previous studies of wave packet evolution (e.g., [Dosser and Sutherland, 2011](#); [Gervais et al., 2018](#)). During development of the code described here, viscous damping and thermal diffusivity were determined to be less effective in three dimensions than in one and two dimensions. This was revealed in test simulations of moderately large amplitude waves which tended to overturn unphysically prior to reflection and partial transmission.

A significant improvement was to implement a certain dealiasing filter, following the suggestion of postdoctoral researcher Dr. David Deepwell. In particular, after computing the right-hand sides of Eqs. (6.10)–(6.12) the code applied a filter that damped exponentially the amplitudes of Fourier modes with wavenumbers greater than a specified cutoff wavenumber ([Godon and Shaviv, 1993](#); [Subich et al., 2013](#); [Boyd, 2001](#)). Explicitly, the filter is defined (in the streamwise direction without loss of generality) by

$$\chi(\kappa_n) = \begin{cases} 1, & |\kappa_n| < \kappa_{\text{cut}}, \\ \exp \left[ -\alpha \left( \frac{|\kappa_n| - \kappa_{\text{cut}}}{\kappa_{\text{nyq}} - \kappa_{\text{cut}}} \right)^\beta \right], & |\kappa_n| \geq \kappa_{\text{cut}}, \end{cases} \quad (6.13)$$

where  $\alpha$  and  $\beta$  are the filter strength and filter order, respectively, and  $\kappa_{\text{nyq}} = \pi/\Delta x$  and  $\kappa_{\text{cut}}$  are the Nyquist and cutoff wavenumbers, respectively. For all simulations, the filter parameters were fixed at the default values of  $\alpha = 20$ ,  $\beta = 2$ , and  $\kappa_{\text{cut}} = 0.6\kappa_{\text{nyq}}$  described by [Subich et al. \(2013\)](#). In practice the filter Eq. (6.13) was applied in the  $\kappa$ ,  $\lambda$ , and  $\mu$  directions, i.e.,  $\chi_{\mathbf{n}} = \chi(\kappa_n)\chi(\lambda_\ell)\chi(\mu_m)$ , with  $\lambda_{\text{cut}} = 0.6\lambda_{\text{nyq}} = 0.6\pi/\Delta y$  and  $\mu_{\text{cut}} = 0.6\mu_{\text{nyq}} = 0.6\pi/\Delta z$ . A small number of test simulations were performed with  $\alpha = 40$  and  $\beta = 4$ . Results were qualitatively and quantitatively indistinguishable from those of reference simulations.

## 6.6 Transmission diagnostics

Transmission is quantified by the horizontally integrated pseudomomentum corresponding to upward-propagating waves, vertically integrated above the reflection level. The upward- (downward-) propagating components of a given wave field correspond to the half of the Fourier spectrum with  $\mu < 0$  ( $\mu > 0$ ), and are straightforwardly extracted using the Hilbert filter (Garnier et al., 2003; Mercier et al., 2008; Gregory and Sutherland, 2010), denoted here by  $H^\uparrow$  ( $H^\downarrow$ ; cf. Sec. 5.5). However, the upward- and downward-propagating components each also contain one half of the vertical mean component (corresponding to  $\mu = 0$ ), necessary in order to completely reconstruct a given wave field from the respective subsets of its spectrum. Explicitly, the Hilbert filter that extracts the upward-propagating part of a given field  $\eta$  is defined by

$$H^\uparrow\eta(x_i, y_j, z_k) := \mathcal{F}^{-1}\left[\frac{1}{2}\hat{\eta}_{(n,\ell,0)} + \hat{\eta}_{(n,\ell,m)}\right], \quad \mu_m < 0,$$

where  $\mathcal{F}^{-1}$  denotes the inverse fast Fourier transform. The downward-propagating part of a wave field may be found directly by  $H^\downarrow\eta = \eta - H^\uparrow\eta$ .

Using the Hilbert-filtered fields  $H^\uparrow\xi$  and  $H^\uparrow\zeta_y$ , the upward-propagating pseudomomentum density field  $\mathcal{P}^\uparrow(\mathbf{x}, t)$  was computed using Eq. (5.19). The horizontal integral of this quantity, denoted by angle brackets, is found according to

$$\langle \mathcal{P}^\uparrow \rangle = L_x L_y \text{Re}\{\mathcal{F}_{xy}[\mathcal{P}^\uparrow]_{(0,0)}\}, \quad (6.14)$$

where  $\mathcal{F}_{xy}$  denotes the fast Fourier transform with respect to  $x$  and  $y$  only. It is particularly convenient to formulate the horizontal integral using Eq. (6.14) because the real part of the  $(n, \ell) = (0, 0)$  Fourier mode encodes the horizontal mean value of the field at a given height  $z_k$ .

The vertical integral of Eq. (6.14) above the reflection level was computed in physical space using a composite Simpson's rule (e.g., Allen and Isaacson, 1998). In practice, for convenience each partial sum  $S_k$  was taken over three successive vertical grid points, i.e.,

$$\int_{z_k}^{z_{k+2}} \langle \mathcal{P}^\uparrow \rangle dz \approx S_k = \frac{2\Delta z}{6} [\langle \mathcal{P}^\uparrow \rangle_k + 4\langle \mathcal{P}^\uparrow \rangle_{k+1} + \langle \mathcal{P}^\uparrow \rangle_{k+2}],$$

with  $k$  iterating by two from the nearest even-indexed grid point above  $z_r$  up to  $n_z - 2$ . A linear interpolation was used to estimate the partial sum over the subinterval of height  $2\Delta z$  containing  $z_r$ . Iterating  $k$  by two effectively reduced the order of accuracy from  $O(\Delta z^5)$  to  $O((2\Delta z)^5)$ . The absolute error on each subinterval  $[z_k, z_{k+2}]$  was bounded theoretically by  $\frac{32}{90}\Delta z^5 |d^4\langle\mathcal{P}^\dagger\rangle/dz^4|$ , which was anticipated to remain small despite the reduction of accuracy. Finally, the transmission coefficient  $T_{\mathcal{P}}$  was found by normalizing the result of the vertical integration described above by the total pseudomomentum  $\mathcal{P}_0$  according to Eq. (5.20).

### 6.6.1 Pseudomomentum conservation

In theory,  $\mathcal{P}_0$  is conserved for small amplitude wave packets propagating in a height-dependent background flow. In practice, however, small numerical errors accumulate and cause the total pseudomomentum to deviate from its initial value as a simulation advances. In order to quantify this discrepancy, we define the relative pseudomomentum error as a function of time by

$$\mathcal{P}_{\text{err}}(t) := \left| 1 - \frac{\mathcal{P}_{\text{tot}}(t)}{\mathcal{P}_0} \right| \times 100\%.$$

Here,

$$\mathcal{P}_{\text{tot}}(t) = \int_V \mathcal{P}(\mathbf{x}, t) dx dy dz$$

is the pseudomomentum density at a given time  $t$  integrated over the volume  $V$  of the physical domain using the methods described above, and  $\mathcal{P}_0 := \mathcal{P}_{\text{tot}}(0)$ . We somewhat heuristically set a confidence threshold of  $\mathcal{P}_{\text{err}} < 1\%$  and assume simulation results are reliable provided the relative pseudomomentum error is within this tolerance. In practice, this tolerance was typically met over times  $N_0 t \lesssim 400$ , during which reflection and quasisteady final transmission were established.

---

## Results and discussion

---

In this chapter we present the results of fully nonlinear numerical simulations with the intent ultimately to quantify the transmission of localized wave packets above the reflection level predicted by linear theory for the background flow profile prescribed by Eq. (6.7), and to explain the mechanisms driving their linear and nonlinear evolution. Numerical simulations evolved wave packets with initial amplitudes between  $A_0 = 0.01k_0^{-1} \approx 0.0016\lambda_{x0}$  and  $A_0 = 0.55k_0^{-1} \approx 0.0875\lambda_{x0}$ , and initial relative vertical wavenumbers between  $m_0 = -0.4k_0$  and  $-1.4k_0$ , thus spanning a range of small to moderately large amplitude nonhydrostatic wave packets propagating upward and rightward at angles between  $\Theta_0 = 22^\circ$  and  $54^\circ$  initially. The choice of shear strength parameter  $s$  was set somewhat heuristically by the initial relative vertical wavenumber such that waves were predicted by linear theory to reflect in the range  $50 \lesssim (z_r - z_0)k_0 \lesssim 70$ . This range was deemed to be far enough above  $z_0$  for the waves to begin evolving nonlinearly prior to reflection, and far enough below the top boundary for reflected and transmitted waves to remain within the domain for the duration of the simulation. Our investigation focused on initially round wave packets, for which we fixed  $\sigma_x = \sigma_y = \sigma_z = 10k_0^{-1}$ . A total of 38 simulations were performed. The domain and initialization parameters of the subset of simulations explicitly discussed in-text are summarized in Table 7.1.

ID	$A_0 k_0$	$\frac{A_0}{A_{\text{RP}}}$	$\frac{A_0}{A_{\text{SW}}}$	$\frac{ s }{N_0}$	$ \frac{m_0}{k_0} $	$\Theta_0$	$L_x k_0 \times L_z k_0$	$n_x \times n_z$	$(z_r - z_0)k_0$	$t_r N_0$
S1	0.01	0.03	—	0.002	0.4	22°	201.1 × 253.1	512 × 512	50.76	248
S2	0.28	0.95	—	0.002	0.4	22°	402.1 × 502.7	1024 × 1024	50.76	248
S3	0.40	1.02	1.07	0.004	0.7	35°	402.1 × 287.2	1024 × 1024	60.19	214
S4	0.45	1.01	1.08	0.006	1.0	45°	402.1 × 201.1	1024 × 1024	63.82	208
S5	0.50	1.07	1.21	0.008	1.4	54°	402.1 × 287.2	1024 × 2048	67.35	227

**Table 7.1:** Initial conditions, domain size and resolution, and predicted reflection height and time for the simulations discussed in-text. Columns are: simulation ID, initial peak vertical displacement amplitude nondimensionalized by the streamwise wavenumber  $k_0$  and as a fraction of the predicted amplitudes for reflection level penetration and secondary wave generation [ $A_{\text{RP}}$  and  $A_{\text{SW}}$ , given by Eqs. (5.10) and (5.15), respectively], shear strength parameter  $|s|/N_0$ , initial absolute relative vertical wavenumber  $|m_0/k_0|$  and corresponding  $\Theta_0 = \tan^{-1} |m_0/k_0|$ , streamwise  $\times$  vertical domain size  $L_x k_0 \times L_z k_0$  and resolution  $n_x \times n_z$ , height of the reflection level predicted by linear theory above the wave packet initial position,  $(z_r - z_0)k_0$ , and reflection time  $t_r N_0$  predicted by linear theory. All simulations used a spanwise domain of width  $L_y k_0 = 200$  resolved by  $n_y = 256$  grid points.

## 7.1 Evolution of strongly nonhydrostatic wave packets

We examine first the evolution of a small amplitude Gaussian wave packet with  $m_0 = -0.4k_0$ , and describe its partial transmission above and reflection below the reflection level predicted by linear theory. We then examine moderately large amplitude wave packets, with an emphasis on their nonlinear evolution, and the effects of amplitude on transmission.

### 7.1.1 Small amplitude wave packet: Linear evolution

Snapshots of streamwise velocity  $\tilde{u} = u/\max\{u(\mathbf{x}, 0)\}$  through the  $y = 0$  plane of a small amplitude wave packet with  $A_0 = 0.01k_0^{-1}$  and  $m_0 = -0.4k_0$  (simulation S1 in Table 7.1) are shown in Fig. 7.1. The times shown in each panel are representative of the wave packet at early, prereflection, postreflection, and late times. Profiles of the background flow and its shear used in this simulation are plotted as the solid curves in Fig. 6.1.

Initially [Fig. 7.1(a)] the lines of constant phase were oriented at  $\Theta_0 \approx 22^\circ$  from the vertical, and the wave packet propagated upward and rightward at this angle in agreement with linear theory. Upward propagation was confirmed by the overlap between the profiles of  $\langle \tilde{\mathcal{P}}^\uparrow \rangle$  and  $\langle \tilde{\mathcal{P}} \rangle$ . At  $t = 150/N_0$  [Fig. 7.1(b)], the leading flank of the wave packet had propagated into the

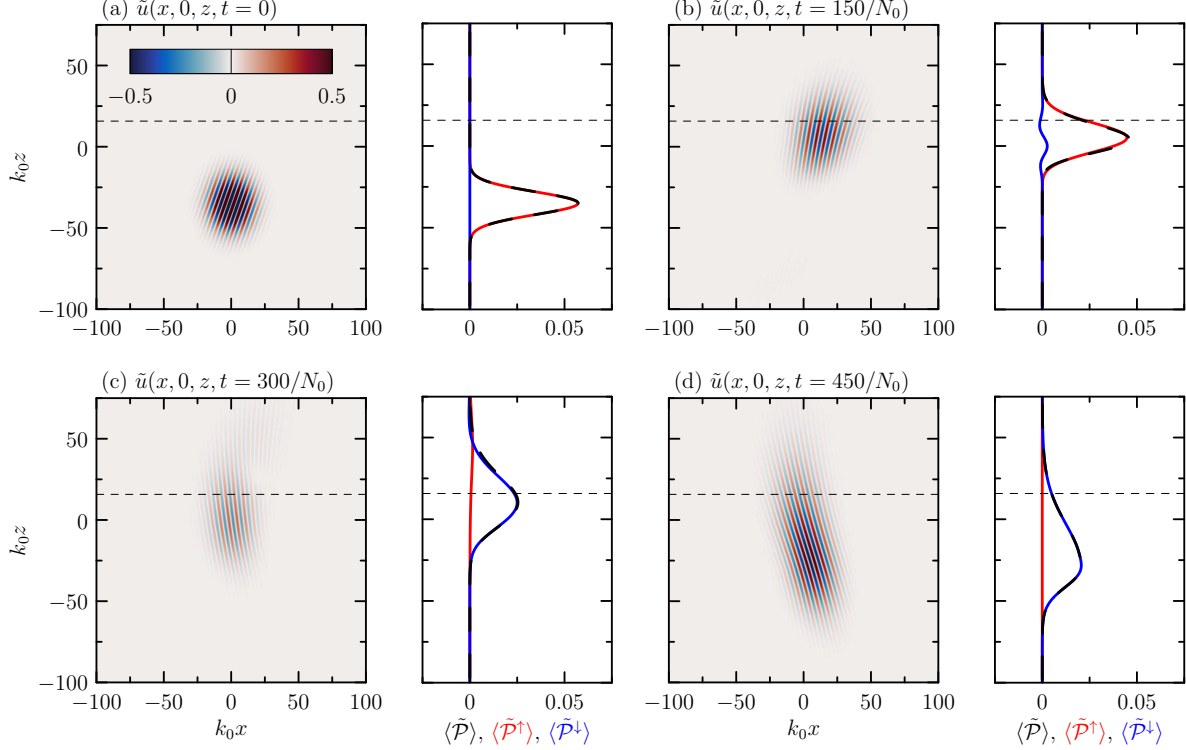


**Figure 7.1:** Cross sections of streamwise velocity  $\tilde{u} = u / \max\{u(\mathbf{x}, 0)\}$  through the vertical plane  $y = 0$  of a small amplitude wave packet with  $A_0 = 0.01k_0^{-1}$  and  $m_0 = -0.4k_0$  (simulation S1 in Table 7.1). The corresponding right panels show vertical profiles of horizontally integrated pseudomomentum density normalized by  $k_0\mathcal{P}_0$ . The red and blue curves are of the upward- and downward-propagating parts,  $\langle \tilde{\mathcal{P}}^\uparrow \rangle$  and  $\langle \tilde{\mathcal{P}}^\downarrow \rangle = \langle \tilde{\mathcal{P}} \rangle - \langle \tilde{\mathcal{P}}^\uparrow \rangle$ , respectively, in which  $\langle \tilde{\mathcal{P}} \rangle$  is the total distribution (dashed black curves). Image resolution was doubled in postprocessing, and images were cropped to focus on the region containing the wave packet. The horizontal dashed line in each panel indicates the height of the reflection level,  $z_r = 15.76k_0^{-1}$ , predicted by linear theory.

background shear flow, and the lines of constant phase were more strongly oriented toward the vertical in response to the increased Doppler-shifted frequency. A relatively small amount of downward-propagating pseudomomentum  $\langle \tilde{\mathcal{P}}^\downarrow \rangle$  accumulated below  $z_r$ , indicating reflection began well before the time  $t_r = 248/N_0$  predicted by linear theory. The vertical extent of  $\langle \tilde{\mathcal{P}} \rangle$  broadened due to linear dispersion, and its peak value decreased as a consequence of pseudomomentum conservation. At  $t = 300/N_0$  [Fig. 7.1(c)], much of the wave packet had reflected and began propagating downward, indicated by the overlap between the profiles of  $\langle \tilde{\mathcal{P}}^\downarrow \rangle$  and  $\langle \tilde{\mathcal{P}} \rangle$ . At  $t = 450/N_0$  [Fig. 7.1(d)] the bulk of the wave packet propagated downward. The wave packet vertical group speed increased slightly as the leading flank of the wave packet propagated into the region with effectively constant  $|\bar{u}|$  (hence as  $\Omega$  decreased toward  $\omega_0$ ). This acceleration is evident in the overlapping profiles of  $\langle \tilde{\mathcal{P}}^\downarrow \rangle$  and  $\langle \tilde{\mathcal{P}} \rangle$ , manifesting as

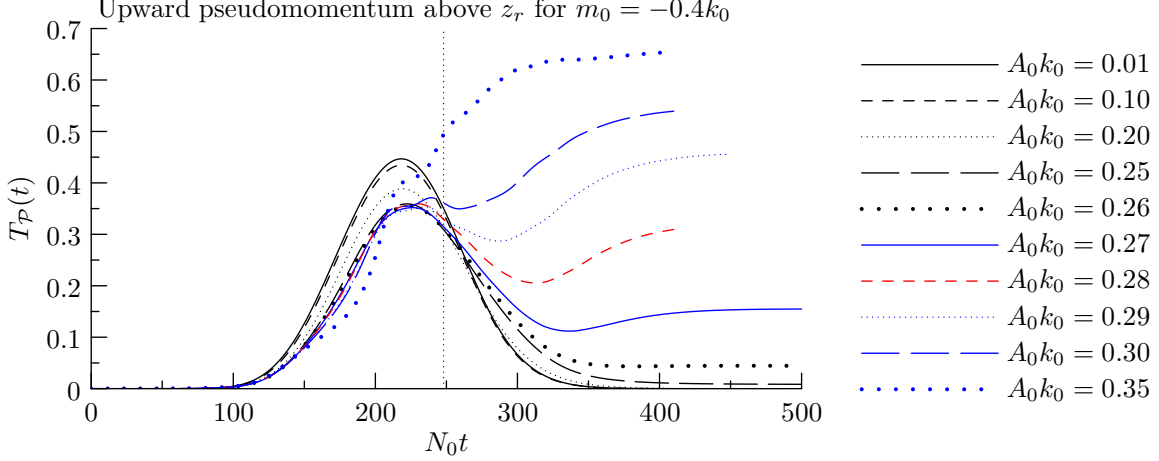


**Figure 7.2:** Time series of upward-propagating pseudomomentum above  $z_r$ , where  $T_{\mathcal{P}}(t)$  is given by Eq. (5.20), for the subset of simulations performed with  $m_0 = -0.4k_0$ . The vertical dotted line indicates the time  $N_0 t_r = 248$  at which reflection was predicted by linear theory. Data are plotted either to the end time of their respective simulations, or until the first time a relative pseudomomentum error of  $\mathcal{P}_{\text{err}} \geq 1\%$  was diagnosed, whichever occurred earlier.

the relatively steep vertical gradient along the leading (lowermost) flank of the wave packet compared to that along the trailing flank.

A time series of upward-propagating pseudomomentum above  $z_r$  for this simulation is shown as the solid black curve in Fig. 7.2. This time series reveals there was a transient penetration of pseudomomentum above  $z_r$  beginning shortly after  $t = 100/N_0$ , peaking at  $t^* = 218/N_0$  before the predicted reflection time of  $t_r = 248/N_0$ . At late times,  $t \gtrsim 350/N_0$ , negligible pseudomomentum remained above the reflection level.

### 7.1.2 Moderately large amplitude wave packet: Transmission, reflection, and secondary wave generation

Moderately large amplitude wave packets are nonnegligibly influenced by nonlinear interactions with their induced mean (Bretherton) flow. Snapshots of the evolution of one such wave packet with  $A_0 = 0.28k_0^{-1}$  and  $m_0 = -0.4k_0$  (S2) are shown in Fig. 7.3. The streamwise velocity field shown is decomposed into  $O(|A|)$  contributions,  $\tilde{u}^{(1)}$ , and  $O(|A|^2)$  contributions,  $\tilde{u}^{(2)}$ , using Eqs. (5.12a) and (5.12b), respectively.

Initially, the velocity fields  $\tilde{u}$  and  $\tilde{u}^{(1)}$  are nearly identical [Fig. 7.3(a,b)], and  $\tilde{u}^{(2)} = u_{\text{BF}}$ , whose Gaussian structure is shown clearly in Fig. 7.3(c). Nonlinearity was evident at  $t = 150/N_0$ , indicated by the anticipated steepening (flattening) of phase lines above (below) the

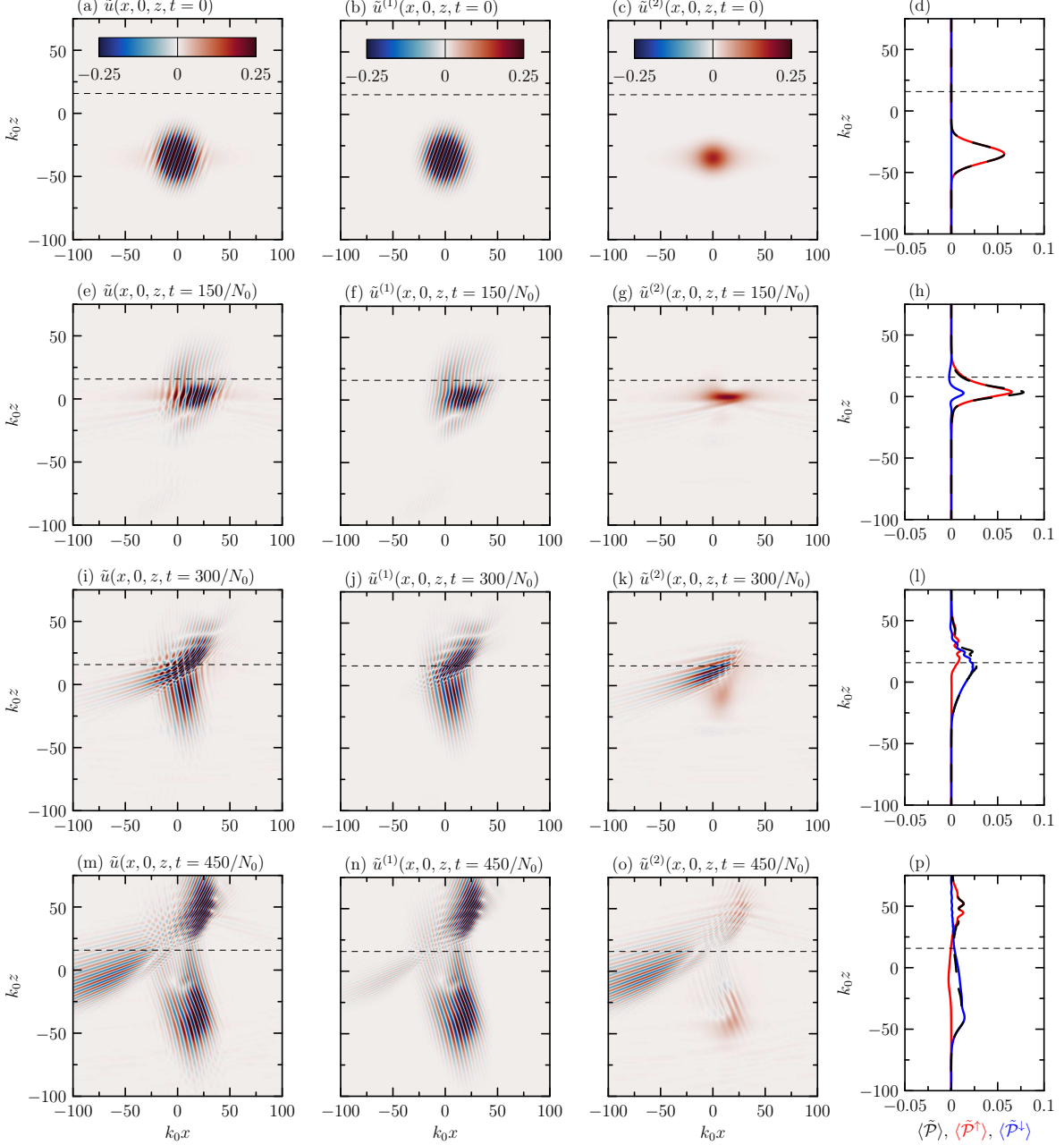


**Figure 7.3:** As in Fig. 7.1 but for a moderately large amplitude wave packet with  $A_0 = 0.28k_0^{-1}$  (S2). The three leftmost columns are of, respectively: total streamwise velocity  $\tilde{u}$ , and its constituent  $O(|A|)$  and  $O(|A|^2)$  parts, denoted by  $\tilde{u}^{(1)}$  and  $\tilde{u}^{(2)}$ , respectively, given by Eqs. (5.12a) and (5.12b), respectively. The dashed line in each panel indicates the height of the reflection level,  $z_r = 15.76k_0^{-1}$ , predicted by linear theory.

centre of the wave packet, located near  $z = 0$  [Fig. 7.3(e,f); cf. the discussion in Sec. 4.1]. The vertical extent of the Bretherton flow narrowed and its amplitude grew [Fig. 7.3(g)] as a consequence of modulational instability. This behaviour is similar to that observed in simulations of one-dimensional Gaussian wave packets (Sutherland, 2001, 2006b; Dosser and

ID	$N_0 t$	Transmitted (or incident)			Reflected			Secondary			TRI
		$k_{\{t,i\}}/k_0$	$m_{\{t,i\}}/k_0$	$\omega_{\{t,i\}}/N_0$	$k_r/k_0$	$m_r/k_0$	$\omega_r/N_0$	$ k_s^{(2)} /k_0$	$m_s^{(2)}/k_0$	$\omega_s^{(2)}/N_0$	
S2	300	1.34	-1.20	0.75	0.95	0.20	0.98	0.36	-1.34	0.26	yes
S3	150	1.05	-0.57	0.88	1.00	0.13	0.99	0.16	0.68 <sup>a</sup>	0.22	no
S4	150	1.00	-0.72	0.81	1.03	0.16	0.99	0.27	0.84 <sup>a</sup>	0.30	no
S5	200	1.00	-0.77	0.79	1.03	0.39	0.93	0.25	0.83 <sup>a</sup>	0.29	no

<sup>a</sup> Secondary waves identified are those propagating downward and rightward, assuming TRI between incident and reflected waves (transmitted waves not yet present).

**Table 7.2:** Data used to diagnose triadic resonant instability (TRI) for a given simulation and time. Centre columns: streamwise and vertical Fourier modes corresponding to the spectral peak of transmitted (or incident) and reflected wave packets  $[(k_{\{t,i\}}, m_{\{t,i\}}) = \mathbf{k}_{\{t,i\}}$  and  $(k_r, m_r) = \mathbf{k}_r$ , respectively], and their corresponding frequencies,  $\omega_{\{t,i\}} = \omega(\mathbf{k}_{\{t,i\}})$  and  $\omega_r = \omega(\mathbf{k}_r)$ , diagnosed from the power spectrum of the linear wave field  $u^{(1)}$ . Centre-right column: Fourier modes corresponding to the spectral peak of secondary wave packets diagnosed from the power spectrum of the quadratically nonlinear wave field  $u^{(2)}$   $[(k_s^{(2)}, m_s^{(2)}) = \mathbf{k}_s^{(2)}]$ , and corresponding frequency,  $\omega_s^{(2)} = \omega(\mathbf{k}_s^{(2)})$ . The rightmost column indicates whether TRI is suspected as the cause of the secondary waves according to the criteria in Sec. 5.4.1.

Sutherland, 2011), as one might anticipate on account of the vertically analogous structures of one- and three-dimensional wave-induced mean flows. Although at  $t = 150/N_0$  the bulk of the wave packet had not yet propagated to the reflection level, reflection had nonetheless begun, as indicated by the region of nonzero  $\langle \tilde{\mathcal{P}}^\downarrow \rangle$  [blue curve in Fig. 7.3(h)] below  $z_r$ .

At  $t = 300/N_0$ , the wave packet exhibited three distinct features [Fig. 7.3(i)]: a transmitted wave packet propagated upward and to the right above  $z_r$ ; a reflected wave packet propagated downward; and an asymmetric upward-propagating *secondary wave packet* radiated toward the left, with phase lines approximately perpendicular to those of the reflected wave packet. The reflected wave packet in Fig. 7.3(j) broadened in vertical extent, in a similar manner as in the small amplitude simulation, S1, indicating that linear dynamics continued to play an important role at this stage of wave packet evolution. The secondary waves are shown in Fig. 7.3(k), superimposed with the mean flow induced by the reflecting wave packet. The profile of  $\langle \tilde{\mathcal{P}}^\downarrow \rangle$  corresponding to the latter accounted for most of the total pseudomomentum below  $z_r$ . At  $t = 450/N_0$ , the three wave packets had separated [Fig. 7.3(m)]. In particular, the transmitted wave packet penetrated well above  $z_r$ , being associated with  $\langle \tilde{\mathcal{P}}^\uparrow \rangle$  within the region  $25 \lesssim k_0 z \lesssim 75$  [Fig. 7.3(p)].

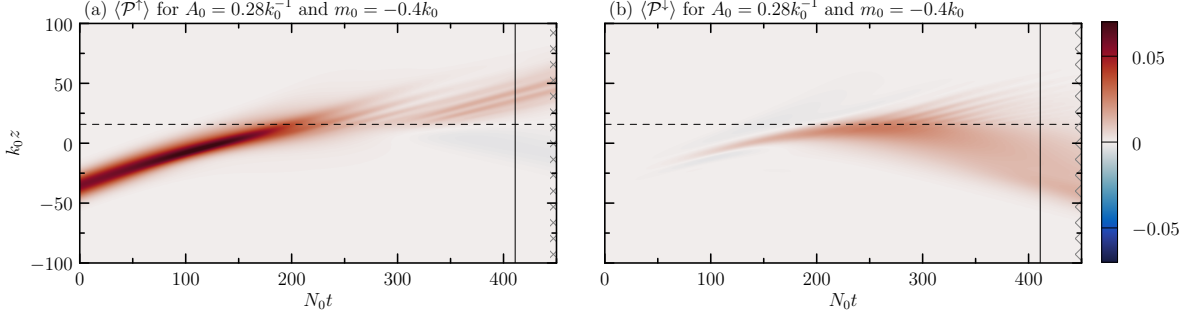


**Figure 7.4:** Vertical time series of (a)  $\langle \tilde{\mathcal{P}}^\uparrow \rangle$  and (b)  $\langle \tilde{\mathcal{P}}^\downarrow \rangle$  for simulation S2. Image resolution was doubled in postprocessing. The horizontal dashed line indicates the height of the reflection level  $z_r = 15.76k_0^{-1}$  predicted by linear theory, the vertical line indicates the first time,  $t = 411/N_0$ , at which  $\mathcal{P}_{\text{err}} \geq 1\%$ , and crosshatching indicates the time  $t \geq 444/N_0$  for which  $\mathcal{P}_{\text{err}} \geq 5\%$ .

That the secondary waves in Fig. 7.3 existed at  $O(|A|^2)$  indicates they were generated nonlinearly. In particular, we find these to have been generated by triadic resonant instability between the transmitted and reflected wave packets. The wavenumber vectors and frequencies corresponding to the respective wave packets are included in Table 7.2. The predicted and diagnosed spectral peaks  $\mathbf{k}_s$  and  $\mathbf{k}_s^{(2)}$ , and corresponding frequencies  $\omega_s$  and  $\omega_s^{(2)}$ , agreed to within 95%. Crucially, the secondary waves were generated by nonbreaking primary waves, as we confirmed by evaluating the overturning condition, Eq. (2.35), through the duration of the simulation:  $\min\{N_T^2\} \gtrsim 0.8N_0^2$ , in which  $N_T^2 = N_0^2(1 - \partial\xi/\partial z)$ .

A time series of upward-propagating pseudomomentum above  $z_r$  for S2 is plotted as the dashed red curve in Fig. 7.2. The time series shows a peak at  $t^* \approx 230/N_0$ . Unlike the small amplitude simulation (S1), transmission in S2 decreased until  $t = 313/N_0$ , after which transmission increased once more. Transmission started tending toward a fixed value as the bulk of the transmitted wave packet penetrated above  $z_r$ .

Vertical time series of  $\langle \tilde{\mathcal{P}}^\uparrow \rangle$  and  $\langle \tilde{\mathcal{P}}^\downarrow \rangle$  for S2 are shown in Figs. 7.4(a) and 7.4(b), respectively. Modulational instability is evident by the increased peak value of  $\langle \tilde{\mathcal{P}}^\uparrow \rangle$  and the slightly narrowed vertical extent of the wave packet. From  $t \approx 200/N_0$  onward, transmitted waves propagate upward with approximately fixed vertical group speed.

### 7.1.3 Amplitude dependence of transmission

Time series of upward-propagating pseudomomentum above  $z_r$  for strongly nonhydrostatic wave packets with  $m_0 = -0.4k_0$  and initial amplitudes ranging from small ( $A_0 = 0.01k_0^{-1} \approx$

$0.03A_{\text{RP}} \approx 0.04A_{\text{SW}}$ ) to moderately large ( $A_0 = 0.35k_0^{-1} \approx 1.19A_{\text{RP}} \approx 1.34A_{\text{SW}}$ ) are shown in Fig. 7.2. As initial amplitude increased, three trends emerged: (1) the onset of upward pseudomomentum penetration above  $z_r$  and the time of peak transmission were delayed; (2) for  $A_0 \leq 0.28k_0^{-1}$ , the wave packets exhibited an increasing, then decreasing, transmission above  $z_r$ , but for  $A_0 > 0.28k_0^{-1}$ , transmission increased again; and, (3) at late times, the transmission remained nonzero for  $A_0 \geq 0.25k_0^{-1}$ .

The delayed onset and peak times of pseudomomentum penetration above  $z_r$  were due to modulational instability acting to retard the vertical advance of the incident wave packets. The observed post-first peak decreases of transmission corresponded to downward transport of pseudomomentum by the reflected wave packets, and the subsequent increases resulted from the upward propagation of transmitted primary, and eventually radiated secondary, wave packets. Decreasing peak transmission with initial amplitude up to  $A_0 = 0.28k_0^{-1}$  was due to the radiation of progressively larger-amplitude secondary waves below  $z_r$ , which retained at least some of their pseudomomentum below  $z_r$  until after primary wave transmission had peaked. The trend reversed for wave packets with initial amplitudes  $A_0 \geq 0.29k_0^{-1} \approx 0.99A_{\text{RP}} \approx 1.11A_{\text{SW}}$ .

## 7.2 Evolution of moderately nonhydrostatic wave packets

Here we examine the evolution of moderately large amplitude wave packets initialized with  $m_0 = -0.7k_0$  (S3),  $-k_0$  (S4), and  $-1.4k_0$  (S5). The simulations were chosen such that their initial amplitudes were greater than both the predicted amplitudes for reflection level penetration,  $A_{\text{RP}}$ , and secondary wave generation,  $A_{\text{SW}}$ , given by Eqs. (5.10) and (5.15), respectively.

A snapshot of the streamwise velocity through the  $y = 0$  plane from S3 ( $A_0 = 0.4k_0^{-1}$ ) at  $t = 200/N_0$  is shown in Fig. 7.5(a). Like S2, upward-propagating secondary waves were radiated leftward, possibly as a result of triadic resonant instability (TRI) between the transmitted and reflected wave packets, although this was not diagnosed. Unlike S2, *downward-* and *rightward-propagating* secondary waves were also radiated by the incident wave packet, existing at  $t = 200/N_0$  as a distinct secondary wave packet with broad streamwise extent,

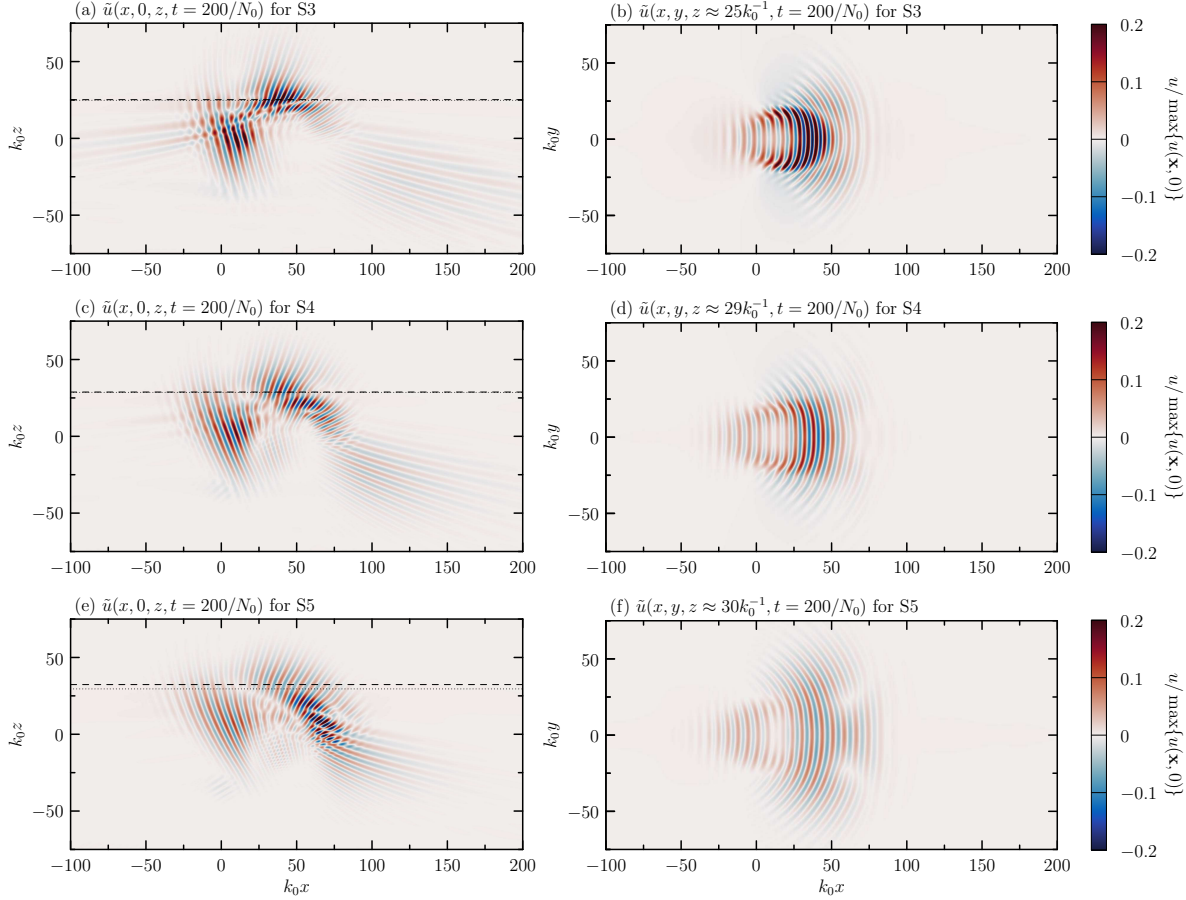


**Figure 7.5:** Snapshots of  $\tilde{u}$  at  $t = 200/N_0$  from (a,b) S3, in which  $A_0 = 0.4k_0^{-1}$  and  $m_0 = -0.7k_0$ ; (c,d) S4, in which  $A_0 = 0.45k_0^{-1}$  and  $m_0 = -k_0$ ; and, (e,f) S5, in which  $A_0 = 0.5k_0^{-1}$  and  $m_0 = -1.4k_0$ , through the  $y = 0$  plane (left column) and through the horizontal plane  $z = z_0 - c_{gz}t$  predicted by linear theory (right column), indicated by the dotted line in the corresponding panel in the left column. The horizontal dashed lines indicate the respective heights of the reflection level predicted by linear theory,  $z_r = 25.19k_0^{-1}$  (a),  $28.82k_0^{-1}$  (c), and  $32.35k_0^{-1}$  (e). Image resolution was enhanced in postprocessing.

spatially disjoint from the other wave packets. Simulation S4 [ $A_0 = 0.45k_0^{-1}$ ; Fig. 7.5(c)] and S5 [ $A_0 = 0.5k_0^{-1}$ ; Fig. 7.5(e)] similarly evolved to exhibit reflection and partial transmission, but with secondary waves radiated preferentially by the (nonbreaking) incident wave packet. TRI could not be identified within the 50% threshold from the power spectra of the linear and quadratically nonlinear wave fields from S3–5 (cf. Table 7.2). The diminishing prevalence of upward-propagating secondary waves in S2–5 may be due in part to the increasing shear strength in these simulations. Increasing shear strength was found to suppress TRI in simulations of one-dimensional wave packets incident upon a retrograde jet (Voelker et al., 2021) by shortening the time interval during which the incident and reflected wave spectra evolved within the resonant regime.

Snapshots of the streamwise velocity through the plane  $z = z_0 - c_{gz}t$  at  $t = 200/N_0$  for S3, S4, and S5 are shown in Figs. 7.5(b), 7.5(d), and 7.5(f), respectively. In each one, the effect of the dipolelike horizontal Bretherton flow was to broaden the extent of the wave packet on its leading flank. The Bretherton flow acted to deform the phase lines, introducing a clear spanwise component to the wave propagation. Waves that were progressively more strongly hydrostatic initially were correspondingly more modulationally stable (hence more dispersive) horizontally [comparing Figs. 7.5(b), 7.5(d), and 7.5(f) in turn].

Horizontal cross sections of  $\tilde{u}$  at heights intersecting the downward-propagating secondary waves were not available for postprocessing. However, comparing visually the streamwise and vertical wavelengths of the downward-propagating secondary waves in Fig. 7.5(a,c,e) indicates these wave packets were moderately hydrostatic, hence horizontally dispersive. On these grounds we assume the secondary wave fronts propagated horizontally in a manner similar qualitatively to the primary wave fronts. This behaviour is reminiscent of the radial propagation of waves generated by an oscillating sphere (Voisin, 1991, 1994). However, this linear generation mechanism neither accounts for the amplitude-squared nature of the secondary waves, nor their preferential direction of radiation, suggesting a similar mechanism was not active in S3–5. Ruling out these mechanisms, we suggest downward- and rightward propagating secondary wave packets may have been generated by self-reflection.

Although S3 and S4–5 were, respectively, marginally stable and modulationally stable initially, Doppler-shifting of the frequency by  $\bar{u}$  eventually drove the wave packets to become modulationally unstable after  $t \approx 75/N_0$  [for S3–4; Fig. 7.6(a,c)]. The modulational stability of S5 was sufficiently strong initially that the destabilizing effect of  $\bar{u}$  was less pronounced, and resulted in a succession of narrowing and peaking events below  $z_r$  during  $125 \lesssim N_0t \lesssim 200$  in Fig. 7.6(e).

Vertical time series of  $\langle \tilde{\mathcal{P}}^\downarrow \rangle$  in Fig. 7.6(b,d,f) are similar qualitatively among S3–5 and S2. In particular, there existed downward-propagating pseudomomentum well below  $z_r$  prior to  $t_r$ , due in part to the concurrent radiation of downward-propagating secondary waves generated by the respective incident wave packets.

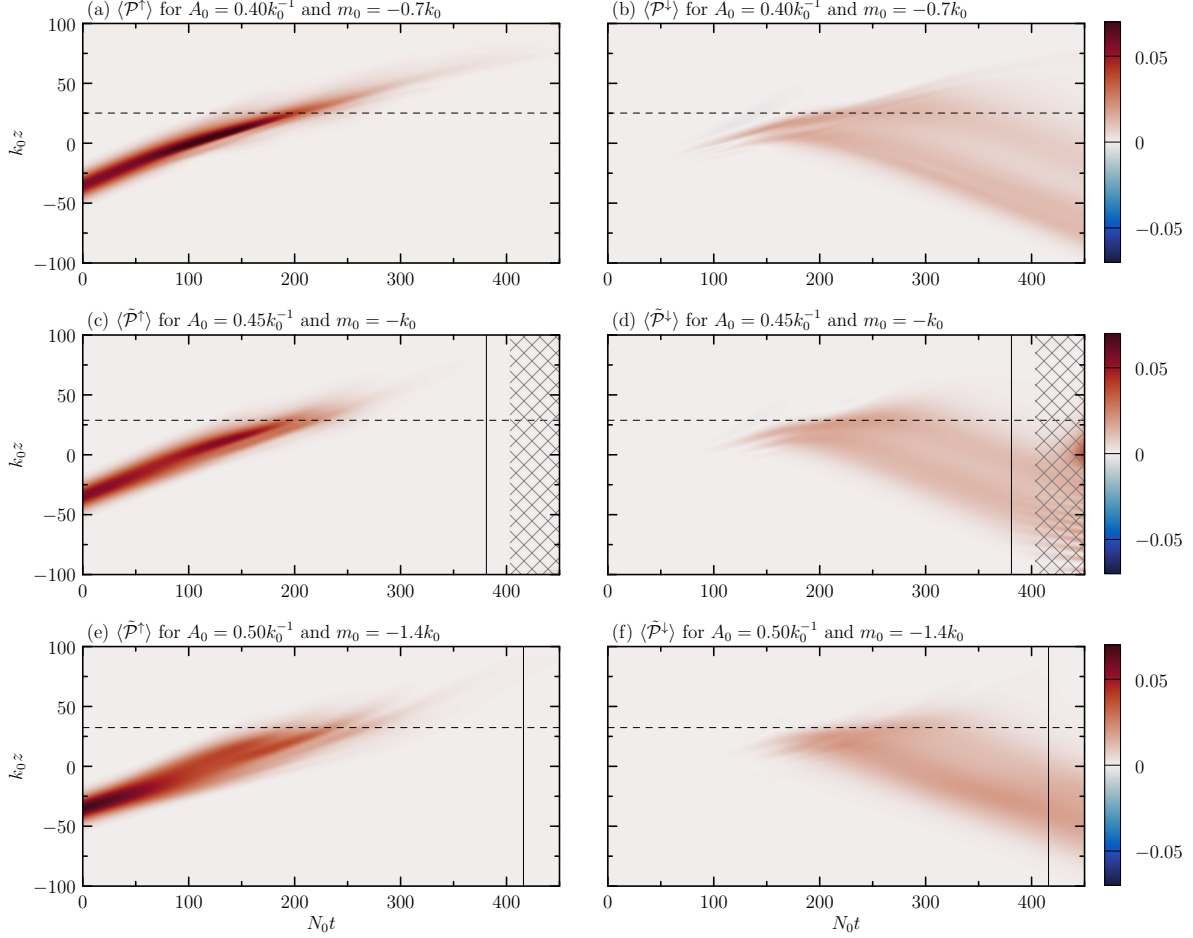


**Figure 7.6:** As in Fig. 7.4 but for simulations S3 (a,b), S4 (c,d), and S5 (e,f). The vertical lines in (c,d) and (e,f) indicate the first times,  $t = 381/N_0$  and  $416/N_0$ , respectively, that  $\mathcal{P}_{\text{err}} \geq 1\%$ , and crosshatching in (c,d) indicates the time  $t \geq 404/N_0$  for which  $\mathcal{P}_{\text{err}} \geq 5\%$ .

### 7.3 Transmission analysis

The first peak transmission coefficient  $T_{\mathcal{P}}^* = T_{\mathcal{P}}(t^*)$ , in which  $t^*$  is the time of first peak transmission and  $T_{\mathcal{P}}$  is defined in Eq. (5.20), is shown as the black data in Fig. 7.7(a) for a range of initial amplitudes and relative vertical wavenumbers. As amplitude increased, peak transmission decreased generally, except for the wave packets with  $m_0 = -0.4k_0$  (diamonds). Black and blue diamonds, respectively, show  $T_{\mathcal{P}}^*$  and  $T_{\mathcal{P}}(t = 400/N_0)$ , reproduced from the time series in Fig. 7.2. Peak transmission of wave packets with  $m_0 = -k_0$  and  $-1.4k_0$  tended to decrease with amplitude. The smallest first peak transmission coefficient for these wave packets was  $T_{\mathcal{P}}^* = 0.24$  and  $0.16$ , respectively, in each case corresponding to wave packets with the largest initial amplitude  $A_0 = 0.55k_0^{-1}$ . This resulted from the envelope-broadening

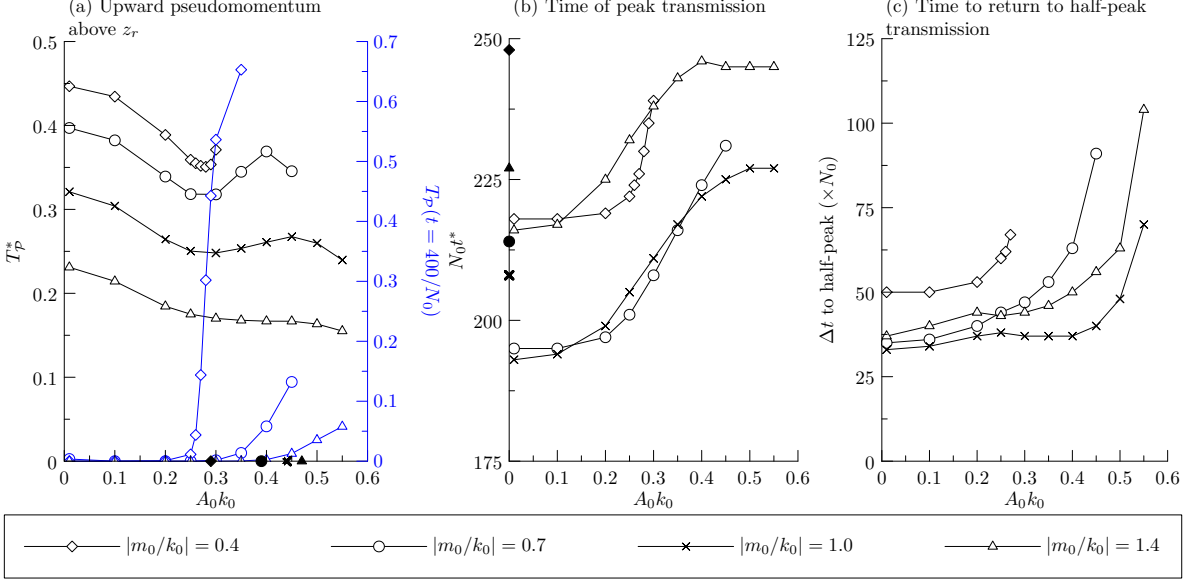


**Figure 7.7:** Transmission diagnostics: (a)  $T_{\mathcal{P}}^*$  (black), and  $T_{\mathcal{P}}(t = 400/N_0)$  (blue), in which the bold symbols on the horizontal axis indicate  $A_{\text{RP}}$ ; (b)  $t^*$ , the time at which first peak transmission was diagnosed, in which the bold symbols on the vertical axis indicate  $N_0 t_r$ ; and, (c)  $\Delta t$ , the time required for transmission to return to half its maximum value shown in (a). Data at  $t = 400/N_0$  for  $m_0 = -k_0$  were excluded from (a) because  $\mathcal{P}_{\text{err}} \geq 1\%$  before  $t = 400/N_0$  in the moderately large amplitude cases. Select black data points in (a) and (b) had their corresponding data point in (c) excluded because either  $\mathcal{P}_{\text{err}} \geq 1\%$  before  $\Delta t$  could be attained, or transmission did not decay to half its peak value during the simulation.

and attenuating effects of modulational stability, and the downward transport of otherwise available pseudomomentum by secondary wave packets. For wave packets with  $m_0 = -0.7k_0$ , the smallest  $T_{\mathcal{P}}^* = 0.32$  was diagnosed for  $A_0 = 0.3k_0^{-1} \approx 0.77A_{\text{RP}} \approx 0.80A_{\text{SW}}$ . Finite transmission above  $z_r$  at late times,  $T_{\mathcal{P}}(t = 400/N_0)$ , is indicated by the respective blue symbols. This is less pronounced for wave packets with  $m_0 = -0.7k_0$  and  $-1.4k_0$  than for those with  $-0.4k_0$ , although in all cases finite transmission occurred with initial amplitudes less than  $A_{\text{RP}}$ .

The time  $t^*$  at which first peak transmission occurred is shown in Fig. 7.7(b). All but the largest-amplitude wave packet with  $m_0 = -0.4k_0$  (which lacked a clear first transmission peak) exhibited increasing values of  $t^*$  due to modulational instability acting to retard the vertical advance of the wave packets. Increasing initial amplitude shortened the time scales for growth of this instability, and promoted the generation of upward-propagating secondary waves. Modulational instability was similarly responsible for increasing values of  $t^*$  in simulations with  $m_0 = -0.7k_0$ . The trend of increasing values of  $t^*$  for wave packets with  $m_0 = -k_0$  and  $-1.4k_0$  was less pronounced, tending toward fixed values of  $t^* = 227/N_0$  and  $245/N_0$ ,

respectively.

Because  $T_{\mathcal{P}}$  was a transient quantity, we diagnosed the time interval  $\Delta t$  required for transmission above  $z_r$  to decay to half the value of  $T_{\mathcal{P}}^*$  [Fig. 7.7(c)]. For wave packets with  $m_0 = -0.4k_0$  and  $0.01 \leq A_0k_0 \leq 0.27$ ,  $\Delta t$  increased with increasing initial amplitude. Transmission above  $z_r$  did not decay to half the corresponding values of  $T_{\mathcal{P}}^*$  for  $A_0 \geq 0.28k_0^{-1}$  due to pronounced penetration of primary waves. As initial amplitude increased in the simulations with  $m_0 = -k_0$  and  $-1.4k_0$  ( $\Theta_0 = 45^\circ$  and  $54^\circ$ , respectively),  $\Delta t$  became longer. This resulted from a sequence of events driven by modulational stability of these wave packets: (1) differential advection by the Bretherton flow enhanced the flattening of phase lines below and behind the centre of the incident wave packet (hence  $\Theta > 45^\circ$  locally); (2) this effect compounded with dispersion in the streamwise direction, causing a ‘fanned-out’ phase pattern to emerge (not shown); then, (3) within the ‘fanned-out’ packet, waves with relatively small  $\Theta$  were Doppler-shifted by  $\bar{u}$  and reflected more readily than more hydrostatic waves with larger  $\Theta$ , leading ultimately to longer  $\Delta t$ . This sequence of effects was more pronounced with increasing  $A_0$  and  $\Theta_0$ . Wave packets with  $m_0 = -0.7k_0$  evolved to exhibit these effects in addition to modulational instability, so that  $\Delta t$  became longer as initial amplitude increased.

## 7.4 Discussion

In this chapter we investigated predictions of the critical amplitude for “reflection level penetration” (above which there is finite transmission of pseudomomentum above the reflection level at late times), and for “self-reflection” (a mechanism that predicts for which amplitudes significant generation of secondary wave packets by nonbreaking primary waves occurs). These predictions were investigated by performing fully nonlinear simulations of nonhydrostatic three-dimensional wave packets incident upon a retrograde shear flow. To my knowledge, these simulations were the first to study the self-interaction of such wave packets with their induced Bretherton flow in a retrograde shear flow. Nonlinear interactions between moderately large amplitude strongly (moderately) nonhydrostatic wave packets and their Bretherton flow led to modulational instability (stability). The corresponding nonlinearly generated upward- (downward-) propagating secondary wave packets acted ultimately

to enhance (hinder) transmission above the predicted reflection level.

The reflection level penetration condition, Eq. (5.10), was generally effective to predict whether a wave packet would exhibit finite transmission above the reflection level  $z_r$  at late times. For example, strongly nonhydrostatic wave packets with  $m_0 = -0.4k_0$  and initial amplitudes as small as  $A_0 = 0.25k_0^{-1} \approx 0.85A_{\text{RP}}$  transmitted partially above  $z_r$  with  $T_{\mathcal{P}}(t = 400/N_0) \approx 0.01$ . Similarly, wave packets with  $m_0 = -0.7k_0$  and  $-1.4k_0$  exhibited finite transmission  $T_{\mathcal{P}}(t = 400/N_0) \gtrsim 0.01$  with  $A_0 \geq 0.35k_0^{-1} \gtrsim 0.9A_{\text{RP}}$  and  $A_0 \geq 0.45k_0^{-1} \gtrsim 0.97A_{\text{RP}}$ , respectively.

The existence of transmitted pseudomomentum above  $z_r$  at late times is analogous to the “steady-state” transmission identified by Sutherland (2000). Because that study did not employ explicitly a transmission coefficient, we forego a direct comparison using the quantitative language of pseudomomentum in favour of a qualitative comparison. It was found that one-dimensional wave packets with initial amplitudes sufficient for self-acceleration could break convectively at the reflection level and deposit momentum to the background flow. This effect was not quantified because the simulations of Sutherland (2000) could not resolve the inherently three-dimensional turbulent dynamics of wave breaking. Conversely, strongly nonhydrostatic two-dimensional wave packets were able to penetrate above the reflection level without breaking. The role of the wave-induced mean flow in those results may be questionable because the expression for the long waves induced by two-dimensional wave packets (Bretherton, 1969) was not used when superimposing the induced mean flow onto the wave packets. In agreement with the fully nonlinear simulation results of Sutherland (2000), but in contrast with the ray-theory results of Robinson (1997), three-dimensional wave packets that exhibited finite transmission above  $z_r$  at late times did not encounter a vertically displaced reflection level higher up.

Triadic resonant instability between transmitted and reflected wave packets was identified as generating upward-propagating secondary waves in the most strongly nonhydrostatic simulations, but not the downward-propagating secondary waves characteristic of moderately nonhydrostatic simulations. The proposed “self-reflection” condition for secondary wave packet generation by nonbreaking moderately nonhydrostatic primary waves tended to overpredict the critical initial amplitude,  $A_{\text{SW}}$ , for the onset of this mechanism. To assess qualitatively

the degree to which  $\bar{u}(z)$  may have contributed to this result, a subset of our simulations was repeated, but with  $\bar{u} \equiv 0$ . Compared to simulations with nonuniform background flow, the prediction for secondary wave generation was generally well borne-out for nonhydrostatic wave packets with  $m_0 = -0.7k_0$  and  $\bar{u} \equiv 0$  (not shown). Secondary wave packets typically became evident on approximately the same time scale as in the simulations with nonuniform background flow. The critical amplitude was underpredicted for wave packets with  $m_0 = -k_0$  and  $-1.4k_0$  and  $\bar{u} \equiv 0$  (not shown). To better assess the robustness of the prediction for secondary wave packet generation, future work will need to adopt quantitative diagnostics to analyze secondary wave packets.

Using weakly (fully) nonlinear WKB (wave-resolving and large-eddy simulation) methods, [Muraschko et al. \(2015\)](#) examined the propagation of one-dimensional wave packets in a range of background flow and stratification profiles. Although wave packet evolution was captured by their weakly and fully nonlinear codes, no secondary waves were identified. This suggests that the qualitative behaviours of the secondary waves reported on in this chapter (in particular those propagating downward) may represent dynamics unique to fully localized three-dimensional wave packets.

Our simulations provided insight into the mechanisms governing wave packet evolution in a nonuniform background flow. However, our results are highly idealized, having assumed a uniformly stratified, infinite Boussinesq fluid with a steady, horizontally homogeneous but vertically nonuniform background flow. In Part [III](#) of this thesis, we extend nontrivially the study of three-dimensional wave packet transmission and reflection to waves in an anelastic gas.

# PART III

---

## Anelastic wave packets in nonuniform background flow

---

In Parts I and II, we considered wave packets that evolved in stratified fluids under the Boussinesq approximation. The theoretical predictions and numerical results were valid in the context of an idealized ocean or atmosphere interior, provided the scale of vertical motions was small compared to the  $e$ -folding depth of mass density. However, in the atmosphere more generally, internal gravity waves generated at relatively low altitudes can propagate upward significantly, attaining large amplitudes in the middle and upper atmosphere (Hines, 1960; Eckermann et al., 2016). Because mass density in the atmosphere decreases approximately exponentially with altitude (e.g., Eliassen and Palm, 1961), internal gravity wave amplitudes grow exponentially with altitude to conserve momentum (an effect referred to as *anelastic growth*; to be shown quantitatively in Chapter 8).

In Part II, the background flow was assumed, for convenience, to transition smoothly from zero (where the waves were initialized) to a linearly decreasing retrograde shear flow. This assumption was useful to understand wave packet transmission in an idealized setting, with the added benefit of being readily comparable to previous results of one- and two-dimensional wave packet transmission. In this study, we will adopt a set of somewhat more realistic background flow profiles and examine the evolution of three-dimensional wave packets as they encounter the background flow. The actual background flow profiles will be modelled from a dataset derived from observations of the Quasi-Biennial Oscillation (QBO).

The QBO, as its name suggests, is a quasiperiodic flow feature, located in the equatorial stratosphere, consisting of slowly descending (at about  $1 \text{ km month}^{-1}$ ) easterly and westerly\* winds that reverse with an average period of approximately 28 months (Baldwin et al., 2001). The QBO was discovered independently by Ebdon (1960) and Reed et al. (1961) from analyses of weather balloon data, and named by Angell and Korshover (1964).

The first satisfactory theoretical explanation for the QBO was proposed by Lindzen and Holton (1968): a spectrum of internal gravity waves with positive and negative zonal phase speeds propagates upward from the tropopause towards an existing stratospheric zonal wind exhibiting a strong semiannual oscillation; waves with  $c_{pz} > 0$  (say) incident upon a critical level deposit their momentum to the existing (westerly) flow (Booker and Bretherton, 1967), thus lowering the critical level altitude; when the critical level descends to a certain height [assumed by Lindzen and Holton (1968) to be 19 km], internal waves with  $c_{pz} < 0$  were assumed to propagate upward to the critical level associated with the stratospheric zonal flow (now in its easterly phase), thus lowering the critical level altitude; when this critical level reaches 19 km, the stratospheric zonal flow has returned to its westerly phase and the process begins anew.

The role of reflecting and transmitting/tunnelling of internal gravity waves was not accounted for in the theory of Lindzen and Holton (1968), based on critical level absorption. However, transmission of relatively small scale internal gravity waves through the stratospheric background wind offered a theoretical explanation for the so-called *mesospheric QBO* first reported in radar and satellite observations (Burrage et al., 1996) and reproduced in numerical simulations (Mayr et al., 1997a,b). Unlike the stratospheric QBO, longer-term observations suggest the mesospheric QBO is more intermittent, and not restricted to tropical latitudes (Kumar, 2020), although the mechanisms responsible for its intermittency and extratropical extent are not known conclusively.

Beyond purely academic interest in the dynamics of the QBO, this flow is important for its teleconnections to atmospheric phenomena outside the tropical atmosphere, first recognized

---

\*To describe geographically the flow direction of the QBO, we adopt the perhaps counterintuitive language common in the atmospheric sciences that *easterly* and *westerly* denote the direction *from which* the wind comes. The east-west (longitudinal) direction more generally is referred to as the *zonal* direction. By convention, zonal wind is positive when it is westerly.

by [Holton and Tan \(1980\)](#): the Northern Hemisphere stratospheric polar vortex in early- to mid-winter was found to strengthen (weaken) when the QBO at 50 hPa was in its westerly (easterly) phase ([Anstey et al., 2021b](#)). A weakened stratospheric polar vortex can in turn affect surface weather, resulting in colder winter temperatures, and increased snow, wind, and number of Atlantic storms (e.g., [Baldwin and Dunkerton, 2001](#); [Anstey and Shepherd, 2014](#)). The extratropical atmosphere is thought to exert an influence on the QBO: for example, a topic of ongoing investigation is to understand the causes and consequences of a sudden and unprecedented disruption to the QBO in 2015–2016 ([Osprey et al., 2016](#); [Newman et al., 2016](#)), in which the descending westerly phase began rising again unexpectedly. A similar, but less dramatic, disruption occurred in 2019–2020 ([Anstey et al., 2021a](#)). Small scale (parameterized) convective internal gravity waves were found to have contributed “significant[ly]” to preconditioning the 2015–2016 QBO jet core for deceleration by Rossby waves of extratropical origin ([Kang et al., 2020](#)); internal gravity waves contributed to the 2019–2020 QBO disruption through a similar mechanism but to a lesser extent ([Kang and Chun, 2021](#)). The prospect of improved understanding of QBO dynamics (e.g., through improved gravity wave parameterizations) motivates detailed studies of wave packet reflection and transmission/tunnelling in nonuniform background flow.

A study of internal wave tunnelling in a Boussinesq fluid with a piecewise-linear shear flow was performed by [Brown and Sutherland \(2007\)](#). Small amplitude one-dimensional waves were able to tunnel through a finite depth unstratified region provided the streamwise wavelength was of comparable magnitude. In a uniformly stratified fluid, waves would be anticipated to tunnel analogously through a layer of shear-stable wind of finite thickness, such as the jetlike QBO winds. A similar study of one- and two-dimensional wave packets in an anelastic gas was performed by [Nault and Sutherland \(2008\)](#). Waves were likewise found to tunnel through unstratified, sheared, regions provided the depth of the nonuniformities was comparable to the streamwise wavelength and mass density  $e$ -folding depth.

The purpose of this study is to extend the work of [Nault and Sutherland \(2008\)](#) and [Brown and Sutherland \(2007\)](#) to investigate the reflection and transmission/tunnelling of three-dimensional anelastic internal gravity wave packets by and through the QBO winds, and the role of the wave-induced mean flow in this process. The present study differs from

these latter two in that we assume a uniformly stratified anelastic atmosphere and we simulate the wave evolution through background flow profiles modelling distinct phases of the QBO. Initial amplitudes and wavenumbers are chosen to be representative of waves generated by deep convection at the equatorial tropopause (e.g., as obtained in the simulations of [Holton and Alexander, 1999](#)).

In Chapter 8 we review briefly the thermodynamics of anelastic gases so that we may derive an integral expression for the Bretherton flow induced by three-dimensional internal gravity wave packets. We then revisit the theory of linear (i.e., small amplitude) wave packets propagating in a nonuniform background flow first presented in Chapter 5 to extend our predictions of reflection level penetration to an anelastic gas and predict the conditions for wave packets to tunnel through the QBO winds. Using the code described in Chapter 9, we perform numerical simulations of round anelastic wave packets with a range of initial amplitudes and wavenumbers in two idealized QBO regimes. Results are described in Chapter 10, compared with theoretical predictions, and discussed in the context of the role of internal gravity waves in driving QBO dynamics.

---

## Theory

---

In this chapter we first review briefly some essential thermodynamics that lead from the Boussinesq (mass-density based) to anelastic (potential-temperature based) descriptions of fluid stratification. We then derive an explicit integral expression for the mean flow induced by three-dimensional wave packets in a uniformly stratified anelastic gas that is stationary in the absence of waves, ignoring diffusive and viscous effects. We follow a somewhat more general version of the approach taken in Chapter 2. Although ultimately the resulting expression will be applied in an idealized atmosphere with a vertically nonuniform background flow, the expression for the wave-induced mean flow is derived to be valid in a region where the background flow speed will be assumed to be zero. We then derive, following the approach in Sec. 5.2, the critical amplitude at which an anelastic wave packet is predicted to penetrate significantly above the reflection level predicted by linear theory. We then describe the modelling of the QBO winds, and the chapter concludes with the definition of an appropriate transmission coefficient.

### 8.1 From Boussinesq theory to an anelastic gas

In a Boussinesq fluid, the key thermodynamic variable is mass density. Implicit in the use of the Boussinesq approximation in Parts I–II was the assumption that vertical wave motions were smaller than the  $e$ -folding depth of background mass density,  $\bar{\rho}$  (e.g., Dutton and Fichtl,

1969). This requirement was satisfied by setting the background density profile to slowly decrease linearly with height. This is a suitable approximation of the background mass density profile in the ocean and over relatively small vertical distances in the atmosphere (e.g., Vallis, 2006).

The Boussinesq approximation cannot be applied throughout the atmosphere because the mass density varies significantly over the total depth of the atmosphere. It is necessary to model the thermodynamics associated with the expansion and contraction of fluid parcels as they are displaced vertically within the atmosphere. To that end, the stratification of a vertical column within an idealized dry atmosphere is described by the background potential temperature  $\bar{\theta}$ , defined by

$$\bar{\theta}(z) := \bar{T} \left( \frac{\bar{p}}{p_0} \right)^{-R_a/c_p}, \quad (8.1)$$

where  $\bar{T} = \bar{T}(z)$  and  $\bar{p} = \bar{p}(z)$  are background profiles of temperature and pressure, respectively, and  $p_0$  is a constant reference pressure. In the exponent,  $R_a/c_p \approx 2/7$  is the ratio of the ideal gas constant for dry air to the specific heat for dry air at constant pressure (e.g., Holton and Hakim, 2013; Sutherland, 2010).

For simplicity the model atmosphere is assumed isothermal so that  $\bar{T} = T_0 = \theta_0$  is constant, and the background atmospheric pressure is assumed to be in hydrostatic balance. This latter assumption describes the situation that the upward pressure gradient force is equal and opposite to the downward force (per unit volume) of gravity acting on a mass of fluid. Hydrostatic balance is described by the differential equation

$$\frac{d\bar{p}}{dz} = -\bar{\rho}g. \quad (8.2)$$

Using the ideal gas law  $\bar{p} = \bar{\rho}R_a\bar{T}$  on the right-hand side of Eq. (8.2) to eliminate  $\bar{\rho}$ , and solving the resulting separable equation, yields the background pressure profile

$$\bar{p}(z) = \exp \left( - \int \frac{g}{R_a\bar{T}} dz \right) = p_0 e^{-z/H_p}, \quad (8.3)$$

where the  $e$ -folding depth  $H_p := R_a T_0 / g$ , called the *pressure scale height*, is a constant that emerges naturally upon invoking the isothermal assumption.

From Eq. (8.3) are obtained two background profiles of crucial importance for the study

of internal gravity waves in an anelastic gas: using the ideal gas law in Eq. (8.3) gives the background density profile

$$\bar{\rho}(z) = \rho_0 e^{-z/H_\rho}. \quad (8.4)$$

The constant

$$H_\rho := -\left(\frac{1}{\bar{\rho}} \frac{d\bar{\rho}}{dz}\right)^{-1}$$

is called the *density scale height*, and is intimately related to the exponential growth of wave amplitudes with altitude. In a uniformly stratified atmosphere,  $H_\rho = H_p$ . Using Eq. (8.3) in Eq. (8.1) gives the background potential temperature profile

$$\bar{\theta}(z) = \theta_0 e^{z/H_\theta}, \quad (8.5)$$

where  $H_\theta := H_\rho/(R_a/c_p)$  is the *potential temperature scale height* which defines the constant  $e$ -folding depth of potential temperature with altitude.

With Eqs. (8.4) and (8.5) capturing the essential thermodynamics and stratification of the idealized atmosphere, we proceed to describe atmospheric internal gravity waves below.

## 8.2 Governing equations

The fully nonlinear Euler momentum equations for an anelastic gas (Ogura and Phillips, 1962; Lipps and Hemler, 1982) including the buoyancy term and advection by a horizontally homogeneous, vertically nonuniform background flow, are given in vector form by

$$\frac{D\mathbf{u}}{Dt} + \bar{u} \frac{\partial \mathbf{u}}{\partial x} + w \frac{d\bar{u}}{dz} \hat{\mathbf{e}}_x = -\nabla \left( \frac{p}{\bar{\rho}} \right) + \frac{g}{\theta} \theta \hat{\mathbf{e}}_z, \quad (8.6)$$

where  $D/Dt = \partial/\partial t + \mathbf{u} \cdot \nabla$  is the material derivative, in which  $\mathbf{u} = (u, v, w)$  is the velocity vector in Cartesian coordinates  $\mathbf{x} = (x, y, z)$  with corresponding standard unit basis vectors  $\hat{\mathbf{e}}_x$ ,  $\hat{\mathbf{e}}_y$ , and  $\hat{\mathbf{e}}_z$ ,  $\bar{u}$  is the background flow,  $p$  is dynamic pressure,  $g$  is the acceleration of gravity, and  $\theta$  is perturbation potential temperature.

Also included in the full set of governing equations is that for internal energy (including advection of internal energy by the background flow), expressed as an evolution equation for

perturbation potential temperature,

$$\frac{D\theta}{Dt} + \bar{u} \frac{\partial \theta}{\partial x} = -w \frac{d\bar{\theta}}{dz}. \quad (8.7)$$

The set of governing equations is closed by the inclusion of a statement of mass conservation for an anelastic gas,

$$\nabla \cdot (\bar{\rho} \mathbf{u}) = 0. \quad (8.8)$$

This condition states mathematically the anelastic approximation, which effectively filters acoustic waves from the governing equations while allowing gravity wave amplitudes to grow exponentially with height as these waves propagate through the atmosphere's exponentially decreasing background mass density.

It was stated earlier that wave amplitude grows exponentially with height as a consequence of momentum conservation. Having stated the governing equations, we now demonstrate quantitatively this property of anelastic waves. This extends, rather trivially, the result demonstrated by [Sutherland \(2010, Sec. 3.7.2\)](#) to waves in three dimensions in the presence of a height-dependent background flow.

We use the anelastic nondivergence condition, Eq. (8.8), in the streamwise component of Eq. (8.6) to write the streamwise momentum equation in flux form:

$$\frac{\partial}{\partial t} (\bar{\rho} u) + \bar{u} \frac{\partial}{\partial x} (\bar{\rho} u) + \frac{d\bar{u}}{dz} (\bar{\rho} w) + \nabla \cdot (\bar{\rho} u \mathbf{u}) = -\bar{\rho} \frac{\partial}{\partial x} \left( \frac{p}{\bar{\rho}} \right). \quad (8.9)$$

For convenience, we substitute a plane wave solution\* into this equation, and average the resulting expression over a streamwise wavelength (denoting the average by angle brackets). As a result, we obtain the mass transport equation,

$$\underbrace{\frac{\partial}{\partial t} \langle \bar{\rho} u \rangle + \frac{d\bar{u}}{dz} \langle \bar{\rho} w \rangle + \frac{\partial}{\partial y} \langle \bar{\rho} uv \rangle + \frac{\partial}{\partial z} \langle \bar{\rho} uw \rangle}_{=0} = 0. \quad (8.10)$$

Because we assumed a plane wave solution to Eq. (8.9) and averaged over a wavelength,  $\langle \bar{\rho} u \rangle = \bar{\rho} \langle u \rangle \equiv 0$  and  $\langle \bar{\rho} w \rangle = \bar{\rho} \langle w \rangle \equiv 0$ . As a result of the averaging operation,  $\langle \bar{\rho} uv \rangle$  and  $\langle \bar{\rho} uw \rangle$  are functions of  $z$  alone. Hence, Eq. (8.10) is equivalent to  $\frac{\partial}{\partial z} \langle \bar{\rho} uw \rangle = 0$ . Integrating

---

\*Or at worst, a solution with a plane wave structure in  $x$ ,  $y$ , and  $t$ , multiplied by a  $z$ -dependent *vertical structure function*, whose exact form is related to  $\bar{u}$ . This more general solution would be needed if  $d\bar{u}/dz \neq 0$ , but this technical detail does not change the overall argument for exponential amplitude growth with height.

once gives

$$\langle \bar{\rho} u w \rangle = \text{constant}.$$

In order for this equality to hold as mass density decreases exponentially with height,  $u$  and  $w$  must increase exponentially in response.

### 8.3 Wave-induced mean flow

Following the approach in Sec. 2.2, it is convenient to recast the governing equations in terms of vertical displacement  $\xi$  as opposed to perturbation potential temperature. These quantities are related by

$$\theta = -\xi \frac{d\bar{\theta}}{dz}, \quad (8.11)$$

which, by analogy with its Boussinesq counterpart [cf. Eq. (2.4)], is obtained from a Taylor series expansion of  $\bar{\theta}$  about a vertical displacement  $\xi$ . Substituting Eq. (8.11) into Eqs. (8.6) and (8.7) and setting  $\bar{u} \approx 0$  in the region where the forthcoming derivation is to be valid, we obtain the governing equations in a directly useful form,

$$\frac{\partial u}{\partial t} + \mathbf{u} \cdot \nabla u = -\frac{\partial}{\partial x} \left( \frac{p}{\bar{\rho}} \right), \quad (8.12)$$

$$\frac{\partial v}{\partial t} + \mathbf{u} \cdot \nabla v = -\frac{\partial}{\partial y} \left( \frac{p}{\bar{\rho}} \right), \quad (8.13)$$

$$\frac{\partial w}{\partial t} + \mathbf{u} \cdot \nabla w = -\frac{\partial}{\partial z} \left( \frac{p}{\bar{\rho}} \right) - N_0^2 \xi, \quad (8.14)$$

$$\frac{\partial \xi}{\partial t} + \mathbf{u} \cdot \nabla \xi + \frac{1}{H_\theta} w \xi = w, \quad (8.15)$$

where the coefficient  $1/H_\theta = (d^2\bar{\theta}/dz^2)/(d\bar{\theta}/dz)$  results from using Eq. (8.11) in Eq. (8.7). The above system is closed by inclusion of Eq. (8.8), which does not change as a result of Eq. (8.11). The buoyancy term in Eq. (8.14) is now expressed in terms of the squared buoyancy frequency,

$$N_0^2 = \frac{g}{\bar{\theta}} \frac{d\bar{\theta}}{dz} = \frac{g}{H_\theta}, \quad (8.16)$$

which is constant in our assumed uniformly stratified anelastic gas. The Boussinesq governing equations, Eqs. (2.3) and (2.5)–(2.8) (with Coriolis parameter  $f_0 = 0$ ) are recovered by taking the so-called ‘‘Boussinesq limit’’ of Eqs. (8.8) and (8.12)–(8.15), respectively. In this limit,

$H_\rho \rightarrow \infty$ , hence  $H_\theta \rightarrow \infty$  and  $\bar{\rho} \rightarrow \rho_0$ , and the Boussinesq equations are recovered.

### 8.3.1 Perturbation theory

We now proceed somewhat more explicitly than in Sec. 2.2 by performing a perturbation expansion of the momentum equations with respect to the amplitude parameter  $\alpha := A_0 k_0$ , where  $A_0$  is the maximum vertical displacement of the waves initially [this step was only implied in Sec. 2.2 and by van den Bremer and Sutherland (2018)]. The choice of expansion parameter is not unique (cf. Sec. 2.2.1), but for consistency we maintain the definition of  $\alpha$  already in use.

#### 8.3.1.1 Expansion with respect to amplitude

With these considerations, a wave field  $\eta$  is expanded with the notation  $\eta = \eta^{(1)} + \eta^{(2)} + \dots$ , where the superscript denotes the field's order with respect to  $\alpha$ . Substituting expressions of this form into Eqs. (8.12)–(8.15) and (8.8) we obtain, up to second order,

$$\frac{\partial}{\partial t}(u^{(1)} + u^{(2)}) + \mathbf{u}^{(1)} \cdot \nabla u^{(1)} = -\frac{\partial}{\partial x} \left( \frac{p^{(1)}}{\bar{\rho}} + \frac{p^{(2)}}{\bar{\rho}} \right), \quad (8.17)$$

$$\frac{\partial}{\partial t}(v^{(1)} + v^{(2)}) + \mathbf{u}^{(1)} \cdot \nabla v^{(1)} = -\frac{\partial}{\partial y} \left( \frac{p^{(1)}}{\bar{\rho}} + \frac{p^{(2)}}{\bar{\rho}} \right), \quad (8.18)$$

$$\frac{\partial}{\partial t}(w^{(1)} + w^{(2)}) + \mathbf{u}^{(1)} \cdot \nabla w^{(1)} = -\frac{\partial}{\partial z} \left( \frac{p^{(1)}}{\bar{\rho}} + \frac{p^{(2)}}{\bar{\rho}} \right) - N_0^2(\xi^{(1)} + \xi^{(2)}), \quad (8.19)$$

$$\frac{\partial}{\partial t}(\xi^{(1)} + \xi^{(2)}) + \mathbf{u}^{(1)} \cdot \nabla \xi^{(1)} + \frac{1}{H_\theta} w^{(1)} \xi^{(1)} = w^{(1)} + w^{(2)}, \quad (8.20)$$

$$\nabla \cdot [\bar{\rho}(\mathbf{u}^{(1)} + \mathbf{u}^{(2)})] = 0. \quad (8.21)$$

Because the wave-induced mean flow is an order amplitude-squared response to mean wave-wave interactions on the scale of the wave packet, a partial differential equation for the wave-induced mean flow is obtained by considering the mean of the  $O(\alpha^2)$  part of the expanded governing equations. Furthermore, we recall that the Bretherton flow in particular is forced by the vertical component of vorticity. To that end, taking the vertical component of the curl of the  $O(\alpha^2)$  part of Eqs. (8.17)–(8.19) to eliminate the pressure terms, and averaging the resulting equation over the fast wave scales, we obtain the equation for the Bretherton flow

$$\frac{\partial}{\partial t}(\nabla \times \mathbf{u}_{\text{BF}}) \cdot \hat{\mathbf{e}}_z = \overline{\boldsymbol{\zeta}^{(1)} \cdot \nabla w^{(1)} - \mathbf{u}^{(1)} \cdot \nabla \zeta_z^{(1)}}, \quad (8.22)$$

to be solved subject to the anelastic Bretherton nondivergence condition,  $\nabla \cdot (\bar{\rho} \mathbf{u}_{\text{BF}}) = 0$ .

### 8.3.1.2 Expansion with respect to inverse wave packet extent

Following the approach in Sec. 2.2, we seek solutions of Eq. (8.22) in terms of quasimonochromatic wave packets. We orient our coordinate system such that waves propagate in the  $xz$ -plane with wavenumber vector  $\mathbf{k}_0 = (k_0, 0, m_0)$ , with  $k_0 > 0$  and  $m_0 < 0$  so that the waves propagate forward in  $x$  and  $t$  and upward in  $z$ . The corresponding frequency,  $\omega_0 > 0$ , is given by the dispersion relation,

$$\omega_0 = \frac{N_0 k_0}{K_0}, \quad (8.23)$$

where  $K_0 = (k_0^2 + m_0^2 + 1/4H_\rho^2)^{1/2}$ , derived in Appendix A.2.1.

We introduce a slow timescale  $T$  and slow spatial variables,  $\mathbf{X} = (X, Y, Z)$ , in a frame of reference translating at the group velocity of the wave packet,  $\mathbf{c}_{g0} = (c_{gx0}, 0, c_{gz0})$ , where

$$c_{gx0} = \frac{N_0(K_0^2 - k_0^2)}{K_0^3} \quad (8.24a)$$

$$c_{gz0} = -\frac{N_0 k_0 m_0}{K_0^3}. \quad (8.24b)$$

Explicitly,  $X = \epsilon_x(x - c_{gx0}t)$ ,  $Y = \epsilon_y y$ , and  $Z = \epsilon_z(x - c_{gz0}t)$ , where  $\epsilon_x = 1/(k_0\sigma_x)$ ,  $\epsilon_y = 1/(k_0\sigma_y)$ , and  $\epsilon_z = 1/(k_0\sigma_z)$  are small parameters that are inversely proportional to the wave packet extent,  $\sigma_x$ ,  $\sigma_y$ , and  $\sigma_z$ , in their respective directions. The slow timescale  $T = \epsilon^2 t$  describes dispersion of the wave packet, where  $\epsilon = \max\{\epsilon_x, \epsilon_y, \epsilon_z\} \ll 1$  is assumed, hence the effects of dispersion are effectively ignored.

With this notation, the leading-order representation of an anelastic wave field  $\eta$  as a quasimonochromatic wave packet is

$$\eta_0^{(1)} := \frac{1}{2} A_\eta(\mathbf{X}, T) e^{i\varphi_0} e^{z/2H_\rho} + \text{c.c.}, \quad (8.25)$$

where the subscript on  $\eta_0^{(1)}$  denotes the field's order with respect to  $\epsilon$ ,  $\varphi_0 = \mathbf{k}_0 \cdot \mathbf{x} - \omega_0 t$  is the phase, and c.c. denotes the complex conjugate. Note that we employ variables  $k_0$ ,  $m_0$ ,  $\omega_0$ ,  $\mathbf{c}_{g0}$ ,  $\varphi_0$ , and others as necessary, adorned with a subscript 0, following the rationale discussed in Sec. 5.1, in anticipation of applying ultimately the expressions derived in this chapter in a nonuniform background flow. The key difference between Eq. (8.25) and Eq. (2.15)

representing quasimonochromatic wave packets in a Boussinesq fluid is the anelastic growth factor  $e^{z/2H_\rho}$ , which accounts for the exponential growth of anelastic waves with altitude by a factor of  $1/\sqrt{\bar{\rho}/\rho_0}$ . This term does not translate with the wave packet at the vertical group speed, thus allowing the wave packet to remain stationary with respect to the moving frame of reference  $\mathbf{X}$  while continuing to grow anelastically as it propagates upward with respect to the fixed  $z$  variable.

As a result of the change to slow variables, derivatives of wave fields as defined by Eq. (8.25) become

$$\partial_x \rightarrow \epsilon_x \partial_X + ik_0, \quad (8.26a)$$

$$\partial_y \rightarrow \epsilon_y \partial_Y, \quad (8.26b)$$

$$\partial_z \rightarrow \epsilon_z \partial_Z + im_0 + \frac{1}{2H_\rho}, \quad (8.26c)$$

$$\partial_t \rightarrow \epsilon^2 \partial_T - \epsilon_x c_{gx0} \partial_X - \epsilon_z c_{gz0} \partial_Z - i\omega_0. \quad (8.26d)$$

At leading-order, the various wave fields are related algebraically by the polarization relations, derived by substituting a plane wave into the  $O(\alpha^1)$  part of the governing equations, Eqs. (8.17)–(8.21). The resulting polarization relations are summarized in the centre column of Table 8.1, and details of their derivation are included in Appendix A.2.1.

In order to derive the polarization relations at the next order in  $\epsilon$ , accounting for the finite extent of the wave packet, it is necessary to impose the structure of one field. Following Sec. 2.2.1, without loss of generality we impose the structure of the vertical displacement field at leading- and first-order in  $\epsilon$ . Explicitly,  $\xi = \xi_0^{(1)} + \xi_1^{(1)}$ , where  $\xi_0^{(1)}$  is analogous to the expression in Eq. (8.25), and  $\xi_1^{(1)} = \frac{1}{2}i\Sigma_\beta A e^{i\varphi_0} e^{z/2H_\rho}$ , where we have defined the slow partial differential operator

$$\Sigma_\beta := \epsilon_x \beta_x \partial_X + \epsilon_y \beta_y \partial_Y + \epsilon_z \beta_z \partial_Z$$

for convenience, where  $\beta_x$ ,  $\beta_y$ , and  $\beta_z$  are constants to be determined. The other polarization relations at  $O(\alpha^1 \epsilon^1)$  are found by substituting a wave packet solution of the form defined by Eq. (8.25) into the  $O(\alpha^1)$  part of Eqs. (8.17)–(8.21) and using the leading-order polarization relations and Eqs. (8.26a)–(8.26d) up to  $O(\epsilon^1)$ . The results are summarized in the right column of Table 8.1, and details of their derivation are included in Appendix A.2.2.

Field	$O(\alpha^1 \epsilon^0)$	$O(\alpha^1 \epsilon^1)$
Vertical displacement	$\xi_0^{(1)} = A$	$\xi_1^{(1)} = -\frac{i}{\omega_0}(\mathbf{c}_{g0} \cdot \nabla)A$
Streamwise velocity	$u_0^{(1)} = -\frac{k_0}{\omega_0} \frac{N_0^2 - \omega_0^2}{M_0} A$	$u_1^{(1)} = \frac{1}{i\omega_0 M_0} \left[ \frac{k_0}{\omega_0} N_0^2 \mathbf{c}_{g0} \cdot \nabla - (N_0^2 - \omega_0^2) \left( \epsilon_x \partial_X - \frac{ik_0}{M_0} \epsilon_z \partial_Z \right) \right] A$
Spanwise velocity	$v_0^{(1)} = 0$	$v_1^{(1)} = -\frac{N_0^2 - \omega_0^2}{i\omega_0 M_0} \epsilon_y \partial_Y A$
Vertical velocity	$w_0^{(1)} = -i\omega_0 A$	$w_1^{(1)} = -2\mathbf{c}_{g0} \cdot \nabla A$
Streamwise vorticity	$\zeta_{x0}^{(1)} = 0$	$\zeta_{x1}^{(1)} = -i \frac{N_0^2}{\omega_0} \epsilon_y \partial_Y A$
Spanwise vorticity	$\zeta_{y0}^{(1)} = -\frac{N_0^2 k_0}{\omega_0} A$	$\zeta_{y1}^{(1)} = i \frac{N_0^2}{\omega_0} \epsilon_x \partial_X A$
Vertical vorticity	$\zeta_{z0}^{(1)} = 0$	$\zeta_{z1}^{(1)} = 0$
Pressure	$\frac{1}{\bar{\rho}} p_0^{(1)} = -\frac{N_0^2 - \omega_0^2}{M_0} A$	$\frac{1}{\bar{\rho}} p_1^{(1)} = \frac{1}{M_0} \left[ \frac{N_0^2 - \omega_0^2}{M_0} \epsilon_z \partial_Z + \frac{i}{\omega_0} (N_0^2 - 3\omega_0^2) \mathbf{c}_{g0} \cdot \nabla \right] A$

**Table 8.1:** Expressions for the amplitude envelopes of various fields as they relate to the amplitude envelope,  $A$ , of the vertical displacement field. The centre column contains the leading-order (wave-scale) relationships and the right column contains their respective first-order (envelope-scale) corrections (with respect to  $\epsilon$ ). We have defined  $M_0 := im_0 + 1/2H_\rho$  for convenience. The expressions in the right column are equivalent to the corresponding polarization relations derived in Appendix A.2.2 but with the constants  $\beta_x$ ,  $\beta_y$ , and  $\beta_z$ , given by Eqs. (8.33a)–(8.33c), substituted into the partial differential operator  $\Sigma_\beta$ . By convention, the actual fields are taken to be the real parts of  $e^{i(\mathbf{k}_0 \cdot \mathbf{x} - \omega_0 t)} e^{z/2H_\rho}$  times the tabulated expressions.

### 8.3.2 Divergent-flux induced flow and response flow

We use  $\zeta_{z0}^{(1)} = \zeta_{z1}^{(1)} = 0$  from Table 8.1 in Eq. (8.22) which simplifies to

$$\partial_t(\nabla \times \mathbf{u}_{\text{BF}}) \cdot \hat{\mathbf{e}}_z = \overline{(\boldsymbol{\zeta}^{(1)} \cdot \nabla) w^{(1)}} := F_z \quad (8.27)$$

solved subject to the horizontal nondivergence condition  $\epsilon_x \partial_X u_{\text{BF}} + \epsilon_y \partial_Y v_{\text{BF}} = 0$ , which has been simplified from the full anelastic Bretherton nondivergence condition  $\nabla \cdot (\bar{\rho} \mathbf{u}_{\text{BF}}) = 0$  using the fact that  $w_{\text{BF}} = 0$  at leading order (Bretherton, 1969; Bühler and McIntyre, 1998, 2003; Tabaei and Akylas, 2007; Wagner and Young, 2015; Xie and Vanneste, 2015; van den Bremer and Sutherland, 2018).

The Bretherton flow is now decomposed into the sum of the divergent-flux induced flow and response flow,  $\mathbf{u}_{\text{BF}} = \mathbf{u}_{\text{DF}} + \mathbf{u}_{\text{RF}}$  [cf. Eq. (2.18)]. The divergent-flux induced flow, forced

by the nonlinear advection terms in the momentum equations, is given in flux form by

$$\frac{\partial(\bar{\rho}\mathbf{u}_{\text{DF}})}{\partial t} = -\overline{\nabla \cdot (\bar{\rho}\mathbf{u}^{(1)} \otimes \mathbf{u}^{(1)})}, \quad (8.28)$$

analogous to its Boussinesq counterpart, Eq. (2.19). An explicit expression for Eq. (8.28) is found by substituting into the right-hand side of the leading-order polarization relations and computing the mean. Hence, we find

$$\frac{\partial(\bar{\rho}\mathbf{u}_{\text{DF}})}{\partial t} = -\frac{1}{2}\rho_0 \left( \frac{N_0^2 k_0}{\omega_0} (\epsilon_x c_{gx0} \partial_X + \epsilon_z c_{gz0} \partial_Z) |A|^2, 0, -\omega_0^2 \frac{m_0}{k_0} (\epsilon_x \partial_X - \frac{k_0}{m_0} \epsilon_z \partial_Z) |A|^2 \right), \quad (8.29)$$

where  $|\cdot|$  denotes the modulus. The details leading to Eq. (8.29) are included in Appendix B.2.1. In the equivalent Boussinesq expression (without rotation) derived by vdBS18, it was possible to integrate Eq. (8.29) with respect to time to obtain an explicit expression for  $\mathbf{u}_{\text{DF}}$  itself. The crux of the integration in the nonrotating Boussinesq derivation was the equivalence  $-k_0/m_0 \equiv c_{gz0}/c_{gx0}$  in the third component of the Boussinesq equivalent of Eq. (8.29), after which  $\partial_t \approx -\mathbf{c}_{g0} \cdot \nabla$  was used to convert spatial partial derivatives to temporal ones. Conversely, the above ratio of group speeds does not hold when  $c_{gx0}$  and  $c_{gz0}$  are defined for an anelastic gas with finite  $H_\rho$  by Eqs. (8.24a)–(8.24b), and so we cannot obtain directly an explicit algebraic solution for  $\mathbf{u}_{\text{DF}}$  as it depends on  $|A|^2$ . However, this issue poses no problem because the Bretherton flow is driven by the vertical component of vorticity, hence by the vertical component of the curl of Eq. (8.29), which is independent of  $\partial_t(\bar{\rho}w_{\text{DF}})$ . Consequently, we will eventually use  $\partial_t \approx -\mathbf{c}_{g0} \cdot \nabla$  to perform the time integration, but we defer the solution of Eq. (8.29) until we solve for the components of  $\mathbf{u}_{\text{BF}}$  itself.

Expanding the nonlinear forcing  $F_z$ , given by the right-hand side of Eq. (8.27), up to second-order in  $\epsilon$ , yields

$$F_z = \overline{(\zeta_{x0}^{(1)} + \zeta_{x1}^{(1)})(ik_0 + \epsilon_x \partial_X)(w_0^{(1)} + w_1^{(1)}) + (\zeta_{y0}^{(1)} + \zeta_{y1}^{(1)})\epsilon_y \partial_Y(w_0^{(1)} + w_1^{(1)})}. \quad (8.30)$$

This expression is analogous to that in Eq. (2.22), except there is no explicit derivative with respect to time on the right-hand side of Eq. (8.30) here.<sup>†</sup> Substituting the polarization

<sup>†</sup>The time derivative was applied in Sec 2.2 in the derivation of the vorticity equation governing the evolution of general wave-induced mean flows [cf. Eq. (2.11)]. The terms eliminated by that procedure did not appear ultimately in the vertical component of vorticity which governs the Bretherton flow. The derivative with respect to time was therefore not required to obtain Eq. (8.22).

relations into this expression and computing the mean we find, in sequence,  $(F_z)_0^{(2)} \equiv 0$  and  $(F_z)_1^{(2)} \equiv 0$ . The leading-order nonzero expression is found at  $O(\alpha^2 \epsilon^2)$ , and is given explicitly by

$$\begin{aligned}
(F_z)_2^{(2)} = \frac{1}{4} \rho_0 N_0^2 \frac{k_0}{\omega_0} \epsilon_y \left\{ 2\epsilon_x c_{gx0} \partial_{XY} |A|^2 + 2\epsilon_z c_{gz0} \partial_{YZ} |A|^2 \right. \\
- \epsilon_x c_{gx0} (AA_{XY}^* + A^* A_{XY}) - \epsilon_z c_{gz0} (AA_{YZ}^* + A^* A_{YZ}) \\
- \omega_0 \epsilon_x \beta_x (AA_{XY}^* + A^* A_{XY}) - \omega_0 \epsilon_z \beta_z (AA_{YZ}^* + A^* A_{YZ}) \\
\left. - \omega_0 \epsilon_y \beta_y (AA_{YY}^* + A^* A_{YY}) \right\}, \tag{8.31}
\end{aligned}$$

where  $A^*$  is the complex conjugate of  $A$ . The detailed derivations of the expressions for  $F_z$  at the various orders are provided in Appendix B.2.2. The right-hand side of Eq. (8.31) is analogous to that in Eq. (2.23) without the time derivative, and we have used explicitly the fact that  $A$  is complex.

Using Eq. (8.29) it is straightforward to show that the first two terms on the right-hand side of Eq. (8.31) are equal to  $[\nabla \times \partial_t(\bar{\rho} \mathbf{u}_{\text{DF}})] \cdot \hat{\mathbf{e}}_z$ . Substituting Eq. (8.31) into the right-hand side of Eq. (8.27) and using the Bretherton flow decomposition  $\mathbf{u}_{\text{BF}} = \mathbf{u}_{\text{DF}} + \mathbf{u}_{\text{RF}}$ , then cancelling the  $[\nabla \times \partial_t(\bar{\rho} \mathbf{u}_{\text{DF}})] \cdot \hat{\mathbf{e}}_z$  term on both sides of the resulting expression, we find that

$$\begin{aligned}
\partial_t[\nabla \times (\bar{\rho} \mathbf{u}_{\text{RF}})] \cdot \hat{\mathbf{e}}_z = -\frac{1}{4} \rho_0 N_0^2 \frac{k_0}{\omega_0} \epsilon_y \left\{ \epsilon_x c_{gx0} (AA_{XY}^* + A^* A_{XY}) + \epsilon_z c_{gz0} (AA_{YZ}^* + A^* A_{YZ}) \right. \\
+ \omega_0 \epsilon_x \beta_x (AA_{XY}^* + A^* A_{XY}) + \omega_0 \epsilon_z \beta_z (AA_{YZ}^* + A^* A_{YZ}) \\
\left. + \omega_0 \epsilon_y \beta_y (AA_{YY}^* + A^* A_{YY}) \right\}. \tag{8.32}
\end{aligned}$$

We now use the fact that the response flow is horizontally irrotational (Bretherton, 1969), which imposes values of  $\beta_x$ ,  $\beta_y$ , and  $\beta_z$  so that the right-hand side of Eq. (8.32) is identically zero. Explicitly,

$$\beta_x = -c_{gx0}/\omega_0, \tag{8.33a}$$

$$\beta_y = 0, \tag{8.33b}$$

$$\beta_z = -c_{gz0}/\omega_0. \tag{8.33c}$$

Using Eqs. (8.33a)–(8.33c) in Eq. (8.27) and using explicitly the vertical component of the

curl of Eq. (8.29), we obtain

$$\frac{\partial}{\partial t} [\bar{\rho}(\epsilon_x \partial_X v_{\text{BF}} - \epsilon_y \partial_Y u_{\text{BF}})] = \frac{\partial}{\partial t} \left\{ -\frac{1}{2} \rho_0 N_0 K_0 \epsilon_y \partial_Y |A|^2 \right\}, \quad (8.34)$$

where we used  $\partial_t \approx -\mathbf{c}_{g0} \cdot \nabla$  on the right-hand side to convert spatial derivatives of  $|A|^2$  to a time derivative.

### 8.3.3 Bretherton flow

Integrating Eq. (8.34) with respect to time and dividing the result by  $\bar{\rho}$  we obtain

$$\epsilon_x \partial_X v_{\text{BF}} - \epsilon_y \partial_Y u_{\text{BF}} = -\frac{1}{2} e^{z/H\rho} N_0 K_0 \epsilon_y \partial_Y |A|^2 + \bar{\zeta}_z(\mathbf{x}), \quad (8.35)$$

where  $\bar{\zeta}_z$  represents the (steady) vertical component of the background vorticity present in the domain. In the assumed stationary atmosphere, it follows that  $\bar{\zeta}_z(\mathbf{x}) = 0$ .

A partial differential equation for the horizontal components of  $\mathbf{u}_{\text{BF}}$  is found in a manner similar to that employed in Sec. 2.2.3. In particular, we take derivatives with respect to  $X$  and  $Y$  of Eq. (8.35) and of the anelastic Bretherton nondivergence condition, using this to eliminate mixed partial derivatives of  $u_{\text{BF}}$  and  $v_{\text{BF}}$ . As a result, we obtain the following two Poisson equations:

$$-(\epsilon_x^2 \partial_{XX} + \epsilon_y^2 \partial_{YY}) u_{\text{BF}} = -\frac{1}{2} N_0 K_0 e^{z/H\rho} \epsilon_y^2 \partial_{YY} |A|^2, \quad (8.36)$$

$$(\epsilon_x^2 \partial_{XX} + \epsilon_y^2 \partial_{YY}) v_{\text{BF}} = -\frac{1}{2} N_0 K_0 e^{z/H\rho} \epsilon_x \epsilon_y \partial_{XY} |A|^2. \quad (8.37)$$

These equations are solved using Fourier transforms with respect to the first two components of the unscaled translating coordinates  $(\tilde{x}, \tilde{y}, \tilde{z}) = (X/\epsilon_x, Y/\epsilon_y, Z/\epsilon_z)$ , following the approach in Sec. 2.2.3 and of vdBS18. Denoting by  $\hat{\eta}$  the horizontal Fourier transform of a field  $\eta$ , we define the Fourier transform pair

$$\hat{\eta}(\kappa, \lambda, \tilde{z}) := \frac{1}{(2\pi)^2} \int_{\mathbb{R}^2} \eta(\tilde{\mathbf{x}}) e^{-i(\kappa\tilde{x} + \lambda\tilde{y})} d\tilde{x} d\tilde{y}, \quad (8.38a)$$

$$\eta(\tilde{x}, \tilde{y}, \tilde{z}) := \int_{\mathbb{R}^2} \hat{\eta}(\kappa, \lambda, \tilde{z}) e^{i(\kappa\tilde{x} + \lambda\tilde{y})} d\kappa d\lambda, \quad (8.38b)$$

analogous to Eqs. (2.30a)–(2.30b), where  $\kappa$  and  $\lambda$  are the streamwise and spanwise transform variables, respectively.

Under the change to unscaled variables and then under the Fourier transform,  $\epsilon_x \partial_X \rightarrow \partial_{\tilde{x}} \rightarrow i\kappa$  and  $\epsilon_y \partial_Y \rightarrow \partial_{\tilde{y}} \rightarrow i\lambda$ . Using these with Eqs. (8.36)–(8.37) and inverse transforming the result finally yields the integral expression for the anelastic Bretherton flow,

$$\begin{bmatrix} u_{\text{BF}} \\ v_{\text{BF}} \end{bmatrix} = \frac{1}{2} N_0 K_0 e^{z/H_\rho} \int_{\mathbb{R}^2} \frac{\lambda}{\kappa^2 + \lambda^2} \begin{bmatrix} \lambda \\ -\kappa \end{bmatrix} \widehat{|A|^2} e^{i(\kappa\tilde{x} + \lambda\tilde{y})} d\kappa d\lambda. \quad (8.39)$$

In the Boussinesq limit, this equation recovers Eq. (3.15) of vdBS18. Equation (8.39) represents a nontrivial extension to a uniformly stratified anelastic gas of the solution to Eq. (22) in Tabaei and Akylas (2007), and to Eq. (9.29) of Bühler and McIntyre (1998) in the limit of no background flow or rotation effects.

Although in principle Eq. (8.39) predicts the evolution at early times of the anelastic Bretherton flow induced by sufficiently localized wave packets, in practice we prescribe an initial Gaussian amplitude envelope

$$A(x, y, z, t = 0) = A_0 \exp \left[ -\frac{1}{2} \left( \frac{x^2}{\sigma_x^2} + \frac{y^2}{\sigma_y^2} + \frac{z^2}{\sigma_z^2} \right) \right]. \quad (8.40)$$

We square the amplitude envelope, and Fourier transform the result using Eq. (8.38a) to find conveniently that

$$\widehat{|A|^2} = \frac{1}{4\pi} \sigma_x \sigma_y A_0^2 e^{-z^2/\sigma_z^2} \exp \left[ -\frac{1}{4} (\sigma_x^2 \kappa^2 + \sigma_y^2 \lambda^2) \right]. \quad (8.41)$$

The horizontal components of the corresponding Bretherton flow are found numerically upon substituting this expression into Eq. (8.39).

Vertical cross sections of initial nondimensionalized Bretherton flow,  $\tilde{u}_{\text{BF}}(x, 0, z, t = 0) = u_{\text{BF}}(x, 0, z, 0)/(N_0/k_0)$ , are shown in Fig. 8.1 for wave packets with  $\sigma_x = \sigma_y = \sigma_z = 10k_0^{-1}$  in a uniformly stratified anelastic gas with density scale height  $H_\rho = 10k_0^{-1}$ . The wave packet was initialized using Eq. (8.40) with  $A_0 = 0.05k_0^{-1}$  and  $m_0/k_0 = -0.7$ , corresponding to waves propagating initially with approximately the fastest vertical group speed at an angle of  $\Theta_0 = \tan^{-1} |m_0/k_0| \approx 35^\circ$  to the vertical. The solid and dashed black curves in each panel, defined by  $(x/\sigma_x)^2 + (z/\sigma_z)^2 = a^2$ , indicate  $a = 1$  and  $a = 2$  standard deviations about the wave packet centre, respectively. Fig. 8.1(a) shows the Bretherton flow with the effect of anelastic growth scaled out, and is similar to the vertical structure of the Bretherton flow induced by a Boussinesq wave packet. For comparison, Fig. 8.1(b) shows the Bretherton flow

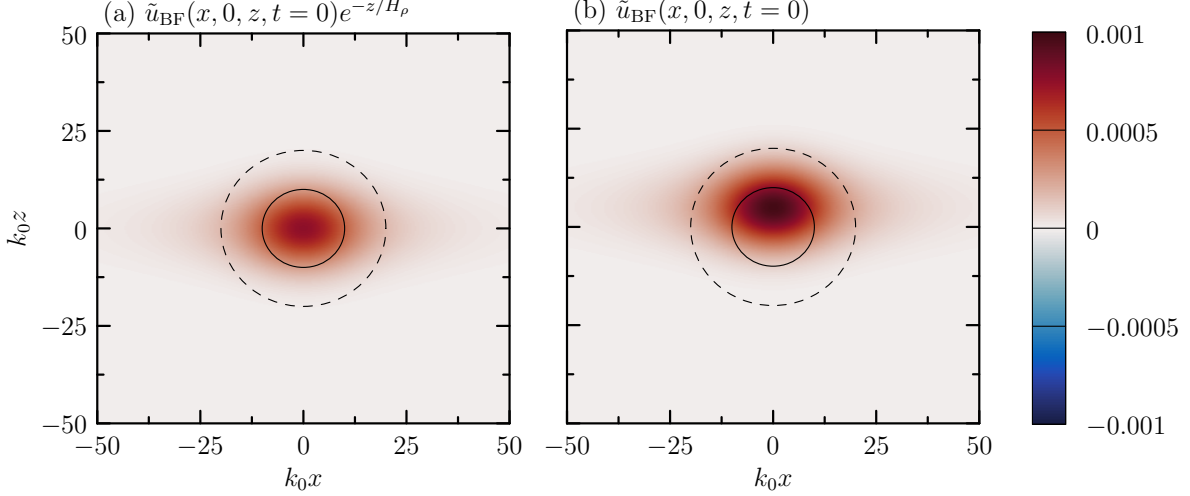


**Figure 8.1:** Vertical slices of the initial nondimensionalized Bretherton flow,  $\tilde{u}_{\text{BF}} = u_{\text{BF}}(x, 0, z, t = 0)/(N_0/k_0)$ , given by Eq. (8.39), in an anelastic gas with  $H_\rho = 10k_0^{-1}$ , where the anelastic growth factor is (a) scaled out; and, (b) retained. The wave packet shown was initialized with a peak vertical displacement amplitude of  $A_0 = 0.05k_0^{-1}$ , a relative vertical wavenumber of  $m_0/k_0 = -0.7$ , and a spatial extent  $\sigma_x = \sigma_y = \sigma_z = 10k_0^{-1}$ . Solid and dashed black curves show the first and second standard deviations, respectively, of the Gaussian wave packet.

including anelastic growth by the factor  $e^{z/H_\rho}$ . Qualitatively, this factor tends to skew the region of strongest Bretherton flow toward the leading flank of the wave packet. Anelastic growth acts to increase the magnitude of the Bretherton flow above  $z_0$ , visible in the more intense colouring compared to Fig. 8.1(a). In particular, the peak magnitude of the Bretherton flow in Fig. 8.1(b) is 28% greater than that in Fig. 8.1(a).

## 8.4 Propagation of wave packets through a nonuniform background shear flow

The linear theory of internal gravity wave packet propagation in a uniformly stratified Boussinesq fluid with a horizontally homogeneous but vertically nonuniform background shear flow was presented in Sec. 5.1. Here, we review briefly the linear theory in the context of an anelastic gas, then derive critical amplitudes for partial transmission and tunnelling of moderately large amplitude waves following the approach in Sec. 5.2.

### 8.4.1 Linear theory

Crucially, the background flow acts to Doppler-shift the intrinsic frequency  $\omega_0$ , given by Eq. (8.23), with the resulting Doppler-shifted frequency given by

$$\Omega = \omega_0 - k_0 \bar{u},$$

analogous to Eq. (5.2). Qualitatively, the background flow advects the waves in the streamwise direction, altering the path of the wave packet as it propagates through the nonuniform background flow.

Starting from an initial position  $(x_0, 0, z_0)$ , the path traced by the centroid of a small amplitude wave packet through a uniformly stratified anelastic gas is predicted, using ray theory, by the solution of the differential equations

$$\frac{dx}{dt} = c_{gx}(m(z)) + \bar{u}(z), \quad (8.42a)$$

$$\frac{dz}{dt} = c_{gz}(m(z)), \quad (8.42b)$$

provided  $\bar{u}$  does not change significantly over a vertical wavelength (e.g. Sutherland, 2010, Sec. 6.5). According to Eqs. (8.42a)–(8.42b), the position of the wave packet is determined by the background flow and the local group velocity  $\mathbf{c}_g = (c_{gx}, 0, c_{gz})$ , where

$$c_{gx} = \frac{N_0(K^2 - k_0^2)}{K^3} \quad (8.43a)$$

$$c_{gz} = -\frac{N_0 k_0 m}{K^3}, \quad (8.43b)$$

where  $K = (k_0^2 + m^2 + 1/4H_\rho^2)^{1/2}$ . The lack of subscript on  $m$  in Eqs. (8.42a)–(8.43b) indicates that the vertical wavenumber is not fixed, but varies with height in response to Doppler-shifting by the background flow [cf. Eq. (5.5)]. Explicitly,

$$m = m(z(t)) = \text{sign}(m) k_0 \sqrt{\frac{N_0^2}{\Omega^2(z(t))} - 1}, \quad (8.44)$$

where  $\text{sign}(m) = -1$  and  $+1$  correspond, respectively, to upward- ( $c_{gz} > 0$ ) and downward-propagating waves ( $c_{gz} < 0$ ), according to Eq. (8.43b).

The height  $z_r$  and time  $t_r$  at which an initially upward-propagating wave packet is anticipated to reflect are diagnosed from the numerical solution of Eqs. (8.42a)–(8.42b), subject

to the initial condition  $(x(t_0), 0, z(t_0)) = (x_0, 0, z_0)$ , with  $k_0 > 0$  and  $m(z_0) = m_0 < 0$ . It is necessary to solve Eqs. (8.42a)–(8.42b) numerically because these differential equations lack analytically tractable solutions for general background flow profiles  $\bar{u}(z)$ . Details of the numerical solution procedure are provided in Appendix D.

The reflection behaviour described above is anticipated to be modified significantly by nonlinear interactions with the Bretherton flow, as described below.

### 8.4.2 Reflection level penetration

In the study of transmission and reflection of one- and two-dimensional wave packets in a uniformly stratified Boussinesq fluid with uniform shear flow, Sutherland (2000) found that wave packets could transmit partially above the reflection level predicted by linear theory, provided the vertical shear in the wave-induced mean flow was somewhere greater than the background shear. A similar result was found in Part II for three-dimensional wave packets propagating in a nonuniform background shear flow. Mathematically, the penetration condition for three-dimensional wave packets, whose induced mean flow is the Bretherton flow, is given by

$$\left| \frac{\partial u_{\text{BF}}}{\partial z} \right| > |s_0|, \quad (8.45)$$

analogous to Eq. (5.7). To derive the critical amplitude for partial penetration above the reflection level predicted by linear theory, we follow the approach of Sec. 5.2. We consider solutions of Eq. (8.45) for initially trivariate Gaussian wave packet envelopes, given in terms of vertical displacement by Eq. (8.40).

At a given height, the peak magnitude of  $|u_{\text{BF}}|$ , hence also that of  $|\partial u_{\text{BF}}/\partial z|$ , is located at the horizontal centre of the wave packet. With this consideration, using Eq. (8.41) in the streamwise component of Eq. (8.39), then setting  $(x, y) = (0, 0)$ , we obtain the vertical profile of the largest Bretherton flow. Explicitly,

$$\max_{x,y} |u_{\text{BF}}| = \frac{1}{2} N_0 K_0 \frac{A_0^2}{R_y + 1} e^{-z^2/\sigma_z^2} e^{z/H_\rho}, \quad (8.46)$$

where  $R_y = \sigma_y/\sigma_x$  is the spanwise aspect ratio of the wave packet.

Differentiating Eq. (8.46) with respect to  $z$  yields a vertical profile of largest wave-induced

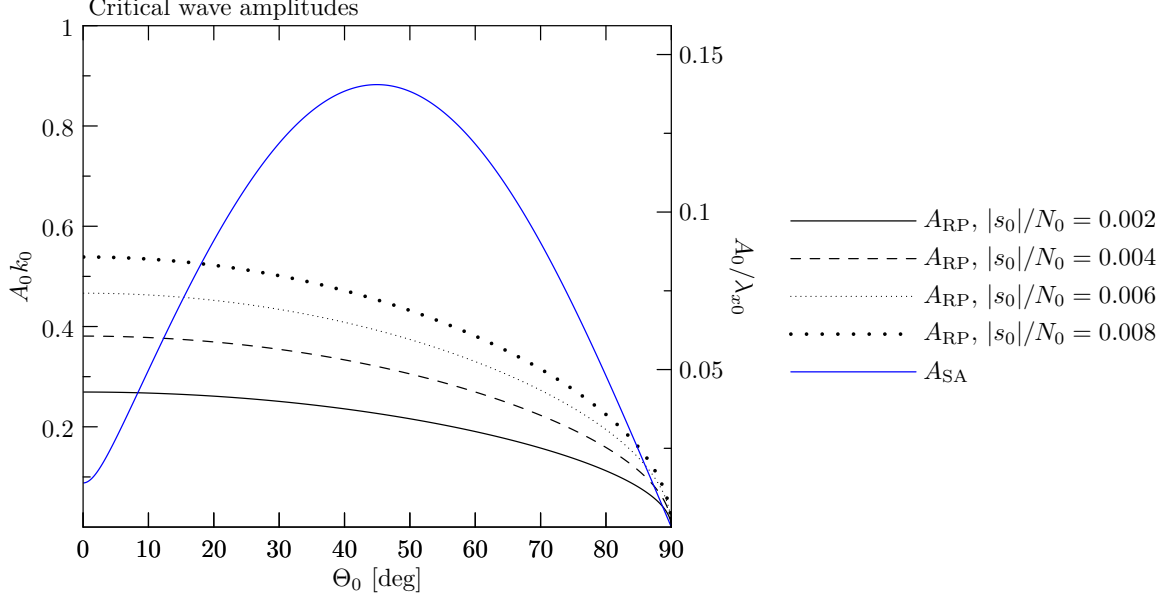


**Figure 8.2:** Critical amplitudes for wave packets with amplitude envelope given initially by Eq. (8.40) for: (black curves) reflection level penetration  $A_{\text{RP}}$ , given by Eq. (8.47) for a range of shear strength parameters  $|s_0|/N_0$ ; and, (blue curve) instability due to self-acceleration  $A_{\text{SA}}$ , given by Eq. (8.53), as a function of initial wave packet propagation angle  $\Theta_0 = \tan^{-1} |m_0/k_0|$  to the vertical. All curves are plotted with  $\sigma_x = \sigma_y = \sigma_z = 10k_0^{-1}$  and  $H_\rho = 10k_0^{-1}$  fixed.

mean shear,

$$s_{\text{BF}} := \frac{d}{dz} \max_{x,y} |u_{\text{BF}}| = -\frac{1}{2} N_0 K_0 \frac{A_0^2}{R_y + 1} \left[ 2 \frac{z}{\sigma_z^2} - \frac{1}{H_\rho} \right] e^{-z^2/\sigma_z^2} e^{z/H_\rho}.$$

Differentiating  $s_{\text{BF}}$  with respect to  $z$  and setting the result equal to zero, it is straightforward but somewhat tedious to show that the induced mean shear profile is maximized at  $z = \frac{1}{2} \sigma_z^2 (1/H_\rho - \sqrt{2}/\sigma_z)$ , with corresponding maximum

$$\frac{1}{R_y + 1} \frac{N_0 K_0}{\sqrt{2e\sigma_z}} A_0^2 e^{\sigma_z^2/(4H_\rho^2)}.$$

Substituting this into Eq. (8.45) yields the critical amplitude,  $A_{\text{RP}}$ , above which fully localized Gaussian wave packets are anticipated to penetrate partially above the reflection level predicted by linear theory:

$$A_{\text{RP}} = \sqrt{\frac{\sigma_z (R_y + 1) \sqrt{2e} |s_0|}{K_0 e^{\sigma_z^2/(4H_\rho^2)} N_0}}. \quad (8.47)$$

This critical amplitude is plotted for a range of shear strength parameters  $|s_0|/N_0$  as the black curves in Fig. 8.2, with  $H_\rho = 10k_0^{-1}$ ,  $R_y = 1$  and  $\sigma_z = 10k_0^{-1}$  fixed.

In the Boussinesq limit, Eq. (8.47) recovers the expression for the reflection level pene-

tration amplitude of waves in a uniformly stratified Boussinesq fluid, given by Eq. (5.10). For finite values of  $H_\rho$ , Eq. (8.47) quantifies the role of anelastic growth that one anticipates intuitively, namely, that  $A_{\text{RP}}$  is smaller relative to its Boussinesq counterpart, the difference accounted for by exponential amplitude growth with height in an anelastic atmosphere. In particular, the ratio of Eq. (8.47) and Eq. (5.10) is

$$\underbrace{\left[ \frac{k_0^2 + m_0^2}{k_0^2 + m_0^2 + \frac{1}{4H_\rho^2}} \right]^{1/4}}_{\approx 1} e^{-\sigma_z^2/(8H_\rho^2)} \approx e^{-\sigma_z^2/(8H_\rho^2)}.$$

Using typical values of  $\sigma_z \approx H_\rho = O(10k_0^{-1})$ , the factor  $e^{-\sigma_z^2/(8H_\rho^2)}$  indicates that anelastic growth accounts for a reduction in predicted penetration amplitude to about 88% of the corresponding Boussinesq value.

### 8.4.3 Internal wave tunnelling

In general, a reflection level is predicted at the height where the wave frequency (or the Doppler-shifted frequency, if one considers a fluid with nonzero background flow) equals the local buoyancy frequency. Although we have focused so far on partial transmission of waves above a reflection level that exists due to a retrograde shear flow in a uniformly stratified fluid (in which  $N = N_0$  is constant), recall that a reflection level is similarly predicted in a nonuniformly stratified fluid in which  $N = N(z)$  decreases with height. In either context, in order to apply ray theory to predict the height of the reflection level, it is assumed that the background state (e.g., the background flow, as in Secs. 5.2 and 8.4.2) varies slowly with height relative to the wavelength of the waves.

Conversely, in the context of nonuniform stratification in particular, if  $N(z)$  decreases rapidly, linear theory predicts a phenomenon called *internal wave tunnelling*,<sup>‡</sup> provided the region of weakened stratification is not too broad (Sutherland, 2010). Whereas ray theory predicts incorrectly (on account of the rapid change in  $N$ ) that waves incident upon the region of weak stratification should reflect, instead the vertical wavenumber can become complex so that the wave amplitude decays exponentially in the region of weak stratification. The waves

---

<sup>‡</sup>Internal wave tunnelling is so named because this phenomenon is directly analogous to quantum tunnelling but for classical waves, as described theoretically and demonstrated in laboratory experiments by Sutherland and Yewchuk (2004).

are said to be evanescent in such regions. Provided  $N$  decays sufficiently that  $N^2(z) < \omega_0^2$ , exponential amplitude decay is predicted directly from Eq. (8.44), which sets the local value of the vertical wavenumber according to

$$m \propto \sqrt{\frac{N^2(z)}{\omega_0^2} - 1}.$$

For clarity, we have set  $\Omega = \omega_0$ , and thus we have considered tunnelling in the relatively simple context of a stationary fluid.

By analogy with a fluid in which  $N(z)$  decreases over a finite depth, we now consider internal wave tunnelling in a uniformly stratified fluid in which the magnitude of the background flow increases relatively rapidly over a finite vertical distance below which it decreases again. The motivating geophysical situation is the upward propagation of internal waves as they encounter a jetlike retrograde flow representing the Quasi-Biennial Oscillation (QBO). In this case waves become evanescent if the retrograde background flow is of sufficient magnitude that  $\Omega^2(z) > N_0^2$  according to Eq. (8.44):

$$m \propto \sqrt{\frac{N_0^2}{[\omega_0 - k_0 \bar{u}(z)]^2} - 1}, \quad (8.48)$$

where we have explicitly retained the effect of the background flow. The critical minimum magnitude of the background flow that ensures waves become evanescent,  $\bar{u}_c$ , is found by setting the discriminant of Eq. (8.48) equal to zero, from which we find

$$\bar{u}_c = -\frac{N_0 - \omega_0}{k_0}. \quad (8.49)$$

Transmission and reflection of internal waves propagating in a retrograde shear flow satisfying Eq. (8.49) was studied in a Boussinesq fluid by [Brown and Sutherland \(2007\)](#) and in an anelastic gas by [Nault and Sutherland \(2008\)](#). In particular, the transmission coefficient was defined as the ratio of transmitted to incident pseudoenergy flux, equivalent to

$$T_{\mathcal{E}} := 1 - \frac{|A^-|^2}{|A^+|^2}, \quad (8.50)$$

where  $A^-$  and  $A^+$  were the amplitudes of the reflected and incident waves found numerically at the bottom of the domain [[Nault and Sutherland \(2008\)](#), Eq. (15)]. Assuming the waves

were purely two-dimensional and monochromatic, the amplitudes were diagnosed from the numerical solution to the anelastic Taylor–Goldstein equation (Gossard and Hooke, 1975),

$$\psi'' + \frac{1}{H_\rho} \psi' + k_0^2 \left( \frac{N_0^2}{\Omega^2} + \frac{\bar{u}''}{k_0 \Omega} + \frac{\bar{u}'}{k_0 \Omega H_\rho} - 1 \right) \psi = 0, \quad (8.51)$$

where  $\psi = \psi(z)$  is the vertical structure of the mass-streamfunction  $\Psi(x, z, t) = \psi(z)e^{i(k_0 x - \omega_0 t)}$ , defined implicitly by

$$u = -\frac{1}{\bar{\rho}} \frac{\partial \Psi}{\partial z},$$

$$w = \frac{1}{\bar{\rho}} \frac{\partial \Psi}{\partial x}.$$

The reason to adopt the simplified approach of Nault and Sutherland (2008) is to predict transmission and reflection of wave packets to inform the choice of parameters for fully non-linear numerical simulations using model profiles of the QBO, elaborated upon in Secs. 8.6 and 8.7.

## 8.5 Wave packet self-acceleration

In Sec. 2.3.3 we adapted the approach of Sutherland (2001) to predict the amplitude at which a fully localized wave packet in a rotating uniformly stratified Boussinesq fluid was prone to self-acceleration instability [cf. Eq. (2.41)]. In Sec. 5.2 we evaluated Eq. (2.41) in the nonrotating limit to predict a lower bound for the initial amplitudes of wave packets that were prone to eventually overturn due to self-acceleration instability [cf. Eq. (5.11)]. The practical reason to establish that bound was to guide the choice of initial amplitudes used in numerical simulations to avoid simulating waves that overturned (hence leading to numerical instability and rapid blowup) prior to attaining significant quasisteady transmission above the reflection level. Conversely, the anelastic code is equipped to model the relatively small-scale turbulent wave breaking that follows shortly after overturning (elaborated upon in detail in Sec. 9.5), thus eliminating the restriction to waves that evolve to remain below overturning amplitude. The removal of this restriction is important in particular for waves in an anelastic gas whose amplitude grows exponentially with height.

To derive an expression for the critical amplitude for self-acceleration, we again take the

approach of [Sutherland \(2001\)](#), who proposed somewhat heuristically that one-dimensional wave packets were prone to self-acceleration if their wave-induced mean flow was somewhere greater than their streamwise group speed. For three-dimensional wave packets in a uniformly stratified anelastic gas, whose wave-induced mean flow is the Bretherton flow, it is necessary to compare  $c_{gx0}$  with  $\max\{u_{\text{BF}}(\mathbf{x}, 0)\}$ . The critical amplitude for self-acceleration,  $A_{\text{SA}}$ , is then given generally by

$$A_{\text{SA}} = A_0 \sqrt{\frac{c_{gx0}}{u_{\text{BF}}(\mathbf{x}^*, 0)}}, \quad (8.52)$$

where  $\mathbf{x}^*$  is the point at which  $u_{\text{BF}}$  is maximized initially. For a Gaussian wave packet, with amplitude envelope given by Eq. (8.40), using Eq. (8.46) it is straightforward to show that the maximum Bretherton flow is located initially at  $\mathbf{x}^* = (0, 0, \sigma_z^2/2H_\rho)$ . Using this maximizer in the first row of Eq. (8.39) and substituting the result into Eq. (8.52), we find that the critical amplitude for self-acceleration is

$$A_{\text{SA}} = \sqrt{\frac{2(K_0^2 - k_0^2)(R_y + 1)}{K_0^4 e^{\sigma_z^2/(4H_\rho^2)}}}. \quad (8.53)$$

This critical amplitude is plotted as the blue curve in Fig. 8.2, with  $H_\rho = 10k_0^{-1}$ ,  $R_y = 1$  and  $\sigma_z = 10k_0^{-1}$  fixed.

In the Boussinesq limit, the expression in Eq. (8.53) recovers that in Eq. (5.11). Comparing Eq. (8.53) with its Boussinesq counterpart we find that, except for waves with frequency near  $N_0$ , the role of anelastic growth is to reduce the critical amplitude by a factor of approximately  $e^{-\sigma_z^2/(8H_\rho^2)}$ . Conversely, for waves with frequency approaching  $N_0$ , corresponding to waves propagating initially at an angle approaching  $\Theta_0 = 0^\circ$ , the critical amplitude tends toward a nonzero value. This behaviour is unlike waves in a Boussinesq fluid, for which  $A_{\text{SA}} \rightarrow 0$  as  $\Theta_0 \rightarrow 0$ , and are therefore unstable to self-acceleration at any amplitude.

Like internal gravity waves in a Boussinesq fluid, self-acceleration can drive anelastic internal waves to overturning amplitudes. By analogy with waves in a Boussinesq fluid, anelastic waves are said to be overturning if they are of such large amplitude that potentially cooler fluid is lifted over potentially warmer fluid. As a result the gradient of the total potential temperature is negative somewhere in the fluid:  $d\bar{\theta}(z)/dz + \partial\theta(\mathbf{x}, t)/\partial z < 0$ . Recasting this inequality in terms of vertical displacement using Eq. (8.11), multiplying the result by  $g/\bar{\theta}$ ,

and using Eq. (8.16), we obtain the anelastic overturning condition,

$$N_T^2(\mathbf{x}, t) := N_0^2 + \Delta N^2 = N_0^2 - N_0^2 \frac{\partial \xi}{\partial z} - M^2 \xi < 0, \quad (8.54)$$

where we have defined  $M^2 := (g/\bar{\theta})\bar{\theta}''$  for convenience. In a uniformly stratified anelastic gas,  $\bar{\theta}$  is given by Eq. (8.5), and so  $M^2 = M_0^2 = N_0^2/H_\theta$ , hence  $\Delta N^2 = -N_0^2(\frac{\partial \xi}{\partial z} + \frac{1}{H_\theta}\xi)$ . If one then substitutes a plane wave solution into Eq. (8.54) to predict the critical amplitude at which a wave will overturn, one finds that

$$A_{\text{OT}}(z) = \left[ \frac{1}{H_*} \cos(\varphi_0) - m_0 \sin(\varphi_0) \right]^{-1} e^{-z/2H_\rho}$$

where we have defined  $1/H_* := 1/2H_\rho + 1/H_\theta$  for convenience. The dependence of  $A_{\text{OT}}$  on height predicts anelastic waves to overturn at lower amplitudes as they propagate upward in the fluid. Although overturning of anelastic waves is not the focus of this study, Eq. (8.54) provides a useful diagnostic which will be applied in the numerical code, described in Chapter 9.

## 8.6 Idealized modelling of the Quasi-Biennial Oscillation

The physical context in which we study wave packets in an anelastic atmosphere is the propagation of waves incident upon the QBO wind. By convention our coordinate system is oriented such that the direction of forward wave propagation in space corresponds to propagation along the positive  $x$  axis, which can be taken geographically to point east. With this orientation a *retrograde* background flow refers to one which flows in the direction opposite to the streamwise phase speed,  $c_{px}$ . The easterly (westerly) phase of the QBO characterizes such a background flow when  $c_{px} > 0$  ( $c_{px} < 0$ ). In practice, both QBO phases can be set up with  $\bar{u} \leq 0$ ; results corresponding to the westerly phase of the QBO can then be reflected about the  $z$ -axis in postprocessing. To that end, here we describe our use of observational QBO wind data to obtain idealized model QBO wind profiles.

### 8.6.1 Data selection

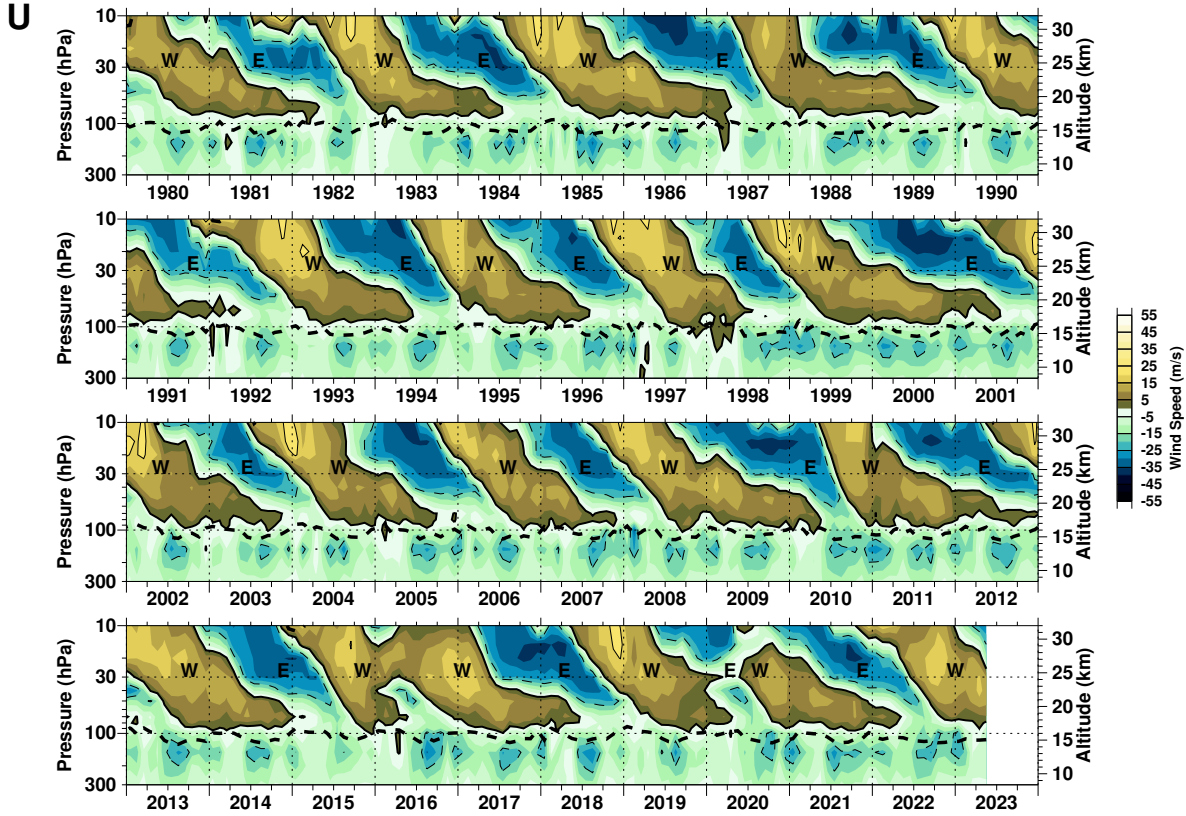
The data are derived from vertical profiles of zonal wind measured twice daily by radiosondes launched at the Meteorological Service Singapore Upper Air Observatory, located at 1.34041N, 103.888E (Newman, 2023). The processed wind data available online, denoted here by  $u_{\text{obs}}$ , consisted of the monthly-mean of the raw data interpolated spatially to missing pressure levels, and interpolated temporally to missing pressure levels above the top of the radiosonde profile. The data online were reported at fourteen pressure levels from 300 hPa to 10 hPa. A vertical time series of the processed data is shown in Fig. 8.3. Typical profiles of the QBO easterly phase (QBO-E) were identified somewhat heuristically from a visual inspection of Fig. 8.3 as those profiles within the easterly flow regime such that the flow speed was as close to  $0 \text{ m s}^{-1}$  as practical at 300 hPa and 10 hPa. Typical profiles of the QBO westerly phase (QBO-W) were identified in a similar manner. For the time being we will refer only to QBO-E profiles to describe the QBO modelling process, and comment on QBO-W afterwards.

### 8.6.2 Data postprocessing

The selected QBO-E profiles were first converted to use height as the vertical coordinate as opposed to pressure. This was done by assuming the atmosphere was isothermal and that its background state was in hydrostatic balance. Under these assumptions the background pressure profile is given by  $\bar{p}(z) = p_0 e^{-z/H_\rho}$  [cf. Eq. (8.3)]. The density scale height  $H_\rho$  was determined by assuming the atmosphere was uniformly stratified so that the buoyancy frequency was constant. In particular, we set  $N_0 = 0.02 \text{ s}^{-1}$  as this is a typical value in the stratosphere (e.g., Pedlosky, 1987). Then, using the definition of the squared buoyancy frequency for an anelastic gas, given by Eq. (8.16), and the relationship between the scale heights for density and potential temperature, we find

$$H_\rho = \frac{2}{7} H_\theta = \frac{2}{7} \frac{g}{N_0^2} \approx 7.0 \text{ km},$$

where we assumed  $g = 9.81 \text{ m s}^{-2}$  is an appropriate magnitude of the acceleration of gravity in the stratosphere. Using a reference pressure of  $p_0 = 1000 \text{ hPa}$  (corresponding approximately to the pressure at ground level), this procedure yields a pressure-to-height conversion effectively



Paul A. Newman, Larry Coy, Leslie R. Lait, Eric R. Nash (NASA/GSFC) Fri Jun 2 16:20:02 2023

**Figure 8.3:** Vertical time series of monthly-mean zonal QBO winds measured by radiosondes launched from the Meteorological Service Singapore Upper Air Observatory (Newman, 2023). The westerly and easterly phases of the QBO are denoted by W and E, respectively. The heavy dashed line indicates the estimated tropopause height calculated from the measured thermal lapse rate.

identical to that obtained independently in Fig. 8.3. Having recast the profiles as a function of height, we compute a simple average of QBO-E and QBO-W profiles, denoting the result by  $\bar{u}_{\text{obs}}$ . The selected QBO-E profiles are shown with the mean profile superimposed in Fig. 8.4(a).

### 8.6.3 Model QBO profile

The mean QBO-E profile shows two easterly jetlike features. The lowermost peak, centred at  $z = 13.3$  km, corresponds to a prevailing tropospheric easterly wind, and will be ignored. The uppermost peak, centred at  $z_{\bar{u}} := z = 27.4$  km, corresponds to the QBO-E profile we wish to model. The model is a Gaussian curve of the form

$$\bar{u}(z) = a_{\bar{u}} \exp[-(z^*/2\sigma_{\bar{u}}^2 + z^*/\gamma_{\bar{u}})], \quad (8.55)$$

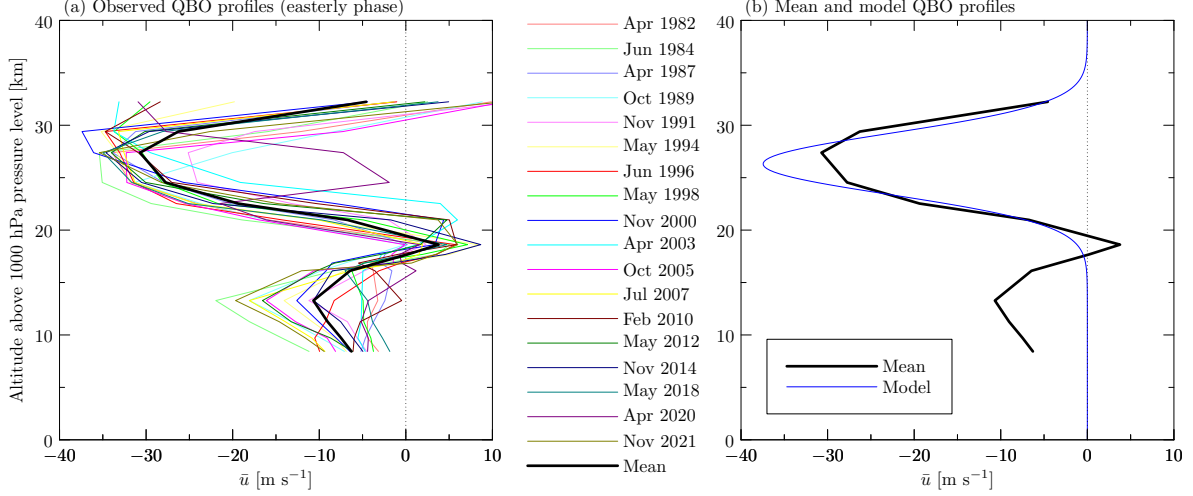


**Figure 8.4:** Profiles of the QBO-E monthly-mean zonal wind velocity (a) obtained from measurements by radiosondes launched from the Meteorological Service Singapore Upper Air Observatory (Newman, 2023); and, (b) modelled using a least-squares fit to a Gaussian curve of the form given by Eq. (8.55).

where we defined  $z^* := z - z_{\bar{u}}$ , and the parameters  $a_{\bar{u}}$ ,  $\sigma_{\bar{u}}$ , and  $\gamma_{\bar{u}}$  are, respectively, the velocity at  $z = z_{\bar{u}}$ , vertical extent, and offset correction, to be determined using a least-squares fit. The offset correction is necessary to account for distinct peak altitudes in the mean and model profiles. Although Eq. (8.55) is equivalent to a shifted Gaussian (in which the vertical shift  $z_{\bar{u}}$  is unknown and  $\gamma_{\bar{u}} = \infty$ ), to estimate  $z_{\bar{u}}$  one would need to solve a system of nonlinear optimization equations involving products of  $z_{\bar{u}}$  and  $\sigma_{\bar{u}}$ . The use of the offset correction avoids this entirely.

In order to apply the least-squares fit, we only use data corresponding to  $|\bar{u}_{\text{obs}}|$  at altitudes  $z \geq 20.97$  km, thus effectively ignoring the lowermost jet. It is necessary to use the magnitude of  $\bar{u}_{\text{obs}}$  so that  $\ln |\bar{u}|$ , which is a quadratic polynomial in  $z^*$ , may be fit using *linear* least squares (e.g., Burden and Faires, 2010). The corresponding least-squares error is defined by

$$E_2 := \frac{1}{2} \sum_{j=1}^n [\hat{u}_{\text{obs}}(z_j^*) - \hat{u}(z_j^*)]^2,$$

in which we have defined  $\hat{u} := \ln |\bar{u}|$ ,  $\hat{u}_{\text{obs}} := \ln |\bar{u}_{\text{obs}}|$ , and  $\hat{a}_{\bar{u}} := \ln |a_{\bar{u}}|$  for convenience. The error  $E_2$  is minimized with respect to the fitting parameters by setting  $\partial E_2 / \partial \hat{a}_{\bar{u}} = 0$ ,

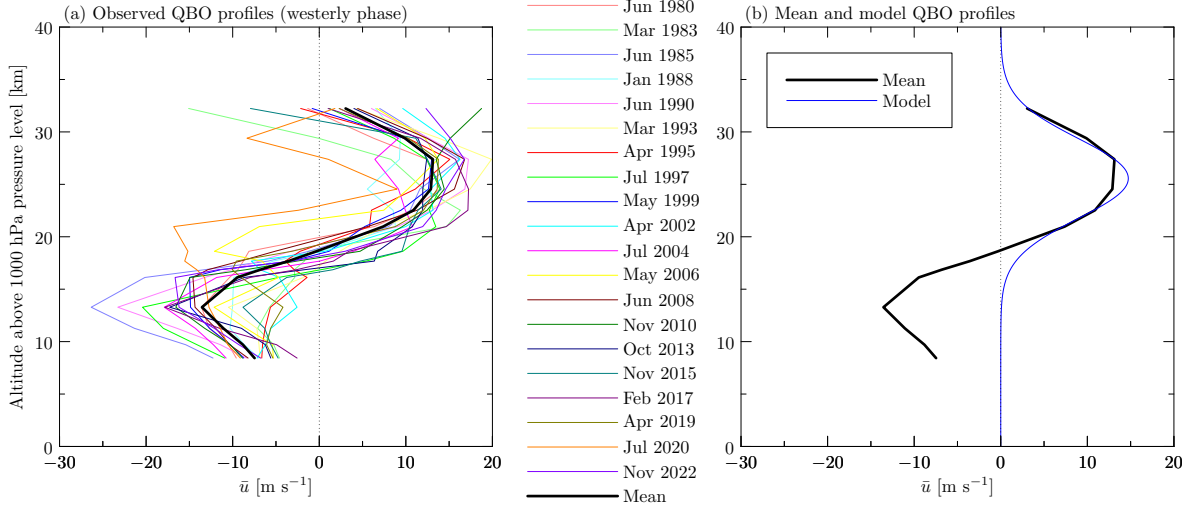


**Figure 8.5:** As in Fig. 8.4 but for the westerly phase of the QBO.

$\partial E_2 / \partial \sigma_{\bar{u}}^{-2} = 0$ , and  $\partial E_2 / \partial \gamma_{\bar{u}}^{-1} = 0$ , yielding the system of equations

$$\begin{bmatrix} n & -\frac{1}{2} \sum_{j=1}^n z_j^{*2} & -\sum_{j=1}^n z_j^* \\ \frac{1}{2} \sum_{j=1}^n z_j^{*2} & -\frac{1}{4} \sum_{j=1}^n z_j^{*4} & -\frac{1}{2} \sum_{j=1}^n z_j^{*3} \\ \sum_{j=1}^n z_j^* & -\frac{1}{2} \sum_{j=1}^n z_j^{*3} & -\sum_{j=1}^n z_j^{*2} \end{bmatrix} \begin{bmatrix} \hat{a}_{\bar{u}} \\ \frac{1}{\sigma_{\bar{u}}^2} \\ \frac{1}{\gamma_{\bar{u}}} \end{bmatrix} = \begin{bmatrix} \sum_{j=1}^n \hat{u}_{\text{obs}}(z_j^*) \\ \frac{1}{2} \sum_{j=1}^n \hat{u}_{\text{obs}}(z_j^*) z_j^{*2} \\ \sum_{j=1}^n \hat{u}_{\text{obs}}(z_j^*) z_j^* \end{bmatrix},$$

from which the parameter values are found. In particular, we find  $a_{\bar{u}} = -e^{\hat{a}_{\bar{u}}} = -35 \text{ m s}^{-1}$ ,  $\sigma_{\bar{u}} = 2.93 \text{ km}$ , and  $\gamma_{\bar{u}} = 8.00 \text{ km}$ . Using these values and completing the square in the exponential term in Eq. (8.55), the QBO-E model is equivalent to

$$\bar{u}(z) = \bar{u}_0 \exp \left[ -\frac{1}{2\sigma_{\bar{u}}^2} \left( z^* + \frac{\sigma_{\bar{u}}^2}{\gamma_{\bar{u}}} \right)^2 \right], \quad (8.56)$$

where we have defined the peak velocity  $\bar{u}_0 := a_{\bar{u}} \exp(\sigma_{\bar{u}}^2 / 2\gamma_{\bar{u}}^2) = -37.5 \text{ m s}^{-1}$ . The model parameters are summarized in Table 8.2. Expressing the model as in Eq. (8.56) makes explicit that the model peak is offset below (above) the peak in the mean profile by a distance equal to  $\sigma_{\bar{u}}^2 / \gamma_{\bar{u}} > 0$  ( $< 0$ ). Using the fitted parameters,  $\sigma_{\bar{u}}^2 / \gamma_{\bar{u}} = 1.1 \text{ km}$ .

The QBO-E model given by Eq. (8.56) is compared with the mean QBO-E profile in Fig. 8.4(b). The model agrees well qualitatively with the upper easterly jet in the mean profile, except for its peak velocity, which exceeds the peak of the mean profile by 22%, but

Model	Fitted parameters			Derived parameters		
	$a_{\bar{u}}$ [m s <sup>-1</sup> ]	$\sigma_{\bar{u}}$ [km]	$\gamma_{\bar{u}}$ [km]	$\bar{u}_0$ [m s <sup>-1</sup> ]	$\sigma_{\bar{u}}^2/\gamma_{\bar{u}}$ [km]	Peak altitude [km]
QBO-E	-35.0	2.9	8.0	-37.5	1.1	26.3
QBO-W	13.1	3.8	8.0	14.7	1.8	25.6

**Table 8.2:** QBO model parameters obtained by least-squares fitting the mean upper QBO-E/W jet above  $z = 20.97$  km to the model given by Eq. (8.55). The peak speed  $\bar{u}_0$  of the model was found from the fitted parameters according to  $\bar{u}_0 = a_{\bar{u}} \exp(\sigma_{\bar{u}}^2/2\gamma_{\bar{u}}^2)$ , and the corresponding altitude was found by subtracting  $\sigma_{\bar{u}}^2/\gamma_{\bar{u}}$  from  $z_{\bar{u}} = 27.4$  km. Note that the peak altitudes are above the 1000 hPa pressure level.

is nonetheless within the range of observed QBO-E values.

A procedure similar to the one described above was used to obtain a model QBO-W profile. Profiles of QBO-W derived from radiosonde measurements, identified visually from Fig. 8.3, are shown in Fig. 8.5(a) with the corresponding mean profile superimposed. Selected profiles, chosen such that the flow at the top was near zero whenever practical, correspond to the times when the QBO begins transitioning from the westerly to easterly phase. Like the mean QBO-E profile, the mean QBO-W profile shows two jetlike features, but with opposite signs. The lowermost peak, centred at  $z = 13.3$  km (the same altitude as the corresponding peak in the mean QBO-E profile), corresponds to a prevailing tropospheric easterly wind (to be ignored in the model), with magnitude  $13.5$  m s<sup>-1</sup> (compared to  $10.7$  m s<sup>-1</sup> for the QBO-E mean profile). The QBO-W mean profile has a broad peak with magnitude  $12.9$ – $13.1$  m s<sup>-1</sup> between  $z = 24.5$ – $27.4$  km.

Data from the mean QBO-W profile at altitudes  $z_{\bar{u}} \geq 20.97$  km were used to obtain a least-squares fit model of the form given by Eq. (8.55). The fitted parameters were  $a_{\bar{u}} = 13.1$  m s<sup>-1</sup>,  $\sigma_{\bar{u}} = 3.8$  km, and  $\gamma_{\bar{u}} = 8.00$  km. The resulting profile is written equivalently in the form of Eq. (8.56) with peak magnitude  $\bar{u}_0 = 14.7$  m s<sup>-1</sup> located  $1.8$  km below the peak in the mean profile. The model parameters are summarized in Table 8.2. The model profile is compared with the computed mean profile in Fig. 8.5(b). The model agrees well qualitatively with the westerly jet in the mean profile, except for its peak velocity, which is 12% greater than the peak of the mean profile, but well within the range of observed QBO-W values.

## 8.7 Transmission coefficient

In Sec. 5.5 we defined conserved quantities generally [cf. Eq. (5.16)] and motivated the use of a pseudomomentum-based transmission coefficient, as opposed to one based on wave energy. The latter is perhaps a more familiar quantity, but one which is crucially not conserved in a fluid with a nonuniform background flow. In particular, the transmission coefficient as a function of time was defined by Eq. (5.20) as the horizontally integrated pseudomomentum density associated with upward-propagating waves, integrated above the reflection level, and normalized by the (constant) total pseudomomentum,  $\mathcal{P}_0$ .

We derive here an analogous transmission coefficient, to be defined using the expression for pseudomomentum density  $\mathcal{P}(\mathbf{x}, t)$  appropriate for three-dimensional disturbances in an anelastic gas. The corresponding conservation law [Shaw and Shepherd (2008), Eq. (1.1)] is

$$\frac{\partial \mathcal{P}}{\partial t} = -\nabla \cdot \mathbf{F}_{\mathcal{P}}. \quad (8.57)$$

Our intention is to obtain an explicit expression for pseudomomentum by integrating directly this conservation law. Integrating Eq. (8.57) with respect to  $x$ ,  $y$ , and  $t$ , using the Divergence theorem and the horizontal periodicity of the domain, we obtain

$$\langle \mathcal{P} \rangle = \int_{-\infty}^t \frac{\partial}{\partial t'} \langle \mathcal{P} \rangle dt' = \int_{-\infty}^{t_0} \frac{\partial}{\partial t'} \langle \mathcal{P} \rangle dt' + \int_{t_0}^t -\frac{\partial}{\partial z} \langle \bar{\rho} u w \rangle dt',$$

where angle brackets denote the horizontal integral,  $t_0$  is the time at which a simulation is initialized, and  $\bar{\rho} u w = \mathbf{F}_{\mathcal{P}} \cdot \hat{\mathbf{e}}_z$  is the vertical component of the anelastic pseudomomentum density flux, given explicitly by the right-hand side of Eq. (3.25) of Shaw and Shepherd (2008). The integral  $\int_{-\infty}^{t_0} \frac{\partial}{\partial t'} \langle \mathcal{P} \rangle dt'$  represents the horizontally integrated distribution of pseudomomentum density at initial time  $t = t_0$ .

The transient transmission of waves through the QBO winds is then quantified by

$$T_{\mathcal{P}}(t) := \frac{1}{\mathcal{P}_0} \int_{z_{\bar{u}+\sigma_{\bar{u}}}^{z_{\max}}} \langle \mathcal{P}(\mathbf{x}, t) \rangle dz, \quad (8.58)$$

where  $\mathcal{P}_0 = \int_{z_{\min}}^{z_{\max}} \langle \mathcal{P} \rangle dz$ . The numerical method to evaluate Eq. (8.58) is described in Chapter 9.

Partial transmission of wave packets through the QBO winds will be quantified using

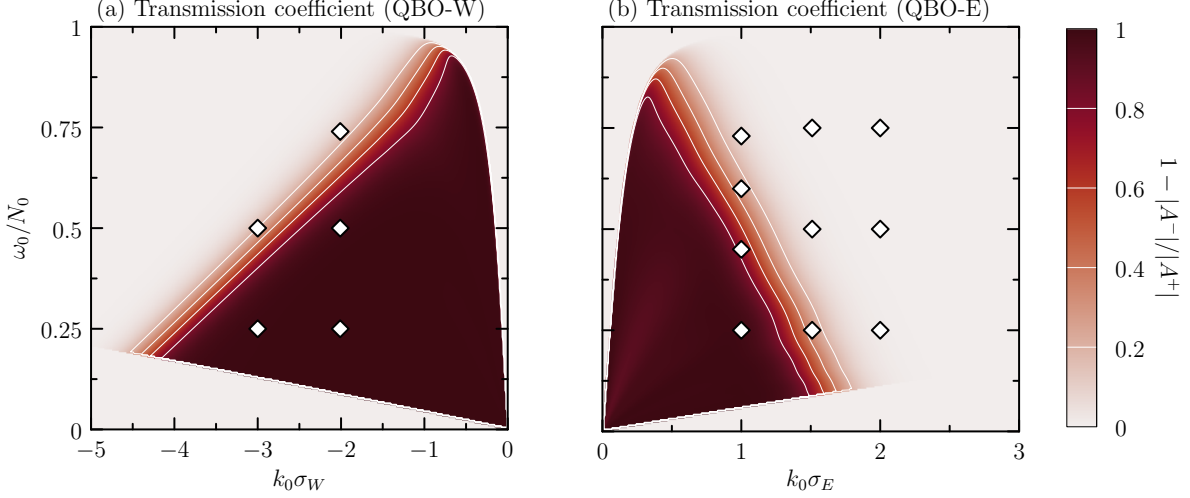


**Figure 8.6:** Transmission coefficient predicted from the numerical solution of the anelastic Taylor–Goldstein equation, Eq. (8.51), for a range of streamwise wavenumbers and frequencies, and QBO wind profiles described in Table 8.2. The white contours are isolines indicating constant predicted transmission separated by a constant interval of 0.2. Diamonds indicate the wavenumber–frequency combinations used to initialize numerical simulations of wave packets incident upon the QBO winds.

Eq. (8.58), and compared with the transmission coefficient  $T_{\mathcal{E}}$ , defined by Eq. (8.50), as obtained from solutions of the anelastic Taylor–Goldstein equation, Eq. (8.51). Although these respective metrics are distinct quantitatively, their comparison will enable us to assess the extent to which the relatively straightforward coefficient  $T_{\mathcal{E}}$  is suitable to quantify transmission of fully three-dimensional, quasimonochromatic wave packets.

To that end, Eq. (8.51) was solved numerically using the QBO wind profiles with parameters described in Table 8.2, for a range of streamwise wavenumbers and wave frequencies. The resulting predicted transmission coefficients, using the QBO-W and QBO-E profiles, are shown in Figs. 8.6(a) and 8.6(b), respectively. The largest transmission coefficients are predicted for wave packets with  $|k_0\sigma_{\{E,W\}}| = O(1)$ , corresponding to streamwise wavelengths that are long relative to the vertical extent of the QBO jet. Transmission through the QBO-W jet is predicted for a broader range of streamwise wavenumbers than for the QBO-E jet because the peak magnitude of the QBO-W is relatively weak compared to that of the QBO-E (14.7 compared to 37.5 m s<sup>-1</sup>, respectively).

---

## Numerical methods

---

The fully nonlinear code described in this chapter was adapted from the one described in Chapter 6. The key modification was to implement finite-difference methods in the vertical instead of the Fourier spectral method. The main reason for this major change is the loss of vertical periodicity of the wave fields, whose amplitudes grow anelastically (exponentially) with height. The finite difference approach, and the additional code changes this entrained, are described in the following sections.

### 9.1 Governing equations

The code solved the anelastic Euler equations (Lipps and Hemler, 1982; Ogura and Phillips, 1962) including explicitly a forcing by the height-dependent background flow  $\bar{u}(z)$ . Using the notation of Sutherland (2010), the prognostic equations for velocity and internal energy conservation (in which vertical displacement is used as a proxy for perturbation potential temperature) in flux form are given dimensionally by

$$\frac{\partial u}{\partial t} = -\frac{\partial}{\partial x} \left( \frac{p}{\bar{\rho}} \right) - \frac{1}{\bar{\rho}} \nabla \cdot (\bar{\rho} u \mathbf{u}) - \bar{u} \frac{\partial u}{\partial x} - w \bar{u}', \quad (9.1)$$

$$\frac{\partial v}{\partial t} = -\frac{\partial}{\partial y} \left( \frac{p}{\bar{\rho}} \right) - \frac{1}{\bar{\rho}} \nabla \cdot (\bar{\rho} v \mathbf{u}) - \bar{u} \frac{\partial v}{\partial x}, \quad (9.2)$$

$$\frac{\partial w}{\partial t} = -\frac{\partial}{\partial z} \left( \frac{p}{\bar{\rho}} \right) - \frac{1}{\bar{\rho}} \nabla \cdot (\bar{\rho} w \mathbf{u}) - \bar{u} \frac{\partial w}{\partial x} - N^2 \xi, \quad (9.3)$$

$$\frac{\partial \xi}{\partial t} = w - \frac{1}{\bar{\rho}} \nabla \cdot (\bar{\rho} \xi \mathbf{u}) - \frac{\bar{\theta}''}{\bar{\theta}'} w \xi - \bar{u} \frac{\partial \xi}{\partial z}, \quad (9.4)$$

$$\nabla \cdot [\bar{\rho}(\mathbf{u} + \bar{u} \hat{\mathbf{e}}_x)] = 0 = \nabla \cdot (\bar{\rho} \mathbf{u}). \quad (9.5)$$

where  $\mathbf{u} = (u, v, w)$  is the velocity vector, and  $\xi$  is vertical displacement, related to perturbation potential temperature by  $\xi = -\theta/\bar{\theta}'$ , and a prime denotes an ordinary derivative of a background field with respect to  $z$ . The background flow profiles  $\bar{u}$  were set by the QBO model, Eq. (8.56). The specific parameters for the QBO-E/W profiles are given in Table 8.2.

The system of equations (9.1)–(9.5) is closed by the inclusion of a diagnostic equation for perturbation pressure. Such an equation is found by multiplying the velocity evolution equations (9.1)–(9.3) by  $\bar{\rho}$  to obtain the momentum equations, and taking the divergence of the result, using the anelastic condition  $\nabla \cdot (\bar{\rho} \mathbf{u}) = 0$  to eliminate the time derivative terms. As a result,

$$\begin{aligned} \nabla^2 \left( \frac{p}{\bar{\rho}} \right) = & - \left[ \frac{\partial^2 (\bar{\rho} u^2)}{\partial x^2} + \frac{\partial^2 (\bar{\rho} v^2)}{\partial y^2} + \frac{\partial^2 (\bar{\rho} w^2)}{\partial z^2} \right] - 2 \left[ \frac{\partial^2 (\bar{\rho} uv)}{\partial x \partial y} + \frac{\partial^2 (\bar{\rho} uw)}{\partial x \partial z} + \frac{\partial^2 (\bar{\rho} vw)}{\partial y \partial z} \right] \\ & - 2\bar{u}' \frac{\partial w}{\partial x} - (N^2)' \xi - N^2 \frac{\partial \xi}{\partial z}. \end{aligned}$$

### 9.1.1 Anelastic scaling

Following the approach taken with the fully nonlinear two-dimensional anelastic code of [Gervais et al. \(2018\)](#), we scale the anelastic growth with height from the perturbation fields to reduce the risk of model blowup. This scaling is performed by first defining  $\bar{r} := \bar{\rho}/\rho_0$ . We then define the scaled fields implicitly by

$$(\mathbf{u}, \xi, p/\bar{\rho}) := (\mathbf{u}_s, \xi_s, p_s/\rho_0) \bar{r}^{-1/2}. \quad (9.6)$$

As a result the scaled governing equations (9.1)–(9.5) are given by

$$\frac{\partial u_s}{\partial t} = -\frac{1}{\rho_0} \frac{\partial p_s}{\partial x} - \bar{r}^{-1/2} \nabla \cdot (u_s \mathbf{u}_s) - \bar{u} \frac{\partial u_s}{\partial x} - w_s \frac{d\bar{u}}{dz}, \quad (9.7)$$

$$\frac{\partial v_s}{\partial t} = -\frac{1}{\rho_0} \frac{\partial p_s}{\partial y} - \bar{r}^{-1/2} \nabla \cdot (v_s \mathbf{u}_s) - \bar{u} \frac{\partial v_s}{\partial x}, \quad (9.8)$$

$$\frac{\partial w_s}{\partial t} = -\frac{1}{\rho_0} \frac{\partial p_s}{\partial z} + \frac{1}{2} \frac{\bar{r}'}{\bar{r}} \frac{p_s}{\rho_0} - \bar{r}^{-1/2} \nabla \cdot (w_s \mathbf{u}_s) - \bar{u} \frac{\partial w_s}{\partial x} - N^2 \xi_s, \quad (9.9)$$

$$\frac{\partial \xi_s}{\partial t} = w_s - \bar{r}^{-1/2} \left[ \nabla \cdot (\xi_s \mathbf{u}_s) + \frac{\bar{\theta}'}{\bar{\theta}} w_s \xi_s \right] - \bar{u} \frac{\partial \xi_s}{\partial x}, \quad (9.10)$$

$$\nabla \cdot \mathbf{u}_s = -\frac{1}{2} \frac{\bar{r}'}{\bar{r}} w_s. \quad (9.11)$$

Early attempts to obtain vertical velocity from Eq. (9.11), equivalent to the approach used in the Boussinesq codes described in Chapters 3 and 6, were unsuccessful: as the domain was vertically aperiodic, vertical integration in real space resulted in small numerical errors that accumulated only *above* the wave packet (unlike the ‘columns’ spanning the vertical domain as described in Sec. 6.4). Any residual error remaining after attempting to subtract the error from above the wave packet only compounded as the test simulation advanced in time, so that the numerical solution was rapidly dominated by contamination from growth of this error. For this reason, the anelastic code did not solve Eq. (9.11), but rather evolved the vertical momentum field explicitly using Eq. (9.9).

Incompressibility was enforced indirectly through the scaled pressure equation, given by

$$\begin{aligned} \nabla^2 \left( \frac{p_s}{\rho_0} \right) + \frac{p_s}{\rho_0} \left[ \frac{1}{4} \left( \frac{\bar{r}'}{\bar{r}} \right)^2 - \frac{1}{2} \frac{\bar{r}''}{\bar{r}} \right] = & -\bar{r}^{-1/2} \left[ \frac{\partial^2 (u_s^2)}{\partial x^2} + \frac{\partial^2 (v_s^2)}{\partial y^2} + \frac{\partial^2 (w_s^2)}{\partial z^2} \right] \\ & - 2\bar{r}^{-1/2} \left[ \frac{\partial^2 (u_s v_s)}{\partial x \partial y} + \frac{\partial^2 (u_s w_s)}{\partial x \partial z} + \frac{\partial^2 (v_s w_s)}{\partial y \partial z} \right] \\ & - 2\bar{u}' \frac{\partial w_s}{\partial x} - (N^2)' \xi_s - N^2 \left( \frac{1}{2} \frac{\bar{r}'}{\bar{r}} + \frac{\partial \xi_s}{\partial z} \right). \end{aligned} \quad (9.12)$$

The scaled governing equations (9.7)–(9.12) are general enough to allow for arbitrary background stratification [in which one of  $\bar{\rho}$  or  $\bar{\theta}$  are specified, and the other follows from the ideal gas law and the definition of background potential temperature, given by Eq. (8.1)]. However, due to time constraints, in practice the code was set up to simulate waves in an atmosphere with constant buoyancy frequency  $N(z) = N_0$ . This choice imposed the background density and potential temperature profiles

$$\bar{\rho} = \rho_0 e^{-z/H_\rho}, \quad (9.13)$$

$$\bar{\theta} = \theta_0 e^{z/H_\theta}, \quad (9.14)$$

where  $H_\rho$  and  $H_\theta$  are the (constant) density and potential temperature scale heights, respectively.

## 9.2 Discretization, grid generation, and resolution

Because  $\bar{u}$  is nonuniform with height and the wave amplitudes grow exponentially with height according to linear anelastic theory, it is not possible to solve Eqs. (9.7)–(9.10) and (9.12) in fully three-dimensional spectral space using fast Fourier transforms as was done with the Boussinesq codes described in Chapters 3 and 6. The anelastic code takes a hybrid pseudospectral-finite-difference approach in which Eqs. (9.7)–(9.10) and (9.12) are fast Fourier transformed with respect to the horizontal coordinates only, while retaining physical fields vertically, as described below.

The relative scales for space and time variables were set by fixing  $N_0$  and  $k_0$  (with arbitrary units of inverse time and inverse length, respectively; exact values specified later). The physical domain was periodic in the streamwise and spanwise directions. The vertical domain represented part of the vertical extent of the atmosphere, from a base altitude  $z_{\min}$  (which could be taken as ground level, although not necessarily) up to some a truncation altitude  $z_{\max}$ . Therefore the physical domain was of size  $L_x \times L_y \times L_z$ , where

$$L_x = \frac{2\pi}{k_0} n_{w,x}, \quad L_y = \frac{200}{k_0}, \quad L_z = z_{\max} - z_{\min},$$

in which  $n_{w,x}$  was the number of wavelengths that spanned the streamwise domain initially. As in the Boussinesq codes, the spanwise domain was specified directly because our coordinate system was oriented such that there was no wave propagation in this direction. The vertical domain was specified directly, enabling us relative flexibility in setting exact size compared to multiples of the number of vertical wavelengths, as was done in the Boussinesq codes. Applying experience with the Boussinesq codes, the domain was assumed large enough that self-interaction across the periodic horizontal boundaries would be negligible over the time scales for reflection and partial transmission. The vertical domain height was a compromise between being large enough to contain any partially transmitted waves, while not being so large that small-scale numerical noise could be amplified exponentially by the anelastic growth terms (although in practice this occurred often).

The physical domain was set by specifying 32 evenly spaced grid points per streamwise wavelength, by  $n_y = 256$  evenly spaced grid points in the spanwise direction, and by  $n_z$  evenly

spaced grid points in the vertical. Hence, the physical computational mesh consisted of the set of colocated nodes  $\{x_i\}_{i=0}^{n_x} \times \{y_j\}_{j=0}^{n_y} \times \{z_k\}_{k=0}^{n_z}$ . Values of  $n_x$ ,  $n_y$ , and  $n_z$  for specific simulations are provided in Chapter 10. Applying experience with the Boussinesq codes, domain size and resolution tests were not performed, because the domain size and resolution for most simulations was comparable to complementary Boussinesq simulations, and because of the computational cost involved.

For all simulations,  $n_x$  and  $n_y$  were set to be powers of two in order to use the fast Fourier transform in the horizontal directions. Hence, the (horizontal) Fourier spectral domain was  $\{\kappa_n\}_{n=0}^{1+n_x/2} \times \{\lambda_\ell\}_{\ell=0}^{n_y}$ . Unlike the Boussinesq codes described in Chapters 3 and 6, it was not necessary to set  $n_z$  to be a power of two because the fast Fourier transform was not applied vertically. Under the Fourier transform, partial derivative operators in the horizontal directions were  $\partial/\partial x \rightarrow i\kappa_n$  and  $\partial/\partial y \rightarrow i\lambda_\ell$ . Vertical partial derivatives were approximated with various finite-difference schemes, described below.

### 9.2.1 Approximation of vertical derivatives

We denote by a caret the Fourier transform of a field  $\eta$  with respect to  $x$  and  $y$ , and denote by the subscript  $k$  the discretized height  $z_k$  among  $n_z + 1$  evenly spaced vertical nodes. For the time being,  $n_z$  is arbitrary. The nodes are labelled by their index  $0, 1, \dots, n_z$ , the lower and upper boundaries having index  $k = 0$  and  $k = n_z$ , respectively. Vertical derivatives of *linear* wave fields were approximated by  $O(\Delta z^4)$  accurate centred finite differences using

$$\frac{d}{dz}\hat{\eta}(\kappa, \lambda, z_k) := \hat{\eta}'_k \approx \frac{1}{\Delta z} \left[ \frac{1}{12}\hat{\eta}_{k-2} - \frac{2}{3}\hat{\eta}_{k-1} + \frac{2}{3}\hat{\eta}_{k+1} - \frac{1}{12}\hat{\eta}_{k+2} \right], \quad (9.15)$$

$$\frac{d^2}{dz^2}\hat{\eta}(\kappa, \lambda, z_k) := \hat{\eta}''_k \approx \frac{1}{\Delta z^2} \left[ -\frac{1}{12}\hat{\eta}_{k-2} + \frac{4}{3}\hat{\eta}_{k-1} - \frac{5}{2}\hat{\eta}_k + \frac{4}{3}\hat{\eta}_{k+1} - \frac{1}{12}\hat{\eta}_{k+2} \right], \quad (9.16)$$

where we omitted the subscripts  $(n, \ell)$  for convenience. The main reason to use relatively high-order finite difference approximations is to compensate for relatively poor vertical resolution (compared to the *spectrally well-resolved* numerical solutions obtained with the Boussinesq simulations). In principle, it is possible to use familiar  $O(\Delta z^2)$  finite-difference approximations (e.g., as in Gervais et al., 2018) but the corresponding high-resolution vertical mesh would be anticipated to require memory in excess of that available on the HPC compute nodes on

which this code is designed to run (cf. the discussion in Sec. 6.4).

High-order approximations of vertical flux divergence were obtained by first interpolating the vertical fluxes halfway between vertical grid points, i.e.,  $\hat{F}_{k+1/2}$ , where  $\hat{F}_k$  is the fast Fourier-transformed product of any two perturbation fields. A certain “optimal” linear combination of three  $O(\Delta z^3)$  “essentially non-oscillatory” approximations to  $\hat{F}_{k+1/2}$  yields a  $O(\Delta z^5)$  approximation for this flux [Ghosh and Constantinescu, 2016, Eqs. (19)–(22); Durran, 2010, Sec. 5.7]. Explicitly,

$$\hat{F}_{k+1/2} \approx \frac{1}{30}\hat{F}_{k-2} - \frac{13}{60}\hat{F}_{k-1} + \frac{47}{60}\hat{F}_k + \frac{27}{60}\hat{F}_{k+1} - \frac{1}{20}\hat{F}_{k+2}.$$

The vertical flux divergence at height  $z_k$  was then approximated by

$$\frac{d}{dz}\hat{F}(\kappa, \lambda, z_k) \approx \frac{1}{\Delta z}(\hat{F}_{k+1/2} - \hat{F}_{k-1/2}). \quad (9.17)$$

In practice, for fixed  $(\kappa, \lambda)$  only the  $\hat{F}_{k+1/2}$  fluxes were computed, as the right-hand side of Eq. (9.17) is simply the difference of two successive approximations of  $\hat{F}_{k+1/2}$ . Computing vertical flux divergence using Eq. (9.17) was anticipated to yield improved numerical conservation compared to Eq. (9.15) at comparable computational cost.

If one instead constructs a convex combination of the aforementioned essentially non-oscillatory approximations using weights that depend nonlinearly on the fluxes at the grid points, one obtains a “weighted essentially non-oscillatory” scheme that is  $O(\Delta z^5)$  accurate away from shocks (the so-called WENO5 scheme). Provided no shocks are present (as is anticipated of our numerical solutions), the nonlinear weights converge to the optimal linear weights that were used to construct Eq. (9.17) (Jiang and Shu, 1996; Ghosh and Constantinescu, 2016). In this way our code benefits from the accuracy of the WENO5 scheme without the significant computational burden of determining nonlinear weights.

Assuming the wave fields are sufficiently smooth, the approximations given by Eqs. (9.15)–(9.17) are valid for all but the next-to-boundary interior nodes, i.e., those indexed  $2 \leq k \leq n_z - 2$ . One option for approximating derivatives at the vertical boundaries is to use one-sided finite differences. However, this is numerically unstable when combined with a time-stepping scheme and leads eventually to numerical blowup. To maintain stability at the boundaries,

second-order centred finite differences given by

$$\frac{d}{dz}\hat{\eta}(\kappa, \lambda, z_1) = \hat{\eta}'_1 \approx \frac{1}{2\Delta z}(\hat{\eta}_2 - \hat{\eta}_0), \quad (9.18)$$

$$\frac{d^2}{dz^2}\hat{\eta}(\kappa, \lambda, z_1) = \hat{\eta}''_1 \approx \frac{1}{\Delta z^2}(\hat{\eta}_0 - 2\hat{\eta}_1 + \hat{\eta}_2) \quad (9.19)$$

were used at the first interior node above the bottom boundary ( $z_k = z_1$ ), while a domain-extension technique and centred fourth-order finite differences were used at the top boundary. Because wave packets had negligible amplitude near the bottom boundary, the reduced accuracy of second-order approximations there was negligible. The boundary values and domain extrapolation procedure are elaborated on below.

## 9.2.2 Boundary conditions

The domain was horizontally periodic, and so no horizontal boundary conditions needed to be applied explicitly. Dirichlet boundary conditions were applied to all perturbation fields along the bottom of the domain. In particular, the no slip condition was applied to the velocity fields, and vertical displacement and dynamic pressure were set to zero. These conditions are physically meaningful (i.e., the bulk of the wave packet exists far above the bottom boundary), and are straightforward to implement. Conditions at the top boundary are discussed in detail below.

### 9.2.2.1 Radiation boundary condition

The choice of boundary conditions at the top of the domain is nontrivial. The main reason for this is that the atmosphere has no definitive ‘top,’ and so numerical models of the atmosphere that use height as the vertical coordinate directly must impose an artificial upper boundary. This is a challenging issue for numerical models of the atmosphere. An upper boundary imposed at any height is necessarily located somewhat arbitrarily. Placing an upper boundary well above the region containing the dynamics of interest incurs possibly an unacceptable computational burden by needing to solve equations at a large number of additional nodes; placing one too close risks the introduction of numerical errors arising from interactions between simulated phenomena within the domain and unresolved dynamics out-

side. One approach is to apply a *radiation boundary condition*, which allows the phenomena within the domain to evolve essentially without interacting with the artificial upper boundary: fluids and their properties simply pass through it.

Boundary conditions on the velocity fields were most straightforwardly imposed. The horizontal components  $u_s$  and  $v_s$ , being parallel to the upper boundary, evolved freely at the domain top according to the momentum equations Eqs. (9.7)–(9.8). Evolving the vertical velocity  $w_s$  and vertical displacement  $\xi_s$  fields using Eqs. (9.9)–(9.10) was equally straightforward. In all these cases, however, in order to maintain numerical stability when approximating vertical derivatives at the upper boundary, centred finite differences were necessary, for which no data existed outside of the domain. One solution is to synthesize the required data at a few so-called ‘ghost nodes’ above the upper boundary by extrapolating data within the domain. Following Durrán (2010) (see also Kreiss, 1968; Klemp and Durrán, 1983), the value of a given perturbation field  $\hat{\eta}_s$  at a ghost node  $k^+$  was approximated using a Lagrange polynomial such that

$$\sum_{k=0}^q \frac{q!}{k!(q-k)!} (-1)^k \hat{\eta}_s(\kappa, \lambda, z_{k^+-k}) = 0,$$

where  $k^+ = n_z + 1$  and  $n_z + 2$ . The Lagrange polynomial is of degree  $q - 1$  and of accuracy  $O(\Delta z^q)$ . For consistency with the fourth-order finite difference scheme,  $q = 4$  was chosen.

It was somewhat less trivial to impose the upper boundary condition for dynamic pressure  $p_s$ . Using linear theory and assuming a stationary background flow under the Boussinesq approximation, Klemp and Durrán (1983) derived a radiation upper boundary condition for dynamic pressure,

$$\frac{1}{\rho_0} \hat{p}_s \Big|_{z=z_{\max}} = \frac{N_0}{\sqrt{\kappa^2 + \lambda^2}} \hat{w}_s \Big|_{z=z_{\max}}. \quad (9.20)$$

Klemp and Durrán found that Eq. (9.20) performed well in a series of numerical tests that violated systematically the assumptions underlying the derivation. On this basis it is anticipated that this radiation boundary condition for dynamic pressure was suitable for anelastic simulations. This was confirmed by comparison with numerical tests (not shown) using other upper boundary conditions, all of which led to numerical blowup at the domain top.

With these boundary conditions, the equations for the perturbation fields constitute a fully determined system, simulated numerically as described below.

### 9.3 Initialization

The initialization procedure was similar to that described in Sec. 6.3. In particular, the background flow was set using Eq. (8.56).

The perturbation fields were set to be centred initially at  $z = z_0 \ll z_{\bar{u}}$ , at an altitude such that  $\bar{u}(z_0) \approx 0$ . Under this condition, the polarization relations for waves in a stationary, uniformly stratified, anelastic gas were valid, and so were used to initialize the leading-order wave fields in Fourier space as they related to the fast Fourier-transformed initial vertical displacement,  $\widehat{\xi}_{s0}^{(1)}$ , scaled using Eq. (9.6). The first-order correction to scaled vertical displacement, given in the right column of Table 8.1 was defined in physical space, fast Fourier transformed, and superimposed onto the leading-order field. Together, the initial vertical displacement field corresponded explicitly in physical space to

$$\xi_s(\mathbf{x}, 0) = A(\mathbf{x}, 0) \cos(\varphi_0) \left\{ 1 - \beta_x \left[ \frac{x}{\sigma_x^2} - \frac{k_0}{m_0} \frac{z}{\sigma_z^2} \right] \right\},$$

where  $\varphi_0 = k_0 x + m_0 z$  was the initial phase,  $\beta_x = -c_{gx0}/\omega_0$  according to Eq. (8.33a), and  $A(\mathbf{x}, 0)$  was a triply Gaussian envelope identical to the one used to initialize the Boussinesq simulations [cf. Eq. (6.8)].

The scaled leading-order velocity field  $\mathbf{u}_{s0}^{(1)}(\mathbf{x}, 0)$  was initialized in Fourier space using the polarization relations for  $u_0^{(1)}$ ,  $v_0^{(1)}$ , and  $w_0^{(1)}$ , given in the centre column of Table 8.1, and scaled using Eq. (9.6). These fields corresponded explicitly to the physical fields

$$\begin{aligned} u_{s0}^{(1)}(\mathbf{x}, 0) &= -A(\mathbf{x}, 0) \frac{k_0}{\omega_0} \frac{N_0^2 - \omega_0^2}{K_0^2 - k_0^2} \left\{ m_0 \sin(\varphi_0) + \frac{1}{2H_\rho} \cos(\varphi_0) \right\}, \\ v_{s0}^{(1)}(\mathbf{x}, 0) &= 0, \\ w_{s0}^{(1)}(\mathbf{x}, 0) &= A(\mathbf{x}, 0) \omega_0 \sin(\varphi_0), \end{aligned}$$

where  $K_0^2 = k_0^2 + m_0^2 + 1/(2H_\rho)^2$ . The respective first-order corrections to the velocity fields,  $u_1^{(1)}$ ,  $v_1^{(1)}$ , and  $w_1^{(1)}$ , given in the right column of Table 8.1 and scaled using Eq. (9.6), were defined in physical space, fast Fourier transformed, and superimposed onto the leading-order

fields. Explicitly,

$$\begin{aligned}
u_{s1}^{(1)}(\mathbf{x}, 0) &= -\frac{A(\mathbf{x}, 0)}{\omega_0(K_0^2 - k_0^2)} \left\{ \frac{k_0}{\omega_0} (N_0^2 + \omega_0^2) \Phi_0 c_{gx0} B(x, z) \right. \\
&\quad \left. - (N_0^2 - \omega_0^2) \left[ \Phi_0 \frac{x}{\sigma_x^2} - \frac{k_0 \Phi_{00}}{K_0^2 - k_0^2} \frac{z}{\sigma_z^2} - k_0 \beta_x B(x, z) \right] \right\}, \\
v_{s1}^{(1)}(\mathbf{x}, 0) &= -A(\mathbf{x}, 0) \frac{N_0^2 - \omega_0^2}{\omega_0(K_0^2 - k_0^2)} \frac{y}{\sigma_y^2} \Phi_0, \\
w_{s1}^{(1)}(\mathbf{x}, 0) &= 2A(\mathbf{x}, 0) c_{gx0} \cos(\varphi_0) B(x, z),
\end{aligned}$$

where we defined

$$\begin{aligned}
\Phi_0 &:= m_0 \cos(\varphi_0) - \frac{1}{2H_\rho} \sin(\varphi_0), \\
\Phi_{00} &:= \left( m_0^2 - \frac{1}{4H_\rho^2} \right) \cos(\varphi_0) - \frac{m_0}{H_\rho} \sin(\varphi_0), \\
B(x, z) &:= \frac{x}{\sigma_x^2} - \frac{k_0}{m_0} \frac{z}{\sigma_z^2}
\end{aligned}$$

for convenience.

### 9.3.1 Wave-induced mean flow

The (scaled) Bretherton flow was initialized with its horizontal components in Fourier space and its vertical structure in physical space, then horizontally inverse fast Fourier transformed before being superimposed onto the scaled initial horizontal velocity field (van den Bremer and Sutherland, 2014, 2018; Dosser and Sutherland, 2011; Sutherland et al., 2020). The scaled initial Bretherton flow in physical space was predicted using Eq. (8.39) to be

$$\begin{bmatrix} u_{\text{BFs}} \\ v_{\text{BFs}} \end{bmatrix} = \frac{1}{2} N_0 K e^{z/2H_\rho} \int_{\mathbb{R}^2} \frac{\lambda}{\kappa^2 + \lambda^2} \begin{bmatrix} \lambda \\ -\kappa \end{bmatrix} \widehat{|A|^2} e^{i(\kappa x + \lambda y)} d\kappa d\lambda, \quad (9.21)$$

where

$$\widehat{|A|^2} = \frac{1}{4\pi} \sigma_x \sigma_y A_0^2 e^{-(\sigma_x^2 \kappa^2 + \sigma_y^2 \lambda^2)/4} e^{-z^2/\sigma_z^2}$$

is the Fourier transform of the Gaussian envelope given by Eq. (6.8) with respect to  $x$  and  $y$  only. Following the procedure described in Sec. 3.3, array entries corresponding to the singularity  $\kappa^2 + \lambda^2 = 0$  were overwritten with zeros. Remark that as a result of the anelastic scaling, a factor of  $\sqrt{e^{z/H_\rho}}$  remains on the right-hand side of Eq. (9.21), consistent with

unscaled quadratically nonlinear wave fields which contain a factor of  $e^{z/H_\rho}$ : upon superimposing linear and quadratically nonlinear unscaled fields, at most one factor of  $e^{z/2H_\rho}$  can be eliminated from all terms in the resulting equation.

## 9.4 Pressure, advection, and temporal advancement

A typical iteration of the main loop that advanced the anelastic code followed a similar control flow as the Boussinesq codes. This section describes, in particular, the finite-difference solution method to determine the dynamic pressure field, which is significantly more involved than in the Boussinesq codes.

### 9.4.1 Dynamic pressure diagnostic

At a given time step, the code diagnosed the dynamic pressure field using the Fourier transform of Eq. (9.12), given explicitly by

$$\begin{aligned} \hat{\mathcal{L}}_{\mathbf{n}} \frac{\hat{p}_{s\mathbf{n}}}{\rho_0} = & \bar{r}_k^{-1/2} \left[ \kappa_n^2 (\widehat{u_s^2})_{\mathbf{n}} + \lambda_\ell^2 (\widehat{v_s^2})_{\mathbf{n}} - \frac{d^2}{dz^2} (\widehat{w_s^2})_{\mathbf{n}} \right] \\ & + 2\bar{r}_k^{-1/2} \left[ \kappa_n \lambda_\ell (\widehat{u_s v_s})_{\mathbf{n}} - i\kappa_n \frac{d}{dz} (\widehat{u_s w_s})_{\mathbf{n}} - i\lambda_\ell \frac{d}{dz} (\widehat{v_s w_s})_{\mathbf{n}} \right] \\ & - 2i\kappa_n \bar{u}'_k \widehat{w}_{s\mathbf{n}} - (N^2)'_k \widehat{\xi}_{s\mathbf{n}} - N^2 \left[ \frac{1}{2} \frac{\bar{r}'_k}{\bar{r}_k} \widehat{\xi}_{s\mathbf{n}} + \frac{d}{dz} \widehat{\xi}_{s\mathbf{n}} \right] \end{aligned} \quad (9.22)$$

where  $\hat{\mathcal{L}}_{\mathbf{n}} = -\kappa_n^2 - \lambda_\ell^2 + d^2/dz^2 + \frac{1}{4}(\bar{r}'_k/\bar{r}_k)^2 - \frac{1}{2}\bar{r}''_k/\bar{r}_k$  is the Fourier-transformed and discretized linear operator on the left-hand side of the pressure equation, Eq. (9.12), and  $\mathbf{n} = (n, \ell, k)$  is the vector index specifying the horizontal Fourier mode  $(\kappa_n, \lambda_\ell)$  and physical altitude  $z_k$ . All instances of the operator  $d/dz$  acting on nonlinear terms in in Eq. (9.22) correspond to vertical flux divergence, and so were approximated by one or two applications of Eq. (9.17), as needed. Conversely,  $d\widehat{\xi}_{s\mathbf{n}}/dz$  is not a flux and so was instead approximated using Eq. (9.15).

Although Eq. (9.22) is given in a general form to account for possibly nonuniform background stratification, in practice the nondimensional background mass density and potential temperature profiles were set by Eqs. (9.13) and (9.14) so that  $\bar{r}'_k/\bar{r}_k = -1/H_\rho$  and  $(N^2)' = (N_0^2)' \equiv 0$ . Consequently, in the linear operator  $\hat{\mathcal{L}}_{\mathbf{n}}$ , we have  $\frac{1}{4}(\bar{r}'_k/\bar{r}_k)^2 - \frac{1}{2}\bar{r}''_k/\bar{r}_k = -1/4H_\rho^2$ .

The second-order vertical derivative part of  $\hat{\mathcal{L}}_{\mathbf{n}}$  was approximated using Eq. (9.16) [except

at the bottom boundary, which used Eq. (9.18), as discussed in Sec. 9.2.1]. Therefore, for a fixed  $(\kappa_n, \lambda_\ell)$ , Eq. (9.22) is an *implicit* problem in which the left-hand side operator is an  $(n_z - 1) \times (n_z - 1)$  real matrix. The solution, including vertical boundary values, is a vertical pressure profile  $\hat{\mathbf{p}}_s \in \mathbb{C}^{n_z}$  for each horizontal Fourier mode pair. It follows that Eq. (9.22) must be solved  $2 \cdot (1 + n_x/2) \times (1 + n_y)$  times to obtain the full three-dimensional dynamic pressure field in Fourier space (the factor of two accounting for the real and imaginary parts). For typical values of  $n_x$  and  $n_y$ , this amounts to  $O(2.5 \times 10^5)$  matrix inversions for *every Runge–Kutta substep* (described below), and so represents potentially a severe bottleneck in the code. A highly efficient matrix inversion algorithm is crucial.

To this end, the structure of  $\hat{\mathcal{L}}_{\mathbf{n}}$  is a source of much optimism: for each  $(\kappa_n, \lambda_\ell)$ , this is a pentadiagonal banded matrix, and so efficient methods for sparse systems are available (e.g., Allen and Isaacson, 1998); furthermore,  $\hat{\mathcal{L}}_{\mathbf{n}}$  contains no time dependence, and so in principle needs to be inverted only once for each  $(\kappa_n, \lambda_\ell)$ . Depending on the value of  $\kappa_n^2 + \lambda_\ell^2$ ,  $\hat{\mathcal{L}}_{\mathbf{n}}$  was not necessarily diagonally dominant, a condition that would guarantee the numerical stability of many common matrix inversion algorithms (e.g., Allen and Isaacson, 1998). In practice, however, inversion of  $\hat{\mathcal{L}}_{\mathbf{n}}$  was found to be numerically stable to LU factorization. It was straightforward, if somewhat tedious, to derive an efficient LU factorization that made use of nonzero matrix entries only. Details of the optimized LU factorization are provided in Appendix E. The diagonals of the resulting factored matrices  $\mathbf{L}_{(n,\ell)}$  and  $\mathbf{U}_{(n,\ell)}$  were then stored compactly. Using the factored matrices, determination of the full three-dimensional dynamic pressure field in Fourier space consisted simply of a sequence of  $2 \cdot (1 + n_x/2) \times (1 + n_y)$  forward- and back-substitutions.

#### 9.4.2 Advancing the prognostic fields

Using the existing perturbation fields and dynamic pressure field determined using the procedure described above, the code computed the time derivatives of the scaled prognostic fields,  $\dot{\hat{\mathbf{u}}}_{s\mathbf{n}}$  and  $\dot{\hat{\xi}}_{s\mathbf{n}}$ , according to the Fourier-transformed right-hand sides of Eqs. (9.7)–(9.10). Explicitly,

$$\dot{\hat{\mathbf{u}}}_{s\mathbf{n}} = -\bar{r}_k^{-1/2} \left[ i\kappa_n (\widehat{u_s^2})_{\mathbf{n}} + i\lambda_\ell (\widehat{u_s v_s})_{\mathbf{n}} + \frac{d}{dz} (\widehat{u_s w_s})_{\mathbf{n}} \right] - i\kappa_n \bar{u}_k \widehat{u}_{s\mathbf{n}} - \bar{u}'_k \widehat{w}_{s\mathbf{n}} - i\kappa_n \frac{\widehat{p}_{s\mathbf{n}}}{\rho_0}, \quad (9.23)$$

$$\dot{\hat{v}}_{s\mathbf{n}} = -\bar{r}_k^{-1/2} \left[ i\kappa_n (\widehat{u_s v_s})_{\mathbf{n}} + i\lambda_\ell (\widehat{v_s^2})_{\mathbf{n}} + \frac{d}{dz} (\widehat{v_s w_s})_{\mathbf{n}} \right] - i\kappa_n \bar{u}_k \widehat{v}_{s\mathbf{n}} - i\lambda_n \frac{\widehat{p}_{s\mathbf{n}}}{\rho_0}, \quad (9.24)$$

$$\begin{aligned} \dot{\hat{w}}_{s\mathbf{n}} = & -\bar{r}_k^{-1/2} \left[ i\kappa_n (\widehat{u_s w_s})_{\mathbf{n}} + i\lambda_\ell (\widehat{v_s w_s})_{\mathbf{n}} + \frac{d}{dz} (\widehat{w_s^2})_{\mathbf{n}} \right] - i\kappa_n \bar{u}_k \widehat{w}_{s\mathbf{n}} - \frac{d}{dz} \frac{\widehat{p}_{s\mathbf{n}}}{\rho_0} + \frac{\bar{r}'_k}{\bar{r}_k} \frac{\widehat{p}_{s\mathbf{n}}}{\rho_0} \\ & - N^2 \widehat{\xi}_{s\mathbf{n}}, \end{aligned} \quad (9.25)$$

$$\dot{\hat{\xi}}_{s\mathbf{n}} = -\bar{r}_k^{-1/2} \left[ i\kappa_n (\widehat{u_s \xi_s})_{\mathbf{n}} + i\lambda_\ell (\widehat{v_s \xi_s})_{\mathbf{n}} + \frac{d}{dz} (\widehat{w_s \xi_s})_{\mathbf{n}} + \frac{\bar{\theta}'_k}{\bar{\theta}_k} (\widehat{w_s \xi_s})_{\mathbf{n}} \right] - i\kappa_n \bar{u}_k \widehat{\xi}_{s\mathbf{n}} + \widehat{w}_{s\mathbf{n}}, \quad (9.26)$$

where the nonlinear fields were retained from the pressure calculation, and vertical derivatives of these fields were approximated using the flux divergence Eq. (9.17). The derivative in  $\frac{1}{\rho_0} d\widehat{p}_{s\mathbf{n}}/dz$  in Eq. (9.25) was approximated using Eq. (9.15). Although Eqs. (9.23)–(9.26) are written to account for nonuniform stratification, in practice  $\bar{\rho}$  and  $\bar{\theta}$  were given by Eqs. (9.13) and (9.14), respectively, and so  $\bar{r}'_k/\bar{r}_k = \bar{\rho}'_k/\bar{\rho}_k = -1/H_\rho$  in Eq. (9.25) and  $\bar{\theta}'_k/\bar{\theta}_k = 1/H_\theta$  in Eq. (9.26).

### 9.4.3 Aliasing prevention

To guard against the unphysical growth of grid-scale oscillations arising from the quadratic products of wave fields, the code applied the filter given by Eq. (6.13) to the horizontal components of the Fourier spectrum of all quadratically nonlinear products immediately after convolving the linear input fields. In the vertical, the code applied a five-point trapezoidal filter (Taylor, 2008), given explicitly by

$$\bar{\hat{F}}_k = \frac{1}{8} \hat{F}_{k-2} + \frac{1}{4} (\hat{F}_{k-1} + \hat{F}_k + \hat{F}_{k+1}) + \frac{1}{8} \hat{F}_{k+2}. \quad (9.27)$$

where  $\hat{F}$  is the horizontally fast Fourier transformed quadratically nonlinear product of any two perturbation fields. At the first interior node above the bottom boundary, the code applies a three-point filter,  $\bar{\hat{F}}_1 = \frac{1}{4} \hat{F}_0 + \frac{1}{2} \hat{F}_1 + \frac{1}{4} \hat{F}_2$ .

The prognostic fields were advanced in time using the Williamson–Runge–Kutta scheme described in Sec. 3.4, using a time step of size  $\Delta t = 0.05N_0^{-1}$ . Simulations with a time step of half this size were not performed, based on experience with the Boussinesq codes.

## 9.5 Turbulence model

In previous studies of wave packet evolution and breaking in one dimension (Sutherland, 2001, 2006a,b; Dosser and Sutherland, 2011), two dimensions (Gervais et al., 2018) and three dimensions (Gervais et al., 2021), the codes were designed to simulate the wave evolution until just after overturning. After this time, the statically unstable fluid in the overturning region quickly gave way to convective instabilities that ultimately led to simulation blowup, as these inherently three-dimensional turbulent dynamics exist on small unresolved physical and temporal scales. The lack of turbulence model was of no concern in the one- and two-dimensional studies, as those studies focused on the hydrodynamic mechanisms *driving* the waves to overturn. The study of three-dimensional wave packets in a rotating Boussinesq fluid similarly lacked a turbulence model as the aim of the study was to quantify overturning heights and times, and so the postoverturning behaviour of the waves was of no importance. The three-dimensional study of wave packet transmission and reflection (Gervais et al., 2022) focused on wave packets that did not evolve to overturning amplitudes, and so no turbulence model was necessary. This is not the case in the current study: after initialization at small amplitude the waves experience amplitude growth not only due to nonlinear interactions with their wave-induced mean flow, but also undergo anelastic growth with height. This exponential increase in amplitude, concentrated above the centre of the wave packet where the amplitude is already largest and wave-induced mean flow is strongest [cf. Fig. 8.1(b)], can lead to localized overturning. Simultaneously, the waves on the leading flank of the wave packet continue to propagate independently of the breaking waves below. In order to simulate this, a turbulence scheme is needed to model the localized wave breaking (the details of which are of no interest in this study), which would otherwise contaminate the numerical solution and lead to blowup.

One approach is that of direct numerical simulation of turbulence, in which the equations of motion are solved to resolve the full range of scales from the largest motions down to the viscous dissipation scale (e.g., Ferziger and Perić, 2002). Although conceptually straightforward, this approach is impractical in three dimensions due to the high resolution and corresponding computer memory required, which can quickly exceed available computational resources.

An alternative approach that is better suited to the needs of the anelastic code is that of large eddy simulation (LES), in which a range of motions (‘eddies’) are resolved only down to a certain scale (e.g., [Ferziger and Perić, 2002](#)). Motions on a smaller scale must be modelled. The scale of motions resolved by the code is set by filtering out motions smaller than a specified length scale. For simplicity, the filter in the horizontal directions is the spectral antialiasing filter given by Eq. (6.13), and in the vertical is the trapezoidal filter given by Eq. (9.27).

Denoting filtered quantities by an overbar and adopting summation notation for the time being, the unscaled, inviscid equations for filtered momentum are given by

$$\frac{\partial \bar{u}_i}{\partial t} + \frac{1}{R} \frac{\partial \overline{R u_i u_j}}{\partial x_j} = -\frac{\partial}{\partial x_i} \left( \frac{\bar{p}}{R} \right) - U \frac{\partial \bar{u}_i}{\partial x_1} - \bar{u}_3 \frac{dU}{dx_3} \delta_{i1} - N^2 \bar{\xi} \delta_{i3}, \quad (9.28)$$

where  $i = 1, 2, 3$  correspond to the  $x$ -,  $y$ -, and  $z$ -directions,  $R$  and  $U$  are the profiles of background density and background flow, respectively (where we have adopted this notation for the time being to avoid confusion with the standard interpretation of the overbar in the context of LES), and  $\delta_{ij}$  is the kronecker delta. Similarly, the unscaled equation for filtered perturbation potential temperature is

$$\frac{\partial \bar{\theta}}{\partial t} + \frac{1}{R} \frac{\partial \overline{R u_i \theta}}{\partial x_i} = -\bar{u}_3 \frac{d\Theta}{dx_3} - U \frac{\partial \bar{\theta}}{\partial x_1}, \quad (9.29)$$

where again, for the time being,  $\bar{\theta}$  is the filtered perturbation potential temperature and  $\Theta$  is the background potential temperature profile. The filtered anelastic nondivergence condition is

$$\frac{\partial (R \bar{u}_i)}{\partial x_i} = 0.$$

A central challenge in LES is the modelling of the nonlinear advection terms, as these involve products of the unknown subfilter-scale fields. For simplicity, we take the approach of the classic constant Smagorinsky scheme ([Smagorinsky, 1963](#)). Borrowing the notation of [Taylor \(2008\)](#), we define the subfilter stress tensor  $\tau_{ij}$  and subfilter potential temperature flux  $\lambda_i$ , by

$$\begin{aligned} \tau_{ij} &:= \overline{u_i u_j} - \bar{u}_i \bar{u}_j, \\ \lambda_i &:= \overline{u_i \theta} - \bar{u}_i \bar{\theta}. \end{aligned}$$

Substituting these into Eqs. (9.28) and (9.29) and rearranging yields the evolution equations for resolved velocity and potential temperature,

$$\frac{\partial \bar{u}_i}{\partial t} + \frac{1}{R} \frac{\partial (R \bar{u}_i \bar{u}_j)}{\partial x_j} = -\frac{\partial}{\partial x_i} \left( \frac{\bar{p}}{R} \right) - U \frac{\partial \bar{u}_i}{\partial x_1} - \bar{u}_3 \frac{dU}{dx_3} \delta_{i1} - N^2 \bar{\xi} \delta_{i3} - \frac{1}{R} \frac{\partial (R \tau_{ij})}{\partial x_j}, \quad (9.30)$$

$$\frac{\partial \bar{\theta}}{\partial t} + \frac{1}{R} \frac{\partial (R \bar{u}_i \bar{\theta})}{\partial x_i} = -\bar{u}_3 \frac{d\Theta}{dx_3} - U \frac{\partial \bar{\theta}}{\partial x_1} - \frac{1}{R} \frac{\partial (R \lambda_i)}{\partial x_i}, \quad (9.31)$$

in which the rightmost terms represent the forcing by (modelled) subfilter-scale motions.

Following Taylor (2008), the subfilter stress tensor is modelled by

$$\tau_{ij} = -2\nu_T \bar{S}_{ij}, \quad (9.32)$$

where  $\nu_T = C_s^2 \Delta^2 \|\bar{S}\|$  is the ‘eddy viscosity.’ Here,  $\|\bar{S}\| = (2\bar{S}_{ij}\bar{S}_{ij})^{1/2}$  is the modulus of the resolved strain rate tensor  $\bar{S}_{ij} = \frac{1}{2}(\partial_{x_i}\bar{u}_j + \partial_{x_j}\bar{u}_i)$ , and  $\Delta = (\Delta_x\Delta_y\Delta_z)^{1/3}$  is the filter length scale. The constituent filter length scales in the horizontal directions are set by the choice of cutoff wavenumber in the antialiasing/LES filter, i.e.,  $\Delta_x = 2\pi/\kappa_{\text{cut}}$  and  $\Delta_y = 2\pi/\lambda_{\text{cut}}$ . The vertical filter length scale is set by the width of the trapezoidal filter, i.e.,  $\Delta_z = 5\Delta_z$ . The filter length scales in each direction are nondimensionalized by the streamwise wavenumber  $k_0$ . The value of the Smagorinsky constant has been estimated to be  $C_s \approx 0.2$  (e.g., Ferziger and Perić, 2002). This value leads to excessive dissipation, and so in practice values of  $C_s = 0.1$  are used (e.g., Lesieur et al., 2005, Sec. 3.3.1), and this is the value of the Smagorinsky constant used in simulations reported on later.

The subfilter potential temperature flux is modelled by

$$\lambda_i = -\frac{\nu_T}{\text{Pr}} \frac{\partial \bar{\theta}}{\partial x_i} = \frac{\nu_T}{\text{Pr}} \frac{\partial}{\partial x_i} \left( \bar{\xi} \frac{d\Theta}{dx_3} \right), \quad (9.33)$$

where  $\text{Pr} = 1$  is the Prandtl number, assumed constant, and we used the relationship  $\bar{\theta} = -\bar{\xi}(d\Theta/dx_3)$  between (resolved) perturbation potential temperature and vertical displacement.

Finally, using Eqs. (9.32) and (9.33) and applying the anelastic scaling relationships given by Eq. (9.6), the evolution equations for resolved velocity and vertical displacement advanced

by the code, including the explicit subfilter-scale forcings, are

$$\frac{\partial \bar{u}_{si}}{\partial t} = -r^{-1/2} \frac{\partial(\bar{u}_{si}\bar{u}_{sj})}{\partial x_j} - \frac{1}{\rho_0} \frac{\partial \bar{p}_s}{\partial x_i} + \frac{1}{2} \frac{r'}{r} \frac{\bar{p}_s}{\rho_0} \delta_{i3} - U \frac{\partial \bar{u}_{si}}{\partial x_1} - \bar{u}_{s3} U' \delta_{i1} - N^2 \bar{\xi}_s \delta_{i3} - r^{-1/2} \frac{\partial \tau_{sij}}{\partial x_j}, \quad (9.34)$$

$$\begin{aligned} \frac{\partial \bar{\xi}_s}{\partial t} = & -r^{-1/2} \left[ \frac{\partial(\bar{u}_{si}\bar{\xi}_s)}{\partial x_i} + \frac{1}{H_\theta} \bar{u}_{s3} \bar{\xi}_s \right] + \bar{u}_{s3} - U \frac{\partial \bar{\xi}_s}{\partial x_1} \\ & + r^{-1/2} \left\{ \left[ \frac{\partial \bar{\xi}_s}{\partial x_i} + \frac{1}{H_*} \bar{\xi}_s \delta_{i3} \right] \frac{\partial}{\partial x_i} \left( \frac{\nu_{Ts}}{\text{Pr}} \right) + \left[ \frac{\partial^2 \bar{\xi}_s}{\partial x_i^2} + \left( \frac{1}{H_*} + \frac{1}{H_\theta} \right) \frac{\partial \bar{\xi}_s}{\partial x_3} + \frac{1}{H_* H_\theta} \bar{\xi}_s \right] \frac{\nu_{Ts}}{\text{Pr}} \right\}, \end{aligned} \quad (9.35)$$

in which we used the background density and potential temperature profiles  $r = R/\rho_0 = e^{-x_3/H_\rho}$  and  $\Theta = \theta_0 e^{x_3/H_\theta}$ , and we defined  $1/H_* := 1/H_\theta + 1/2H_\rho$  for convenience. Primes on background quantities denote derivatives with respect to  $x_3$ . It is tedious but straightforward to derive the rightmost terms in Eqs. (9.34)–(9.35) from the subfilter-scale forcing terms in Eqs. (9.30)–(9.31), the details of which are included in Appendix F. Finally, we note briefly that the subfilter-scale forcing terms are *subtracted* from the right-hand side of Eq. (9.31) but *added* to the right-hand side of Eq. (9.35) as a result of using  $\bar{\theta} = -\bar{\xi}\Theta'$ .

Taking the divergence of the unscaled momentum equations with subfilter-scale forcing terms, then scaling the result, one obtains the corresponding Poisson equation for scaled dynamic pressure,

$$\begin{aligned} \frac{1}{\rho_0} \frac{\partial^2 \bar{p}_s}{\partial x_i^2} + \left[ \frac{1}{4} \left( \frac{r'}{r} \right)^2 - \frac{1}{2} \frac{r''}{r} \right] \frac{\bar{p}_s}{\rho_0} = & -r^{-1/2} \frac{\partial^2(\bar{u}_{si}\bar{u}_{sj})}{\partial x_i \partial x_j} - 2U' \frac{\partial \bar{u}_{s3}}{\partial x_1} - (N^2)' \bar{\xi}_s \\ & - N^2 \left[ \frac{1}{2} \frac{r'}{r} \bar{\xi}_s + \frac{\partial \bar{\xi}_s}{\partial x_3} \right] - r^{-1/2} \frac{\partial^2 \tau_{sij}}{\partial x_i \partial x_j}, \end{aligned}$$

in which the rightmost term models the effects of subfilter-scale motions on the dynamic pressure field.

Having derived the explicit form of the governing equations advanced by the code when running in LES mode, we now relinquish our use of summation notation and return to our original notation henceforth.

Numerical tests revealed that the calculation of the subfilter-scale forcings approximately doubled the computational burden to advance the code by one time step compared to tests run without LES. To improve performance relative to running in LES mode for the duration

of a given simulation, by default the code advanced the evolution equations assuming laminar flow [i.e., Eqs. (9.22) and (9.23)–(9.26), which do not contain subfilter-scale forcing terms]. At each time step, the code diagnosed wave overturning according to the condition  $\min\{[1 - (\frac{\partial \xi}{\partial z} + \frac{\xi}{H_\theta})]/N_0^2\} < 0$  [cf. Eq. (8.54)]. If overturning was diagnosed, the code ran in LES mode instead.

## 9.6 Pseudomomentum diagnostics

The pseudomomentum density  $\mathcal{P}(\mathbf{x}, t)$  of three-dimensional disturbances was derived by [Shaw and Shepherd \(2008\)](#), and the total pseudomomentum  $\mathcal{P}_0$  is defined as the volume integral of  $\mathcal{P}(\mathbf{x}, t)$ . In our previous study we diagnosed wave transmission and reflection by considering vertical integrals of the vertical distribution of horizontally integrated pseudomomentum density. The equivalent approach here is to evaluate the horizontal part of the integral in Eq. (3.23) in [Shaw and Shepherd \(2008\)](#), although extensive testing of this approach consistently yielded an apparent pseudomomentum ‘leak’ which could not be corrected.

An alternative approach is to integrate directly the pseudomomentum conservation law,

$$\frac{\partial \mathcal{P}}{\partial t} = -\nabla \cdot \mathbf{F}_{\mathcal{P}}, \quad (9.36)$$

reproducing Eq. (8.57). Here,  $-\nabla \cdot \mathbf{F}_{\mathcal{P}}$  is the pseudomomentum flux convergence, given explicitly by the right-hand side of Eq. (3.25) in [Shaw and Shepherd \(2008\)](#), although this expression is algebraically cumbersome and is not reproduced here. In Sec. 8.7 we integrated Eq. (8.57) [Eq. (9.36)] with respect to  $x$ ,  $y$ , and  $t$  to obtain

$$\langle \mathcal{P} \rangle = \int_{-\infty}^t \frac{\partial}{\partial t'} \langle \mathcal{P} \rangle dt' = \underbrace{\int_{-\infty}^0 \frac{\partial}{\partial t'} \langle \mathcal{P} \rangle dt'}_{\text{I}} + \underbrace{\int_0^t -\frac{\partial}{\partial z} \langle \bar{\rho} u w \rangle dt'}_{\text{II}}. \quad (9.37)$$

Integral I represents the initial vertical distribution of horizontally integrated pseudomomentum density, assumed to be finite. Typically, one would obtain from this the total pseudomomentum by integrating the corresponding density distribution [i.e., Eq. (3.23) in [Shaw and Shepherd \(2008\)](#)] at  $t = t_0$  over the volume of the domain, as was done in Part II. However, the aforementioned pseudomomentum ‘leak’ was determined to result from an unidentified error in the diagnosis of this quantity, and so the actual total pseudomomentum was obtained

using an approach involving integral II, described below.

Integral II is the time-integrated vertical convergence of the vertical pseudomomentum flux, and is in general a *nonzero* function. In practice, upon dividing Eq. (9.37) by mass,  $\bar{\rho}uw$  is equivalent to  $\bar{r}uw = u_s w_s$ , according to Eq. (9.6). The field  $u_s w_s$  is carried explicitly by the code. Using the most up-to-date value of this field upon completion of each set of Runge–Kutta substeps, a profile of

$$-\frac{\partial}{\partial z}\langle u_s w_s \rangle = -\frac{\partial}{\partial z} L_x L_y \text{Re}\{\mathcal{F}_{xy}[u_s w_s]_{(0,0)}\}$$

was retained (cf. the discussion of horizontal integration in Sec. 6.6). A sequence of such profiles at  $\Delta t$  resolution corresponding to one nondimensional time step was then integrated in time using a composite Simpson’s rule to produce a vertical profile of

$$\int_{N_0 t-1}^{N_0 t} -\frac{\partial}{\partial z}\langle u_s w_s \rangle dt'.$$

A time series of vertical distributions of horizontally integrated pseudomomentum density is therefore obtained by computing the cumulative sum of integrals of this form.

Integrating Eq. (9.37) with respect to  $z$  yields the total pseudomomentum per mass,

$$\frac{\mathcal{P}_0}{\rho_0} = \frac{1}{\rho_0} \underbrace{\int_{z_{\min}}^{z_{\max}} \int_{-\infty}^0 \frac{\partial}{\partial t'} \langle \mathcal{P} \rangle dt' dz}_{=\mathcal{P}_0} + \underbrace{\int_{z_{\min}}^{z_{\max}} \int_0^t -\frac{\partial}{\partial z} \langle u_s w_s \rangle dt' dz}_{=0}.$$

Because  $\mathcal{P}_0$  cannot be obtained from the first integral directly, we use cleverly the second integral. This approach relies on the integrand in the second term being a function of height with a net area of zero between its curve and the  $z$ -axis all  $t \geq 0$ : as a wave packet propagates sufficiently far from its initial position (carrying with it the entirety of its pseudomomentum), there remains an artificial pseudomomentum ‘deficit’ centred at the initial position of the wave packet. The area under this part of the curve represents the initial pseudomomentum. Therefore,  $\mathcal{P}_0$  is obtained for a given set of wave and atmospheric parameters by running two complementary simulations, one with and one without background flow. The latter is allowed to evolve until the curve representing the pseudomomentum deficit has converged to a steady state. The area under this curve is the initial pseudomomentum. This procedure will be demonstrated using data from a simulation of wave packet evolution in Chapter 10.

---

## Results and discussion

---

In this chapter we present the results of fully nonlinear numerical simulations of three-dimensional internal gravity wave packets with their predicted anelastic Bretherton flow superimposed. Our intent is ultimately to quantify the transmission of localized anelastic wave packets through idealized QBO wind profiles, and to compare the transmission coefficient with that predicted by linear theory for monochromatic waves. The model atmosphere was a uniformly stratified anelastic gas with density scale height  $H_\rho = 7$  km, corresponding to a buoyancy frequency of  $N_0 = 0.02 \text{ s}^{-1}$ , as these are typical values in the stratosphere. Numerical simulations evolved moderately nonhydrostatic wave packets with a range of initial wavenumbers and amplitudes. Streamwise wavenumbers  $k_0$  (specified later) were found by fixing the value of  $k_0 \sigma_{\{E,W\}}$ , and vertical wavenumbers were found using Eq. (8.44) with  $\Omega/N_0 = \omega_0/N_0 \approx 0.25, 0.5, 0.75$ , thus spanning effectively the entire range of predicted transmission coefficients  $T_{\mathcal{E}} \in [0, 1]$ , given by Eq. (8.50). Although the transmission coefficient  $T_{\mathcal{E}}$  is distinct from the one based on pseudomomentum [ $T_{\mathcal{P}}$ ; cf. Eq. (8.58)], by comparing predicted and measured transmission using these respective quantities, we will assess the extent to which a relatively simple prediction (i.e.,  $T_{\mathcal{E}}$ ) is suitable to predict transmission of three-dimensional wave packets. Our investigation focused on initially round wave packets, for which we fixed  $\sigma_x = \sigma_y = \sigma_z = 7$  km. The domain and initialization parameters of the subset of simulations explicitly discussed in-text are summarized in Table 10.1.

ID	$A_0$	$k_0$	$m_0$	$\Theta_0$	QBO	$L_x \times L_y \times L_z$	$n_x \times n_y \times n_z$	$T_{\mathcal{E}}$
AN1	0.01	0.75	-0.68	42°	—	268.1 × 200.0 × 240.0	1024 × 256 × 1400	—
AN2	0.1	0.34	-0.68	63°	E	591.4 × 200.0 × 240.0	1024 × 256 × 1400	0.74
AN3	0.01	0.34	-0.68	63°	E	591.4 × 200.0 × 240.0	1024 × 256 × 1400	0.74
AN4	0.2	0.34	-0.68	63°	E	591.4 × 200.0 × 240.0	1024 × 256 × 1400	0.74
AN5	0.01	0.34	-1.32	76°	E	591.4 × 200.0 × 240.0	1024 × 256 × 1400	0.98
AN6	0.01	0.34	-0.45	53°	E	591.4 × 200.0 × 240.0	1024 × 256 × 1400	0.27
AN7	0.01	0.34	-0.31	42°	E	591.4 × 200.0 × 240.0	1024 × 256 × 1400	0.06
AN8	0.01	0.52	-2.02	76°	E	386.7 × 200.0 × 240.0	1024 × 256 × 1400	0.28
AN9	0.01	0.52	-0.90	60°	E	386.7 × 200.0 × 240.0	1024 × 256 × 1400	0.02
AN10	0.01	0.52	-0.46	41°	E	386.7 × 200.0 × 240.0	1024 × 256 × 1400	0.00
AN11	0.01	0.69	-2.67	76°	E	291.4 × 200.0 × 240.0	1024 × 256 × 1400	0.01
AN12	0.01	0.69	-1.20	60°	E	291.4 × 200.0 × 240.0	1024 × 256 × 1400	0.00
AN13	0.01	0.69	-0.61	41°	E	291.4 × 200.0 × 240.0	1024 × 256 × 1400	0.00
AN14	0.2	-0.53	-0.47	42°	W	379.4 × 200.0 × 240.0	1024 × 256 × 1400	0.09
AN15	0.01	-0.53	-0.92	60°	W	379.4 × 200.0 × 240.0	1024 × 256 × 1400	0.98
AN16	0.1	-0.79	-1.37	60°	W	254.5 × 200.0 × 240.0	1024 × 256 × 1400	0.19
AN17	0.2	-0.79	-1.37	60°	W	254.5 × 200.0 × 240.0	1024 × 256 × 1400	0.19

**Table 10.1:** Initial conditions, domain size and resolution, and transmission coefficient predicted by linear theory for the simulations discussed in-text. Columns are: simulation ID, initial peak vertical displacement amplitude  $A_0$  [km], streamwise and vertical wavenumbers [ $k_0$  and  $m_0$ , respectively;  $\text{km}^{-1}$ ] and corresponding  $\Theta_0 = \tan^{-1} |m_0/k_0|$ , QBO-E/W wind profile identifier (cf. Table 8.2), domain size  $L_x \times L_y \times L_z$  [ $\text{km}^3$ ] and resolution  $n_x \times n_y \times n_z$ , and transmission coefficient predicted by the numerical solution of the anelastic Taylor–Goldstein equation [Eq. (8.51); unitless].

Initial amplitudes were set to either  $A_0 = 10, 100$ , or  $200$  m. The upper bound for this range corresponds to the temperature perturbation of  $\Delta\theta = 2$  K used by [Holton and Alexander \(1999\)](#) in their simulations of storm-generated internal waves. To convert this to the vertical displacement perturbation amplitude, we use Eq. (8.11), evaluated at  $z = z_0$ , which gives

$$A_0 = \Delta\xi = \frac{\Delta\theta}{\bar{\theta}'} \Big|_{z=z_0} = \frac{H_\theta \Delta\theta}{\bar{\theta}} \Big|_{z=z_0} = \frac{\frac{7}{2} H_\rho \Delta\theta}{\theta_0}, \quad (10.1)$$

where  $\bar{\theta}' = \bar{\theta}/H_\theta$  and  $H_\theta = \frac{7}{2} H_\rho$  in our assumed uniformly stratified atmosphere. The reference potential temperature  $\theta_0$  follows from the same assumption, and the definition of

the density scale height,  $H_\rho = R_a T_0 / g = R_a \theta_0 / g$ . Here,  $T_0 = \theta_0$  in our assumed isothermal atmosphere, and  $R_a \approx 287 \text{ J kg}^{-1} \text{ K}^{-1}$  is the dry gas constant. Substituting these values into the right-hand side of Eq. (10.1) with gravitational acceleration  $g = 9.81 \text{ m s}^{-2}$ , gives

$$A_0 = \frac{7 R_a}{2 g} \Delta\theta \approx 200 \text{ m}.$$

This physical value represents the practical upper bound for initial amplitudes of simulations that remained numerically stable long enough to quantify steady-state transmission (for some, but not all, relative vertical wavenumbers  $m_0/k_0$ ).

## 10.1 Evolution of a small amplitude wave packet in a stationary atmosphere

We examine first the evolution of an initially small amplitude Gaussian wave packet with  $A_0 = 10 \text{ m}$ , and  $\mathbf{k}_0 = (0.75, 0, -0.68) \text{ km}^{-1}$ , so  $A_0/\lambda_x = A_0/(2\pi/k_0) = 0.0012$  (simulation AN1 in Table 10.1), and we describe its evolution in an otherwise stationary anelastic atmosphere. The purpose is twofold: (1) to demonstrate the basic behaviour of anelastic internal gravity wave packets without the complicating factor of nonuniform background flow, as the packet evolves from small to moderately large amplitude via anelastic growth; and, (2) to illustrate the method to obtain the initial pseudomomentum distribution (described in Sec. 9.6), to be applied later to quantify transmission of wave packets across a model QBO wind.

Snapshots of the vertical displacement field  $\xi$  through the planes  $y = 0$  and  $z = z_0 - c_{gz}t$  are shown in Fig. 10.1. The times shown in each row are representative of the wave packet at early, middle, and late times.

Initially [Fig. 10.1(a)] the lines of constant phase were oriented at  $\Theta_0 = 42^\circ$  from the vertical, and the wave packet propagated upward and rightward at this angle. Although the wave packet was centred at  $z_0 = 0$  (corresponding to the 300 hPa height in the atmosphere, at approximately 8.5 km altitude), the peak initial amplitude was located at  $\sigma_z^2/2H_\rho = 3.5 \text{ km}$  higher altitude due to the anelastic growth factor  $e^{z/2H_\rho}$ . This factor likewise increased the initial amplitude by  $e^{\sigma_z^2/8H_\rho^2} \approx 13\%$ . The initial profile of  $\langle \mathcal{P} \rangle / \rho_0$  [Fig. 10.1(c)], representative of the vertical extent of the wave packet without the influence of the anelastic growth factor,

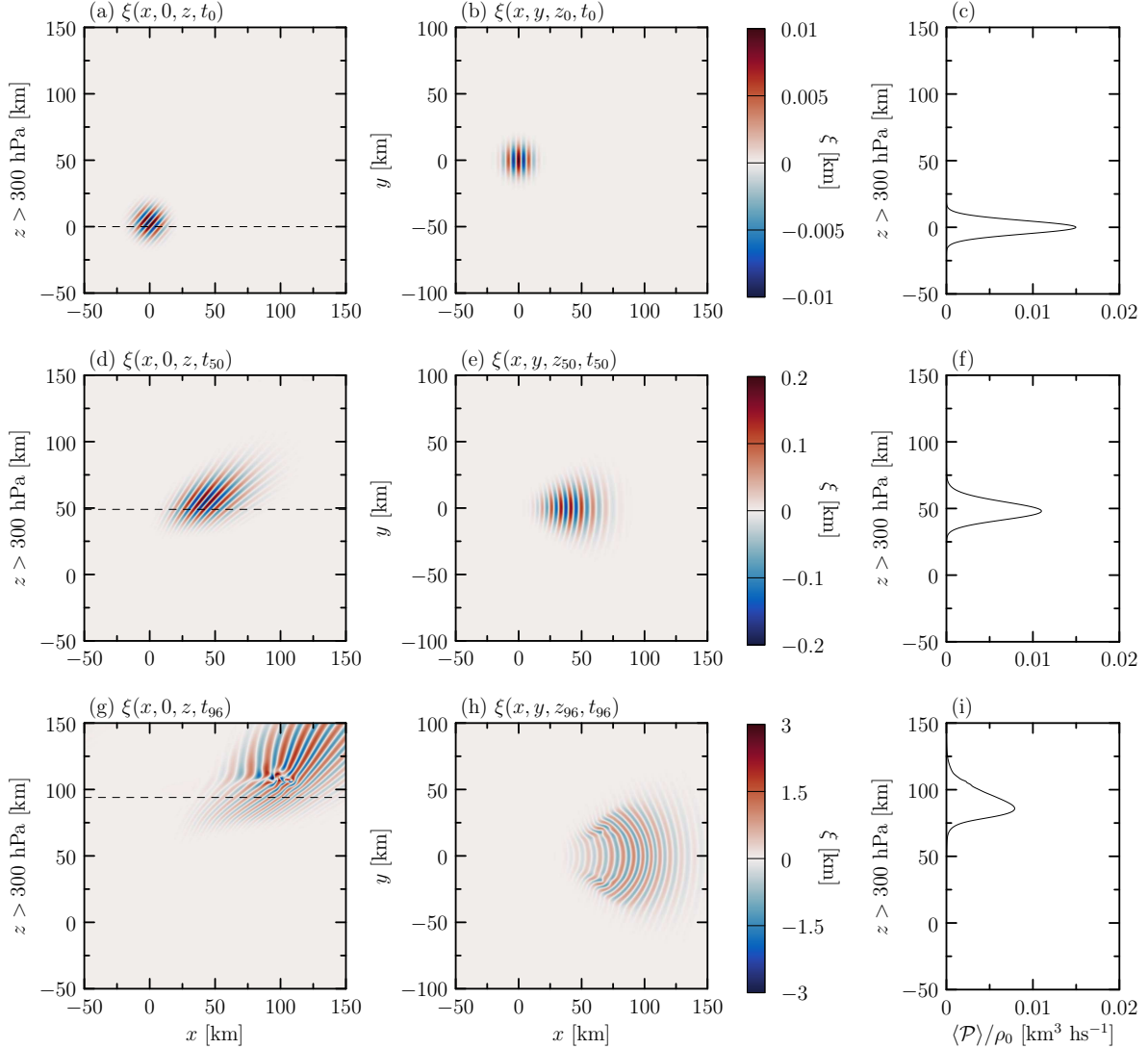


**Figure 10.1:** Snapshots of vertical displacement  $\xi$  [km] from simulation AN1 through the vertical plane  $y = 0$  (left column) and through the horizontal plane  $z_j = z_0 - c_{gz0} t_j$  predicted by linear theory (centre column) at time  $t = t_0 = 0$  (top row),  $t_{50} = 5000$  s (middle row), and  $t_{96} = 9600$  s (bottom row). The right column shows corresponding vertical profiles of the horizontally integrated pseudomomentum density per mass. The horizontal dashed lines in the left column denote the heights of the horizontal cross sections shown in the centre column. Image resolution in (b,e,h) was enhanced in postprocessing. Note that, for numerical stability, exponential damping was applied at altitudes  $z \geq 150$  km, and so the wave packet in (g) cannot be represented truthfully if centred in the viewing window.

confirms the wave packet was indeed centred at  $z_0 = 0$  initially.

At  $t = t_{50} = 5000$  s, significant dispersion occurred asymmetrically in the streamwise direction [Fig. 10.1(d); analogous to the “oblique” dispersion identified for two-dimensional wave packets by Gervais et al. (2018)] and spanwise direction along the leading flank of the wave packet [Fig. 10.1(e)]. The wave packet was anticipated to be modulationally stable

vertically because  $|m_0/k_0| \approx 0.91 \gtrsim 0.7$  [cf. Fig. 1.5(a)]. Indeed, vertical dispersion manifested in the broadened vertical extent of  $\langle \mathcal{P} \rangle / \rho_0$ , whose magnitude decayed correspondingly to approximately 73% of its initial value as a consequence of pseudomomentum conservation. This decay was offset by anelastic growth, together accounting effectively for the net amplitude growth of the wave packet by a factor of approximately 19 compared to the initial amplitude. This indicates that after 5000 s, linear dynamics continued to dominate the evolution of the wave packet. Despite the linear evolution, the dipolelike horizontal Bretherton flow at this time acted to deform the lines of constant phase on the leading flank of the wave packet [Fig. 10.1(e); analogous to the deformation of the phase lines of moderately nonhydrostatic Boussinesq wave packets in Fig. 7.5].

At  $t \approx 8545$  s (not shown), the wave packet grew to such large amplitude that waves overturned locally, as diagnosed by the overturning condition, Eq. (8.54). The waves continued overturning, evolving toward local turbulent breaking, which had developed well locally within less than 20 minutes [ $t_{96} = 9600$  s; Fig. 10.1(g)], as captured by the fully nonlinear code's dynamically-activated large eddy simulation (LES) module (cf. Sec. 9.5). The maximum displacement was approximately 3.46 km, with this maximum located at  $(x, z) \approx (93.7, 108.4)$  km. Linear theory predicts that the location of this maximum would be located at  $(x, z) = (85.5, 93.3)$  km if the wave packet had propagated at its group velocity, the discrepancy quantifying the contribution of the wave-induced mean flow to the advance of the wave packet. The effect of vertical dispersion and the wave-induced mean flow manifest in the profile of  $\langle \mathcal{P} \rangle / \rho_0$ , which was asymmetric about its peak [Fig. 10.1(i)]. Eventually the wave breaking became so intense that the LES was unable to keep the code numerically stable, crashing shortly after  $t_{101} = 10100$  s.

### 10.1.1 Total pseudomomentum

The total (initial) pseudomomentum corresponding to the wave packet in simulation AN1 was obtained using the method described in Sec. 9.6. The method is demonstrated here.

Vertical profiles of horizontally integrated pseudomomentum density per mass,  $\langle \mathcal{P} \rangle / \rho_0$ , are shown from  $t = t_{10} = 1000$  s onwards at intervals of 1000 s in Fig. 10.2(a). Each profile consisted of a positive part that propagated upward at the vertical group speed of

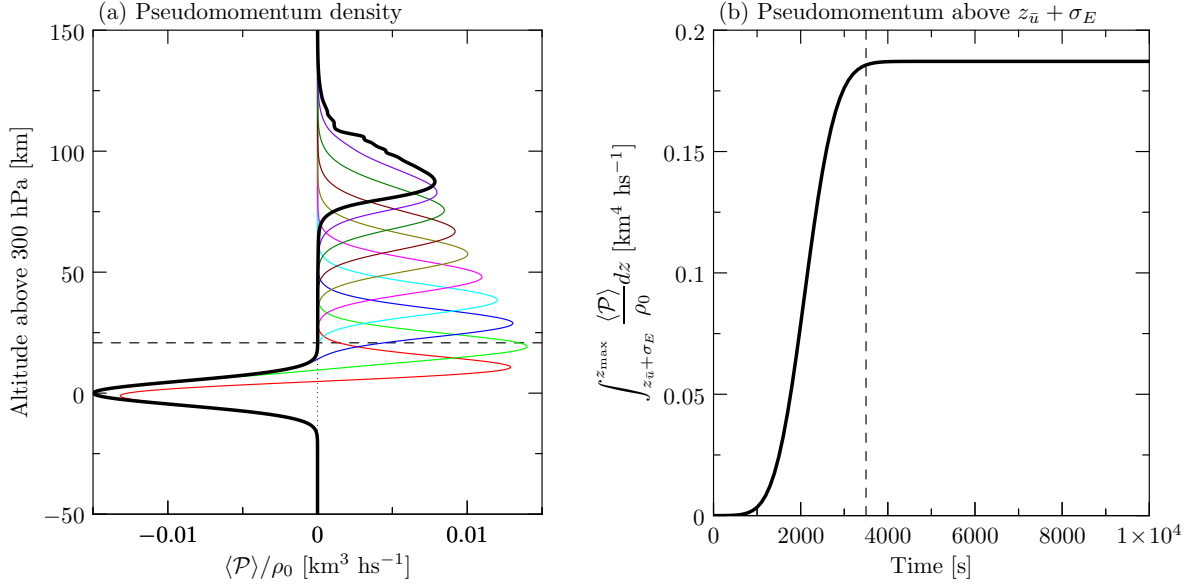


**Figure 10.2:** Pseudomomentum quantities corresponding to an anelastic wave packet with  $A_0 = 10$  m,  $k_0 = 0.75 \text{ km}^{-1}$  and  $m_0 = -0.68 \text{ km}^{-1}$  (simulation AN1 in Table 10.1): (a) vertical profiles of horizontally integrated pseudomomentum density per mass every 1000 s from  $t = t_{10} = 1000$  s to 10000 s; and, (b) time series of horizontally integrated pseudomomentum density per mass integrated vertically above  $z_{\bar{u}} + \sigma_E$ , denoted by the horizontal dashed line in (a). The dashed line in (b) indicates the time after which the vertical integral of horizontally integrated pseudomomentum density converged to  $\geq 99\%$  of the total pseudomomentum.

the wave packet, and a negative part centred near the initial position of the wave packet corresponding to the pseudomomentum ‘deficit.’ Although the upper part of the distribution broadened in vertical extent and decayed in amplitude as a consequence of pseudomomentum conservation, the lower part converged to a steady state, as indicated by the overlapping curves at successive times. This convergence is quantified in Fig. 10.2(b), which shows a time series of the area between  $\langle \mathcal{P} \rangle / \rho_0$  and the  $z$ -axis above  $z_{\bar{u}} + \sigma_E$ , denoted by the dashed line in Fig. 10.2(a). The dashed line in Fig. 10.2(b) denotes the time at which the area converged to  $\geq 99\%$  of its steady-state value, equal to the initial pseudomomentum,  $\mathcal{P}_0 \approx 0.187 \rho_0 \text{ km}^4 \text{hs}^{-1} \approx 8.16 \times 10^8 \text{ kg m s}^{-1}$ . This is the area between the  $z$ -axis and the pseudomomentum ‘deficit’ curve, which is the negative of the initial distribution of horizontally integrated pseudomomentum density. Note that in the pseudomomentum quantity,  $\rho_0$  is the mass density at the 300 hPa height. Using the ideal gas law and the definition of the density scale height,  $\rho_0 = p_0 / (R_a T_0) = p_0 / (g H_\rho) \approx 0.436 \text{ kg m}^{-3}$ .

The procedure described above produces valid results provided the wave packet propagated sufficiently far from its initial position in an otherwise stationary and uniformly stratified at-

mosphere. The first condition ensures there was no overlap between the pseudomomentum ‘deficit’ and the true pseudomomentum density corresponding to the propagating wave packet. The second condition is necessary so that there was no vertical redistribution of pseudomomentum density (e.g., below a reflection level) by nonuniformities in the background wind or stratification that would otherwise obscure the pseudomomentum density profile of the wave packet.

## 10.2 Evolution of wave packets incident upon the QBO-E

We now discuss the partial transmission/tunnelling and reflection of a moderately nonhydrostatic wave packet through the model QBO-E jet. The wave packet was initialized with  $\mathbf{k}_0 = (0.34, 0, -0.68) \text{ km}^{-1}$  and  $A_0 = 100 \text{ m}$  ( $A_0/\lambda_x \approx 0.0054$ ; AN2). The amplitude was chosen to be representative of the order of magnitude of the amplitude of simulated waves generated by convection (e.g., [Holton and Alexander, 1999](#)). The streamwise wavenumber corresponds to  $k_0\sigma_E = 1$ , and so  $\lambda_x = 18.48 \approx 20 \text{ km}$ , the shortest streamwise wavelength reported by [Holton and Alexander \(1999\)](#) and the longest practical wavelength of quasimonochromatic wave packets in our simulations. The vertical wavenumber corresponds to waves with a transmission coefficient predicted by linear theory of  $T \approx 0.74$ , in the relatively narrow transitional region in [Fig. 8.6\(b\)](#).

Snapshots of the vertical displacement fields  $\xi$  and  $\xi_s = \xi e^{-z/2H\rho}$  are shown in the left and centre columns, respectively, of [Fig. 10.3](#). The times shown are representative of the wave packet evolution at initial, early-, mid-, and posttunneling times.

Initially, [[Fig. 10.3\(a,b\)](#)], the unscaled and scaled fields overlap slightly with the QBO jet, indicated by the nonzero amplitude between the parallel horizontal lines (denoting the altitude one standard deviation,  $\sigma_E$ , above and below the QBO jet maximum). The overlapping part of the wave packet was just above  $2\sigma_z$  from the centre of the wave packet, and so the contribution of this part of the wave packet to the pseudomomentum above  $z_{\bar{u}} + \sigma_E$  is negligibly small. This is shown in [Fig. 10.3\(c\)](#) by the relative lack of pseudomomentum above  $z_{\bar{u}} + \sigma_E$ , represented by the (absence of a) shaded area between the  $z$ -axis and  $\langle \mathcal{P} \rangle / \rho_0$ .

Tunnelling, transmission, and reflection were underway at  $t_{10} = 1000 \text{ s}$  [[Fig. 10.3\(d,e\)](#)]. The

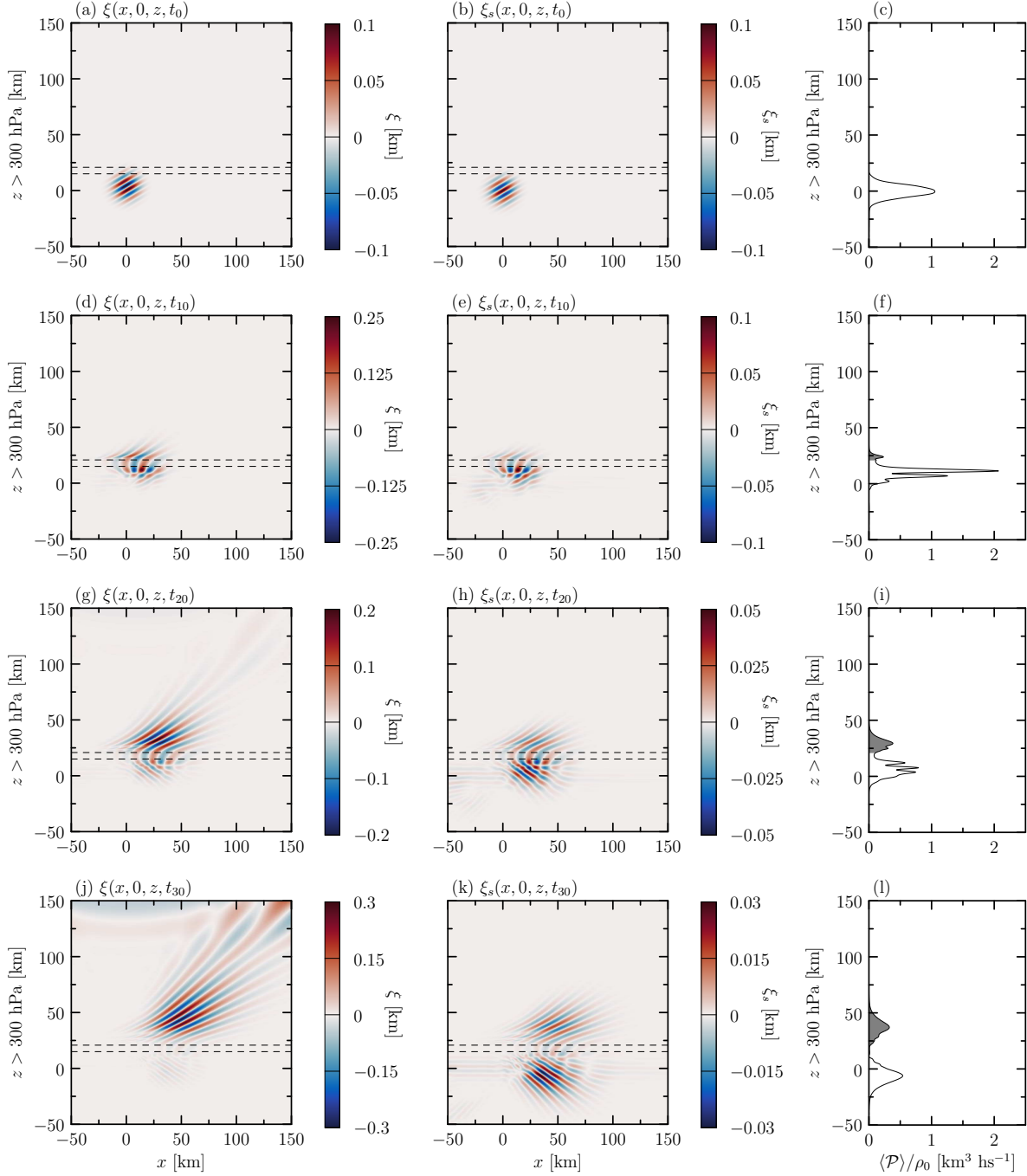


**Figure 10.3:** Snapshots of vertical displacement  $\xi$  (left column) and scaled vertical displacement  $\xi_s = \xi e^{-z/2H_p}$  (centre column) through the plane  $y = 0$ , and corresponding profiles of horizontally integrated pseudomomentum density per mass (right column) for a wave packet with  $A_0 = 100$  m, and  $k_0 = 0.34$   $\text{km}^{-1}$  and  $m_0 = -0.68$   $\text{km}^{-1}$  (AN2) at times (a–c)  $t = t_0 = 0$  s; (d–f)  $t_{10} = 1000$  s; (g–i)  $t_{20} = 2000$  s; and, (j–l)  $t_{30} = 3000$  s. The dashed lines denote the heights  $z_{\pm} \pm \sigma_E$ . The shaded regions in the right column represent the pseudomomentum density integrated above  $z_{\bar{u}} + \sigma_E$ .

tunnelling waves were evanescent (i.e., their amplitude decayed exponentially with altitude) in the region between the dashed lines. Because of the finite vertical extent of the QBO jet over

which the waves were evanescent, the reduced amplitude above  $z_{\bar{u}} + \sigma_E$  was large enough for the waves to resume their upward and rightward propagation. The largest amplitudes were located below  $z_{\bar{u}} - \sigma_E$ , corresponding to the superposition of the upward-propagating incident and downward-propagating reflected waves, manifesting in Fig. 10.3(d,e) as a checkerboard pattern of constructive and destructive interference, and in Fig. 10.3(f) as multiple peaks in the profile of  $\langle \mathcal{P} \rangle / \rho_0$ . Tunnelling, transmission, and reflection continued through  $t_{20} = 2000$  s [Fig. 10.3(g,h)], although the peak amplitude decreased compared to that at  $t_{10}$  as the bulk of the incident wave packet had encountered the QBO jet. Vertical separation of the transmitted and reflected wave packets occurred, manifesting as the distinct peaks in the profile of  $\langle \mathcal{P} \rangle / \rho_0$  [Fig. 10.3(i)].

Transmission and reflection were effectively complete at  $t_{30} = 3000$  s [Fig. 10.3(j–l)]. Significant vertical dispersion of the transmitted wave packet occurred, resulting in amplitude perturbations that propagated rapidly toward the top of the domain [Fig. 10.3(j)]. The vertical separation of the transmitted and reflected wave packets is more clear in Fig. 10.3(k), as quantified by the pseudomomentum density profile in Fig. 10.3(l). The wave packets continued to evolve until  $t = 4420$  s (not shown), at which time the vertically dispersed leading flank of the transmitted wave packet grew to  $O(1.5 \text{ km})$  amplitude, so large that the code became numerically unstable and the simulation ended. Final steady-state pseudomomentum transmission was well established, with  $T_{\mathcal{P}} \approx 0.367$ .

### 10.2.1 Effect of amplitude on transmission

A time series of horizontally integrated pseudomomentum density per mass vertically integrated above  $z_{\bar{u}} + \sigma_E$  for AN2 is shown as the red curve in Fig. 10.4(a). This quantity is compared with that obtained from otherwise identical simulations with amplitudes  $A_0 = 10$  and  $A_0 = 200$  m (AN3 and AN4; black and blue curves, respectively). Compared to waves with  $A_0 = 10$  m, the absolute pseudomomentum transmitted by wave packets with  $A_0 = 100$  and 200 m increased by a factor of approximately 100 and 400, respectively, as anticipated from the definition of the transmission coefficient involving pseudomomentum flux, which is quadratic in wave amplitude.

Figure 10.4(b) shows the same data as in Fig. 10.4(a) but as a fraction of the total pseudo-

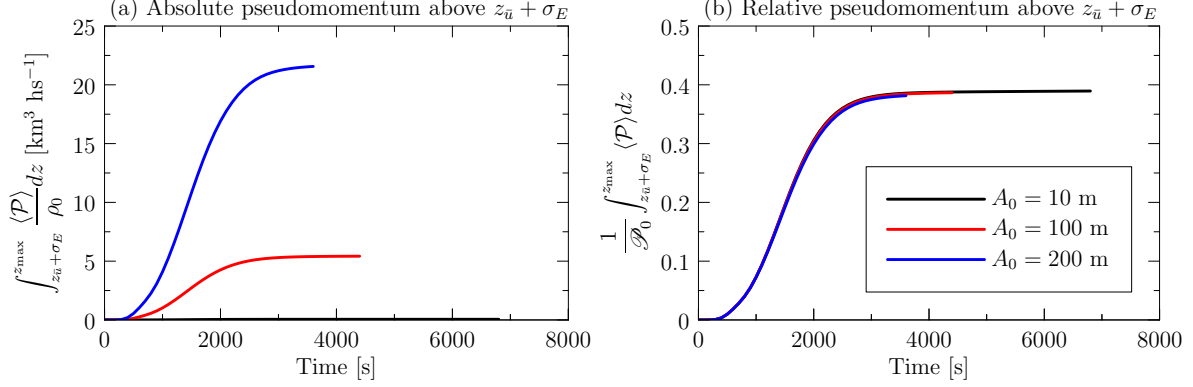


**Figure 10.4:** Time series of pseudomomentum transmission for wave packets with  $\mathbf{k}_0 = (0.34, 0, -0.68)$   $\text{km}^{-1}$  and a range of initial amplitudes (AN2–4) given (a) dimensionally; and, (b) as a fraction of total pseudomomentum  $\mathcal{P}_0$ . Each curve is plotted until the respective simulation ended due to numerical instability associated with the exponential growth of amplitude perturbations at the top of the domain.

momentum,  $\mathcal{P}_0$ , for the respective simulations. The agreement between the curves confirms that waves with initial amplitudes at least as large as 200 m evolved linearly. This suggests that the time scale for the Bretherton flow to interact nonlinearly with the wave packet is significantly longer than the time scale for reflection and transmission of these waves (despite the Bretherton flow field being superimposed on the wave packets initially).

### 10.2.2 Effect of vertical wavenumber on transmission

The results shown in Fig. 10.4 suggested that the final steady-state transmission of wave packets through the QBO-E scaled effectively quadratically with the physical range of initial amplitudes of interest. On this basis, we proceed to investigate the partial transmission of wave packets incident upon the QBO-E, with a range of relative vertical wavenumbers  $m_0/k_0$  but fixed initial amplitude  $A_0 = 10$  m.

Time series of pseudomomentum transmission for wave packets with  $k_0\sigma_E = 1$  are shown in Fig. 10.5(a). The range of vertical wavenumbers  $0.31 \text{ km}^{-1} \leq |m_0| \leq 1.32 \text{ km}^{-1}$  spans moderately to weakly nonhydrostatic wave packets, corresponding to  $0.91 \lesssim |m_0/k_0| \lesssim 3.88$ . Qualitatively, as wave packets were initialized to be progressively more nonhydrostatic (i.e., for decreasing  $|m_0|$ , equivalently as  $\omega_0 \rightarrow N_0$ ), steady-state transmission decreased as anticipated from linear theory. Quantitatively, transmission for wave packets with  $m_0 = -1.32, -0.68$ , and  $-0.45 \text{ km}^{-1}$  was less than the values predicted by linear theory by a factor of 24.5%,

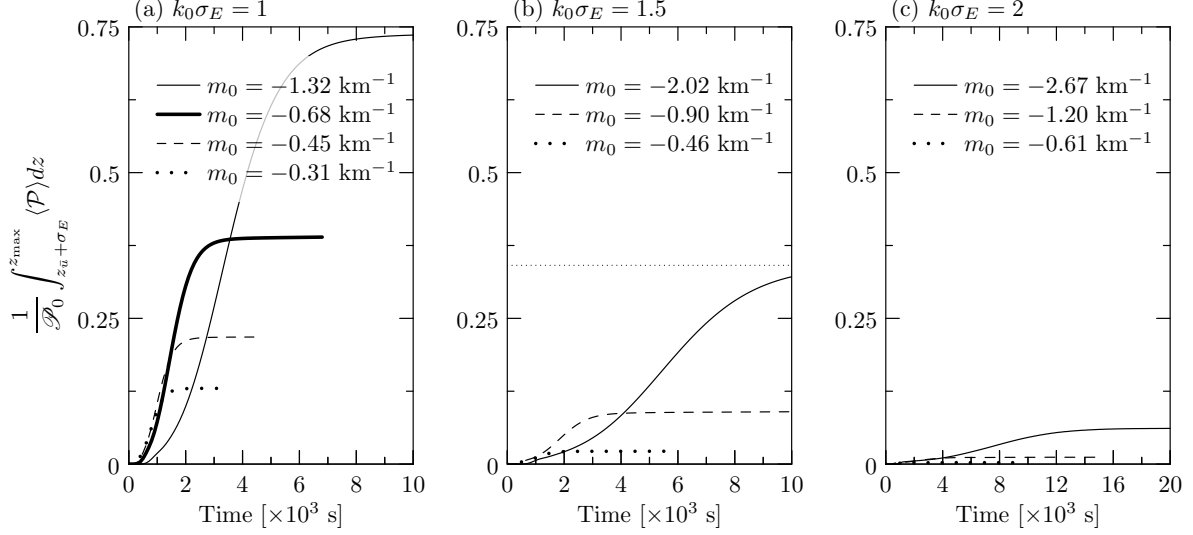


**Figure 10.5:** Time series of pseudomomentum transmission for wave packets with initial amplitude  $A_0 = 10$  m and (a)  $k_0 = 0.34$   $\text{km}^{-1}$  (AN2 and AN5–7); (b)  $k_0 = 0.52$   $\text{km}^{-1}$  (AN8–10); and, (c)  $k_0 = 0.69$   $\text{km}^{-1}$  (AN11–13), for a range of vertical wavenumbers. The heavy solid curve in (a) is identical to that in Fig. 10.4(b). The simulation with  $m_0 = -1.32$   $\text{km}^{-1}$  in (a) converged to within 99% of its steady-state transmission value at  $t \approx 8800$  s; the horizontal dotted line in (b) denotes the steady-state transmission value of the simulation with  $m_0 = -2.02$   $\text{km}^{-1}$ , which converged to within  $\geq 99\%$  of this value at  $t \approx 13500$  s (not shown).

47.6%, and 17.8%, respectively; transmission for the most strongly nonhydrostatic wave packet (with  $m_0 = -0.31$   $\text{km}^{-1}$ ) exceeded the value predicted by linear theory by 51.4%.

Time series of pseudomomentum transmission for wave packets with  $k_0\sigma_E = 1.5$  are shown in Fig. 10.5(b). Vertical wavenumbers were chosen so that the corresponding frequency was  $\omega_0/N_0 = 0.25, 0.5,$  and  $0.75$  ( $m_0 = -2.02, -0.9,$  and  $-0.46$   $\text{km}^{-1}$ , respectively). Like wave packets with  $k_0\sigma_E = 1$ , steady-state transmission decreased as the wave packets were initialized to be more nonhydrostatic. However, unlike wave packets with  $k_0\sigma_E = 1$ , transmission exceeded the values predicted by linear theory, by 18.9%, 74.5%, and 94.6% for wave packets with  $m_0 = -2.02, -0.9,$  and  $-0.46$   $\text{km}^{-1}$ , respectively.

Time series of pseudomomentum transmission for wave packets with  $k_0\sigma_E = 2$  are shown in Fig. 10.5(c), with  $m_0 = -2.67, -1.2,$  and  $-0.61$   $\text{km}^{-1}$  corresponding to  $\omega_0/N_0 = 0.25, 0.5,$  and  $0.75$ , respectively. Transmission was significantly less than for waves with  $k_0\sigma_E < 2$ , as shown by comparing the steady-state transmission values in Fig. 10.5(c) with those in Figs. 10.5(a) and 10.5(b). These values exceed those predicted by linear theory by 669.8%, 95.5%, and 99.1% for wave packets with  $m_0 = -2.67, -1.2,$  and  $-0.61$   $\text{km}^{-1}$ , respectively.

### 10.3 Evolution of wave packets incident upon the QBO-W

We now examine the partial transmission and reflection of wave packets through the QBO-W jet. The transmission coefficient predicted by linear theory is near unity for a broader range of streamwise wavenumbers, investigated in this section, of wave packets incident upon the QBO-W than the upon the QBO-E [comparing Figs. 8.6(a) and 8.6(b)]. In particular, streamwise wavenumbers were set by  $|k_0| = 2/\sigma_W = 0.53 \text{ km}^{-1}$  and  $3/\sigma_W = 0.79 \text{ km}^{-1}$ . Wave packets with  $|k_0| = 1/\sigma_W$  were not investigated because these were anticipated to evolve in a manner similar to waves with  $k_0 = 1/\sigma_E = 0.34 \text{ km}^{-1}$  described earlier. For the streamwise wavenumbers investigated here, vertical wavenumbers were chosen so that the waves would have frequency  $\omega_0/N_0 = 0.25, 0.5, \text{ or } 0.75$ .

Waves propagating leftward initially have  $k_0 < 0$ . To ensure the waves propagated forward in time (i.e.,  $\omega_0 > 0$ ), we take the negative root of Eq. (A.19) so that  $\omega_0 = -N_0 k_0 / K_0$ . Using this expression for the dispersion relation, the corresponding expressions for the components of group velocity are given simply by the right-hand sides of Eqs. (8.24a)–(8.24b) multiplied by  $-1$ . In practice, however, simulations using the QBO-W profile were initialized with  $k_0 > 0$  and  $m_0 < 0$  and  $\bar{u} \leq 0$  so that waves propagated upward and rightward initially, incident upon an *easterly* background flow; results were reflected about the  $z$ -axis in postprocessing to propagate ultimately toward the (intended) *westerly* QBO-W.

#### 10.3.1 Reflection, transmission, and turbulent breaking of a nonhydrostatic wave packet

We examine, in particular, the evolution of the wave packet with  $\mathbf{k}_0 = -(0.53, 0, 0.47) \text{ km}^{-1}$  and  $A_0 = 200 \text{ m}$  ( $A_0/\lambda_x \approx 0.0169$ ; AN14). Snapshots of the vertical displacement fields  $\xi$  and  $\xi_s$  are shown in the left and centre columns, respectively, of Fig. 10.6. The times shown are representative of the wave packet evolution at initial, mid-, posttunnelling, and turbulent breaking times.

Initially [Fig. 10.6(a,b)], the waves propagated upward and leftward, with phase lines oriented at an angle of  $\Theta_0 = 42^\circ$  from the vertical, but in a sense opposite to waves propagating rightward initially [cf. Fig. 10.3(a,b)]. Although there was some overlap between the wave

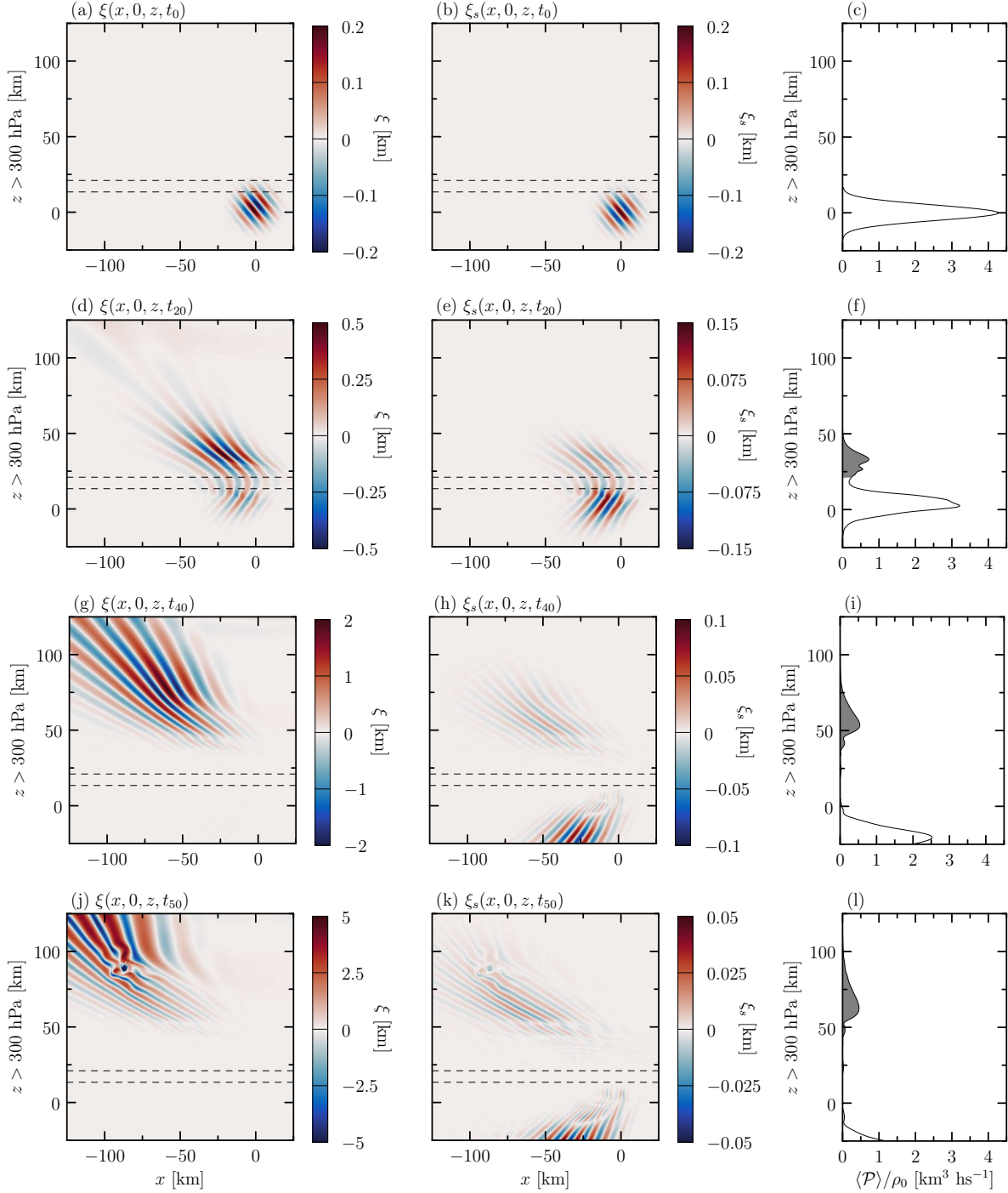


**Figure 10.6:** As in Fig. 10.3 but for a wave packet incident upon the QBO-W jet with  $A_0 = 200$  m, and  $k_0 = -0.53$  km $^{-1}$  and  $m_0 = -0.47$  km $^{-1}$  (AN14) at times (a–c)  $t = t_0 = 0$  s; (d–f)  $t_{20} = 2000$  s; (g–i)  $t_{40} = 4000$  s; and, (j–l)  $t_{50} = 5000$  s. The dashed lines denote the heights  $z_{\bar{u}} \pm \sigma_W$ . The shaded regions in the right column represent the pseudomomentum density integrated above  $z_{\bar{u}} + \sigma_W$ . The panels are zoomed in slightly compared to those in Fig. 10.3 to focus on a physical wave signal without obvious numerical artifacts.

packet and the QBO-W jet (denoted by the horizontal dashed lines), the corresponding pseudomomentum is negligibly small, as suggested by the absence of this quantity shaded in under the curve in Fig. 10.6(c).

At  $t = t_{20} = 2000$  s [Fig. 10.6(d,e)], partial reflection and transmission were well underway, with the transmitted wave packet displaying significant vertical dispersion. At  $t_{40} = 4000$  s [Fig. 10.6(g,h)], the leading flank of the transmitted wave packet continued to disperse vertically and in the streamwise direction, with the streamwise wavelength increasing compared to those near the trailing flank. The transmitted wave packet grew to sufficiently large amplitude to induce a mean flow, its nonlinear interaction with the waves manifesting as a kink in the phase lines near  $z \approx 70$  km, coincident with the largest amplitudes [Fig. 10.6(g)]. The post-tunnelling development of the wave-induced mean flow is similarly shown in vertical profiles of the horizontally integrated pseudomomentum density per mass in Fig. 10.6(i), manifesting in the asymmetric distribution of pseudomomentum density about the upper peak of this quantity.

Linear (anelastic) and nonlinear amplitude growth continued through  $t = 4055$  s (not shown), at which time wave overturning was diagnosed according to Eq. (8.54). The ensuing turbulence was well developed at  $t_{50} = 5000$  s [Fig. 10.6(j,k)]. The value and location of  $\min\{N_T^2\}$  provide a crude indication of where the most intense turbulence may be found (lacking diagnostics of a more appropriate measure such as turbulence kinetic energy). Time series of  $\min\{N_T^2\}$  (not shown) suggest the localized wave breaking region translated with the wave packet, advecting approximately 26.3 km West of and 21.8 km above the location where overturning was first diagnosed, during the intervening 1000 s separating the waves shown at  $t_{40} = 4000$  and  $t_{50} = 5000$  s in Figs. 10.6(g,h) and 10.6(j,k), respectively.

Time series of pseudomomentum transmission for AN14 are shown as the heavy curve in Fig. 10.7(a). Steady-state pseudomomentum transmission,  $T_{\mathcal{P}} = 0.206$ , was well established to within 99% of its final value at  $t_{26} = 2600$  s.

### 10.3.2 Effect of vertical wavenumber and amplitude on transmission

Like wave packets incident upon the QBO-E, pseudomomentum transmission of wave packets incident upon the QBO-W scaled effectively quadratically with the range of physical ampli-

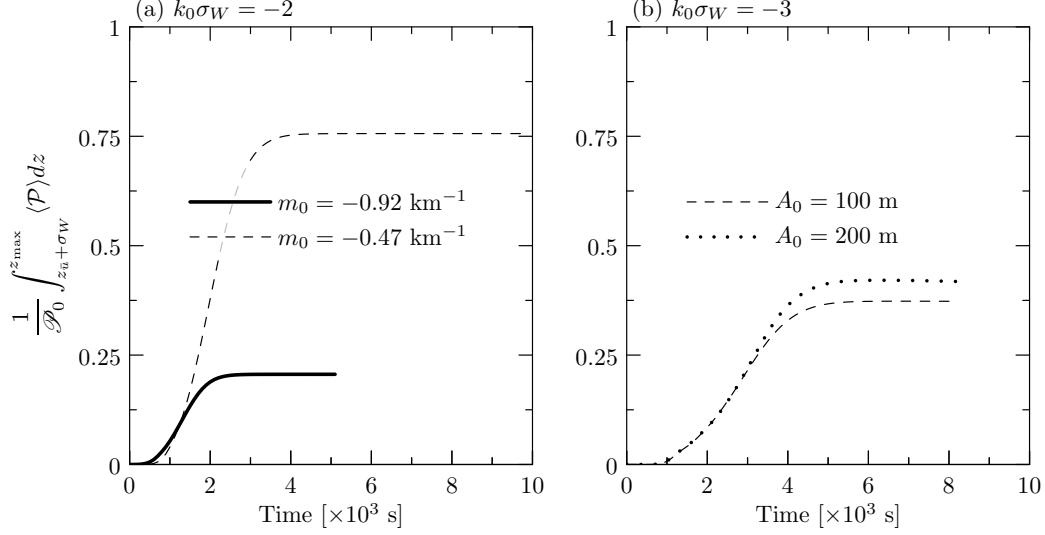


**Figure 10.7:** As in Fig. 10.5 but for wave packets incident upon the QBO-W jet with a range of small amplitudes and vertical wavenumbers, and (a)  $k_0 = -0.53 \text{ km}^{-1}$  (AN14–15); and, (b)  $k_0 = -0.79 \text{ km}^{-1}$  (AN16–17).

tudes of interest (not shown). Here, we investigate the transmission of wave packets incident upon the QBO-W with a range of relative vertical wavenumbers. The effects of varying initial amplitude are discussed briefly.

Time series of pseudomomentum transmission for wave packets with  $k_0 \sigma_W = -2$  are shown in Fig. 10.7(a). The range of vertical wavenumbers  $0.47 \text{ km}^{-1} \leq |m_0| \leq 0.92 \text{ km}^{-1}$  spans two moderately nonhydrostatic wave packets, corresponding to frequencies  $0.5 \leq \omega_0/N_0 \leq 0.75$  (equivalently,  $0.89 \lesssim |m_0/k_0| \lesssim 1.74$ ). Qualitatively, steady-state transmission decreased as wave packets were initialized to be more nonhydrostatic. Quantitatively, transmission for wave packets with  $m_0 = -0.92$  and  $-0.47 \text{ km}^{-1}$  exceeded (was less than) the values predicted by linear theory by (22.6%) and 58.6%, respectively.

A time series of pseudomomentum transmission for a wave packet with  $A_0 = 100 \text{ m}$  and  $m_0 = -1.37 \text{ km}^{-1}$  for  $k_0 \sigma_W = -3$  (AN16) is shown in Fig. 10.7(b). This vertical wavenumber corresponded to  $\omega_0/N_0 = 0.5$ . Steady-state transmission exceeded the value predicted by linear theory by 95.4%. A simulation identical to AN16 was performed, but with  $A_0 = 200 \text{ m}$  (AN17). Unlike most other wave packets with this initial amplitude, transmission did not attain a steady state, but peaked before decreasing in time [dotted curve in Fig. 10.7(b)]. The decrease was due to the generation and evolution of downward-propagating secondary wave packets (not shown). Secondary wave packets radiated from the leading flank of the

transmitted wave packet, resembling the early stages of secondary wave packet evolution by moderately nonhydrostatic Boussinesq wave packets (cf. Sec. 7.1.2). AN17 was the only simulation in which varying initial amplitude resulted in a quantitative change in final steady-state transmission, exceeding the value predicted by linear theory by 120.5%, and the value measured in AN16 by 12.9%.

## 10.4 Discussion

In this chapter we investigated predictions of the partial transmission of internal gravity wave packets through two idealized QBO jet profiles. These predictions were investigated by performing fully nonlinear numerical simulations of moderately nonhydrostatic three-dimensional wave packets with their predicted Bretherton flow superimposed, initialized using a range of wavenumbers and amplitudes motivated by the numerically simulated waves of [Holton and Alexander \(1999\)](#). To my knowledge, the simulations reported on in this chapter were the first to study, in an anelastic atmosphere, the self-interaction of such wave packets with their induced Bretherton flow incident upon a retrograde jet. More (less) hydrostatic wave packets tended to exhibit larger (smaller) pseudomomentum transmission above the QBO jet, relative to the initial pseudomomentum of the wave packet. Absolute (i.e., dimensional) transmission values increased effectively quadratically with the range of physical initial amplitudes of interest. Hence, varying initial amplitude had no quantitative effect on transmission relative to the initial pseudomomentum. This was ultimately because the time scale for self-interaction of the waves with their Bretherton flow, anticipated to enhance transmission, was significantly longer than that of transmission.

Wave packet transmission was considered quantitatively using two metrics,  $T_{\mathcal{E}}$  and  $T_{\mathcal{P}}$ . Transmission values were predicted ( $T_{\mathcal{E}}$ ) from the numerical solution of the anelastic Taylor–Goldstein equation [Eq. (8.51); [Nault and Sutherland \(2008\)](#)], and measured in simulation outputs using time-integrated pseudomomentum density flux integrated above  $z_{\bar{u}} + \sigma_{\{E,W\}}$  as a fraction of the initial pseudomomentum of the wave packet, i.e., the steady-state value of  $T_{\mathcal{P}}(t)$ . These distinct quantities agreed qualitatively in that transmission tended to decrease as wave packets were initialized to be progressively more nonhydrostatic. Quantitatively,  $T_{\mathcal{E}}$

performed poorly to predict the values of  $T_{\mathcal{P}}$ . For example,  $T_{\mathcal{P}}$  for wave packets with  $k_0\sigma_E = 1.5$  exceeded  $T_{\mathcal{E}}$  by 18.9–94.6% as wave packets were initialized to be more nonhydrostatic ( $-2.02 \text{ km}^{-1} \leq m_0 \leq -0.46 \text{ km}^{-1}$ ); conversely, as wave packets with  $k_0\sigma_E = 1$  were initialized to be more nonhydrostatic ( $-1.32 \text{ km}^{-1} \leq m_0 \leq -0.31 \text{ km}^{-1}$ ),  $T_{\mathcal{P}}$  was less than (more than)  $T_{\mathcal{E}}$  by amounts ranging nonmonotonically from 17.8–47.6% (51.4%), despite the comparable relative range of  $|m_0/k_0|$  values. The discrepancies between  $T_{\mathcal{E}}$  and  $T_{\mathcal{P}}$  for wave packets with  $k_0\sigma_W = -2$  and  $-3$  were similarly erratic.

The role of internal gravity waves propagating in a prograde sense relative to the QBO wind, ultimately to break and deposit their momentum at a critical level and hence lowering the altitude of the QBO jet, is well known (Lindzen and Holton, 1968; Baldwin et al., 2001). The role of partial transmission of gravity wave packets through a retrograde QBO wind, and the role of the wave-induced mean flow in this process, has been less well studied. Although the Bretherton flow had a negligible effect on diagnosed steady-state transmission values, transmitted wave packets tended to grow anelastically and induce a mean flow that acted to self-accelerate the waves, leading ultimately to their turbulent breaking. This occurred at altitudes corresponding to the real middle and upper atmosphere, where there exists in general a background wind, which we omitted entirely in our numerical simulations. Linear theory predicts that, depending on the wind velocity, the transmitted waves would be Doppler-shifted possibly to encounter a reflection (critical) level; the waves, existing at moderately large amplitude at these altitudes, may transmit partially above this height [or be absorbed partially at the critical level, perhaps acting to drive the mesospheric QBO (Burrage et al., 1996)].

Although reflection, tunnelling, and transmission proceeded qualitatively as anticipated by linear theory, our simulations provided insight into the nonlinear posttunnelling dynamics of transmitted wave packets. However, our results are highly idealized, having assumed a uniformly stratified atmosphere that was stationary above the modelled QBO jets. A more complete description of the role of internal gravity wave packets in driving atmospheric dynamics more generally should account for these effects, although due to time constraints such an endeavour was beyond the scope of this thesis.

---

## Summary and conclusions of thesis

---

### 11.1 Summary and main results

I have presented three projects examining the nonlinear evolution of fully localized three-dimensional internal gravity wave packets in three physically distinct contexts: (1) in a rotating Boussinesq fluid; (2) in a nonrotating Boussinesq fluid in which the background flow was nonuniform with height; and, (3) in a nonrotating anelastic gas in which the background flow modelled the Quasi-Biennial Oscillation (QBO). The nonlinearity manifested in the self-interaction of internal gravity wave packets with their wave-induced mean (Bretherton) flow. I derived explicit integral expressions for the Bretherton flow induced by wave packets in a rotating Boussinesq fluid, and in a nonrotating anelastic gas. On the basis of wave-mean-flow interactions, I obtained analytic predictions for several instability mechanisms that can drive waves ultimately to overturn. In the context of waves incident upon a retrograde shear flow, I obtained analytic predictions for wave packets to penetrate above the reflection level predicted by linear theory, to generate secondary wave packets, and to tunnel through the QBO winds. To evaluate these predictions, I wrote a series of three fully nonlinear, high performance numerical codes and ran simulations for a range of wave packet and environmental parameters. I compared results with predictions, and discussed various results in the context of observations and simulations of one- and two-dimensional internal gravity wave packets.

### 11.1.1 First project: Boussinesq wave packets with rotation

In Part I, I extended the derivation of [van den Bremer and Sutherland \(2018\)](#) to obtain the integral expression for the Bretherton flow in a rotating fluid, and in so doing I identified and reconciled an error in the original derivation without rotation. Extending the predictions of [Sutherland \(2001\)](#), I derived expressions for the critical initial amplitude above which internal waves were prone to overturning instability, and instabilities due to convection, self-acceleration, and shear between adjacent velocity crests and troughs of strongly hydrostatic waves. The critical amplitude for static instability was identical to that obtained for plane waves without rotation, whereas the critical amplitude for convection instability depended explicitly on the Coriolis parameter. The critical amplitude for self-acceleration accounted explicitly for rotation and the finite spatial extent of the wave packet, although the corresponding expression included an integral that needed to be evaluated numerically. Two critical amplitudes for shear instability, using different definitions of the gradient Richardson number, accounted for rotation and the spanwise component of wave velocity, but gave conflicting predictions for the onset of shear instability relative to the other instability amplitudes.

To examine the instability predictions numerically, I upgraded an existing fully nonlinear code to superimpose the predicted Bretherton flow onto the initial wave fields (for which I designed and implemented a method to evaluate the singular integral describing the initial Bretherton flow); included Coriolis terms in the numerically integrated evolution equations; introduced a third-order accurate time integration scheme; and, parallelized the code with [OpenMP](#) to run simulations efficiently on high performance computing platforms operated by the [Digital Research Alliance of Canada](#). Further efficiency was gained by preallocating memory for large three-dimensional arrays (as opposed to dynamically allocating and deallocating within repeated function calls), at the cost of a larger overall memory footprint.

I performed simulations of round three-dimensional wave packets with their Bretherton flow superimposed, having wavenumbers ranging from nonhydrostatic to near-inertial and amplitudes from small to overturning. I compared the initial amplitudes for which waves eventually overturned with the predictions of linear theory and characterized the results in terms of the instability mechanisms governing wave evolution. Due to interactions with the

mean flow induced by the waves, the waves in general were found to overturn even though their initial amplitude was well below the overturning amplitude predicted by linear theory. Likewise, in all but the most strongly nonhydrostatic simulations, the self-acceleration condition overpredicted the amplitude for which wave packets eventually overturned. Strongly hydrostatic waves, propagating at nearly horizontal angles  $\Theta \gtrsim 80^\circ$ , were found to overturn due to localized isopycnal steepening. Shear instability was not evident in time series of the minimum gradient Richardson number for strongly hydrostatic waves, in agreement with our predictions and those of [Gossard et al. \(1971\)](#), but not with those of, e.g., [Fritts and Rastogi \(1985\)](#) and [Achatz \(2007\)](#). This result was insensitive to the definition of gradient Richardson number used.

A small number of simulations of nonhydrostatic long and wide wave packets suggested that long (wide) wave packets overturned at approximately the same times (earlier times) as round wave packets with the same amplitude and relative vertical wavenumber, against the predicted increased (decreased) vulnerability to self-acceleration compared to round wave packets. Wave packet aspect ratio was found to have little effect on the overturning times of hydrostatic long and wide wave packets.

One simulation was performed using wave packet parameters estimated from observations of a lee wave generated in the Shackleton Fracture Zone ([Cusack et al., 2017](#)). Overturning of the simulated wave was diagnosed just below the height at which the sea surface would have intersected the numerical domain, and well within the horizontal region in which the strongest velocity perturbations were measured. Shear instability was predicted not to play a role in driving the wave to overturn, as confirmed by time series of the minimum gradient Richardson number.

Overall, the results of this project suggested that waves tend to become unstable and overturn at smaller amplitudes than those predicted by linear theory. From this we infer that upward-propagating waves overturn, break, and deposit their momentum at earlier times, and hence at lower heights, than those predicted by linear theory. Clearly, this implication has potential consequences for internal gravity wave drag parameterization schemes based on linear theory of monochromatic waves (such as those currently employed in the operational weather prediction models of [Environment and Climate Change Canada](#)). However, this

outlook must be viewed in light of the assumptions and limitations of our model: for example, the use of the Boussinesq approximation, uniform stratification, infinite periodic domain, no background flow, and finite spatial and temporal resolution in the numerical code. These issues represent potential starting points for further research, elaborated on below.

### 11.1.2 Second project: Boussinesq wave packets in nonuniform background shear

In Part II, I extended the predictions of [Sutherland \(2000\)](#) to predict the critical initial amplitude for “reflection level penetration” of three-dimensional wave packets, above which there is finite transmission above the reflection level at late times. I described how triadic resonant instability (TRI) between strongly nonhydrostatic incident and reflected waves could generate upward-propagating secondary wave packets, and proposed a novel weakly nonlinear mechanism I called “self-reflection” as a possible mechanism to generate downward-propagating secondary wave packets by nonbreaking primary waves. To quantify the transmission of wave packets above the reflection level, I defined a time-dependent transmission coefficient based on the horizontally integrated pseudomomentum density associated with upgoing waves, integrated above the reflection level.

To obtain transmission coefficients numerically, I upgraded the code used in Part I to include the Doppler-shifting terms in the numerically integrated evolution equations; implemented a more effective antialiasing filter; and, designed and implemented the algorithms to obtain transmission diagnostics from the upward-propagating components of the wave fields. I identified the ideal placement (within the time integration loop) of the function calls to most efficiently diagnose transmission using existing data, thus reducing the number of potentially unnecessary floating point operations.

I performed simulations of round nonhydrostatic three-dimensional wave packets with their Bretherton flow superimposed, with a range of small to moderately large amplitudes, but not so large that the waves overturned due to self-acceleration. Depending on the wavenumber and amplitude, the characteristics of transmission varied significantly. Using upward-propagating pseudomomentum above the predicted reflection level as a measure of transmission, it was found generally that small amplitude wave packets yielded larger transmission values (relative

to the conserved total pseudomomentum in their respective domains) at earlier times than otherwise identical larger-amplitude wave packets. This trend materialized for all but the most strongly nonhydrostatic wave packets with moderately large initial amplitudes, which instead exhibited a dramatic increase in transmission with amplitude. This increase was attributed to upward-propagating secondary wave packets generated by TRI between the incident and reflected wave packets. The time of peak transmission, and the subsequent time interval to return to half this peak, tended to increase with increasing amplitude. The existence of transmitted upward-propagating pseudomomentum above the reflection level at late times was analogous to “steady-state” transmission of one- and two-dimensional wave packets in linear retrograde shear flow simulated by [Sutherland \(2000\)](#). As moderately large amplitude wave packets were initialized to be progressively more hydrostatic, downward-propagating secondary wave packets (which I attributed to self-reflection, upon ruling out TRI) were generated preferentially to radiate below and forward of the upward-propagating primary wave packet.

The predicted critical amplitude for reflection level penetration was generally well borne-out in the results of this project. If future research determines this finding to be robust across a broader range of retrograde shear flow profiles, general circulation models may ultimately benefit from gravity wave drag parameterization schemes that account for finite penetration of pseudomomentum above the reflection level. The condition for self-reflection tended to over-predict the critical amplitude for secondary wave packet generation by moderately hydrostatic primary waves. A more consequential result, however, is that all secondary wave packets were generated by nonbreaking primary waves. To my knowledge, this finding represents the first instance in which (simulated) secondary waves were generated by nonbreaking, as opposed to breaking, primary waves [as is typically invoked as the generation mechanism for secondary waves in observations, and numerical and theoretical models (e.g., [Bossert et al., 2017](#); [Fritts et al., 2021](#); [Vadas and Fritts, 2006](#))]. Beyond purely scientific interest in secondary wave packets, accounting for their pseudomomentum transport (without invoking breaking primary waves) offers a potential direction to improve the energy budgets of general circulation models.

### 11.1.3 Third project: Anelastic wave packets in nonuniform background flow

In Part III, I extended the derivation of the Bretherton flow in Part I to three-dimensional wave packets in a nonrotating anelastic gas. Using the resulting integral expression, I derived the corresponding critical amplitude for self-acceleration, and an analytic prediction for reflection level penetration (applicable to anelastic waves incident upon a background shear flow that changed relatively slowly with height, which I did not ultimately simulate). Solving numerically a certain Taylor–Goldstein equation, I obtained predictions for small amplitude waves to tunnel across two distinct jet profiles, corresponding to the easterly and westerly phases of the Quasi-Biennial Oscillation (QBO). I described a procedure for selecting and fitting observational data to obtain the two QBO profiles. The transmission coefficient for tunnelling waves was quantified using the ratio of horizontally and temporally integrated vertical fluxes of pseudomomentum as this quantity tended asymptotically to a quasisteady limiting value.

To simulate the evolution of wave packets in an anelastic model atmosphere, I implemented a regime of comprehensive modifications to the code described in Chapter 6. The overall purpose of the sweeping changes was to account for the exponential (anelastic) growth of the wave fields with altitude. To that end, I converted the numerical method used in the vertical direction from fast Fourier transforms to fourth-order finite differences. This entailed several major changes to the code’s dynamical core, including solving the vertical momentum equation (as opposed to integrating the anelastic nondivergence condition), and deriving and implementing an efficient method to solve a large number of Poisson equations for vertical profiles of perturbation pressure (each the solution of a unique pentadiagonal matrix inversion problem). I implemented a Smagorinsky turbulence scheme that was activated dynamically to enhance numerical stability when the simulated waves were overturning.

I performed simulations of round, moderately nonhydrostatic, three-dimensional wave packets with their predicted Bretherton flow superimposed. Simulations were initialized using a range of physically motivated wavenumbers and amplitudes corresponding to those of existing numerically simulated waves generated by tropical convection. I compared the

measured transmission coefficient (based on the pseudomomentum density flux integrated in time and spatially above the QBO, relative to the initial, conserved, pseudomomentum of the wave packet) to the one predicted by linear theory. The measured transmission reproduced the broad qualitative prediction for transmission to decrease as waves were initialized to be progressively more nonhydrostatic. Quantitatively, the transmission coefficient predicted by linear theory performed poorly, inconsistently predicting higher or lower values than those diagnosed in the fully nonlinear simulations. This confirms, as one might suspect intuitively, that the transmission of small amplitude monochromatic waves through a QBO jet does not necessarily provide a reliable prediction of the transmission of quasimonochromatic wave packets. This finding has potentially significant consequences for internal gravity wave drag parameterization schemes based on the theory of monochromatic waves.

Initial amplitude was varied across a range of physically meaningful values. Because wave amplitudes were small initially (relative to the streamwise wavelength), nonlinear interactions with the induced Bretherton flow had no quantitative effect on transmission and reflection, as these linear dynamics evolved on time scales much shorter than those of nonlinear self-interactions with the Bretherton flow. Despite this, transmitted wave packets typically evolved to grow to moderately large amplitudes due to the exponentially decreasing background mass density of the idealized atmosphere. This anelastic growth drove the waves to sufficiently large amplitudes to induce a significant Bretherton flow, which acted nonlinearly through self-acceleration to drive the waves to overturning amplitudes, and ultimately to break turbulently.

The Smagorinsky turbulence scheme was generally effective to model the relatively small-scale motions associated with turbulent wave breaking following overturning. In several numerical simulations this turbulence model enhanced the numerical stability postoverturning for sufficiently many additional time steps to measure steady-state transmission, compared to previous simulations of overturning waves without a turbulence model (i.e., the codes used in Parts I and II). Although the Smagorinsky turbulence scheme was not sufficiently sophisticated to model pseudomomentum *deposition* to the background flow by breaking waves, this scheme nonetheless provided revealing quantitative diagnostics of the time and location of wave breaking. For example, in one simulation spanning over 5000 s of wave evolution, waves overturned and broke turbulently in a localized region that translated with the wave

packet [cf. Fig. 10.6(j,k)]. Through the time interval during which overturning (and hence turbulence) was diagnosed, the breaking region translated approximately 25 km downstream (located finally approximately 85 km from where the wave packet was initialized). Assuming wave breaking would have resulted in some pseudomomentum deposition had this process been resolved, this demonstrates the need (as suggested by [Plougonven et al., 2019](#)) to account for delayed pseudomomentum deposition and lateral wave propagation in parameterization schemes, as opposed to instantaneous deposition at a predicted height directly above the wave generation site.

## 11.2 Future work and final remarks

Possible directions for future work to further advance the research presented in this thesis may be categorized generally, with some overlap, as (1) theoretical; (2) modelling; and, (3) numerical.

Several suggestions mentioned in Sec. 11.1.1 in the context of the first project were addressed subsequently in this thesis; in particular, I relinquished the assumption that the fluid was stationary in the absence of waves in Parts II and III, and adopted the anelastic approximation in Part III. One assumption that remained in use across all three Parts was that of uniform background stratification. Existence of theoretical results for internal gravity waves in nonuniformly stratified fluids (e.g., [Brown and Sutherland, 2007](#); [Nault and Sutherland, 2008](#)) suggests that a natural next step would be to extend the theory presented in Part III to a nonuniformly stratified anelastic atmosphere. In anticipation of such a follow-up study, the corresponding fully nonlinear governing equations (including those modelling small scale turbulence) for the numerical simulation of wave packets in such a fluid were stated in Chapter 9 and Appendix F.

It may be beneficial to supplement the studies reported on in this thesis by performing corresponding weakly nonlinear studies. The nonlinear Schrödinger equation models the weakly nonlinear interactions between the wave-induced mean flow and the wave packet envelope (e.g., [Akylas and Tabaei, 2005](#); [Sutherland, 2006b](#)). On this basis, a sequence of nonlinear Schrödinger equations could be derived under the respective assumptions of Parts I–III, and

solved numerically for comparison with the results of the fully nonlinear simulations presented in this thesis. Such an approach was used in studies of the weakly nonlinear evolution of one- and two-dimensional wave packets propagating in uniformly stratified fluids (Dosser and Sutherland, 2011; Gervais et al., 2018). In the case of two-dimensional wave packets, the significant reduction in the computational cost of weakly nonlinear simulations, as opposed to fully nonlinear ones, while yielding comparable results, was specifically noted. Furthermore, valuable theoretical insights (such as “oblique dispersion”) were gleaned from an analysis of the two-dimensional nonlinear Schrödinger equation that were not obvious from a high-level analysis of the two-dimensional governing equations. This suggests similar benefits may follow from studies in three dimensions.

Throughout this thesis, for convenience wave packets were initialized to be triply Gaussian. It may be interesting, even if only intrinsically, to consider wave packets with alternative structures initially. One could similarly consider the generation and evolution of the Bretherton flow induced by three-dimensional wave packets excited transiently. Such studies would be anticipated to elucidate the nonlinear dynamics of internal gravity wave packets in a broader range of physically meaningful scenarios.

Although in Parts II and III we quantified pseudomomentum *transport* by internal gravity wave packets, we were neither able to predict nor quantify the *deposition* of pseudomomentum by breaking waves (in Part III in particular). In order ultimately to improve internal gravity wave drag parameterization schemes, it is necessary to quantify the time, location, and amount of pseudomomentum deposited to the mean flow. A dedicated research program could investigate the role of the Bretherton flow in this process. The corresponding simulations may require fine spatial resolution beyond what the existing anelastic code can attain [considering the hardware limitations of the high performance computing (HPC) platforms on which the code was designed to be run, and the corresponding use of the shared-memory parallelization paradigm]. Therefore, a significant first step in such a research program could be to parallelize the code using, e.g., a hybrid MPI-OpenMP framework, thereby enabling access to the memory and computational power of distributed HPC resources. Leveraging the more flexible parallelization, the overall speed of the code will almost certainly improve by upgrading the fast Fourier transform algorithm to, e.g., FFTW, and by adopting the use

of a modern high-performance output file type, e.g., [HDF5](#). The strongly nonlinear turbulent dynamics simulated by the resulting code may further benefit from more sophisticated numerical methods in the code’s dynamical core. For example, the WENO5 finite differencing scheme (cf. Sec. [9.2.1](#)) could be implemented in the vertical using this scheme’s actual nonlinear weights (e.g., [Ghosh and Constantinescu, 2016](#)). The large eddy simulation (LES) turbulence scheme itself could be upgraded to set local values of the Smagorinsky constant adaptively, as in the LES scheme of [Germano et al. \(1991\)](#).

In light of the number and diversity of possible future research directions, it is fair to say that much work remains to be done to continue improving our understanding of nonlinear internal gravity wave evolution, with the aim ultimately to improve internal gravity wave drag parameterization schemes. Although I would have liked to pursue these issues in this thesis, these exciting tasks now stand before the next generation of graduate students, because “my research must be ended somehow.”\*

---

\*Lyric composed by Tatiana Shmalyuk (singer) for the song *I Speak Astronomy* by Ukrainian metalcore band [Jinjer \(2016\)](#).

---

## Bibliography

---

- Achatz, U., 2007: Gravity-wave breaking: Linear and primary nonlinear dynamics. *Adv. Space. Res.*, **40**, 719–733, doi:10.1016/j.asr.2007.03.078.
- Acheson, D. J., 1976: On over-reflexion. *J. Fluid Mech.*, **77**, 433–472.
- Aguilar, D. A., B. R. Sutherland, and D. J. Muraki, 2006: Generation of internal waves over sinusoidal topography. *Deep-Sea Res. II*, **53**, 96–115.
- Ahrens, C. D., P. L. Jackson, and C. E. Jackson, 2012: *Meteorology Today*. 1st Canadian ed., Nelson Education, Toronto, Canada, 616 pp.
- Akylas, T. R., and A. Tabaei, 2005: Resonant self-acceleration and instability of nonlinear internal gravity wavetrains. *Frontiers of Nonlinear Physics*, A. Litvak, Ed., Institute of Applied Physics, Nizhny Novgorod, Russia, 129–135.
- Alford, M. H., 2010: Sustained, full-water-column observations of internal waves and mixing near Mendocino Escarpment. *J. Phys. Oceanogr.*, **40**, 2643–2660, doi:10.1175/2010JPO4502.1.
- Alford, M. H., J. A. MacKinnon, H. L. Simmons, and J. D. Nash, 2016: Near-inertial internal gravity waves in the ocean. *Annu. Rev. Mar. Sci.*, **8**, 95–123, doi:10.1146/annurev-marine-010814-015746.
- Allen, M. B., and E. L. Isaacson, 1998: *Numerical Analysis for Applied Science*. Wiley-Interscience, New York, USA, 492 pp.
- Andreassen, Ø., C. E. Wasberg, D. C. Fritts, and J. R. Isler, 1994: Gravity wave break-

- ing in two and three dimensions 1. Model description and comparison of two-dimensional evolutions. *J. Geophys. Res.*, **99** (D4), 8095–8108.
- Andrews, D. G., and M. E. McIntyre, 1976: Planetary waves in horizontal and vertical shear: The generalized Eliassen–Palm relation and the mean flow acceleration. *J. Atmos. Sci.*, **33**, 2031–2048.
- Andrews, D. G., and M. E. McIntyre, 1978a: An exact theory of nonlinear waves on a Lagrangian-mean flow. *J. Fluid Mech.*, **89**, 609–646.
- Andrews, D. G., and M. E. McIntyre, 1978b: On wave action and its relatives. *J. Fluid Mech.*, **89**, 647–664.
- Angell, J. K., and J. Korshover, 1964: Quasi-biennial variations in temperature, total ozone, and tropopause height. *J. Atmos. Sci.*, **21**, 479–492.
- Anstey, J. A., T. P. Banyard, N. Butchart, L. Coy, P. A. Newman, S. Osprey, and C. J. Wright, 2021a: Prospect of increased disruption to the QBO in a changing climate. *Geophys. Res. Lett.*, **48**, e2021GL093058, doi: 10.1029/2021GL093058.
- Anstey, J. A., and T. G. Shepherd, 2014: High-latitude influence of the quasi-biennial oscillation. *Q. J. Roy. Meteor. Soc.*, **140**, 1–21, doi: 10.1002/qj.2132.
- Anstey, J. A., I. R. Simpson, J. H. Richter, H. Naoe, M. Taguchi, F. Serva, L. J. Gray, N. Butchart, K. Hamilton, S. Osprey, O. Bellprat, P. Braesicke, A. Bushell, C. Cagnazzo, C.-C. Chen, H.-Y. Chun, R. R. Garcia, L. Holt, Y. Kawatani, T. Kerzenmacher, Y.-H. Kim, F. Lott, C. McLandress, J. Scinocca, T. N. Stockdale, S. Versick, S. Watanabe, K. Yoshida, and S. Yukimoto, 2021b: Teleconnections of the Quasi-Biennial Oscillation in a multi-model ensemble of QBO-resolving models. *Q. J. Roy. Meteor. Soc.*, **148**, 1568–1592, doi: 10.1002/qj.4048.
- Asselin, R., 1972: Frequency filter for time integrations. *Mon. Wea. Rev.*, **100** (6), 487–490.
- Baldock, T. E., C. Swan, and P. H. Taylor, 1996: A laboratory study of nonlinear surface waves on water. *Philos. Trans. R. Soc. A*, **354**, 649–676.

- Baldwin, M. P., and T. J. Dunkerton, 2001: Stratospheric harbingers of anomalous weather regimes. *Science*, **294**, 581–584, doi: 10.1126/science.1063315.
- Baldwin, M. P., L. J. Gray, T. J. Dunkerton, K. Hamilton, P. H. Haynes, W. J. Randel, J. R. Holton, M. J. Alexander, I. Hirota, T. Horinouchi, D. B. A. Jones, J. S. Kinnnersley, C. Marquardt, K. Sato, and M. Takahashi, 2001: The quasi-Biennial Oscillation. *Rev. Geophys.*, **39** (2), 179–229, doi: 8755-1209/01/1999RG000073.
- Becker, E., and S. L. Vadas, 2018: Secondary gravity waves in the winter mesosphere: Results from a high-resolution global circulation model. *J. Geophys. Res. Atmos.*, **123**, 1–23, doi: 10.1002/2017JD027460.
- Blumen, W., 1985: Reflection of hydrostatic gravity waves in a stratified shear flow. Part I: Theory. *J. Atmos. Sci.*, **42** (21), 2255–2263.
- Booker, J. R., and F. P. Bretherton, 1967: The critical layer for internal gravity waves in shear flow. *J. Fluid Mech.*, **27**, 513–539.
- Bossert, K., C. G. Kruse, C. J. Heale, D. C. Fritts, P. B. Williams, J. B. Snively, P.-D. Pautet, and M. J. Taylor, 2017: Secondary gravity wave generation over New Zealand during the DEEPWAVE campaign. *J. Geophys. Res. Atmos.*, **122**, 7834–7850, doi: 10.1002/2016JD026079.
- Bowman, J., and A. Hammerlindl, 2008: Asymptote: A vector graphics language. *TUGboat: Commun. T<sub>E</sub>X Users Group*, **29** (2), 288–294.
- Boyd, J. P., 2001: *Chebyshev and Fourier Spectral Methods*. Dover Publications, Mineola, USA, 594 pp.
- Bramberger, M., A. Dörnbrack, H. Wilms, S. Gersma, K. Raynor, and R. Sharman, 2018: Vertically propagating mountain waves—A hazard for high-flying aircraft? *J. Appl. Meteorol. Clim.*, **57**, 1957–1975, doi: 0.1175/JAMC-D-17-0340.1.
- Bramberger, M., A. Dörnbrack, K. Bossert, B. Ehard, D. C. Fritts, B. Kaifler, C. Mallaun, A. Orr, P.-D. Pautet, M. Rapp, M. J. Taylor, S. Vosper, B. P. Williams, and B. Witschas,

- 2017: Does strong tropospheric forcing cause large-amplitude mesospheric gravity waves? A DEEPWAVE case study. *J. Geophys. Res. Atmos.*, **122**, 11 422–11 443, doi: 10.1002/2017JD027371.
- Bretherton, F. P., 1966: The propagation of groups of internal gravity waves in a shear flow. *Quart. J. Roy. Meteorol. Soc.*, **92**, 466–480.
- Bretherton, F. P., 1969: On the mean motion induced by gravity waves. *J. Fluid Mech.*, **36** (4), 785–803.
- Bretherton, F. P., and C. J. R. Garrett, 1969: Wavetrains in inhomogeneous moving media. *Proc. R. Soc. London, Ser. A*, **302**, 529–554.
- Brown, G. L., and B. R. Sutherland, 2007: Internal wave tunnelling through non-uniformly stratified shear flow. *Atmos. Ocean*, **45**, 47–56.
- Bühler, O., 2009: *Waves and Mean Flows*. Cambridge University Press, Cambridge, UK, 341 pp.
- Bühler, O., and M. E. McIntyre, 1998: On non-dissipative wave-mean interactions in the atmosphere or oceans. *J. Fluid Mech.*, **354**, 301–343.
- Bühler, O., and M. E. McIntyre, 2003: Remote recoil: A new wave-mean interaction effect. *J. Fluid Mech.*, **492**, 207–230, doi:10.1017/S002211200300563.
- Burden, R. L., and J. D. Faires, 2010: *Numerical Analysis*. 9th ed., Brooks/Cole, 872 pp.
- Burrage, M. D., R. A. Vincent, H. G. Mayr, W. R. Skinner, N. F. Arnold, and P. B. Hays, 1996: Long-term variability in the equatorial middle atmosphere zonal wind. *J. Geophys. Res.*, **101** (D8), 12 847–12 854.
- Cooley, J. W., and J. W. Tukey, 1965: An algorithm for the machine calculation of complex fourier series. *Math. Comput.*, **19**, 297–301.
- Cusack, J. M., A. C. N. Garabato, D. A. Smeed, and J. B. Girton, 2017: Observation of a large lee wave in the Drake Passage. *J. Phys. Oceanogr.*, **47**, 793–810, doi:10.1175/JPO-D-16-0153.1.

- Dauxois, T., S. Joubaud, P. Odier, and A. Venaille, 2018: Instabilities of internal gravity wave beams. *Annu. Rev. Fluid. Mech.*, **50**, 131–156, doi: 10.1146/annurev-fluid-122316-044539.
- Davis, R. E., and A. Acrivos, 1967: The stability of oscillatory internal waves. *J. Fluid Mech.*, **30**, 723–736.
- Digital Research Alliance of Canada: <https://alliancecan.ca/en>.
- Dosser, H. V., and B. R. Sutherland, 2011: Anelastic internal wave packet evolution and stability. *J. Atmos. Sci.*, **68**, 2844–2859.
- Drazin, P. G., and W. H. Reid, 1981: *Hydrodynamic Stability*. Cambridge University Press, Cambridge, England, 525 pp.
- Dunkerton, T. J., and D. C. Fritts, 1984: Transient gravity wave-critical layer interaction. Part I: Convective adjustment and the mean zonal acceleration. *J. Atmos. Sci.*, **41** (6), 992–1007.
- Durrán, D. R., 1989: Improving the anelastic approximation. *J. Atmos. Sci.*, **46**, 1453–1461.
- Durrán, D. R., 2010: *Numerical Methods for Fluid Dynamics*. 2nd ed., Springer-Verlag, New York, USA, 516 pp.
- Dutton, J. A., and G. H. Fichtl, 1969: Approximate equations of motion for gases and liquids. *J. Atmos. Sci.*, **26**, 241–254.
- Ebdon, R. A., 1960: Notes on the wind flow at 50 mb in the tropical and subtropical regions in January 1957 and in 1958. *Q. J. Roy. Meteor. Soc.*, **86**, 540–542.
- Eberly, L., and B. R. Sutherland, 2014: Anelastic internal wave reflection and transmission in uniform retrograde shear. *Phys. Fluids*, **26**, 026 601:1–20, doi:10.1063/1.4864104.
- Eckermann, S. D., 1997: Influence of wave propagation on the Doppler spreading of atmospheric gravity waves. *J. Atmos. Sci.*, **54**, 2554–2573.
- Eckermann, S. D., D. Broutman, J. Ma, J. D. Doyle, P.-D. Pautet, M. J. Taylor, K. Bossert, B. P. Williams, D. C. Fritts, and R. B. Smith, 2016: Dynamics of orographic gravity waves

- observed in the mesosphere over the Auckland Islands during the Deep Propagating Gravity Wave Experiment (DEEPWAVE). *J. Atmos. Sci.*, **73**, 3855–3876, doi:10.1175/JAS-D-16-0059.1.
- Eliassen, A., and E. Palm, 1961: On the transfer of energy in stationary mountain waves. *Geophys. Publ.*, **22**, 1–23.
- Environment and Climate Change Canada, 2021a: The Global Deterministic Prediction System (GDPS) version 8.0.0 of the Meteorological Service (MSC) of Canada. Government of Canada, accessed: 2023-06-20, [https://collaboration.cmc.ec.gc.ca/cmc/cmoi/product\\_guide/docs/tech\\_specifications/tech\\_specifications\\_GDPS\\_e.pdf](https://collaboration.cmc.ec.gc.ca/cmc/cmoi/product_guide/docs/tech_specifications/tech_specifications_GDPS_e.pdf).
- Environment and Climate Change Canada, 2021b: The Regional Deterministic Prediction System (RDPS) version 8.0.0 of the Meteorological Service (MSC) of Canada. Government of Canada, accessed: 2023-06-20, [https://collaboration.cmc.ec.gc.ca/cmc/cmoi/product\\_guide/docs/tech\\_specifications/tech\\_specifications\\_RDPS\\_e.pdf](https://collaboration.cmc.ec.gc.ca/cmc/cmoi/product_guide/docs/tech_specifications/tech_specifications_RDPS_e.pdf).
- Ferziger, J. H., and M. Perić, 2002: *Computational Methods for Fluid Dynamics*. 3rd ed., Springer-Verlag, New York, USA, 426 pp.
- FFTW: <https://www.fftw.org/>.
- Fritts, D. C., and M. J. Alexander, 2003: Gravity wave dynamics and effects in the middle atmosphere. *Rev. Geophys.*, **41**, 1003.
- Fritts, D. C., W. Dong, T. S. Lund, S. Weiland, and B. Laughman, 2020: Self-acceleration and instability of gravity wave packets: 3. Three-dimensional packet propagation, secondary gravity waves, momentum transport, and transient mean forcing in tidal winds. *J. Geophys. Res. Atmos.*, **125**, 1–19, doi: 10.1029/2019JD030692.
- Fritts, D. C., and T. J. Dunkerton, 1984: A quasi-linear study of gravity-wave saturation and self-acceleration. *J. Atmos. Sci.*, **41**, 3272–3289.
- Fritts, D. C., J. R. Isler, and Ø. Andreassen, 1994: Gravity wave breaking in two and three dimensions 2. Three-dimensional evolution and instability structure. *J. Geophys. Res.*, **99 (D4)**, 8109–8123.

- Fritts, D. C., T. S. Lund, K. Wan, and H.-L. Liu, 2021: Numerical simulation of mountain waves over the Southern Andes. Part II: Momentum fluxes and wave–mean-flow interactions. *J. Atmos. Sci.*, **78**, 3069–3088, doi: 10.1175/JAS-D-20-0207.1.
- Fritts, D. C., and P. K. Rastogi, 1985: Convective and dynamical instabilities due to gravity wave motions in the lower and middle atmosphere: Theory and observations. *Radio Sci.*, **20**, 1247–1277.
- Fritts, D. C., S. L. Vadas, and Y. Yamada, 2002: An estimate of strong local body forcing and gravity wave radiation based on OH airglow and meteor radar observations. *Geophys. Res. Lett.*, **29** (10), 71:1–4, doi: 10.1029/2001GL013753.
- Garnier, N. B., A. Chiffaudel, F. Daviaud, and A. Prigent, 2003: Nonlinear dynamics of waves and modulated waves in 1D thermocapillary flows. I. General presentation and periodic solutions. *Physica D*, **174**, 1–29.
- Germano, M., U. Piomelli, P. Moin, and W. H. Cabot, 1991: A dynamic subgrid-scale eddy viscosity model. *Phys. Fluids A-Fluid*, **3**, 1760–1765, doi: 10.1063/1.857955.
- Gervais, A. D., Q. Ede, G. E. Swaters, T. S. van den Bremer, and B. R. Sutherland, 2021: Propagation and overturning of three-dimensional Boussinesq wave packets with rotation. *Phys. Rev. Fluids*, **6**, 044 801, doi: 10.1103/PhysRevFluids.6.044801.
- Gervais, A. D., G. E. Swaters, and B. R. Sutherland, 2022: Transmission and reflection of three-dimensional Boussinesq internal gravity wave packets in nonuniform retrograde shear flow. *Phys. Rev. Fluids*, **7**, 114 802, doi: 10.1103/PhysRevFluids.7.114802.
- Gervais, A. D., G. E. Swaters, T. S. van den Bremer, and B. R. Sutherland, 2018: Evolution and stability of two-dimensional anelastic internal gravity wave packets. *J. Atmos. Sci.*, **75**, 3703–3724, doi:10.1175/JAS-D-17-0388.1.
- Ghosh, D., and E. M. Constantinescu, 2016: Well-balanced, conservative finite difference algorithm for atmospheric flows. *AIAA Journal*, **54** (4), 1370–1385, doi: 10.2514/1.J054580.
- Godon, P., and G. Shaviv, 1993: A two-dimensional time dependent Chebyshev method of collocation for the study of astrophysical flows. *Comput. Method. Appl. M.*, **110**, 171–194.

- Goldstein, S., 1931: On the stability of superposed streams of fluids of different densities. *P. R. Soc. London, Ser. A*, **132**, 524–548, doi: <https://doi.org/10.1098/rspa.1931.0116>.
- Gossard, E. E., and W. H. Hooke, 1975: *Waves in the Atmosphere*. Elsevier Scientific Publishing Company, Amsterdam, The Netherlands, 456 pp.
- Gossard, E. E., D. R. Jensen, and J. H. Richter, 1971: An analytical study of tropospheric structure as seen by high-resolution radar. *J. Atmos. Sci.*, **28**, 794–807.
- Gregory, K., and B. R. Sutherland, 2010: Transmission and reflection of internal wave beams. *Phys. Fluids*, **22**, 106 601, doi:10.1063/1.3486613.
- Grimshaw, R. H. J., 1977: The modulation of an internal gravity-wave packet, and the resonance with the mean motion. *Stud. App. Math.*, **56**, 241–266.
- HDF5: <https://www.hdfgroup.org/solutions/hdf5>.
- Heale, C. J., and J. B. Snively, 2015: Gravity wave propagation through a vertically and horizontally inhomogeneous background wind. *J. Geophys. Res. Atmos.*, **120**, 5931–5950, doi: 10.1002/2015JD023505.
- Hines, C. O., 1960: Internal atmospheric gravity waves at ionospheric heights. *Can. J. Phys.*, **38**, 1441–1481.
- Holton, J. R., and M. J. Alexander, 1999: Gravity waves in the mesosphere generated by tropospheric convection. *Tellus A*, **51**, 45–58.
- Holton, J. R., and G. J. Hakim, 2013: *An Introduction to Dynamic Meteorology*. 5th ed., Academic Press, Waltham, USA, 532 pp.
- Holton, J. R., and H.-C. Tan, 1980: The influence of the equatorial Quasi-Biennial Oscillation on the global circulation at 50 mb. *J. Atmos. Sci.*, **37**, 2200–2208, doi: 10.1175/1520-0469(1980)037<2200:TIOTEQ>2.0.CO;2.
- Homeyer, C. R., J. D. McAuliffe, and K. M. Bedka, 2017: On the development of above-anvil cirrus plumes in extratropical convection. *J. Atmos. Sci.*, **74**, 1617–1633, doi: 10.1175/JAS-D-16-0269.1.

- Howard, L. N., 1961: Note on a paper by John W. Miles. *J. Fluid Mech.*, **10**, 509–512.
- Huang, K. M., S. D. Zhang, and F. Yi, 2008: Propagation and reflection of gravity waves in a meridionally sheared wind field. *J. Geophys. Res.*, **113**, D09106, doi: 10.1029/2007JD008877.
- Huang, K. M., S. D. Zhang, and F. Yi, 2010: Reflection and transmission of atmospheric gravity waves in a stably sheared horizontal wind field. *J. Geophys. Res.*, **115**, D16103, doi: 10.1029/2009JD012687.
- Jiang, G.-S., and C.-W. Shu, 1996: Efficient implementation of weighted ENO schemes. *J. Comput. Phys.*, **126**, 202–228.
- Jinjer (T. Shmailyuk and R. Ibramkhalilov and E. Abdiukhanov and D. Kim), 2016: I speak astronomy. *King of Everything*. Napalm Records, CD.
- Kaifler, B., N. Kaifler, B. Ehard, A. Dörnbrack, M. Rapp, and D. C. Fritts, 2015: Influence of source conditions on mountain wave penetration into the stratosphere and mesosphere. *Geophys. Res. Lett.*, **42**, 9488–9494, doi: 10.1002/2015GL066465.
- Kang, M.-J., and H.-Y. Chun, 2021: Contributions of equatorial waves and small-scale convective gravity waves to the 2019/20 quasi-biennial oscillation (QBO) disruption. *Atmos. Chem. Phys.*, **21**, 9839–9857, doi: 10.5194/acp-21-9839-2021.
- Kang, M.-J., H.-Y. Chun, and R. R. Garcia, 2020: Role of equatorial waves and convective gravity waves in the 2016/16 quasi-biennial oscillation disruption. *Atmos. Chem. Phys.*, **20**, 14669–14693, doi: 10.5194/acp-20-14669-2020.
- Klein, R., 2009: Asymptotics, structure, and integration of sound-proof atmospheric flow equations. *Theo. Comp. Fluid Dyn.*, **23**, 161–195, doi:10.1007/s00162-009-0104-y.
- Klemp, J. B., and D. R. Durran, 1983: An upper boundary condition permitting internal gravity wave radiation in numerical mesoscale models. *Mon. Weather Rev.*, **111**, 430–444.
- Klostermeyer, J., 1991: Two-dimensional and three-dimensional parametric instabilities in finite amplitude internal gravity waves. *Geophys. Astrophys. Fluid Dyn.*, **61**, 1–25.

- Kreiss, H.-O., 1968: Stability theory for difference approximations of mixed initial boundary value problems. I. *Math. Comput.*, **22** (104), 703–714.
- Kumar, K. K., 2020: Is mesospheric Quasi Biennial Oscillation ephemeral? *Geophys. Res. Lett.*, **48**, e2020GL091033, doi: 10.1029/2020GL091033.
- Kundu, P. K., I. M. Cohen, D. R. Dowling, and G. Tryggvason, 2016: *Fluid Mechanics*. 6th ed., Academic Press, London, UK, 921 pp.
- Lane, T. P., and R. D. Sharman, 2006: Gravity wave breaking, secondary wave generation, and mixing above deep convection in a three-dimensional cloud model. *Geophys. Res. Lett.*, **33**, L23813:1–5, doi: 10.1029/2006GL027988.
- Lecoanet, D., 2020: Waves and convection in stellar astrophysics. *Fluid Mechanics of Planets and Stars*, M. Le Bars, and D. Lecoanet, Eds., International Centre for Mechanical Sciences: Courses and Lectures, Vol. 595, Springer, Cham, Switzerland, 31–70.
- Lesieur, M., O. Métais, and P. Comte, 2005: *Large-Eddy Simulations of Turbulence*. Cambridge University Press, New York, USA, 219 pp.
- Lindzen, R. S., 1981: Turbulence and stress owing to gravity wave and tidal breakdown. *J. Geophys. Res.*, **86**, 9707–9714.
- Lindzen, R. S., and J. R. Holton, 1968: A theory of the quasi-biennial oscillation. *J. Atmos. Sci.*, **25**, 1095–1107.
- Lipps, F. B., and R. S. Hemler, 1982: A scale analysis of deep moist convection and some related numerical calculations. *J. Atmos. Sci.*, **39** (10), 2192–2210.
- Long, R. R., 1953: Some aspects of the flow of stratified fluids. I. A theoretical investigation. *Tellus*, **5**, 42–58.
- Lund, T. S., D. C. Fritts, K. Wan, B. Laughman, and H.-L. Liu, 2020: Numerical simulation of mountain waves over the Southern Andes. Part I: Mountain waves and secondary wave character, evolutions, and breaking. *J. Atmos. Sci.*, **77**, 4337–4356, doi: 10.1175/JAS-D-19-0356.1.

- Mayr, H. G., J. G. Mengel, C. O. Hines, K. L. Chan, N. F. Arnold, C. A. Reddy, and H. S. Porter, 1997a: The gravity wave Doppler spread theory applied in a numerical spectral model of the middle atmosphere 1. Model and global scale seasonal variations. *J. Geophys. Res.*, **102 (D22)**, 26 077–26 091.
- Mayr, H. G., J. G. Mengel, C. O. Hines, K. L. Chan, N. F. Arnold, C. A. Reddy, and H. S. Porter, 1997b: The gravity wave Doppler spread theory applied in a numerical spectral model of the middle atmosphere 2. Equatorial oscillations. *J. Geophys. Res.*, **102 (D22)**, 26 093–26 105.
- McAllister, M. L., T. A. A. Adcock, P. H. Taylor, and T. S. van den Bremer, 2018: The set-down and set-up of directionally spread and crossing surface gravity wave groups. *J. Fluid. Mech.*, **835**, 131–169, doi: 10.1017/jfm.2017.774.
- McFarlane, N. A., 1987: The effect of orographically excited gravity wave drag on the general circulation of the lower stratosphere and troposphere. *J. Atmos. Sci.*, **44**, 1775–1800.
- McLandress, C., 1998: On the importance of gravity waves in the middle atmosphere and their parameterization in general circulation models. *J. Atmos. Sol.-Terr. Phys.*, **60**, 1357–1383.
- Melet, A., R. Hallberg, S. Legg, and M. Nikurashin, 2014: Sensitivity of the ocean state to lee wave-driven mixing. *J. Phys. Oceanogr.*, **44**, 900–921, doi:10.1175/JPO-D-13-072.1.
- Mercier, M. J., N. B. Garnier, and T. Dauxois, 2008: Reflection and diffraction of internal waves analyzed with the Hilbert transform. *Phys. Fluids*, **20**, 086 601, doi:10.1063/1.2963136.
- Mied, R. R., 1976: The occurrence of parametric instabilities in finite-amplitude internal gravity waves. *J. Fluid Mech.*, **78**, 763–784.
- Miles, J. W., 1961: On the stability of heterogeneous shear flows. *J. Fluid Mech.*, **10**, 496–508.
- MPI: <https://www.mpi-forum.org>.
- Müller, P., G. Holloway, F. Henyey, and N. Pomphrey, 1986: Nonlinear interactions among internal gravity waves. *Rev. Geophys.*, **24**, 493–536.

- Muraschko, J., M. D. Fruman, U. Achatz, S. Hickel, and Y. Toledo, 2015: On the application of Wentzel–Kramer–Brillouin theory for the simulation of the weakly nonlinear dynamics of gravity waves. *Q. J. Roy. Meteor. Soc.*, **141**, 676–697, doi: 10.1002/qj.2381.
- Nault, J. T., and B. R. Sutherland, 2008: Beyond ray tracing for internal waves. Part I: Small-amplitude anelastic waves. *Phys. Fluids*, **20**, 106 601:1–10, doi:10.1063/1.2993167.
- Newman, P. A., 2023: The Quasi-Biennial Oscillation. Atmospheric Chemistry and Dynamics Laboratory, National Aeronautics and Space Administration, accessed: 2023-06-31, [https://acd-ext.gsfc.nasa.gov/Data\\_services/met/qbo/qbo.html](https://acd-ext.gsfc.nasa.gov/Data_services/met/qbo/qbo.html).
- Newman, P. A., L. Coy, S. Pawson, and L. R. Lait, 2016: The anomalous change in the QBO in 2015–2016. *Geophys. Res. Lett.*, **43**, 8791–8797, doi: 10.1002/2016GL070373.
- Ogura, Y., and N. A. Phillips, 1962: Scale analysis of deep and shallow convection in the atmosphere. *J. Atmos. Sci.*, **19**, 173–179.
- O’Neill, M. E., L. Orf, G. M. Heymsfield, and K. Halbert, 2021: Hydraulic jump dynamics above supercell thunderstorms. *Science*, **373** (6560), 1248–1251, doi: 10.1126/science.abh385.
- OpenMP: <https://www.openmp.org>.
- Osprey, S. M., N. Butchart, J. R. Knight, A. A. Scaife, K. Hamilton, J. A. Anstey, V. Schenzinger, and C. Zhang, 2016: An unexpected disruption of the atmospheric quasi-biennial oscillation. *Science*, **353** (6306), 1424–1427, doi: 10.1126/science.aah4156.
- Palmer, T. N., G. J. Shutts, and R. Swinbank, 1986: Alleviation of a systematic westerly bias in general circulation and numerical weather prediction models through an orographic gravity wave drag parametrization. *Quart. J. Roy. Meteor. Soc.*, **112**, 1001–1039.
- Pedlosky, J., 1987: *Geophysical Fluid Dynamics*. 2nd ed., Springer Verlag, New York, USA, 710 pp.
- Phillips, O. M., 1960: On the dynamics of unsteady gravity waves of finite amplitude. Part 1. The elementary interactions. *J. Fluid Mech.*, **9**, 193–217.

- Plougonven, R., A. de la Cámara, A. Hertzog, and F. Lott, 2019: How does knowledge of atmospheric gravity waves guide their parameterizations? *Q. J. Roy. Meteor. Soc.*, **146**, 1529–1543, doi: 10.1002/qj.3732.
- Press, W. H., S. A. Teukolsky, W. T. Vetterling, and B. P. Flannery, 2007: *Numerical Recipes: The Art of Scientific Computing*. 3rd ed., Cambridge University Press, New York, USA, 1235 pp.
- Reed, R. J., W. J. Campbell, L. A. Rasmussen, and R. G. Rogers, 1961: Evidence of a downward propagating annual wind reversal in the equatorial stratosphere. *J. Geophys. Res.*, **66**, 813–818.
- Robert, A. J., 1966: The integration of a low order spectral form of the primitive meteorological equations. *J. Meteorol. Soc. Jpn. Ser. II*, **44 (5)**, 237–245.
- Robinson, T. R., 1997: Nonlinear reflection of internal gravity waves by thermospheric winds. *Adv. Space Res.*, **20 (6)**, 1261–1264.
- Sanford, T. B., J. F. Price, and J. B. Girton, 2011: Upper-ocean response to Hurricane Frances (2004) observed by profiling EM-APEX floats. *J. Phys. Oceanogr.*, **41**, 1041–1056, doi:0.1175/2010JPO4313.1.
- Scinocca, J. F., and N. A. McFarlane, 2000: The parameterization of drag induced by stratified flow of anisotropic orography. *Quart. J. Roy. Meteor. Soc.*, **126**, 2353–2393.
- Scinocca, J. F., and T. G. Shepherd, 1992: Nonlinear wave-activity conservation laws and Hamiltonian structure for the two-dimensional anelastic equations. *J. Atmos. Sci.*, **49**, 5–27.
- Shaw, T. A., and T. G. Shepherd, 2008: Wave-activity conservation laws for the three-dimensional anelastic and Boussinesq equations with a horizontally homogeneous background flow. *J. Fluid Mech.*, **594**, 493–506.
- Shrira, V. I., 1981: On the propagation of a three-dimensional packet of weakly non-linear internal gravity waves. *Int. J. Non-Linear Mechanics*, **16**, 129–138.

- Smagorinsky, J., 1963: General circulation experiments with the primitive equations. *Mon. Weather rev.*, **91** (3), 99–164.
- Smith, R. B., 2018: 100 years of progress on mountain meteorology research. *A Century of Progress in Atmospheric and Related Sciences: Celebrating the American Meteorological Society Centennial*, Meteor. Mon., Vol. 59, American Meteorological Society, Boston, USA, chap. 20, 1–73, doi: 10.1175/AMSMONOGRAPHS-D-18-0022.1.
- Smith, S. M., S. L. Vadas, W. J. Baggaley, G. Hernandez, and J. Baumgardner, 2013: Gravity wave coupling between the mesosphere and thermosphere over New Zealand. *J. Geophys. Res. Space*, **118**, 2694–2707, doi: 10.1002/jgra.50263.
- Steffen, M., 1990: A simple method for monotonic interpolation in one dimension. *Astron. Astrophys.*, **239**, 443–450.
- Stokes, G. G., 1847: On the theory of oscillatory waves. *Trans. Camb. Philos. Soc.*, **8**, 441–455.
- Subich, C. J., K. G. Lamb, and M. Stastna, 2013: Simulation of the Navier–Stokes equations in three dimensions with a spectral collocation method. *Int. J. Numer. Meth. Fluids*, **73**, 103–129, doi: 10.1002/fld.3788.
- Sutherland, B. R., 2000: Internal wave reflection in uniform shear. *Q. J. Roy. Meteor. Soc.*, **126**, 3255–3287.
- Sutherland, B. R., 2001: Finite-amplitude internal wavepacket dispersion and breaking. *J. Fluid Mech.*, **429**, 343–380.
- Sutherland, B. R., 2006a: Internal wave instability: Wave-wave vs wave-induced mean flow interactions. *Phys. Fluids.*, **18**, 074107, doi:10.1063/1.2219102.
- Sutherland, B. R., 2006b: Weakly nonlinear internal gravity wavepackets. *J. Fluid Mech.*, **569**, 249–258.
- Sutherland, B. R., 2010: *Internal Gravity Waves*. Cambridge University Press, Cambridge, UK, 378 pp.

- Sutherland, B. R., U. Achatz, C. c. P. Caulfield, and J. M. Klymak, 2019: Recent progress in modeling imbalance in the ocean and atmosphere. *Phys. Rev. Fluids*, **4**, 010 501, doi: 10.1103/PhysRevFluids.4.010501.
- Sutherland, B. R., W. Reeves, and T. S. van den Bremer, 2020: Flows induced by Coriolis-influenced vertically propagating two-dimensional internal gravity wave packets. *Phys. Rev. Fluids*, **5**, 064 805, doi:10.1103/PhysRevFluids.5.064805.
- Sutherland, B. R., and K. Yewchuk, 2004: Internal wave tunnelling. *J. Fluid Mech.*, **511**, 125–134.
- Tabaei, A., and T. R. Akylas, 2007: Resonant long-short wave interactions in an unbounded rotating stratified fluid. *Stud. Appl. Maths*, **119**, 271–296.
- Talley, L. D., 2013: Closure of the global overturning circulation through the Indian, Pacific, and Southern Oceans: Schematics and transports. *Oceanography*, **26 (1)**, 80–97, doi:<https://doi.org/10.5670/oceanog.2013.07>.
- Taylor, G. I., 1931: Effect of variation in density on the stability of superposed streams of fluid. *P. R. Soc. London, Ser. A*, **132**, 499–523, doi: <https://doi.org/10.1098/rspa.1931.0115>.
- Taylor, J. R., 2008: Numerical simulations of the stratified oceanic bottom boundary layer. Ph.D. thesis, University of California, San Diego.
- Thyng, K. M., C. A. Greene, R. D. Hetland, H. M. Zimmerle, and S. F. DiMarco, 2016: True colors of oceanography: Guidelines for effective and accurate colormap selection. *Oceanography*, **29 (3)**, 9–13, doi: 10.5670/oceanog.2016.66.
- Vadas, S. L., and D. C. Fritts, 2001: Gravity wave radiation and mean responses to local body forces in the atmosphere. *J. Atmos. Sci.*, **58**, 2249–2279.
- Vadas, S. L., and D. C. Fritts, 2002: The importance of spatial variability in the generation of secondary gravity waves from local body forces. *Geophys. Res. Lett.*, **29 (20)**, 45:1–4, doi: 10.1029/2002GL015574.

- Vadas, S. L., and D. C. Fritts, 2006: Influence of solar variability on gravity wave structure and dissipation in the thermosphere from tropospheric convection. *J. Geophys. Res.*, **111**, A10S12:1–25, doi: 10.1029/2005JA011510.
- Vadas, S. L., D. C. Fritts, and M. J. Alexander, 2003: Mechanism for the generation of secondary waves in wave breaking regions. *J. Atmos. Sci.*, **60**, 194–214.
- Vallis, G. K., 2006: *Atmospheric and Oceanic Fluid Dynamics*. Cambridge University Press, Cambridge, England, 745 pp.
- van den Bremer, T. S., and B. R. Sutherland, 2014: The mean flow and long waves induced by two-dimensional internal gravity wavepackets. *Phys. Fluids*, **26**, 106 601, doi:10.1063/1.4899262.
- van den Bremer, T. S., and B. R. Sutherland, 2018: The wave-induced flow of wide three-dimensional internal gravity wavepackets. *J. Fluid Mech.*, **834**, 385–408, doi:10.1017/jfm.2017.745.
- Voelker, G. S., T. R. Akylas, and U. Achatz, 2021: An application of WKBJ theory for triad interactions of internal gravity waves in varying background flows. *Q. J. Roy. Meteor. Soc.*, **147**, 1112–1134, doi: 10.1002/qj.3962.
- Voisin, B., 1991: Internal wave generation in uniformly stratified fluids. Part 1. Green’s function and point sources. *J. Fluid Mech.*, **231**, 439–480.
- Voisin, B., 1994: Internal wave generation in uniformly stratified fluids. Part 2. Moving point sources. *J. Fluid Mech.*, **261**, 333–374.
- Wagner, G. L., and W. R. Young, 2015: Available potential vorticity and wave-averaged quasi-geostrophic flow. *J. Fluid Mech.*, **785**, 401–424, doi:10.1017/jfm.2015.626.
- Waterhouse, A. F., J. A. MacKinnon, J. D. Nash, M. H. Alford, E. Kunze, H. L. Simmons, K. L. Polzin, L. C. S. Laurent, O. M. Sun, R. Pinkel, L. D. Talley, C. B. Whalen, T. N. Hussen, G. S. Carter, I. Fer, S. Waterman, A. C. N. Garabato, T. B. Sanford, and C. M. Lee, 2014: Global patterns of diapycnal mixing from measurements of the turbulent dissipation rate. *J. Phys. Oceanogr.*, **44**, 1854–1872, doi:10.1175/JPO-D-13-0104.1.

- Whitham, G. B., 1965: A general approach to linear and nonlinear dispersive waves using a Lagrangian. *J. Fluid. Mech.*, **22**, 273–283.
- Whitham, G. B., 1974: *Linear and Nonlinear Waves*. John Wiley and Sons, Inc., New York, USA, 636 pp.
- Williams, P. D., 2009: A proposed modification to the Robert–Asselin time filter. *Mon. Wea. Rev.*, **137** (8), 2538–2546.
- Williamson, J. H., 1980: Low storage Runge-Kutta schemes. *J. Comp. Phys.*, **35**, 48–56.
- Wright, C. J., 2019: Quantifying the global impact of tropical cyclone-assisted gravity waves using HIRDLS, MLS, SABER, and IBTrACS data. *Q. J. Roy. Meteor. Soc.*, **145**, 3023–3039, doi: 10.1002/qj.3602.
- Xie, J.-H., and J. Vanneste, 2015: A generalised-Lagrangian-mean model of the interactions between near-inertial waves and mean flow. *J. Fluid Mech.*, **774**, 143–169, doi:10.1017/jfm.2015.251.
- Zauderer, E., 2006: *Partial Differential Equations of Applied Mathematics*. 3rd ed., John Wiley and Sons, Inc., New York, USA, 930 pp.

---

## Polarization relations

---

In this appendix we derive the polarization relations for waves in a rotating Boussinesq fluid, and those for waves in an anelastic gas. For convenience, both sets of derivations assume the fluid is uniformly stratified and stationary in the absence of waves. Under these assumptions the leading-order polarization relations consist of a set of purely algebraic relations, and their first-order (envelope-scale) corrections consist of a set of expressions involving partial derivatives of the amplitude envelope.

### A.1 Waves in a Boussinesq fluid

The polarization relations are derived from the inviscid governing equations for momentum, internal energy (recast, without loss of generality, in terms of vertical displacement), and incompressibility, given by Eqs. (2.5)–(2.8) and (2.3), linearized with respect to amplitude. The linearized equations are given by

$$\frac{\partial u}{\partial t} = -\frac{1}{\rho_0} \frac{\partial p}{\partial x} + f_0 v, \tag{A.1}$$

$$\frac{\partial v}{\partial t} = -\frac{1}{\rho_0} \frac{\partial p}{\partial y} - f_0 u, \tag{A.2}$$

$$\frac{\partial w}{\partial t} = -\frac{1}{\rho_0} \frac{\partial p}{\partial z} - N_0^2 \xi, \tag{A.3}$$

$$\frac{\partial \xi}{\partial t} = w, \tag{A.4}$$

$$\nabla \cdot \mathbf{u} = 0. \quad (\text{A.5})$$

The polarization relations at leading- and first-order are derived by making further assumptions about the types of solutions that satisfy these equations, as described below.

### A.1.1 Dispersion relation and leading-order polarization relations

We seek solutions of Eqs. (A.1)–(A.5) in terms of plane (sinusoidal) waves of the form

$$\eta(\mathbf{x}, t) = A_\eta e^{i(\mathbf{K} \cdot \mathbf{x} - \omega t)}, \quad (\text{A.6})$$

where  $A_\eta$  is constant (possibly complex),  $\mathbf{K} = (k_x, \ell, m)$  is the wavenumber vector (the special notation for  $\mathbf{K}$  and  $k_x$  will be made clear shortly), and  $\omega$  is the dispersion relation, to be determined. It is understood that the actual wave field is the real part of Eq. (A.6). To derive the leading-order polarization relations, we substitute Eq. (A.6) into Eqs. (A.1)–(A.5) (e.g., [Sutherland, 2010](#)), which yields the system of algebraic equations

$$\begin{bmatrix} -i\omega & -f_0 & 0 & 0 & ik_x \frac{1}{\rho_0} \\ f_0 & -i\omega & 0 & 0 & i\ell \frac{1}{\rho_0} \\ 0 & 0 & -i\omega & N_0^2 & im \frac{1}{\rho_0} \\ 0 & 0 & -1 & -i\omega & 0 \\ ik_x & i\ell & im & 0 & 0 \end{bmatrix} \begin{bmatrix} A_u \\ A_v \\ A_w \\ A_\xi \\ A_p \end{bmatrix} e^{i(\mathbf{K} \cdot \mathbf{x} - \omega t)} = \mathbf{0}. \quad (\text{A.7})$$

This system has a nontrivial solution if and only if the left-hand side matrix has zero determinant. Setting its determinant to zero yields a single equation,

$$\frac{i\omega}{\rho_0} \left[ (k_x^2 + \ell^2)(N_0^2 - \omega^2) - m^2(\omega^2 - f_0^2) \right] = 0,$$

whose nontrivial solution is the (squared) dispersion relation,

$$\omega^2 = \frac{N_0^2(k_x^2 + \ell^2) + f_0^2 m^2}{k_x^2 + \ell^2 + m^2}.$$

Now we define  $k := \sqrt{k_x^2 + \ell^2}$ , effectively orienting our coordinate system so that waves propagate in the  $xz$ -plane. Substituting  $k$  into the (squared) dispersion relation and taking the positive root (so that waves propagate forward in time), we find

$$\omega = \frac{\sqrt{N_0^2 k^2 + f_0^2 m^2}}{\|\mathbf{k}\|},$$

where  $\mathbf{k} = (k, 0, m)$ . On this basis, henceforth we assume without loss of generality that waves propagate in the  $xz$ -plane, and we adopt the wavenumber vector  $\mathbf{k} = (k, 0, m)$  accordingly.

Having established the dispersion relation, any wave field can be related unambiguously to any other. Without loss of generality, we somewhat heuristically choose to relate each field to the vertical displacement field, as this is a physically intuitive quantity. We define its amplitude envelope by  $A := A_\xi$  for convenience. One then finds from Eq. (A.7), in sequence,

$$\begin{aligned} A_w &= -i\omega A, \\ A_u &= -\frac{m}{k} A_w = i\omega \frac{m}{k} A, \\ A_v &= -i \frac{f_0}{\omega} A_u = f_0 \frac{m}{k} A, \\ A_p &= -i \frac{\rho_0}{k} (i\omega A_u + f_0 A_v) = i\rho_0 \frac{m}{k^2} (\omega^2 - f_0^2) A. \end{aligned}$$

The polarization relations for the three components of vorticity are obtained from the polarization relations for velocity using

$$\boldsymbol{\zeta} = (\zeta_x, \zeta_y, \zeta_z) = \nabla \times \mathbf{u} = \begin{vmatrix} \hat{\mathbf{e}}_x & \hat{\mathbf{e}}_y & \hat{\mathbf{e}}_z \\ ik & 0 & im \\ A_u & A_v & A_w \end{vmatrix} e^{i(\mathbf{k}\cdot\mathbf{x} - \omega t)}.$$

The corresponding amplitudes are

$$\begin{aligned} A_{\zeta_x} &= -imA_v = -if_0 \frac{m^2}{k} A, \\ A_{\zeta_y} &= imA_u - ikA_w = -\omega \frac{\|\mathbf{k}\|^2}{k} A, \\ A_{\zeta_z} &= ikA_v = if_0 mA. \end{aligned}$$

The polarization relations derived above are summarized in the centre column of Table 2.1.

### A.1.2 Envelope-scale corrections to the leading-order polarization relations

We now seek approximate solutions to Eqs. (A.1)–(A.5) in terms of quasimonochromatic wave packets, expressed as a perturbation expansion (implicitly in powers of  $\epsilon$ ) of the form

$$\eta(\mathbf{x}, t) = \eta_0^{(1)} + \eta_1^{(1)} + \dots, \quad (\text{A.8})$$

where the superscript and subscript denote the order of its associated term with respect to amplitude  $\alpha$  and the perturbation parameter  $\epsilon$ , respectively. At leading-order,  $\eta_0^{(1)}$  is equivalent to the expression in Eq. (A.6) but in which  $A_\eta$  is a function of space and time and not a constant. At  $O(\alpha^1\epsilon^1)$ , the amplitude envelope is a linear combination of first-order derivatives of  $A_\eta$  with respect to the slow variables  $\mathbf{X} = (X, Y, Z)$ . Recall from Sec. 2.2.1 that  $X = \epsilon_x(x - c_{gx}t)$ ,  $Y = \epsilon_y y$ ,  $Z = \epsilon_z(z - c_{gz}t)$ , where  $\epsilon_x = 1/(k\sigma_x)$ ,  $\epsilon_y = 1/(k\sigma_y)$ , and  $\epsilon_z = 1/(k\sigma_z)$  are small parameters inversely proportional to the wave packet extent in the respective directions, and  $\epsilon = \max\{\epsilon_x, \epsilon_y, \epsilon_z\}$ . The slow variables translate with the wave packet at its group velocity,  $\mathbf{c}_g = (c_{gx}, 0, c_{gz})$ , and wave packet dispersion is captured by the slow time variable  $T = \epsilon^2 t$ , and is effectively ignored.

For consistency with the approach taken in Sec. A.1.1, the first-order corrections are related by imposing the first-order structure of the vertical displacement field,

$$\xi_1^{(1)} = i\Sigma_\beta A e^{i(\mathbf{k}\cdot\mathbf{x} - \omega t)},$$

where  $\Sigma_\beta := \epsilon_x \beta_x \partial_X + \epsilon_y \beta_y \partial_Y + \epsilon_z \beta_z \partial_Z$ , in which the constants  $\beta_x$ ,  $\beta_y$ , and  $\beta_z$  were determined in Sec. 2.2.3, but are not known *a priori* in the present derivation.

Setting  $\eta = \xi$  in Eq. (A.8), substituting the resulting expansion into Eq. (A.4), and extracting the  $O(\alpha^1\epsilon^1)$  part, we find

$$\begin{aligned} w_1^{(1)} &= -i\omega \xi_1^{(1)} - \mathbf{c}_g \cdot \nabla \xi_0^{(1)} \\ &= -(\mathbf{c}_g \cdot \nabla - \omega \Sigma_\beta) A e^{i\varphi}, \end{aligned} \tag{A.9}$$

where we have used  $\partial_t \approx -i\omega - \mathbf{c}_g \cdot \nabla$  according to Eq. (2.16d), in which  $\mathbf{c}_g \cdot \nabla = c_{gx}\epsilon_x \partial_X + c_{gz}\epsilon_z \partial_Z$ , and we have defined the phase  $\varphi := \mathbf{k} \cdot \mathbf{x} - \omega t$  for convenience.

Using Eq. (A.9) and the leading-order polarization relations in Eq. (A.5), and extracting the  $O(\alpha^1\epsilon^1)$  part, we find

$$\begin{aligned} u_1^{(1)} &= -\frac{1}{ik} \left[ \epsilon_x \partial_X u_0^{(1)} + \epsilon_y \partial_Y v_0^{(1)} + imw_1^{(1)} + \epsilon_z \partial_Z w_0^{(1)} \right] \\ &= -\frac{1}{ik} \left[ i\omega \frac{m}{k} \epsilon_x \partial_X + f_0 \frac{m}{k} \epsilon_y \partial_Y - im(\mathbf{c}_g \cdot \nabla - \omega \Sigma_\beta) - i\omega \epsilon_z \partial_Z \right] A e^{i\varphi} \\ &= \frac{m}{k} \left[ \left( c_{gx} - \frac{\omega}{k} \right) \epsilon_x \partial_X + i \frac{f_0}{k} \epsilon_y \partial_Y + \left( c_{gz} + \frac{\omega}{m} \right) \epsilon_z \partial_Z - \omega \Sigma_\beta \right] A e^{i\varphi}, \end{aligned} \tag{A.10}$$

where we have used  $\nabla = (ik + \epsilon_x \partial_X, \epsilon_y \partial_Y, im + \epsilon_z \partial_Z)$  according to Eqs. (2.16a)–(2.16c).

Using Eq. (A.10) and the leading-order polarization relations in Eq. (A.2), and extracting the  $O(\alpha^1 \epsilon^1)$  part, we find

$$\begin{aligned} v_1^{(1)} &= \frac{1}{i\omega} \left[ f_0 u_1^{(1)} - \mathbf{c}_g \cdot \nabla v_0^{(1)} + \frac{1}{\rho_0} \epsilon_y \partial_Y p_0^{(1)} \right] \\ &= i \frac{m}{k^2} \left[ f_0 \epsilon_x \partial_X - i\omega \epsilon_y \partial_Y - f_0 \frac{k}{m} \epsilon_z \partial_Z + f_0 k \Sigma_\beta \right] A e^{i\varphi}. \end{aligned} \quad (\text{A.11})$$

For completeness, we obtain  $p_1^{(1)}$  by substituting Eqs. (A.10) and (A.11) in Eq. (A.1), extracting the  $O(\alpha^1 \epsilon^1)$  part to find

$$\begin{aligned} \frac{p_1^{(1)}}{\rho_0} &= \frac{1}{ik} \left[ i\omega u_1^{(1)} + \mathbf{c}_g \cdot \nabla u_0^{(1)} + f_0 v_1^{(1)} - \frac{1}{\rho_0} \epsilon_x \partial_X p_0^{(1)} \right] \\ &= \frac{m}{k^2} \left[ 2\omega \mathbf{c}_g \cdot \nabla - (\omega^2 - f_0^2) \left( \frac{2}{k} \epsilon_x \partial_X - \frac{1}{m} \epsilon_z \partial_Z + \Sigma_\beta \right) \right] A e^{i\varphi}. \end{aligned}$$

Lastly, using the leading-order polarization relations and the first-order corrections to the velocity fields, we may obtain the first-order corrections to the vorticity fields from the  $O(\alpha^1 \epsilon^1)$  parts of  $\boldsymbol{\zeta} = \nabla \times \mathbf{u}$ :

$$\begin{aligned} \zeta_{x1}^{(1)} &= \epsilon_y \partial_Y w_0^{(1)} - im v_1^{(1)} - \epsilon_z \partial_Z v_0^{(1)} \\ &= \frac{m^2}{k^2} \left[ f_0 \epsilon_x \partial_X - i\omega \frac{\|\mathbf{k}\|^2}{m^2} \epsilon_y \partial_Y - 2f_0 \frac{k}{m} \epsilon_z \partial_Z + f_0 k \Sigma_\beta \right] A e^{i\varphi}, \\ \zeta_{y1}^{(1)} &= im u_1^{(1)} + \epsilon_z \partial_Z u_0^{(1)} - ik w_1^{(1)} - \epsilon_x \partial_X w_0^{(1)} \\ &= \frac{i}{k^2} \left[ (k \|\mathbf{k}\|^2 c_{gx} + [k^2 - m^2] \omega) \epsilon_x \partial_X + if_0 m^2 \epsilon_y \partial_Y \right. \\ &\quad \left. + k (\|\mathbf{k}\|^2 c_{gx} + 2\omega m) \epsilon_z \partial_Z - \omega \frac{\|\mathbf{k}\|^2}{k} \Sigma_\beta \right] A e^{i\varphi}, \\ \zeta_{z1}^{(1)} &= ik v_1^{(1)} + \epsilon_x \partial_X v_0^{(1)} - \epsilon_y \partial_Y u_0^{(1)} \\ &= f_0 (\epsilon_z \partial_Z - m \Sigma_\beta) A e^{i\varphi}. \end{aligned}$$

The  $O(\alpha^1 \epsilon^1)$  polarization relations derived above are summarized in the right column of Table 2.1.

## A.2 Waves in an anelastic gas

The polarization relations for waves in an anelastic gas are derived in a manner similar to that used in Sec. A.1. The governing equations are the linearized equations for momentum and internal energy (recast in terms of vertical displacement), and the anelastic nondivergence condition, given by the  $O(\alpha)$  parts of Eqs. (8.17)–(8.21), and reproduced here for convenience:

$$\frac{\partial u}{\partial t} = -\frac{\partial}{\partial x} \left( \frac{p}{\bar{\rho}} \right), \quad (\text{A.12})$$

$$\frac{\partial v}{\partial t} = -\frac{\partial}{\partial y} \left( \frac{p}{\bar{\rho}} \right), \quad (\text{A.13})$$

$$\frac{\partial w}{\partial t} = -\frac{\partial}{\partial z} \left( \frac{p}{\bar{\rho}} \right) - N_0^2 \xi, \quad (\text{A.14})$$

$$\frac{\partial \xi}{\partial t} = w, \quad (\text{A.15})$$

$$\nabla \cdot (\bar{\rho} \mathbf{u}) = 0. \quad (\text{A.16})$$

The polarization relations at leading- and first-order are derived in the respective sections below.

### A.2.1 Dispersion relation and leading-order polarization relations

We seek solutions of Eqs. (A.12)–(A.16) in terms of plane waves of the form

$$\eta(\mathbf{x}, t) = A_\eta e^{i(\mathbf{k}_0 \cdot \mathbf{x} - \omega_0 t)} e^{z/2H_\rho}, \quad (\text{A.17})$$

which notably includes the anelastic growth factor  $e^{z/2H_\rho}$ , where  $H_\rho$  is the density scale height. We have adopted symbols adorned with the subscript 0 for consistency with the notation used throughout Part III. We assume waves propagate in the  $xz$ -plane so that the wavenumber vector is given by  $\mathbf{k}_0 = (k_0, 0, m_0)$ . We proceed first to determine the dispersion relation by substituting Eq. (A.17) into Eqs. (A.12)–(A.16) (e.g., Sutherland, 2010), which yields the

system of algebraic equations

$$\begin{bmatrix} -i\omega_0 & 0 & 0 & 0 & ik_0 \\ 0 & -i\omega_0 & 0 & 0 & 0 \\ 0 & 0 & -i\omega_0 & N_0^2 & im_0 + \frac{1}{2H_\rho} \\ 0 & 0 & -1 & -i\omega_0 & 0 \\ ik_0 & 0 & im_0 - \frac{1}{2H_\rho} & 0 & 0 \end{bmatrix} \begin{bmatrix} A_u \\ A_v \\ A_w \\ A_\xi \\ A_p/\bar{\rho} \end{bmatrix} e^{i(\mathbf{k}_0 \cdot \mathbf{x} - \omega_0 t)} e^{z/2H_\rho} = \mathbf{0}. \quad (\text{A.18})$$

This system has a nontrivial solution if and only if the left-hand side matrix has zero determinant. Setting its determinant to zero yields a single equation,

$$i\omega_0 \left[ \omega_0^2 \left( m_0^2 + \frac{1}{4H_\rho^2} \right) - k_0^2 (N_0^2 - \omega_0^2) \right] = 0,$$

whose solution is the (squared) dispersion relation,

$$\omega_0^2 = \frac{N_0^2 k_0^2}{K_0^2}, \quad (\text{A.19})$$

where  $K_0^2 = k_0^2 + m_0^2 + 1/(2H_\rho)^2$ .

Using the dispersion relation to relate unambiguously the wave fields to the vertical displacement field (with amplitude envelope defined by  $A := A_\xi$  for convenience), we find from Eq. (A.18), in sequence,

$$\begin{aligned} A_v &= 0, \\ A_w &= -i\omega_0 A, \\ A_u &= \frac{i}{k_0} \left( im_0 - \frac{1}{2H_\rho} \right) A_w = \frac{\omega_0}{k_0} \left( im_0 - \frac{1}{2H_\rho} \right) A = -\frac{k_0}{\omega_0} \frac{N_0^2 - \omega_0^2}{im_0 + \frac{1}{2H_\rho}} A, \\ \frac{A_p}{\bar{\rho}} &= \frac{\omega_0}{k_0} A_u = -\frac{N_0^2 - \omega_0^2}{im_0 + \frac{1}{2H_\rho}} A. \end{aligned}$$

The polarization relations for the components of vorticity are found using

$$\boldsymbol{\zeta} = (\zeta_x, \zeta_y, \zeta_z) = \nabla \times \mathbf{u} = \begin{vmatrix} \hat{\mathbf{e}}_x & \hat{\mathbf{e}}_y & \hat{\mathbf{e}}_z \\ ik_0 & 0 & im_0 + \frac{1}{2H_\rho} \\ A_u & A_v & A_w \end{vmatrix} e^{i(\mathbf{k}_0 \cdot \mathbf{x} - \omega_0 t)} e^{z/2H_\rho},$$

with corresponding amplitudes

$$\begin{aligned} A_{\zeta_x} &= 0, \\ A_{\zeta_y} &= \left( im_0 + \frac{1}{2H_\rho} \right) A_u - ik_0 A_w = -\frac{N_0^2 k_0}{\omega_0} A, \end{aligned}$$

$$A_{\zeta_z} = 0.$$

The polarization relations derived above are summarized in the centre column of Table 8.1.

## A.2.2 Envelope-scale corrections to the leading-order polarization relations

We now seek approximate solutions to Eqs. (A.12)–(A.16) in terms of quasimonochromatic wave packets, expressed as a perturbation expansion of the form  $\eta(\mathbf{x}, t) = \eta_0^{(1)} + \eta_1^{(1)} + \dots$ , in which each term in the expansion contains explicitly the anelastic growth factor  $e^{z/2H_\rho}$ . The leading-order term  $\eta_0^{(1)}$  is equivalent to the corresponding polarization relation for plane waves, but with an amplitude envelope that is not a constant, but a function of space and time. At  $O(\alpha^1\epsilon^1)$  the amplitude envelope is a linear combination of first-order derivatives of  $A_\eta$  with respect to the slow spatial variables  $\mathbf{X} = (X, Y, Z)$ , where  $X = \epsilon_x(x - c_{gx0}t)$ ,  $Y = \epsilon_y y$ , and  $Z = \epsilon_z(z - c_{gz0}t)$ , as defined in Sec. 8.3.1.

For consistency with the approach taken in Sec. A.2.1, the first-order corrections are related by imposing the first-order structure of the vertical displacement field,

$$\xi_1^{(1)} = i\Sigma_\beta A e^{i\varphi_0} e^{z/2H_\rho},$$

where  $\Sigma_\beta := \epsilon_x \beta_x \partial_X + \epsilon_y \beta_y \partial_Y + \epsilon_z \beta_z \partial_Z$ , in which the constants  $\beta_x$ ,  $\beta_y$ , and  $\beta_z$  were determined in Sec. 8.3.2, and we have defined  $A := A_\xi$  and  $\varphi_0 := \mathbf{k}_0 \cdot \mathbf{x} - \omega_0 t$  for convenience.

Substituting  $\xi \approx \xi_0^{(1)} + \xi_1^{(1)}$  into Eq. (A.15) and extracting the  $O(\alpha^1\epsilon^1)$  part, we find

$$\begin{aligned} w_1^{(1)} &= -i\omega_0 \xi_1^{(1)} - \mathbf{c}_{g0} \cdot \nabla \xi_0^{(1)} \\ &= -(\mathbf{c}_{g0} \cdot \nabla - \omega_0 \Sigma_\beta) A e^{i\varphi_0} e^{z/H_\rho}, \end{aligned} \tag{A.20}$$

in which we have used  $\partial_t \approx -i\omega_0 - \mathbf{c}_{g0} \cdot \nabla$  according to Eq. (8.26d), where  $\mathbf{c}_{g0} \cdot \nabla = c_{gx0} \epsilon_x \partial_X + c_{gz0} \epsilon_z \partial_Z$ .

Using Eq. (A.20) and  $\xi \approx \xi_0^{(1)} + \xi_1^{(1)}$  in Eq. (A.14) and extracting the  $O(\alpha^1\epsilon^1)$  part, we find

$$\begin{aligned} \frac{p_1^{(1)}}{\bar{\rho}} &= \frac{1}{im_0 + \frac{1}{2H_\rho}} \left[ \mathbf{c}_{g0} \cdot \nabla w_0^{(1)} + i\omega_0 w_1^{(1)} - \epsilon_z \partial_Z \left( \frac{p_0^{(1)}}{\bar{\rho}} \right) - N_0^2 \xi_1^{(1)} \right] \\ &= \frac{1}{im_0 + \frac{1}{2H_\rho}} \left[ -2i\omega_0 \mathbf{c}_{g0} \cdot \nabla + \frac{N_0^2 - \omega_0^2}{im_0 + \frac{1}{2H_\rho}} \epsilon_z \partial_Z - i(N_0^2 - \omega_0^2) \Sigma_\beta \right] A e^{i\varphi_0} e^{z/H_\rho}. \end{aligned} \tag{A.21}$$

Substituting this expression into Eq. (A.12) and extracting the  $O(\alpha^1\epsilon^1)$  part, we find

$$\begin{aligned}
u_1^{(1)} &= \frac{1}{i\omega_0} \left[ -\mathbf{c}_{g0} \cdot \nabla u_0^{(1)} + \epsilon_x \partial_X \left( \frac{p_0^{(1)}}{\bar{\rho}} \right) + ik_0 \frac{p_1^{(1)}}{\bar{\rho}} \right] \\
&= \frac{1}{i\omega_0(im_0 + \frac{1}{2H_\rho})} \left[ \frac{k_0}{\omega_0} (N_0^2 + \omega_0^2) \mathbf{c}_{g0} \cdot \nabla \right. \\
&\quad \left. - (N_0^2 - \omega_0^2) \left( \epsilon_x \partial_X - \frac{ik_0}{im_0 + \frac{1}{2H_\rho}} \epsilon_z \partial_Z - k_0 \Sigma_\beta \right) \right] A e^{i\varphi_0} e^{z/2H_\rho}.
\end{aligned} \tag{A.22}$$

One may obtain an equivalent expression for  $u_1^{(1)}$  using Eq. (A.20) in the anelastic nondivergence condition, Eq. (A.16), as was done when the  $O(\alpha^1\epsilon^1)$  polarization relations were derived in Sec. A.1.2. However, the derivation of the mean flow induced by anelastic wave packets uses the expression for  $u_1^{(1)}$  derived from momentum conservation, given by Eq. (A.22).

Substituting Eq. (A.21) into Eq. (A.13) and extracting the  $O(\alpha^1\epsilon^1)$  part, we find

$$\begin{aligned}
v_1^{(1)} &= -\frac{1}{i\omega_0} \epsilon_y \partial_Y \left( \frac{p_0^{(1)}}{\bar{\rho}} \right) \\
&= -\frac{N_0^2 - \omega_0^2}{i\omega_0(im_0 + \frac{1}{2H_\rho})} \epsilon_y \partial_Y A e^{i\varphi_0} e^{z/2H_\rho}.
\end{aligned}$$

Lastly, using the leading-order polarization relations for the velocity fields and their first-order corrections, we may obtain the first-order corrections to the vorticity fields from the  $O(\alpha^1\epsilon^1)$  parts of  $\zeta = \nabla \times \mathbf{u}$ :

$$\begin{aligned}
\zeta_{x1}^{(1)} &= \epsilon_y \partial_Y w_0^{(1)} - \left( im_0 + \frac{1}{2H_\rho} \right) v_1^{(1)} \\
&= -i \frac{N_0^2}{\omega_0} \epsilon_y \partial_Y A e^{i\varphi_0} e^{z/2H_\rho}, \\
\zeta_{y1}^{(1)} &= \left( im_0 + \frac{1}{2H_\rho} \right) u_1^{(1)} + \epsilon_z \partial_Z u_0^{(1)} - ik_0 w_1^{(1)} - \epsilon_x \partial_X w_0^{(1)} \\
&= i \frac{N_0^2}{\omega_0} \left[ \epsilon_x \partial_X - \frac{k_0}{\omega_0} \mathbf{c}_{g0} \cdot \nabla - k_0 \Sigma_\beta \right] A e^{i\varphi_0}, \\
\zeta_{z1}^{(1)} &= ik_0 v_1^{(1)} - \epsilon_y \partial_Y u_0^{(1)} \\
&= 0.
\end{aligned}$$

The  $O(\alpha^1\epsilon^1)$  polarization relations derived above are summarized in the right column of Table 8.1.

---

## Bretherton flow: Explicit form of the nonlinear forcing

---

In this appendix we compute explicitly the correlations (quadratic products) of wave fields which contribute to the mean, wave packet-scale, wave-wave interactions that force the Bretherton flow,  $\mathbf{u}_{\text{BF}}$ . We also compute explicitly the correlations in the partial differential equation governing the divergent-flux induced flow,  $\mathbf{u}_{\text{DF}}$ .

### B.1 Boussinesq wave packets with rotation

Explicitly, we write each Boussinesq wave field as

$$\eta = \frac{1}{2} \left( A_\eta e^{i\varphi} + A_\eta^* e^{-i\varphi} \right), \quad (\text{B.1})$$

where the asterisk denotes the complex conjugate. Quadratic products of fields of this form consist of the sum of complex conjugate superharmonic terms, proportional to  $e^{\pm i2\varphi}$ , and a mean contribution in which the product of the complex exponentials cancels. The averaging operator, denoted in this appendix by an overline, acts to extract this mean term [cf. Eq. (2.20)].

In Sec. 2.2.1 we made explicit the fact that the wave packet envelope  $A_\eta$  evolves slowly relative to the wavelength and frequency by introducing slow spatial variables  $\mathbf{X} = (X, Y, Z)$ . Spatial derivatives of the wave packet envelope as it depends on  $\mathbf{X}$  introduce factors of  $\epsilon_x$ ,  $\epsilon_y$ , and  $\epsilon_z$  [cf. Eqs.(2.16a)–(2.16c)]. Under the averaging operator, spatial differentiation

of products of fields operate according to  $\partial_x \rightarrow \epsilon_x \partial_X$ ,  $\partial_y \rightarrow \epsilon_y \partial_Y$ , and  $\partial_z \rightarrow \epsilon_z \partial_Z$ . The order of an expression in the resulting perturbation expansion with respect to inverse wave packet extent  $\epsilon = \max\{\epsilon_x, \epsilon_y, \epsilon_z\}$  and amplitude  $\alpha$  is denoted by a subscript and superscript, respectively. Expressions for the Boussinesq wave fields with rotation at leading-order, and their envelope-scale corrections, are given in Table 2.1.

### B.1.1 Divergent-flux induced flow

In Sec. 2.2.2, the rotating Bretherton flow was decomposed conceptually into the sum of the divergent-flux induced flow  $\mathbf{u}_{\text{DF}}$ , and the response flow,  $\mathbf{u}_{\text{RF}}$ . The divergent-flux induced flow arose as the result of the mean forcing by the nonlinear advection terms in the momentum equations. The divergent-flux induced flow is governed by Eq. (2.19), reproduced here for convenience in component form:

$$\partial_t u_{\text{DF}} = -\overline{\nabla \cdot (\mathbf{u}^{(1)} u^{(1)})}, \quad (\text{B.2a})$$

$$\partial_t v_{\text{DF}} = -\overline{\nabla \cdot (\mathbf{u}^{(1)} v^{(1)})}, \quad (\text{B.2b})$$

$$\partial_t w_{\text{DF}} = -\overline{\nabla \cdot (\mathbf{u}^{(1)} w^{(1)})}. \quad (\text{B.2c})$$

Expanding the velocity fields on the right-hand side of Eq. (B.2a) up to first-order in  $\epsilon$ , we find that

$$(\partial_t u_{\text{DF}})_1^{(2)} = -\overline{\epsilon_x \partial_X (u_0^{(1)} u_0^{(1)}) - \epsilon_y \partial_Y (v_0^{(1)} u_0^{(1)}) - \epsilon_z \partial_Z (w_0^{(1)} u_0^{(1)})}.$$

Computing correlations, we find

$$\begin{aligned} -\overline{\epsilon_x \partial_X (u_0^{(1)} u_0^{(1)})} &= -\frac{1}{4} \epsilon_x \partial_X \left\{ i\omega \frac{m}{k} A e^{i\varphi} + \text{c.c.} \right\} \left\{ i\omega \frac{m}{k} A e^{i\varphi} + \text{c.c.} \right\} \\ &= -\frac{1}{4} \omega^2 \frac{m^2}{k^2} \epsilon_x \partial_X \left\{ iA e^{i\varphi} + \text{c.c.} \right\} \left\{ iA e^{i\varphi} + \text{c.c.} \right\} \\ &= -\frac{1}{2} \omega^2 \frac{m^2}{k^2} \epsilon_x \partial_X |A|^2, \end{aligned} \quad (\text{B.3})$$

$$\begin{aligned} -\overline{\epsilon_y \partial_Y (v_0^{(1)} u_0^{(1)})} &= -\frac{1}{4} \epsilon_y \partial_Y \left\{ f_0 \frac{m}{k} A e^{i\varphi} + \text{c.c.} \right\} \left\{ i\omega \frac{m}{k} A e^{i\varphi} + \text{c.c.} \right\} \\ &= 0, \end{aligned} \quad (\text{B.4})$$

$$\begin{aligned}
\overline{-\epsilon_z \partial_Z (w_0^{(1)} u_0^{(1)})} &= -\frac{1}{4} \epsilon_z \partial_Z \left\{ -i\omega A e^{i\varphi} + \text{c.c.} \right\} \left\{ i\omega \frac{m}{k} A e^{i\varphi} + \text{c.c.} \right\} \\
&= \frac{1}{2} \omega^2 \frac{m}{k} \epsilon_z \partial_Z \left\{ iA e^{i\varphi} + \text{c.c.} \right\} \left\{ iA e^{i\varphi} + \text{c.c.} \right\} \\
&= \frac{1}{2} \omega^2 \frac{m}{k} \epsilon_z \partial_Z |A|^2,
\end{aligned} \tag{B.5}$$

where we have omitted the overbar on the right-hand sides for convenience, with the understanding that the averaging operator is applied to the right-hand side expressions. From Eqs. (B.3)–(B.5) we find that

$$(\partial_t u_{\text{DF}})_1^{(2)} = -\frac{1}{2} \omega^2 \frac{m^2}{k^2} \left\{ \epsilon_x \partial_X - \frac{k}{m} \epsilon_z \partial_Z \right\} |A|^2. \tag{B.6}$$

Expanding the velocity fields on the right-hand side of Eq. (B.2b) up to first-order in  $\epsilon$ , we find that

$$\overline{(\partial_t v_{\text{DF}})_1^{(2)}} = \overline{-\epsilon_x \partial_X (u_0^{(1)} v_0^{(1)}) - \epsilon_y \partial_Y (v_0^{(1)} v_0^{(1)}) - \epsilon_z \partial_Z (w_0^{(1)} v_0^{(1)})}.$$

By analogy with Eq. (B.4), the first correlation on the right-hand side is zero. The remaining two correlations are

$$\begin{aligned}
\overline{-\epsilon_y \partial_Y (v_0^{(1)} v_0^{(1)})} &= -\frac{1}{4} \epsilon_y \partial_Y \left\{ f_0 \frac{m}{k} A e^{i\varphi} + \text{c.c.} \right\} \left\{ f_0 \frac{m}{k} A e^{i\varphi} + \text{c.c.} \right\} \\
&= -\frac{1}{4} f_0^2 \frac{m^2}{k^2} \left\{ A e^{i\varphi} + \text{c.c.} \right\} \left\{ A e^{i\varphi} + \text{c.c.} \right\} \\
&= -\frac{1}{2} f_0^2 \frac{m^2}{k^2} \epsilon_y \partial_Y |A|^2, \\
\overline{-\epsilon_z \partial_Z (w_0^{(1)} v_0^{(1)})} &= -\frac{1}{4} \epsilon_z \partial_Z \left\{ -i\omega A e^{i\varphi} + \text{c.c.} \right\} \left\{ f_0 \frac{m}{k} A e^{i\varphi} + \text{c.c.} \right\} \\
&= 0.
\end{aligned} \tag{B.7}$$

Hence we find that

$$(\partial_t v_{\text{DF}})_1^{(2)} = -\frac{1}{2} f_0^2 \frac{m^2}{k^2} \epsilon_y \partial_Y |A|^2. \tag{B.8}$$

Expanding the velocity fields on the right-hand side of Eq. (B.2c) up to first-order in  $\epsilon$ , we find that

$$\overline{(\partial_t w_{\text{DF}})_1^{(2)}} = \overline{-\epsilon_x \partial_X (u_0^{(1)} w_0^{(1)}) - \epsilon_y \partial_Y (v_0^{(1)} w_0^{(1)}) - \epsilon_z \partial_Z (w_0^{(1)} w_0^{(1)})}.$$

By analogy with Eq. (B.7), the second correlation on the right-hand side is zero. The remain-

ing two correlations are

$$\overline{-\epsilon_x \partial_X (u_0^{(1)} w_0^{(1)})} = \frac{1}{2} \omega^2 \frac{m}{k} \epsilon_x \partial_X |A|^2$$

[by analogy with Eq. (B.5)], and

$$\begin{aligned} \overline{-\epsilon_z \partial_Z (w_0^{(1)} w_0^{(1)})} &= -\frac{1}{4} \epsilon_z \partial_Z \left\{ -i\omega A e^{i\varphi} + \text{c.c.} \right\} \left\{ -i\omega A e^{i\varphi} + \text{c.c.} \right\} \\ &= -\frac{1}{4} \omega^2 \epsilon_z \partial_Z \left\{ A e^{i\varphi} + \text{c.c.} \right\} \left\{ A e^{i\varphi} + \text{c.c.} \right\} \\ &= -\frac{1}{2} \omega^2 \epsilon_z \partial_Z |A|^2. \end{aligned}$$

Hence we find that

$$(\partial_t w_{\text{DF}})_1^{(2)} = \frac{1}{2} \omega^2 \frac{m}{k} \left\{ \epsilon_x \partial_X - \frac{k}{m} \epsilon_z \partial_Z \right\} |A|^2. \quad (\text{B.9})$$

Taking Eqs. (B.6), (B.8), and (B.9) together, the divergent-flux induced flow in vector form evolves at leading-order according to

$$\frac{\partial \mathbf{u}_{\text{DF}}}{\partial t} = -\frac{1}{2} \frac{m^2}{k^2} \omega^2 \left( (\epsilon_x \partial_X - \frac{k}{m} \epsilon_z \partial_Z) |A|^2, \frac{f_0^2}{\omega^2} \epsilon_y \partial_Y |A|^2, -\frac{k}{m} (\epsilon_x \partial_X - \frac{k}{m} \epsilon_z \partial_Z) |A|^2 \right).$$

### B.1.2 Quadratically nonlinear forcing

The  $O(\alpha^2)$  nonlinear forcing corresponding to the vertical component of the curl of the Bretherton flow in a rotating Boussinesq fluid,  $F_z$ , is given on the right-hand side of Eq. (2.22), reproduced here for convenience:

$$\begin{aligned} F_z &= \overline{\partial_t \left\{ (\zeta_{x0}^{(1)} + \zeta_{x1}^{(1)}) (ik + \epsilon_x \partial_X) (w_0^{(1)} + w_1^{(1)}) + (\zeta_{y0}^{(1)} + \zeta_{y1}^{(1)}) \epsilon_y \partial_Y (w_0^{(1)} + w_1^{(1)}) \right.} \\ &\quad \left. + (\zeta_{z0}^{(1)} + \zeta_{z1}^{(1)}) (im + \epsilon_z \partial_Z) (w_0^{(1)} + w_1^{(1)}) - \epsilon_x \partial_X [(\zeta_{z0}^{(1)} + \zeta_{z1}^{(1)}) (u_0^{(1)} + u_1^{(1)})] \right.} \\ &\quad \left. - \epsilon_y \partial_Y [(\zeta_{z0}^{(1)} + \zeta_{z1}^{(1)}) (v_0^{(1)} + v_1^{(1)})] + \epsilon_z \partial_Z [(\zeta_{z0}^{(1)} + \zeta_{z1}^{(1)}) (w_0^{(1)} + w_1^{(1)})] \right\}. \quad (\text{B.10}) \end{aligned}$$

Expanding the wave fields on the right-hand side of Eq. (B.10) up to first-order in  $\epsilon$ , we find that

$$(F_z)_1^{(2)} = \overline{\partial_t \left\{ \zeta_{x0}^{(1)} (ik w_0^{(1)}) + \zeta_{z0}^{(1)} (w_0^{(1)}) \right\}}.$$

Computing these correlations we have

$$\overline{\zeta_{x0}^{(1)} (ik w_0^{(1)})} = \frac{1}{4} \left\{ -if_0 \frac{m^2}{k} A e^{i\varphi} + \text{c.c.} \right\} \left\{ (ik) (-i\omega) A e^{i\varphi} + \text{c.c.} \right\}$$

$$\begin{aligned}
&= \frac{1}{4} f_0 \omega m^2 \left\{ -i A e^{i\varphi} + \text{c.c.} \right\} \left\{ A e^{i\varphi} + \text{c.c.} \right\} \\
&= 0,
\end{aligned}$$

$$\begin{aligned}
\overline{\zeta_{z0}^{(1)}(i m w_0^{(1)})} &= \frac{1}{4} \left\{ i f_0 m A e^{i\varphi} + \text{c.c.} \right\} \left\{ (i m)(-i \omega) A e^{i\varphi} + \text{c.c.} \right\} \\
&= \frac{1}{4} f_0 \omega m^2 \left\{ -i A e^{i\varphi} + \text{c.c.} \right\} \left\{ A e^{i\varphi} + \text{c.c.} \right\} \\
&= 0,
\end{aligned}$$

and so we find that  $(F_z)_1^{(2)} \equiv 0$ .

Expanding the wave fields on the right-hand side of Eq. (B.10) up to  $O(\alpha^2 \epsilon^2)$ , we find that

$$\begin{aligned}
(F_z)_2^{(2)} &= \overline{\partial_t \left\{ \zeta_{x0}^{(1)}(i k w_1^{(1)}) + \zeta_{x0}^{(1)}(\epsilon_x \partial_X w_0^{(1)}) + \zeta_{x1}^{(1)}(i k w_0^{(1)}) + \zeta_{y0}^{(1)}(\epsilon_y \partial_Y w_0^{(1)}) \right.} \\
&\quad \left. + \overline{\zeta_{z0}^{(1)}(i m w_1^{(1)}) + \zeta_{z0}^{(1)}(\epsilon_z \partial_Z w_0^{(1)}) + \zeta_{z1}^{(1)}(i m w_0^{(1)})} \right. \\
&\quad \left. - \epsilon_x \partial_X (\zeta_{z0}^{(1)} u_0^{(1)}) + \epsilon_y \partial_Y (\zeta_{z0}^{(1)} v_0^{(1)}) + \epsilon_z \partial_Z (\zeta_{z0}^{(1)} w_0^{(1)}) \right\}.
\end{aligned}$$

Computing these correlations we have

$$\begin{aligned}
\overline{\zeta_{x0}^{(1)}(i k w_1^{(1)})} &= \frac{1}{4} \left\{ -i f_0 \frac{m^2}{k} A e^{i\varphi} + \text{c.c.} \right\} \left\{ -i k (\mathbf{c}_g \cdot \nabla - \omega \Sigma_\beta) A e^{i\varphi} + \text{c.c.} \right\} \\
&= \frac{1}{4} f_0 m^2 \left\{ i A e^{i\varphi} + \text{c.c.} \right\} \left\{ i (\mathbf{c}_g \cdot \nabla - \omega \Sigma_\beta) A e^{i\varphi} \right\} \\
&= \frac{1}{4} f_0 m^2 \left\{ \mathbf{c}_g \cdot \nabla - \omega \Sigma_\beta \right\} |A|^2,
\end{aligned}$$

$$\begin{aligned}
\overline{\zeta_{x0}^{(1)}(\epsilon_x \partial_X w_0^{(1)})} &= \frac{1}{4} \left\{ -i f_0 \frac{m^2}{k} A e^{i\varphi} + \text{c.c.} \right\} \left\{ -i \omega \epsilon_x \partial_X A e^{i\varphi} + \text{c.c.} \right\} \\
&= \frac{1}{4} f_0 \frac{m^2}{k} \omega \epsilon_x \left\{ i A e^{i\varphi} + \text{c.c.} \right\} \left\{ i \partial_X A e^{i\varphi} + \text{c.c.} \right\} \\
&= \frac{1}{4} f_0 \omega \frac{m^2}{k} \epsilon_x \partial_X |A|^2,
\end{aligned}$$

$$\begin{aligned}
\overline{\zeta_{x1}^{(1)}(i k w_0^{(1)})} &= \frac{1}{4} \left\{ \frac{m^2}{k^2} \left[ f_0 \epsilon_x \partial_X - i \omega \frac{\|\mathbf{k}\|^2}{m^2} \epsilon_y \partial_Y - 2 f_0 \frac{k}{m} \epsilon_z \partial_Z + f_0 k \Sigma_\beta \right] A e^{i\varphi} + \text{c.c.} \right\} \\
&\quad \times \left\{ i k (-i \omega) A e^{i\varphi} + \text{c.c.} \right\} \\
&= \frac{1}{4} f_0 \omega \frac{m^2}{k} \left\{ \epsilon_x \partial_X - 2 \frac{k}{m} \epsilon_z \partial_Z + k \Sigma_\beta \right\} |A|^2 - \frac{1}{4} i \omega^2 \frac{\|\mathbf{k}\|^2}{k} \epsilon_y (A_Y A^* - A_Y^* A),
\end{aligned}$$

$$\begin{aligned}
\overline{\zeta_{y0}^{(1)}(\epsilon_y \partial_Y w_0^{(1)})} &= \frac{1}{4} \left\{ -\omega \frac{\|\mathbf{k}\|^2}{k} A e^{i\varphi} + \text{c.c.} \right\} \left\{ -i\omega \epsilon_y \partial_Y A e^{i\varphi} + \text{c.c.} \right\} \\
&= \frac{1}{4} \omega^2 \frac{\|\mathbf{k}\|^2}{k} \epsilon_y \left\{ A e^{i\varphi} + \text{c.c.} \right\} \left\{ i \partial_Y A e^{i\varphi} + \text{c.c.} \right\} \\
&= -\frac{1}{4} i \omega^2 \frac{\|\mathbf{k}\|^2}{k} \epsilon_y (A A_Y^* - A^* A_Y),
\end{aligned}$$

$$\begin{aligned}
\overline{\zeta_{z0}^{(1)}(i m w_1^{(1)})} &= \frac{1}{4} \left\{ i f_0 m A e^{i\varphi} + \text{c.c.} \right\} \left\{ -i m (\mathbf{c}_g \cdot \nabla - \omega \Sigma_\beta) A e^{i\varphi} + \text{c.c.} \right\} \\
&= -\frac{1}{4} f_0 m^2 \left\{ i A e^{i\varphi} + \text{c.c.} \right\} \left\{ i (\mathbf{c}_g \cdot \nabla - \omega \Sigma_\beta) A e^{i\varphi} + \text{c.c.} \right\} \\
&= -\frac{1}{4} f_0 m^2 \left\{ \mathbf{c}_g \cdot \nabla - \omega \Sigma_\beta \right\} |A|^2,
\end{aligned}$$

$$\begin{aligned}
\overline{\zeta_{z0}^{(1)}(\epsilon_z \partial_Z w_0^{(1)})} &= \frac{1}{4} \left\{ i f_0 m A e^{i\varphi} + \text{c.c.} \right\} \left\{ -i \omega \epsilon_z \partial_Z A e^{i\varphi} + \text{c.c.} \right\} \\
&= -\frac{1}{4} f_0 \omega m \epsilon_z \partial_Z |A|^2,
\end{aligned}$$

$$\begin{aligned}
\overline{\zeta_{z1}^{(1)}(i m w_0^{(1)})} &= \frac{1}{4} \left\{ f_0 (\epsilon_z \partial_Z - m \Sigma_\beta) A e^{i\varphi} + \text{c.c.} \right\} \left\{ i m (-i \omega) A e^{i\varphi} + \text{c.c.} \right\} \\
&= \frac{1}{4} f_0 \omega m \left\{ (\epsilon_z \partial_Z - m \Sigma_\beta) A e^{i\varphi} + \text{c.c.} \right\} \left\{ A e^{i\varphi} + \text{c.c.} \right\} \\
&= \frac{1}{4} f_0 \omega m \left\{ \epsilon_z \partial_Z - m \Sigma_\beta \right\} |A|^2,
\end{aligned}$$

$$\begin{aligned}
-\overline{\epsilon_x \partial_X (\zeta_{z0}^{(1)} u_0^{(1)})} &= -\frac{1}{4} \epsilon_x \partial_X \left\{ i f_0 m A e^{i\varphi} + \text{c.c.} \right\} \left\{ i \omega \frac{m}{k} A e^{i\varphi} + \text{c.c.} \right\} \\
&= -\frac{1}{4} f_0 \omega \frac{m^2}{k} \epsilon_x \partial_X \left\{ i A e^{i\varphi} + \text{c.c.} \right\} \left\{ i A e^{i\varphi} + \text{c.c.} \right\} \\
&= -\frac{1}{2} f_0 \omega \frac{m^2}{k} \epsilon_x \partial_X |A|^2,
\end{aligned}$$

$$\begin{aligned}
-\overline{\epsilon_y \partial_Y (\zeta_{z0}^{(1)} v_0^{(1)})} &= -\frac{1}{4} \epsilon_y \partial_Y \left\{ i f_0 m A e^{i\varphi} + \text{c.c.} \right\} \left\{ f_0 \frac{m}{k} A e^{i\varphi} + \text{c.c.} \right\} \\
&= 0,
\end{aligned}$$

$$\begin{aligned}
-\overline{\epsilon_z \partial_Z (\zeta_{z0}^{(1)} w_0^{(1)})} &= -\frac{1}{4} \epsilon_z \partial_Z \left\{ i f_0 m A e^{i\varphi} + \text{c.c.} \right\} \left\{ -i \omega A e^{i\varphi} + \text{c.c.} \right\} \\
&= \frac{1}{4} f_0 \omega m \epsilon_z \partial_Z \left\{ i A e^{i\varphi} + \text{c.c.} \right\} \left\{ i A e^{i\varphi} + \text{c.c.} \right\}
\end{aligned}$$

$$= \frac{1}{2} f_0 \omega m \epsilon_z \partial_Z |A|^2.$$

It follows that  $(F_z)_2^{(2)} \equiv 0$ .

Finally, at  $O(\alpha^2 \epsilon^2)$

$$\begin{aligned} (F_z)_3^{(2)} = & \overline{\zeta_{x0}^{(1)}(\epsilon_x \partial_X w_0^{(1)}) + \zeta_{x1}^{(1)}(ikw_1^{(1)}) + \zeta_{x1}^{(1)}(\epsilon_x \partial_X w_0^{(1)}) + \zeta_{y0}^{(1)}(\epsilon_y \partial_Y w_1^{(1)})} \\ & + \overline{\zeta_{y1}^{(1)}(\epsilon_y \partial_Y w_0^{(1)}) + \zeta_{z0}^{(1)}(\epsilon_z \partial_Z w_1^{(1)}) + \zeta_{z1}^{(1)}(imw_1^{(1)}) + \zeta_{z1}^{(1)}(\epsilon_z \partial_Z w_0^{(1)})} \\ & - \overline{\epsilon_x \partial_X (\zeta_{z0}^{(1)} u_1^{(1)}) + \epsilon_x \partial_X (\zeta_{z1}^{(1)} u_0^{(1)}) + \epsilon_y \partial_Y (\zeta_{z0}^{(1)} v_1^{(1)})} \\ & - \overline{\epsilon_y \partial_Y (\zeta_{z1}^{(1)} v_0^{(1)}) + \epsilon_z \partial_Z (\zeta_{z0}^{(1)} w_1^{(1)}) + \epsilon_z \partial_Z (\zeta_{z1}^{(1)} w_0^{(1)})}. \end{aligned}$$

Computing correlations, we find

$$\begin{aligned} \overline{\zeta_{x0}^{(1)}(\epsilon_x \partial_X w_0^{(1)})} &= \frac{1}{4} \left\{ -if_0 \frac{m^2}{k} A e^{i\varphi} + \text{c.c.} \right\} \left\{ -\epsilon_x \partial_X (\mathbf{c}_g \cdot \nabla - \omega \Sigma_\beta) A e^{i\varphi} + \text{c.c.} \right\} \\ &= \frac{1}{4} f_0 \frac{m^2}{k} \left\{ iA e^{i\varphi} + \text{c.c.} \right\} \left\{ \epsilon_x \partial_X (\mathbf{c}_g \cdot \nabla - \omega \Sigma_\beta) A e^{i\varphi} + \text{c.c.} \right\} \\ &= \frac{1}{4} f_0 \frac{m^2}{k} \epsilon_x \left\{ iA (\mathbf{c}_g \cdot \nabla - \omega \Sigma_\beta) A_X^* - iA^* (\mathbf{c}_g \cdot \nabla - \omega \Sigma_\beta) A_X \right\}, \end{aligned}$$

$$\begin{aligned} \overline{\zeta_{x1}^{(1)}(ikw_1^{(1)})} &= \frac{1}{4} \left\{ \frac{m^2}{k^2} \left[ f_0 \epsilon_x \partial_X - i\omega \frac{\|\mathbf{k}\|^2}{m^2} \epsilon_y \partial_Y - 2f_0 \frac{k}{m} \epsilon_z \partial_Z + f_0 k \Sigma_\beta \right] A e^{i\varphi} + \text{c.c.} \right\} \\ &\quad \times \left\{ -ik (\mathbf{c}_g \cdot \nabla - \omega \Sigma_\beta) A e^{i\varphi} + \text{c.c.} \right\} \\ &= \frac{1}{4} \frac{m^2}{k} \left\{ if_0 \left[ \epsilon_x \partial_X - 2\frac{k}{m} \epsilon_z \partial_Z + k \Sigma_\beta \right] A (\mathbf{c}_g \cdot \nabla - \omega \Sigma_\beta) A^* \right. \\ &\quad - if_0 \left[ \epsilon_x \partial_X - 2\frac{k}{m} \epsilon_z \partial_Z + k \Sigma_\beta \right] A^* (\mathbf{c}_g \cdot \nabla - \omega \Sigma_\beta) A \\ &\quad \left. + \omega \frac{\|\mathbf{k}\|^2}{m^2} \epsilon_y \left[ A_Y (\mathbf{c}_g \cdot \nabla - \omega \Sigma_\beta) A^* + A_Y^* (\mathbf{c}_g \cdot \nabla - \omega \Sigma_\beta) A \right] \right\}, \end{aligned}$$

$$\begin{aligned} \overline{\zeta_{x1}^{(1)}(\epsilon_x \partial_X w_0^{(1)})} &= \frac{1}{4} \left\{ \frac{m^2}{k^2} \left[ f_0 \epsilon_x \partial_X - i\omega \frac{\|\mathbf{k}\|^2}{m^2} \epsilon_y \partial_Y - 2f_0 \frac{k}{m} \epsilon_z \partial_Z + f_0 k \Sigma_\beta \right] A e^{i\varphi} + \text{c.c.} \right\} \\ &\quad \times \left\{ -i\omega \epsilon_x \partial_X A e^{i\varphi} + \text{c.c.} \right\} \\ &= \frac{1}{4} \frac{m^2}{k^2} \omega \left\{ if_0 \left[ -2\frac{k}{m} \epsilon_z \partial_Z + k \Sigma_\beta \right] A \epsilon_x A_X^* \right. \\ &\quad \left. - if_0 \left[ -2\frac{k}{m} \epsilon_z \partial_Z + k \Sigma_\beta \right] A^* \epsilon_x A_X + \omega \frac{\|\mathbf{k}\|^2}{m^2} \epsilon_x \epsilon_y (A_Y A_X^* + A_Y^* A_X) \right\}, \end{aligned}$$

$$\begin{aligned}\overline{\zeta_{y0}^{(1)}(\epsilon_y \partial_Y w_1^{(1)})} &= \frac{1}{4} \left\{ -\omega \frac{\|\mathbf{k}\|^2}{k} A e^{i\varphi} + \text{c.c.} \right\} \left\{ -\epsilon_y \partial_Y (\mathbf{c}_g \cdot \nabla - \omega \Sigma_\beta) A e^{i\varphi} + \text{c.c.} \right\} \\ &= \frac{1}{4} \omega \frac{\|\mathbf{k}\|^2}{k} \epsilon_y \left\{ A (\mathbf{c}_g \cdot \nabla - \omega \Sigma_\beta) A_Y^* + A^* (\mathbf{c}_g \cdot \nabla - \omega \Sigma_\beta) A_Y \right\},\end{aligned}$$

$$\begin{aligned}\overline{\zeta_{y1}^{(1)}(\epsilon_y \partial_Y w_0^{(1)})} &= \frac{1}{4} \left\{ \frac{1}{k^2} \left[ i[k\|\mathbf{k}\|^2 c_{gx} + (k^2 - m^2)\omega] \epsilon_x \partial_X - f_0 m^2 \epsilon_y \partial_Y + ik[\|\mathbf{k}\|^2 c_{gz} + 2\omega m] \epsilon_z \partial_Z \right. \right. \\ &\quad \left. \left. - i\omega k \|\mathbf{k}\|^2 \Sigma_\beta \right] A e^{i\varphi} + \text{c.c.} \right\} \left\{ -i\omega \epsilon_y \partial_Y A e^{i\varphi} + \text{c.c.} \right\} \\ &= -\frac{1}{4} \frac{\omega}{k^2} \epsilon_y \left\{ \epsilon_x [k\|\mathbf{k}\|^2 c_{gx} + (k^2 - m^2)\omega] (A_X A_Y^* + A_X^* A_Y) \right. \\ &\quad \left. + \epsilon_z k [\|\mathbf{k}\|^2 + 2\omega m] (A_Z A_Y^* + A_Z^* A_Y) \right. \\ &\quad \left. - \omega k \|\mathbf{k}\|^2 (A_Y \Sigma_\beta A^* + A_Y^* \Sigma_\beta A) \right\},\end{aligned}$$

$$\begin{aligned}\overline{\zeta_{z0}^{(1)}(\epsilon_z \partial_Z w_1^{(1)})} &= \frac{1}{4} \left\{ i f_0 m A e^{i\varphi} + \text{c.c.} \right\} \left\{ -\epsilon_z \partial_Z (\mathbf{c}_g \cdot \nabla - \omega \Sigma_\beta) A e^{i\varphi} + \text{c.c.} \right\} \\ &= -\frac{1}{4} i f_0 m \epsilon_z \left\{ A (\mathbf{c}_g \cdot \nabla - \omega \Sigma_\beta) A_Z^* - A^* (\mathbf{c}_g \cdot \nabla - \omega \Sigma_\beta) A_Z \right\},\end{aligned}$$

$$\begin{aligned}\overline{\zeta_{z1}^{(1)}(i m w_1^{(1)})} &= \frac{1}{4} \left\{ f_0 (\epsilon_z \partial_Z - m \Sigma_\beta) A e^{i\varphi} + \text{c.c.} \right\} \left\{ -i m (\mathbf{c}_g \cdot \nabla - \omega \Sigma_\beta) A e^{i\varphi} + \text{c.c.} \right\} \\ &= \frac{1}{4} i f_0 m \left\{ (\epsilon_z A_Z - m \Sigma_\beta A) (\mathbf{c}_g \cdot \nabla A^* - \omega \Sigma_\beta A^*) \right. \\ &\quad \left. - (\epsilon_z A_Z^* - m \Sigma_\beta A^*) (\mathbf{c}_g \cdot \nabla A - \omega \Sigma_\beta A) \right\},\end{aligned}$$

$$\begin{aligned}\overline{\zeta_{z1}^{(1)}(\epsilon_z \partial_Z w_0^{(1)})} &= \frac{1}{4} \left\{ f_0 (\epsilon_z \partial_Z - m \Sigma_\beta) A e^{i\varphi} + \text{c.c.} \right\} \left\{ -i\omega \epsilon_z \partial_Z A e^{i\varphi} + \text{c.c.} \right\} \\ &= \frac{1}{4} i f_0 \omega \epsilon_z \left\{ (\epsilon_z A_Z - m \Sigma_\beta A) A_Z^* - (\epsilon_z A_Z^* - m \Sigma_\beta A^*) A_Z \right\} \\ &= \frac{1}{4} i f_0 \omega m \epsilon_z \left\{ A_Z \Sigma_\beta A^* - A_Z^* \Sigma_\beta A \right\},\end{aligned}$$

$$\begin{aligned}-\epsilon_x \partial_X (\zeta_{z0}^{(1)} u_1^{(1)}) &= -\frac{1}{4} \epsilon_x \partial_X \left\{ i f_0 m A e^{i\varphi} + \text{c.c.} \right\} \left\{ \frac{m}{k} \left[ \left( c_{gx} - \frac{\omega}{k} \right) \epsilon_x \partial_X + i \frac{f_0}{k} \epsilon_y \partial_Y \right. \right. \\ &\quad \left. \left. + \left( c_{gz} + \frac{\omega}{m} \right) \epsilon_z \partial_Z - \omega \Sigma_\beta \right] A e^{i\varphi} + \text{c.c.} \right\} \\ &= -\frac{1}{4} f_0 \frac{m^2}{k} \epsilon_x \partial_X \left\{ \frac{f_0}{k} \epsilon_y \partial_Y |A|^2 + i \epsilon_x \left( c_{gx} - \frac{\omega}{k} \right) (A A_X^* - A^* A_X) \right\}\end{aligned}$$

$$\begin{aligned}
& + i\epsilon_z \left( c_{gz} + \frac{\omega}{m} \right) (AA_Z^* - A^*A_Z) \\
& - i\omega (A\Sigma_\beta A^* - A^*\Sigma_\beta A) \Big\},
\end{aligned}$$

$$\begin{aligned}
\overline{-\epsilon_x \partial_X (\zeta_{z1}^{(1)} u_0^{(1)})} &= -\frac{1}{4} \epsilon_x \partial_X \left\{ f_0 (\epsilon_z \partial_Z - m\Sigma_\beta) A e^{i\varphi} + \text{c.c.} \right\} \left\{ i\omega \frac{m}{k} A e^{i\varphi} + \text{c.c.} \right\} \\
&= -\frac{1}{4} i f_0 \omega \frac{m}{k} \epsilon_x \partial_X \left\{ \epsilon_z (AA_Z^* - A^*A_Z) - m(A\Sigma_\beta A^* - A^*\Sigma_\beta A) \right\},
\end{aligned}$$

$$\begin{aligned}
\overline{-\epsilon_y \partial_Y (\zeta_{z0}^{(1)} v_1^{(1)})} &= -\frac{1}{4} \epsilon_y \partial_Y \left\{ i f_0 m A e^{i\varphi} + \text{c.c.} \right\} \left\{ \frac{m}{k^2} \left[ i f_0 \epsilon_x \partial_X + \omega \epsilon_y \partial_Y \right. \right. \\
&\quad \left. \left. - i f_0 \frac{k}{m} \epsilon_z \partial_Z + i f_0 k \Sigma_\beta \right] A e^{i\varphi} + \text{c.c.} \right\} \\
&= -\frac{1}{4} f_0 \frac{m^2}{k^2} \epsilon_y \partial_Y \left\{ f_0 \left[ \epsilon_x \partial_X - \frac{k}{m} \epsilon_z \partial_Z + k \Sigma_\beta \right] |A|^2 + i\omega \epsilon_y (AA_Y^* - A^*A_Y) \right\},
\end{aligned}$$

$$\begin{aligned}
\overline{-\epsilon_y \partial_Y (\zeta_{z1}^{(1)} v_0^{(1)})} &= -\frac{1}{4} \epsilon_y \partial_Y \left\{ f_0 (\epsilon_z \partial_Z - m\Sigma_\beta) A e^{i\varphi} + \text{c.c.} \right\} \left\{ f_0 \frac{m}{k} A e^{i\varphi} + \text{c.c.} \right\} \\
&= -\frac{1}{4} f_0^2 \frac{m}{k} \epsilon_y \partial_Y \left\{ (\epsilon_z A_Z - m\Sigma_\beta A) A^* + (\epsilon_z A_Z^* - m\Sigma_\beta A^*) A \right\} \\
&= -\frac{1}{4} f_0^2 \frac{m}{k} \epsilon_y \partial_Y \left\{ \epsilon_z \partial_Z - m\Sigma_\beta \right\} |A|^2,
\end{aligned}$$

$$\begin{aligned}
\overline{-\epsilon_z \partial_Z (\zeta_{z0}^{(1)} w_1^{(1)})} &= -\frac{1}{4} \epsilon_z \partial_Z \left\{ i f_0 m A e^{i\varphi} + \text{c.c.} \right\} \left\{ -(\mathbf{c}_g \cdot \nabla - \omega \Sigma_\beta) A e^{i\varphi} + \text{c.c.} \right\} \\
&= \frac{1}{4} i f_0 m \epsilon_z \partial_Z \left\{ A(\mathbf{c}_g \cdot \nabla - \omega \Sigma_\beta) A^* - A^*(\mathbf{c}_g \cdot \nabla - \omega \Sigma_\beta) A \right\},
\end{aligned}$$

$$\begin{aligned}
\overline{-\epsilon_z \partial_Z (\zeta_{z1}^{(1)} w_0^{(1)})} &= -\frac{1}{4} \epsilon_z \partial_Z \left\{ f_0 (\epsilon_z \partial_Z - m\Sigma_\beta) A e^{i\varphi} + \text{c.c.} \right\} \left\{ -i\omega A e^{i\varphi} + \text{c.c.} \right\} \\
&= -\frac{1}{4} i f_0 \omega \epsilon_z \partial_Z \left\{ A(\epsilon_z \partial_Z - m\Sigma_\beta) A^* - A^*(\epsilon_z \partial_Z - m\Sigma_\beta) A \right\}.
\end{aligned}$$

Finally, putting these fourteen correlations back together, we find

$$\begin{aligned}
(F_z)_3^{(2)} &= \frac{1}{4} f_0 \frac{m^2}{k} i \left\{ \epsilon_x \left[ A \mathbf{c}_g \cdot \nabla A_X^* - A^* \mathbf{c}_g \cdot \nabla A_X + A_X \mathbf{c}_g \cdot \nabla A^* - A_X^* \mathbf{c}_g \cdot \nabla A \right. \right. \\
&\quad + \omega (A\Sigma_\beta A_X^* - A^*\Sigma_\beta A_X) - \epsilon_x \left( c_{gx} - \frac{\omega}{k} \right) (AA_{XX}^* - A^*A_{XX}) \\
&\quad \left. \left. - \epsilon_z c_{gz} (A_X A_Z^* - A_X^* A_Z) - \epsilon_z \left( c_{gz} + 2\frac{\omega}{m} \right) (AA_{XZ}^* - A^*A_{XZ}) \right] \right\}
\end{aligned}$$

$$\begin{aligned}
& -\frac{k}{m}\epsilon_z \left[ \omega(A\Sigma_\beta A_Z^* - A^*\Sigma_\beta A_Z) - \epsilon_z \frac{\omega}{m}(AA_{ZZ}^* - A^*A_{ZZ}) \right] \\
& -\frac{\omega}{k}\epsilon_y^2(AA_{YY}^* - A^*A_{YY}) \Big\} \\
& +\frac{1}{4}\frac{\|\mathbf{k}\|^2}{k}\omega\epsilon_y \left\{ A_Y\mathbf{c}_g \cdot \nabla A^* + A_Y^*\mathbf{c}_g \cdot \nabla A + A\mathbf{c}_g \cdot \nabla A_Y^* + A^*\mathbf{c}_g \cdot \nabla A_Y \right. \\
& \quad -\omega(A\Sigma_\beta A_Y^* + A^*\Sigma_\beta A_Y) - \epsilon_x \left( c_{gx} - \frac{2m^2\omega}{k\|\mathbf{k}\|^2} \right) (A_X A_Y^* + A_X^* A_Y) \\
& \quad \left. -\epsilon_z \left( c_{gz} + \frac{2m\omega}{\|\mathbf{k}\|^2} \right) (A_Z A_Y^* + A_Z^* A_Y) \right\} \\
& -\frac{1}{2}f_0^2\frac{m^2}{k^2}\epsilon_x\epsilon_y\partial_{XY}|A|^2.
\end{aligned}$$

To simplify further, we note the following identities:

$$\begin{aligned}
& A\mathbf{c}_g \cdot \nabla A_X^* - A^*\mathbf{c}_g \cdot \nabla A_X + A_X\mathbf{c}_g \cdot \nabla A^* - A_X^*\mathbf{c}_g \cdot \nabla A \\
& = \epsilon_x c_{gx}(AA_{XX}^* - A^*A_{XX}) + \epsilon_z c_{gz}(AA_{XZ}^* - A^*A_{XZ} + A_X A_Z^* - A_X^* A_Z)
\end{aligned}$$

and

$$\begin{aligned}
& A_Y\mathbf{c}_g \cdot \nabla A^* + A_Y^*\mathbf{c}_g \cdot \nabla A + A\mathbf{c}_g \cdot \nabla A_Y^* + A^*\mathbf{c}_g \cdot \nabla A_Y \\
& = \epsilon_x c_{gx}(AA_{XY}^* + A^*A_{XY} + A_X A_Y^* + A_X^* A_Y) \\
& \quad + \epsilon_z c_{gz}(AA_{YZ}^* + A^*A_{YZ} + A_Y A_Z^* + A_Y^* A_Z).
\end{aligned}$$

Using these identities in the expression for  $(F_z)_3^{(2)}$  we have

$$\begin{aligned}
(F_z)_3^{(2)} & = \frac{1}{4}f_0\omega\frac{m^2}{k}i \left\{ \epsilon_x(A\Sigma_\beta A_X^* - A^*\Sigma_\beta A_X) - \epsilon_z\frac{k}{m}(A\Sigma_\beta A_Z^* - A^*\Sigma_\beta A_Z) \right. \\
& \quad + \epsilon_x^2\frac{1}{k}(AA_{XX}^* - A^*A_{XX}) - \epsilon_x\epsilon_z\frac{2}{m}(AA_{XZ}^* - A^*A_{XZ}) \\
& \quad \left. + \epsilon_z^2\frac{k}{m^2}(AA_{ZZ}^* - A^*A_{ZZ}) - \epsilon_y^2\frac{1}{k}(AA_{YY}^* - A^*A_{YY}) \right\} \\
& -\frac{1}{2}f_0^2\frac{m^2}{k^2}\epsilon_x\epsilon_y\partial_{XY}|A|^2 \\
& +\frac{1}{2}\frac{\omega^2 m^2}{k^2 c_{gx}}\epsilon_y \left\{ \epsilon_x c_{gx}\partial_{XY} + \epsilon_z c_{gz}\partial_{YZ} \right\} |A|^2 \\
& +\frac{1}{4}\frac{\|\mathbf{k}\|^2}{k}\omega\epsilon_y \left\{ \epsilon_x \left( c_{gx} - \frac{2m^2\omega}{k\|\mathbf{k}\|^2} \right) (AA_{XY}^* + A^*A_{XY}) \right. \\
& \quad \left. + \epsilon_z \left( c_{gz} + \frac{2m\omega}{\|\mathbf{k}\|^2} \right) (AA_{YZ}^* + A^*A_{YZ}) - \omega(A\Sigma_\beta A_Y^* + A^*\Sigma_\beta A_Y) \right\}.
\end{aligned}$$

## B.2 Anelastic wave packets

Following the approach taken above for wave packets in a Boussinesq fluid, here we provide the detailed derivations of the divergent-flux induced flow and the nonlinear forcing that drives the Bretherton flow induced by wave packets in an anelastic gas.

Using essentially the same notation as for a generic Boussinesq wave field in Eq. (B.1), we write explicitly each anelastic wave field as

$$\eta = \frac{1}{2} e^{z/2H_\rho} \left( A_\eta e^{i\varphi_0} + A_\eta^* e^{-i\varphi_0} \right).$$

The subscript on  $\varphi_0$ , which was excluded in the derivation of the Boussinesq Bretherton flow with rotation in Sec. B.1, is included here to emphasize that this derivation is valid where we assume background wind is zero, but that Doppler-shifting effects can modify the wave packet as it evolves. This slight change in notation has no effect on the action of the averaging operator. Expressions for the anelastic wave fields at leading-order, and their envelope-scale corrections, are given in Table 8.1.

### B.2.1 Divergent-flux induced flow

The divergent-flux induced flow corresponding to wave packets in an anelastic gas is governed by Eq. (8.28), reproduced here for convenience in component form:

$$\partial_t(\bar{\rho}u_{\text{DF}}) = -\overline{\nabla \cdot (\bar{\rho}\mathbf{u}^{(1)}u^{(1)})}, \quad (\text{B.11a})$$

$$\partial_t(\bar{\rho}v_{\text{DF}}) = -\overline{\nabla \cdot (\bar{\rho}\mathbf{u}^{(1)}v^{(1)})}, \quad (\text{B.11b})$$

$$\partial_t(\bar{\rho}w_{\text{DF}}) = -\overline{\nabla \cdot (\bar{\rho}\mathbf{u}^{(1)}w^{(1)})}. \quad (\text{B.11c})$$

Expanding the velocity fields on the right-hand side of Eq. (B.11a) up to first-order in  $\epsilon$ , we find that

$$[\partial_t(\bar{\rho}u_{\text{DF}})]_1^{(2)} = -\epsilon_x \partial_X (\bar{\rho}u_0^{(1)}u_0^{(1)}) - \epsilon_z \partial_Z (\bar{\rho}w_0^{(1)}u_0^{(1)}).$$

Computing correlations, we find

$$-\overline{\epsilon_x \partial_X (\bar{\rho}u_0^{(1)}u_0^{(1)})} = -\frac{1}{4} \rho_0 \epsilon_x \partial_X \left\{ -\frac{k_0}{\omega_0} \frac{N_0^2 - \omega_0^2}{im_0 + \frac{1}{2H_\rho}} A e^{i\varphi_0} + \text{c.c.} \right\} \left\{ -\frac{k_0}{\omega_0} \frac{N_0^2 - \omega_0^2}{im_0 + \frac{1}{2H_\rho}} A e^{i\varphi_0} + \text{c.c.} \right\}$$

$$\begin{aligned}
&= -\frac{1}{4}\rho_0 \frac{k_0^2}{\omega_0^2} (N_0^2 - \omega_0^2)^2 \epsilon_x \partial_X \left\{ \frac{1}{im_0 + \frac{1}{2H_\rho}} A e^{i\varphi_0} + \text{c.c.} \right\} \left\{ \frac{1}{im_0 + \frac{1}{2H_\rho}} A e^{i\varphi_0} + \text{c.c.} \right\} \\
&= -\frac{1}{4}\rho_0 \frac{k_0^2}{\omega_0^2} (N_0^2 - \omega_0^2)^2 \epsilon_x \partial_X \left\{ 2 \frac{1}{im_0 + \frac{1}{2H_\rho}} \frac{1}{-im_0 + \frac{1}{2H_\rho}} |A|^2 \right\} \\
&= -\frac{1}{2}\rho_0 \frac{k_0^2}{\omega_0^2} \frac{(N_0^2 - \omega_0^2)^2}{K_0^2 - k_0^2} \epsilon_x \partial_X |A|^2,
\end{aligned}$$

where  $K_0^2 = k_0^2 + m_0^2 + 1/4H_\rho^2$ ,

$$\begin{aligned}
\overline{-\epsilon_z \partial_Z (\bar{\rho} w_0^{(1)} u_0^{(1)})} &= -\frac{1}{4}\rho_0 \epsilon_z \partial_Z \left\{ -i\omega_0 A e^{i\varphi_0} + \text{c.c.} \right\} \left\{ -\frac{k_0}{\omega_0} \frac{N_0^2 - \omega_0^2}{im_0 + \frac{1}{2H_\rho}} A e^{i\varphi_0} + \text{c.c.} \right\} \\
&= -\frac{1}{4}\rho_0 k_0 (N_0^2 - \omega_0^2) \epsilon_z \partial_Z \left\{ i A e^{i\varphi_0} + \text{c.c.} \right\} \left\{ \frac{1}{im_0 + \frac{1}{2H_\rho}} A e^{i\varphi_0} + \text{c.c.} \right\} \\
&= -\frac{1}{4}\rho_0 k_0 (N_0^2 - \omega_0^2) \epsilon_z \partial_Z \underbrace{\left\{ \frac{i}{-im_0 + \frac{1}{2H_\rho}} - \frac{i}{im_0 + \frac{1}{2H_\rho}} \right\}}_{=-2m_0/(K_0^2 - k_0^2)} |A|^2 \\
&= \frac{1}{2}\rho_0 \frac{k_0 m_0 (N_0^2 - \omega_0^2)}{K_0^2 - k_0^2} \epsilon_z \partial_Z |A|^2.
\end{aligned} \tag{B.12}$$

Hence we find that, upon simplifying coefficients,

$$[\partial_t (\bar{\rho} u_{\text{DF}})]_1^{(2)} = -\frac{1}{2}\rho_0 \frac{N_0^2 k_0}{\omega_0} \left\{ \epsilon_x c_{gx0} \partial_X + \epsilon_z c_{gz0} \partial_Z \right\} |A|^2. \tag{B.13}$$

Expanding the velocity fields on the right-hand side of Eq. (B.11b) up to first-order in  $\epsilon$ , we readily find that  $[\partial_t (\bar{\rho} v_{\text{DF}})]_1^{(2)} \equiv 0$ . Expanding in a similar manner the velocity fields on the right-hand side of Eq. (B.11c), we find that

$$[\partial_t (\bar{\rho} w_{\text{DF}})]_1^{(2)} = \overline{-\epsilon_x \partial_X (\bar{\rho} u_0^{(1)} w_0^{(1)}) - \epsilon_z \partial_Z (\bar{\rho} w_0^{(1)} w_0^{(1)})}.$$

Computing correlations, we find:

$$\overline{-\epsilon_x \partial_X (\bar{\rho} u_0^{(1)} w_0^{(1)})} = \frac{1}{2}\rho_0 \frac{k_0 m_0 (N_0^2 - \omega_0^2)}{K_0^2 - k_0^2} \epsilon_x \partial_X |A|^2$$

[by analogy with Eq. (B.12)], and

$$\begin{aligned}
\overline{-\epsilon_z \partial_Z (\bar{\rho} w_0^{(1)} w_0^{(1)})} &= -\frac{1}{4}\rho_0 \epsilon_z \partial_Z \left\{ -i\omega_0 A e^{i\varphi_0} + \text{c.c.} \right\} \left\{ -i\omega_0 A e^{i\varphi_0} + \text{c.c.} \right\} \\
&= -\frac{1}{2}\rho_0 \omega_0^2 \epsilon_z \partial_Z |A|^2.
\end{aligned}$$

Hence we find that, upon simplifying coefficients,

$$[\partial_t(\bar{\rho}w_{\text{DF}})]_1^{(2)} = \frac{1}{2}\rho_0\omega_0^2 \left\{ \frac{m_0}{k_0}\epsilon_x\partial_X - \epsilon_z\partial_Z \right\} |A|^2. \quad (\text{B.14})$$

Taking Eqs. (B.13) and (B.14) together with  $[\partial_t(\bar{\rho}v_{\text{DF}})]_1^{(2)} = 0$ , the divergent-flux induced flow evolves at leading-order according to

$$\frac{\partial(\bar{\rho}\mathbf{u}_{\text{DF}})}{\partial t} = -\frac{1}{2}\rho_0 \left( \frac{N_0^2 k_0}{\omega_0} (\epsilon_x c_{gx0}\partial_X + \epsilon_z c_{gz0}\partial_Z) |A|^2, 0, -\omega_0^2 \frac{m_0}{k_0} (\epsilon_x\partial_X - \frac{k_0}{m_0}\epsilon_z\partial_Z) |A|^2 \right).$$

## B.2.2 Quadratically nonlinear forcing

The  $O(\alpha^2)$  nonlinear forcing corresponding to the vertical component of the curl of the Bretherton flow in an anelastic gas,  $F_z$ , is given on the right-hand side of Eq. (8.30), and is reproduced here:

$$F_z = \overline{\zeta_{x1}^{(1)}(ik_0 + \epsilon_x\partial_X)(w_0^{(1)} + w_1^{(1)}) + (\zeta_{y0}^{(1)} + \zeta_{y1}^{(1)})\epsilon_y\partial_Y(w_0^{(1)} + w_1^{(1)})}. \quad (\text{B.15})$$

Expanding the wave fields on the right-hand side of Eq. (B.15) to zeroth-order in  $\epsilon$ , we find that  $(F_z)_0^{(2)} \equiv 0$ . Expanding the wave fields on the right-hand side of Eq. (B.15) to  $O(\alpha^2\epsilon)$ , we find that

$$(F_z)_1^{(1)} = \overline{\zeta_{x1}^{(1)}(ik_0w_0^{(1)}) + \zeta_{y0}^{(1)}(\epsilon_y\partial_Yw_0^{(1)})}.$$

Computing these correlations we have

$$\begin{aligned} \overline{\zeta_{x1}^{(1)}(ik_0w_0^{(1)})} &= \frac{1}{4}e^{z/H\rho} \left\{ -i\frac{N_0^2}{\omega_0}\epsilon_y\partial_Y A e^{i\varphi_0} + \text{c.c.} \right\} \left\{ ik_0(-i\omega_0)A e^{i\varphi_0} + \text{c.c.} \right\} \\ &= \frac{1}{4}N_0^2k_0\epsilon_y e^{z/H\rho} \left\{ -i\partial_Y A e^{i\varphi_0} + \text{c.c.} \right\} \left\{ A e^{i\varphi_0} + \text{c.c.} \right\} \\ &= \frac{1}{4}N_0^2k_0\epsilon_y e^{z/H\rho} \left\{ iAA_Y^* - iA^*A_Y \right\}, \end{aligned}$$

$$\begin{aligned} \overline{\zeta_{y0}^{(1)}(\epsilon_y\partial_Yw_0^{(1)})} &= \frac{1}{4}e^{z/H\rho} \left\{ -\frac{N_0^2k}{\omega_0}A e^{i\varphi_0} + \text{c.c.} \right\} \left\{ -i\omega_0\epsilon_y\partial_Y A e^{i\varphi_0} + \text{c.c.} \right\} \\ &= \frac{1}{4}N_0^2k_0\epsilon_y e^{z/H\rho} \left\{ A e^{i\varphi_0} + \text{c.c.} \right\} \left\{ i\partial_Y A e^{i\varphi_0} + \text{c.c.} \right\} \\ &= \frac{1}{4}N_0^2k_0\epsilon_y e^{z/H\rho} \left\{ -iAA_Y^* + iA^*A_Y \right\}. \end{aligned}$$

It follows immediately that  $(F_z)_1^{(2)} = 0$ .

Finally, at  $O(\alpha^2\epsilon^2)$  we have

$$(F_z)_2^{(2)} = \overline{\zeta_{x1}^{(1)}(ik_0w_1^{(1)}) + \zeta_{x1}^{(1)}(\epsilon_x\partial_Xw_0^{(1)}) + \zeta_{y0}^{(1)}(\epsilon_y\partial_Yw_1^{(1)}) + \zeta_{y1}^{(1)}(\epsilon_y\partial_Yw_0^{(1)})}.$$

Computing the correlations we find:

$$\begin{aligned} \overline{\zeta_{x1}^{(1)}(ik_0w_1^{(1)})} &= \frac{1}{4}e^{z/H_\rho} \left\{ -i\frac{N_0^2}{\omega_0}\epsilon_yA_Ye^{i\varphi_0} + \text{c.c.} \right\} \left\{ -ik_0(\mathbf{c}_{g0} \cdot \nabla - \omega_0\Sigma_\beta)Ae^{i\varphi_0} + \text{c.c.} \right\} \\ &= \frac{1}{4}\frac{N_0^2k_0}{\omega_0}\epsilon_ye^{z/H_\rho} \left\{ -iA_Ye^{i\varphi_0} + \text{c.c.} \right\} \left\{ -i(\mathbf{c}_{g0} \cdot \nabla - \omega_0\Sigma_\beta)Ae^{i\varphi_0} + \text{c.c.} \right\} \\ &= \frac{1}{4}\frac{N_0^2k_0}{\omega_0}\epsilon_ye^{z/H_\rho} \left\{ A(\mathbf{c}_{g0} \cdot \nabla - \omega_0\Sigma_\beta)A^* + A^*(\mathbf{c}_{g0} \cdot \nabla - \omega_0\Sigma_\beta)A \right\}, \end{aligned}$$

$$\begin{aligned} \overline{\zeta_{x1}^{(1)}(\epsilon_x\partial_Xw_0^{(1)})} &= \frac{1}{4}e^{z/H_\rho} \left\{ -i\frac{N_0^2}{\omega_0}\epsilon_yA_Ye^{i\varphi_0} + \text{c.c.} \right\} \left\{ -i\omega_0\epsilon_xA_Xe^{i\varphi_0} + \text{c.c.} \right\} \\ &= \frac{1}{4}N_0^2\epsilon_x\epsilon_ye^{z/H_\rho} \left\{ -iA_Ye^{i\varphi_0} + \text{c.c.} \right\} \left\{ -iA_Xe^{i\varphi_0} + \text{c.c.} \right\} \\ &= \frac{1}{4}N_0^2\epsilon_x\epsilon_ye^{z/H_\rho} \left\{ A_YA_X^* + A_Y^*A_X \right\}, \end{aligned}$$

$$\begin{aligned} \overline{\zeta_{y0}^{(1)}(\epsilon_y\partial_Yw_1^{(1)})} &= \frac{1}{4}e^{z/H_\rho} \left\{ -\frac{N_0^2k_0}{\omega_0}Ae^{i\varphi_0} + \text{c.c.} \right\} \left\{ \epsilon_y\partial_Y(-\mathbf{c}_{g0} \cdot \nabla + \omega_0\Sigma_\beta)Ae^{i\varphi_0} + \text{c.c.} \right\} \\ &= -\frac{1}{4}\frac{N_0^2k_0}{\omega_0}\epsilon_ye^{z/H_\rho} \left\{ Ae^{i\varphi_0} + \text{c.c.} \right\} \left\{ \partial_Y(-\mathbf{c}_{g0} \cdot \nabla + \omega_0\Sigma_\beta)Ae^{i\varphi_0} + \text{c.c.} \right\} \\ &= -\frac{1}{4}\frac{N_0^2k_0}{\omega_0}\epsilon_ye^{z/H_\rho} \left\{ A\partial_Y(-\mathbf{c}_{g0} \cdot \nabla + \omega_0\Sigma_\beta)A^* + A^*\partial_Y(-\mathbf{c}_{g0} \cdot \nabla + \omega_0\Sigma_\beta)A \right\}, \end{aligned}$$

$$\begin{aligned} \overline{\zeta_{y1}^{(1)}(\epsilon_y\partial_Yw_0^{(1)})} &= \frac{1}{4}e^{z/H_\rho} \left\{ i\frac{N_0^2}{\omega_0} \left[ \epsilon_x\partial_X - \frac{k_0}{\omega_0}\mathbf{c}_{g0} \cdot \nabla - k_0\Sigma_\beta \right] Ae^{i\varphi_0} + \text{c.c.} \right\} \left\{ -i\omega_0\epsilon_yA_Ye^{i\varphi_0} + \text{c.c.} \right\} \\ &= -\frac{1}{4}N_0^2\epsilon_ye^{z/H_\rho} \left\{ i \left[ \epsilon_x\partial_X - \frac{k_0}{\omega_0}\mathbf{c}_{g0} \cdot \nabla - k_0\Sigma_\beta \right] Ae^{i\varphi_0} + \text{c.c.} \right\} \left\{ iA_Ye^{i\varphi_0} + \text{c.c.} \right\} \\ &= -\frac{1}{4}N_0^2\epsilon_ye^{z/H_\rho} \left\{ \epsilon_x(A_XA_Y^* + A_X^*A_Y) \right. \\ &\quad \left. - \frac{k_0}{\omega_0} \left[ A_Y^*(\mathbf{c}_{g0} \cdot \nabla + \omega_0\Sigma_\beta)A + A_Y(\mathbf{c}_{g0} \cdot \nabla + \omega_0\Sigma_\beta)A^* \right] \right\}. \end{aligned}$$

Finally, putting these four correlations back together, we find

$$\begin{aligned} (F_z)_2^{(2)} &= \frac{1}{4}\frac{N_0^2k_0}{\omega_0}\epsilon_ye^{z/H_\rho} \left\{ A_Y(\mathbf{c}_{g0} \cdot \nabla - \omega_0\Sigma_\beta)A^* + A_Y^*(\mathbf{c}_{g0} \cdot \nabla - \omega_0\Sigma_\beta)A \right. \\ &\quad \left. + \frac{\omega_0}{k_0}\epsilon_x(A_XA_Y^* + A_YA_X^*) \right\} \end{aligned}$$

$$\begin{aligned}
& + A\partial_Y(\mathbf{c}_{g0} \cdot \nabla - \omega_0\Sigma_\beta)A^* + A^*\partial_Y(\mathbf{c}_{g0} \cdot \nabla - \omega_0\Sigma_\beta)A \\
& - \frac{\omega_0}{k_0}\epsilon_x(A_X A_Y^* + A_Y A_X^*) \\
& + A_Y^*(\mathbf{c}_{g0} \cdot \nabla + \omega_0\Sigma_\beta)A + A_Y(\mathbf{c}_{g0} \cdot \nabla + \omega_0\Sigma_\beta)A^* \Big\} \\
= & \frac{1}{4}N_0^2 \frac{k_0}{\omega_0}\epsilon_y e^{z/H\rho} \Big\{ 2\epsilon_x c_{gx0}(A_X A_Y^* + A_X^* A_Y) + 2\epsilon_z c_{gz0}(A_Y A_Z^* + A_Y^* A_Z) \\
& + \epsilon_x c_{gx0}(AA_{XY}^* + A^* A_{XY}) + \epsilon_z c_{gz0}(AA_{YZ}^* + A^* A_{YZ}) \\
& - \omega_0\epsilon_x\beta_x(AA_{XY}^* + A^* A_{XY}) - \omega_0\epsilon_z\beta_z(AA_{YZ}^* + A^* A_{YZ}) \\
& - \omega_0\epsilon_y\beta_y(AA_{YY}^* + A^* A_{YY}) \Big\}.
\end{aligned}$$

Using the identities

$$A_X A_Y^* + A_X^* A_Y = \partial_{XY}|A|^2 - AA_{XY}^* - A^* A_{XY},$$

$$A_Y A_Z^* + A_Y^* A_Z = \partial_{YZ}|A|^2 - AA_{YZ}^* - A^* A_{YZ},$$

and combining terms yields the expression for the nonlinear forcing:

$$\begin{aligned}
(F_z)_2^{(2)} = & \frac{1}{4}N_0^2 \frac{k_0}{\omega_0}\epsilon_y e^{z/H\rho} \Big\{ 2\epsilon_x c_{gx0}\partial_{XY}|A|^2 + 2\epsilon_z c_{gz0}\partial_{YZ}|A|^2 \\
& - \epsilon_x(c_{gx0} + \omega_0\beta_x)(AA_{XY}^* + A^* A_{XY}) \\
& - \epsilon_z(c_{gz0} + \omega_0\beta_z)(AA_{YZ}^* + A^* A_{YZ}) \\
& - \omega_0\epsilon_y\beta_y(AA_{YY}^* + A^* A_{YY}) \Big\}. \tag{B.16}
\end{aligned}$$

---

## Vertical profile of the maximum Bretherton flow

---

Here we derive analytically the vertical profile of the maximum Bretherton flow. With some loss of generality the derivation is performed in the context of a nonrotating Boussinesq fluid, which corresponds to integrating the analytically tractable part of Eq. (2.40). To that end, we first inverse Fourier transform the first term on the right-hand side of Eq. (2.40) with respect to  $\mu$ , then integrate the result with respect to  $\kappa$  and  $\lambda$ . That is, we need to compute the double integral

$$u_{\text{BF}}(0, 0, z, 0) = \frac{1}{8\pi} \frac{m^2}{k^2} \frac{\omega^2}{c_{gx}} \sigma_x \sigma_y A_0^2 e^{-z^2/\sigma_z^2} \int_{\mathbb{R}^2} \frac{\lambda^2}{\kappa^2 + \lambda^2} e^{-(\sigma_x^2 \kappa^2 + \sigma_y^2 \lambda^2)/4} d\kappa d\lambda. \quad (\text{C.1})$$

For notational convenience, we adopt the change of variables  $\tilde{\kappa} = \sigma_x \kappa$  and  $\tilde{\lambda} = \sigma_y \lambda$  used in Sec. 2.3.3. Absorbing the factor  $\sigma_x \sigma_y$  into the differential, and writing only the integral term for the time being, the result of this change of variables leaves us to integrate

$$\int_{\mathbb{R}^2} \frac{\tilde{\lambda}^2}{R_y^2 \tilde{\kappa}^2 + \tilde{\lambda}^2} e^{-(\tilde{\kappa}^2 + \tilde{\lambda}^2)/4} d\tilde{\kappa} d\tilde{\lambda},$$

where  $R_y = \sigma_y/\sigma_x$  is the spanwise aspect ratio of the wave packet. This integrand is even with respect to both  $\tilde{\kappa}$  and  $\tilde{\lambda}$ , and so we integrate over the two semiinfinite intervals  $[0, \infty) \times [0, \infty)$  and multiply the integrand by 4 in accordance. We now change to polar coordinates, letting  $\tilde{\kappa} = r \cos \theta$  and  $\tilde{\lambda} = r \sin \theta$ . The corresponding intervals of integration are  $0 \leq r < \infty$  and

$0 \leq \theta \leq \pi/2$ , and the resulting integral is

$$4 \int_0^{\pi/2} \int_0^\infty \frac{\sin^2 \theta}{R_y^2 \cos^2 \theta + \sin^2 \theta} r e^{-r^2/4} dr d\theta. \quad (\text{C.2})$$

The integrand in Eq. (C.2) is degenerate and so the integrals with respect to  $r$  and  $\theta$  can be integrated independently. The integral with respect to  $r$  evaluates to 2, so that Eq. (C.2) is equivalent to

$$8 \int_0^{\pi/2} \frac{\sin^2 \theta}{R_y^2 \cos^2 \theta + \sin^2 \theta} d\theta = 8 \int_0^{\pi/2} \frac{\tan^2 \theta}{R_y^2 + \tan^2 \theta} d\theta.$$

Now, let  $u = \tan \theta$ . Then  $du = \sec^2 \theta d\theta \Leftrightarrow d\theta = du/(u^2 + 1)$ . The corresponding interval of integration is  $0 \leq u < \infty$  and the resulting integral is

$$8 \int_0^\infty \frac{u^2}{R_y^2 + u^2} \frac{1}{1 + u^2} du := 8 \int_0^\infty I(u) du.$$

We perform a partial fraction decomposition of the integrand,

$$I(u) = \frac{Au + B}{R_y^2 + u^2} + \frac{Cu + D}{1 + u^2},$$

which in turn yields a system of linear equations for the constants  $A$ ,  $B$ ,  $C$ , and  $D$ . It is straightforward to find that  $A = C = 0$ ,  $B = R_y^2/(R_y^2 - 1)$ , and  $D = -1/(R_y^2 - 1)$ . The integral is then evaluated according to

$$\begin{aligned} 8 \int_0^\infty I(u) du &= \frac{8}{R_y^2 - 1} \int_0^\infty \left[ \frac{1}{1 + (u/R_y)^2} - \frac{1}{1 + u^2} \right] du \\ &= \frac{8}{R_y^2 - 1} \lim_{s \rightarrow \infty} \left[ R_y \tan^{-1} \left( \frac{u}{R_y} \right) \Big|_0^s - \tan^{-1}(u) \Big|_0^s \right] \\ &= \frac{8}{R_y^2 - 1} \left[ R_y \frac{\pi}{2} - \frac{\pi}{2} \right] \\ &= \frac{4\pi}{R_y + 1}. \end{aligned}$$

Substituting this result into Eq. (C.1) finally yields

$$u_{\text{BF}}(0, 0, z, 0) = \frac{1}{2} \frac{m^2}{k^2} \frac{\omega^2}{c_{gx}} \frac{A_0^2}{R_y + 1} e^{-z^2/\sigma_z^2}, \quad (\text{C.3})$$

in agreement with the previous results of Bühler (2009). The expression corresponding to Eq. (C.3) for an anelastic gas is equivalent to multiplying the right-hand side of Eq. (C.3) by the anelastic growth factor  $e^{z/H_\rho}$ .

---

## Ray-theory prediction of wave packet path

---

Ray theory is applied in Sec. D.1 to obtain the differential equations predicting the path,  $(x(t), 0, z(t))$ , of a wave packet propagating in a fluid with nonuniform (height-dependent) background flow. The equations are integrated numerically using the method described in Sec. D.2, and a sample result is included for illustrative purposes in Sec. D.3.

### D.1 Ray theory

Provided the background flow  $\bar{u}(z)$  does not change significantly over a vertical wavelength [so that the WKBJ approximation remains valid; cf. Sutherland (2010, Sec. 6.5)], the path traced by the centroid of a small amplitude internal gravity wave packet is predicted by the solution of the differential equations

$$\frac{dx}{dt} = c_{gx}(z) + \bar{u}(z), \tag{D.1}$$

$$\frac{dz}{dt} = c_{gz}(z). \tag{D.2}$$

The components of the local group velocity vector,  $c_{gx}$  and  $c_{gz}$ , are given by Eqs. (5.4a)–(5.4b) for waves in a Boussinesq fluid, and by Eqs. (8.43a)–(8.43b) for waves in an anelastic gas. The vertical wavenumber as a function of height is determined according to the auxiliary equation

$$m(z) = \delta_m(t)k_0 \sqrt{\frac{N_0^2}{[\omega_0 - k_0\bar{u}]^2} - 1}, \tag{D.3}$$

where  $\delta_m$  is the sign of  $m$ , equal to  $-1$  and  $1$  for upward- and downward-propagating wave packets, respectively, and the intrinsic frequency  $\omega_0$  is given by Eq. (5.1) and (8.23) for waves in a Boussinesq fluid and an anelastic gas, respectively. Equations (D.1)–(D.3) are integrated subject to the initial conditions

$$x(0) = x_0, \tag{D.4}$$

$$z(0) = z_0, \tag{D.5}$$

$$m(0) = m_0. \tag{D.6}$$

The initial condition for  $\delta_m$  is set by  $m_0$ : because we set the wave packet to propagate upward initially ( $c_{gz} > 0$ ), it follows that  $m_0 < 0$ , so necessarily  $\delta_m(0) = -1$ .

Generally, for a given nonzero  $\bar{u}(z)$ , the solution of Eqs. (D.1)–(D.4) is analytically intractable. Consequently, the system must be solved numerically. One such approach is described below.

## D.2 Numerics

Equations (D.1)–(D.4) are solved as one of the initialization steps of a fully nonlinear simulation (cf. Chapters 3 and 9). The solution is used to predict the reflection height and time, which are used in various diagnostic and postprocessing routines. Equations (D.1)–(D.4) are integrated numerically from  $t_0 = 0$  to  $t_{\max}$ , the value of which is taken to be the same as that in use by the fully nonlinear simulation. The time step,  $\Delta t$ , is likewise taken as that in use by the fully nonlinear simulation. Typically,  $\Delta t = 0.05 N_0^{-1}$ . The integration routine in use is a modified version of the Williamson–Runge–Kutta scheme described in Sec 3.4.

The six steps given by Eqs. (3.15) are performed as a sequence of three pairs of steps. A pair of steps proceeds provided  $m(z)$  is real valued, that is, if the discriminant in Eq. (D.3) is positive. Experience suggests this condition is always true if  $m \neq 0$ . Physically, the (retrograde) background flow  $\bar{u}$  Doppler-shifts the frequency of the waves until the lines of constant phase are oriented vertically, corresponding to the wavenumber  $m = 0$ , at which time the wave packet begins to reflect. In practice, prior to executing a pair of steps, the

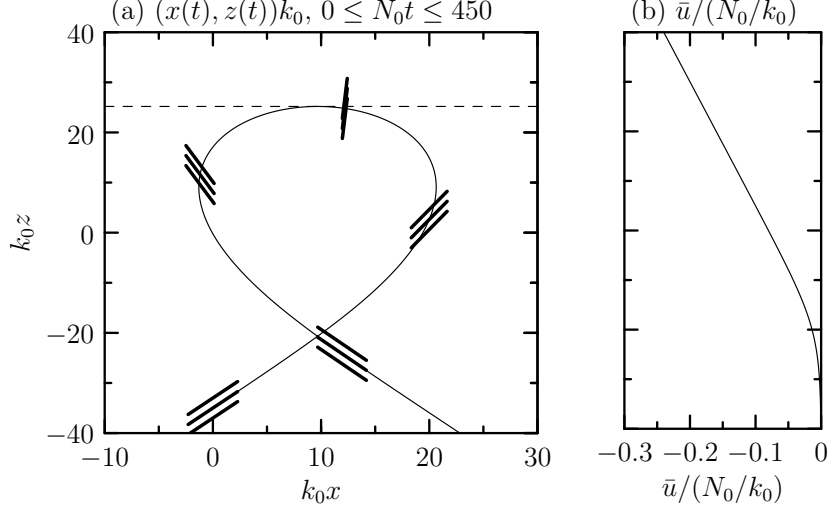


**Figure D.1:** (a) Path in the  $xz$ -plane, as predicted by the numerical solution of Eqs. (D.1)–(D.4), traced by the centroid of a wave packet with initial relative vertical wavenumber  $m_0/k_0 = -0.7$  initially centred at  $(x_0, z_0) = (0, -35)k_0^{-1}$ , through a nonrotating Boussinesq fluid with (b) nonuniform background flow  $\bar{u}(z)$  defined by Eq. (6.7) in which the relative shear magnitude is  $|s|/N_0 = 0.004$ . The dashed horizontal line in (a) indicates the predicted reflection level,  $z_r = 25.19k_0^{-1}$ . Heavy parallel lines indicate the local phase angle  $\varphi(t)$  of the waves every 100 time steps from  $t = 0$  to  $400/N_0$ .

ODE solver verifies whether

$$\frac{N_0^2}{[\omega_0 - k_0 \bar{u}]^2} - 1 < \epsilon_m, \quad (\text{D.7})$$

where the tolerance  $0 < \epsilon_m \ll 1$  is set initially to  $2.5 \times 10^{-4}$ . A given pair of steps proceeds only if Eq. (D.7) holds. Each pair of steps is nested within the previous pair, so that all six steps of Eqs. (3.15) must be completed successfully in order for the solver to advance  $x(t)$  and  $z(t)$  by one  $\Delta t$ . The value of  $\epsilon_m$  is adapted dynamically: if condition Eq. (D.7) fails prior to the execution of any pair of steps, the solver doubles the value of  $\epsilon_m$ , reverses the time integration loop by one  $\Delta t$  (the solver successfully performed this previous iteration of the time loop using a stricter tolerance  $\epsilon_m$ , and therefore is guaranteed to succeed using  $2\epsilon_m$ ). The first instance of such a failure corresponds to the time at which the wave packet reflects, and so the solver permanently resets  $\delta_m = 1$ , and the integration loop resumes forward execution.

### D.3 Illustrative result

The result of the numerical procedure described above is shown in Fig. D.1(a) using the background flow profile shown in Fig. D.1(b). The wave packet was initialized at  $(x_0, z_0) = (0, -35)k_0^{-1}$  with relative vertical wavenumber  $m_0/k_0 = -0.7$ , corresponding to waves propa-

gating upward at an angle of  $\Theta_0 = 35^\circ$  to the vertical with approximately the fastest vertical group speed. The background flow was set by the profile defined by Eq. (6.7) with shear magnitude set by  $|s|/N_0 = 0.004$ . The horizontal line in Fig. D.1(a) indicates the reflection level,  $z_r = 25.19k_0^{-1}$  diagnosed at time  $t_r = 214/N_0$  from the numerical solution. Heavy parallel lines in Fig. D.1(a) indicate the phase angle  $\varphi(t)$  of the waves at intervals of  $100/N_0$  starting from  $t = 0$ . These show the Doppler-shifting of the waves as the initially upward- and rightward-propagating wave packet encountered the shear flow, reflected, and propagated back downward. The decreasing, then increasing, arc length along the path between subsequent sets of parallel lines indicates the decreasing, then increasing, vertical group speed of the wave packet, with  $c_{gz} = 0$  at  $z_r(t_r)$ .

---

## Solution of the anelastic Poisson equation for dynamic pressure

---

In this appendix we provide details of the numerical solution of the Poisson equation for the dynamic pressure field diagnosed in the anelastic code. The solution procedure to obtain a single vertical pressure profile involved essentially two steps: (1) the one-time LU factorization of the matrix representing the Fourier transformed and discretized linear operator on the left-hand side of the Poisson pressure equation; and, (2) a sequence of forward- and back-substitutions using the entries of the factored matrices. Parallelization of these steps, and the compact storage of the results, are also discussed.

For reference, the Poisson equation for dynamic pressure at all interior nodes, Eq. (9.22), in the limit of uniform stratification, is reproduced here:

$$\begin{aligned}
 \hat{\mathcal{L}}_{\mathbf{n}} \frac{\hat{p}_{s\mathbf{n}}}{\rho_0} = & \bar{r}_k^{-1/2} \left[ \kappa_n^2 (\widehat{u_s^2})_{\mathbf{n}} + \lambda_\ell^2 (\widehat{v_s^2})_{\mathbf{n}} - \frac{d^2}{dz^2} (\widehat{w_s^2})_{\mathbf{n}} \right] \\
 & + 2\bar{r}_k^{-1/2} \left[ \kappa_n \lambda_\ell (\widehat{u_s v_s})_{\mathbf{n}} - i\kappa_n \frac{d}{dz} (\widehat{u_s w_s})_{\mathbf{n}} - i\lambda_\ell \frac{d}{dz} (\widehat{v_s w_s})_{\mathbf{n}} \right] \\
 & - 2i\kappa_n \bar{u}'_k \widehat{w}_{s\mathbf{n}} - N_0^2 \left[ -\frac{1}{2H_\rho} \widehat{\xi}_{s\mathbf{n}} + \frac{d}{dz} \widehat{\xi}_{s\mathbf{n}} \right]
 \end{aligned} \tag{E.1}$$

where  $\hat{\mathcal{L}}_{\mathbf{n}} = -\kappa_n^2 - \lambda_\ell^2 - 1/4H_\rho^2 + d^2/dz^2$  is, ostensibly, a real valued tensor of dimensions  $(1 + n_x/2) \times (1 + n_y) \times (n_z - 1) \times (n_z - 1)$  representing the linear operator we wish to invert. It is understood that the differential operators in Eq. (E.1) and in  $\hat{\mathcal{L}}_{\mathbf{n}}$  are replaced by suitable finite difference approximations.

For a fixed horizontal Fourier mode pair  $(\kappa_n, \lambda_\ell)$ , Eq. (E.1) may be written as the matrix





and the last two rows according to

$$\begin{aligned}
\gamma_{n'-1} &= a_{n'-1,k-2}, & \gamma_{n'} &= a_{n',n'-2}, \\
\beta_{n'-1} &= a_{n'-1,k-1} - \gamma_{n'-1}\delta_{n'-3}, & \beta_{n'} &= a_{n',n'-1} - \gamma_{n'}\delta_{n'-2}, \\
\alpha_{n'-1} &= a_{n'-1,n'-1} - (\gamma_{n'-1}\epsilon_{n'-3} + \beta_{n'-1}\delta_{n'-2}), & \alpha_{n'} &= a_{n'n'} - (\gamma_{n'}\epsilon_{n'-2} + \beta_{n'}\delta_{n'-1}). \\
\delta_{n'-1} &= (a_{n'-1,n'} - \beta_{n'-1}\epsilon_{n'-2})/\alpha_{n'-1},
\end{aligned}$$

In practice, the diagonal vectors  $\boldsymbol{\alpha}$ ,  $\boldsymbol{\beta}$ ,  $\boldsymbol{\gamma}$ ,  $\boldsymbol{\delta}$ , and  $\boldsymbol{\epsilon}$ , corresponding to a particular horizontal Fourier mode pair were stored compactly in the columns of an array of size  $(1 + n_x/2) \times (1 + n_y/2) \times 5 \times (n_z - 1)$ . Here,  $1 + n_x/2$  corresponds to the number of streamwise Fourier modes upon invoking Hermitian symmetry of the streamwise Fourier transform, and the factor of  $1/2$  in  $1 + n_y/2$  is a consequence of the fact that  $\kappa_n^2 + \lambda_\ell^2$  is even with respect to  $\lambda_\ell$ .

The LU factorization was parallelized by looping over the  $(n, \ell)$  indices in parallel, with each [OpenMP](#) thread performing the actual decomposition in serial. To perform the LU factorization (including populating dynamically the vectors containing the diagonal entries of  $\mathbf{A}$ ) with  $n_x = 1024$ ,  $n_y = 256$ , and  $n_z = 1400$  with 64 CPU cores typically took less than 0.2 s. One factor contributing to this performance was to precompute and store  $\kappa_n^2 + \lambda_\ell^2$  in a dedicated array for use here and elsewhere in the code. Another factor was to preallocate temporary storage to contain the diagonals of  $\mathbf{A}$  for a given  $(\kappa_n, \lambda_\ell)$ , as opposed to allocating and deallocating these vectors dynamically. To that end, an array of dimensions  $n_T \times (n_z - 1) \times 5$  was allocated, where  $n_T$  was the number of [OpenMP](#) threads (equal to the number of CPU cores), and each thread overwrote a dedicated subarray of this temporary array. The matrices  $\mathbf{L}$  and  $\mathbf{U}$  were obtained once, as a step during the initialization of the larger anelastic code, and used to compute  $\hat{p}_s$  at every Runge–Kutta substep of the time integration.

A similar strategy for parallelization and allocation of temporary storage was employed to use  $\mathbf{L}$  and  $\mathbf{U}$  after building the right-hand side of Eq. (E.1), with each [OpenMP](#) thread performing the forward- and back-substitutions to obtain a single vertical pressure profile. To obtain the full three-dimensional pressure field consisted of  $2 \cdot (1 + n_x/2) \times (1 + n_y)$  iterations of forward- and back-substitutions on complex valued data vectors of length  $n_z - 1$ , corresponding to columns of  $\hat{\mathbf{F}}_s$ . Typically this took  $O(10^{-1})$  s using 64 CPU cores.

---

## Subfilter-scale forcing terms for the anelastic evolution equations

---

Here we derive the explicit form of the subfilter-scale forcing terms in the evolution equations under the anelastic scaling (which factors the exponential amplitude growth term out of the perturbation fields with the aim of enhancing numerical stability). The focus of this section is on the derivation of the scaled subfilter-scale forcing term  $-\frac{1}{R}\partial_{x_i}(R\lambda_i)$  in the internal energy equation Eq. (9.31), reproduced here:

$$\frac{\partial\bar{\theta}}{\partial t} + \frac{1}{R}\frac{\partial(R\bar{u}_i\bar{\theta})}{\partial x_i} = -\bar{u}_3\frac{d\Theta}{dx_3} - U\frac{\partial\bar{\theta}}{\partial x_1} - \frac{1}{R}\frac{\partial(R\lambda_i)}{\partial x_i}.$$

Recall that in Sec. 9.5 we adopted temporarily the usual meaning (in the context of LES) of the overbar to mean a filtered (resolved) quantity, a meaning which we retain here, and so we denote the background profiles of mass density, potential temperature, and shear flow by  $R$ ,  $\Theta$ , and  $U$ , respectively. For convenience we denote vertical derivatives of these background quantities by a prime.

The mass density-weighted subfilter-scale potential temperature flux divergence, written in terms of resolved vertical displacement, is

$$\begin{aligned} \frac{\partial(R\lambda_i)}{\partial x_i} &= \frac{\partial}{\partial x_i} \left[ R \frac{\nu_T}{\text{Pr}} \frac{\partial(\bar{\xi}\Theta')}{\partial x_i} \right] = \frac{\partial}{\partial x_i} \left[ \Theta' R \frac{\nu_T}{\text{Pr}} \frac{\partial\bar{\xi}}{\partial x_i} + \Theta'' R \frac{\nu_T}{\text{Pr}} \bar{\xi} \delta_{i3} \right] \\ &= \Theta' \underbrace{\frac{\partial}{\partial x_i} \left[ R \frac{\nu_T}{\text{Pr}} \frac{\partial\bar{\xi}}{\partial x_i} \right]}_{\text{I}} + \Theta'' \left[ \underbrace{2R \frac{\nu_T}{\text{Pr}} \frac{\partial\bar{\xi}}{\partial x_3}}_{\text{II}} + \underbrace{\bar{\xi} \frac{\partial}{\partial x_3} \left( R \frac{\nu_T}{\text{Pr}} \right)}_{\text{III}} \right] + \Theta''' \underbrace{R \frac{\nu_T}{\text{Pr}} \bar{\xi}}_{\text{IV}}. \end{aligned}$$

Our aim is to express terms I–IV explicitly in terms of scaled vertical displacement  $\bar{\xi}_s = \bar{\xi}r^{1/2}$  and scaled eddy viscosity  $\nu_{Ts} = \nu_T r^{1/2}$ , where  $r = R/\rho_0$ , so that the resulting equation can be implemented readily in code. The scaled eddy viscosity is defined implicitly in terms of scaled quantities,  $\nu_{Ts} = C_s^2 \Delta^2 r^{1/2} \|\bar{S}\|$ , where the Smagorinsky constant  $C_s$  and filter length scale  $\Delta$  were described in Sec. 9.5, and  $\|\bar{S}\|$  is the modulus of the resolved strain rate tensor  $\bar{S}_{ij}$  written in terms of scaled velocities:

$$\bar{S}_{ij} = \frac{1}{2} r^{-1/2} \left[ \frac{\partial \bar{u}_{si}}{\partial x_j} + \frac{\partial \bar{u}_{sj}}{\partial x_i} - \frac{1}{2} \frac{r'}{r} \bar{u}_{si} \delta_{i3} \right]. \quad (\text{F.1})$$

Under the anelastic scaling, term I is written as

$$\begin{aligned} \frac{\partial}{\partial x_i} \left[ R \frac{\nu_T}{\text{Pr}} \frac{\partial \bar{\xi}}{\partial x_i} \right] &= \rho_0 \frac{\partial}{\partial x_i} \left[ r^{1/2} \frac{\nu_{Ts}}{\text{Pr}} \frac{\partial (\bar{\xi}_s r^{-1/2})}{\partial x_i} \right] = \rho_0 \frac{\partial}{\partial x_i} \left[ \frac{\nu_{Ts}}{\text{Pr}} \frac{\partial \bar{\xi}_s}{\partial x_i} - \frac{1}{2} \frac{r'}{r} \frac{\nu_{Ts}}{\text{Pr}} \bar{\xi}_s \delta_{i3} \right] \\ &= \rho_0 \left[ \frac{\partial \bar{\xi}_s}{\partial x_i} \frac{\partial}{\partial x_i} \left( \frac{\nu_{Ts}}{\text{Pr}} \right) + \frac{\nu_{Ts}}{\text{Pr}} \frac{\partial^2 \bar{\xi}_s}{\partial x_i^2} - \frac{1}{2} \frac{r'}{r} \frac{\partial}{\partial x_3} \left( \frac{\nu_{Ts}}{\text{Pr}} \bar{\xi}_s \right) - \frac{1}{2} \left( \frac{r'}{r} \right)' \frac{\nu_{Ts}}{\text{Pr}} \bar{\xi}_s \right]. \end{aligned}$$

Similarly, terms II, III, and IV, respectively, are written as

$$\begin{aligned} 2R \frac{\nu_T}{\text{Pr}} \frac{\partial \bar{\xi}}{\partial x_3} &= 2\rho_0 r^{1/2} \frac{\nu_{Ts}}{\text{Pr}} \frac{\partial (\bar{\xi}_s r^{-1/2})}{\partial x_3} = 2\rho_0 \frac{\nu_{Ts}}{\text{Pr}} \left[ \frac{\partial \bar{\xi}_s}{\partial x_3} - \frac{1}{2} \frac{r'}{r} \bar{\xi}_s \right], \\ \bar{\xi} \frac{\partial}{\partial x_3} \left( R \frac{\nu_T}{\text{Pr}} \right) &= \rho_0 \bar{\xi}_s r^{-1/2} \frac{\partial}{\partial x_3} \left( \frac{\nu_{Ts}}{\text{Pr}} r^{1/2} \right) = \rho_0 \bar{\xi}_s \left[ \frac{\partial}{\partial x_3} \left( \frac{\nu_{Ts}}{\text{Pr}} \right) + \frac{1}{2} \frac{r'}{r} \frac{\nu_{Ts}}{\text{Pr}} \right], \\ R \frac{\nu_T}{\text{Pr}} \bar{\xi} &= \rho_0 \bar{\xi}_s \frac{\nu_{Ts}}{\text{Pr}}. \end{aligned}$$

Taken together, the subfilter-scale potential temperature flux divergence, in terms of the scaled variables, is

$$\begin{aligned} \frac{1}{R} \frac{\partial (R\lambda_i)}{\partial x_i} &= \frac{\Theta'}{r} \left\{ \frac{\partial \bar{\xi}_s}{\partial x_i} \frac{\partial}{\partial x_i} \left( \frac{\nu_{Ts}}{\text{Pr}} \right) + \frac{\nu_{Ts}}{\text{Pr}} \frac{\partial^2 \bar{\xi}_s}{\partial x_i^2} + \left[ \frac{\Theta''}{\Theta'} - \frac{1}{2} \frac{r'}{r} \right] \bar{\xi}_s \frac{\partial}{\partial x_3} \left( \frac{\nu_{Ts}}{\text{Pr}} \right) \right. \\ &\quad \left. + \left[ 2 \frac{\Theta''}{\Theta'} - \frac{1}{2} \frac{r'}{r} \right] \frac{\nu_{Ts}}{\text{Pr}} \frac{\partial \bar{\xi}_s}{\partial x_3} + \left[ \frac{\Theta'''}{\Theta'} - \frac{1}{2} \frac{r'}{r} \frac{\Theta''}{\Theta'} - \frac{1}{2} \left( \frac{r'}{r} \right)' \right] \bar{\xi}_s \frac{\nu_{Ts}}{\text{Pr}} \right\}. \quad (\text{F.2}) \end{aligned}$$

In a uniformly stratified anelastic gas, the background potential temperature profile is  $\Theta = \theta_0 e^{x_3/H_\theta}$  and the background mass density profile is  $R = \rho_0 e^{-x_3/H_\rho}$ , and consequently  $\Theta''/\Theta' = 1/H_\theta$ ,  $\Theta'''/\Theta' = 1/H_\theta^2$ , and  $r'/r = R'/R = -1/H_\rho$  are constants. As a result, the coefficients on the perturbation fields on the right-hand side of Eq. (F.2) simplify considerably, so that

$$\frac{1}{R} \frac{\partial (R\lambda_i)}{\partial x_i} = \frac{\Theta'}{r} \left\{ \left[ \frac{\partial \bar{\xi}_s}{\partial x_i} + \frac{1}{H_*} \bar{\xi}_s \delta_{i3} \right] \frac{\partial}{\partial x_i} \left( \frac{\nu_{Ts}}{\text{Pr}} \right) + \left[ \frac{\partial^2 \bar{\xi}_s}{\partial x_i^2} + \left( \frac{1}{H_*} + \frac{1}{H_\theta} \right) \frac{\partial \bar{\xi}_s}{\partial x_3} + \frac{1}{H_* H_\theta} \bar{\xi}_s \right] \frac{\nu_{Ts}}{\text{Pr}} \right\},$$

where we defined  $1/H_* := 1/H_\theta + 1/2H_\rho$  for convenience.

Using the scaled eddy viscosity  $\nu_{Ts}$  and the resolved strain rate tensor  $\bar{S}_{ij}$ , it is straightforward to define the scaled subfilter-scale stress tensor implicitly in terms of scaled variables by

$$\tau_{sij} := r\tau_{ij} = -2r\nu_{Ts}r^{-1/2}\bar{S}_{ij} = -2\nu_{Ts}\bar{S}_{sij},$$

where  $\bar{S}_{sij} = r^{1/2}\bar{S}_{ij}$  is the scaled resolved strain rate tensor given in terms of scaled variables by Eq. (F.1).

:wq